

ALMA MATER STUDIORUM
UNIVERSITÀ DI BOLOGNA

DOTTORATO DI RICERCA IN

ASTROFISICA

Ciclo 38

Settore Concorsuale: 02/C1 - ASTRONOMIA, ASTROFISICA, FISICA DELLA TERRA E DEI PIANETI

Settore Scientifico Disciplinare: FIS/05 - ASTRONOMIA E ASTROFISICA

ORBITAL ANISOTROPY ANSATZ FOR THE JEANS MODELING OF AXISYMMETRIC GALAXIES

Presentata da: Leonardo De Deo

Coordinatore Dottorato

Andrea Miglio

Supervisore

Luca Ciotti

Co-supervisore

Silvia Pellegrini

Esame finale anno 2026

"E così questo immenso occhio comincia a guardare nelle profondità dello spazio, forse proprio a centomila milioni di miliardi di chilometri, e noi comprendiamo che in fondo - come tutte le cose fatte dall'uomo - esso serve soltanto a guardare dentro di noi."

Marcello Ceccarelli (1927-1984) - *L'avventura di vivere*

ABSTRACT

The kinematic properties of galaxies are recovered for samples of ever-growing size and increasing quality thanks to the recent large integral-field spectroscopic surveys, and more sophisticated data analysis and modeling techniques. In this context, the Jeans equations (JEs) are one of the standard tools for studying the stellar dynamics of galaxies, and to extract physically relevant information from observations. However, they suffer from a closure problem, and in order to solve the equations a possible choice is the phenomenologically motivated "b-ansatz", widely used in the Jeans modeling of axisymmetric galaxies classified as regular rotators and stellar disks. In this thesis, we first provide a general discussion on how the b-ansatz affects the solution of the JEs, being able to predict, a priori from solving the JEs, the qualitative features of the resulting kinematic fields for different choices of b. In this way, as a function of the structural properties of the model under investigation, we can constrain the values of b that assure the positivity of the azimuthal velocity field $\overline{v_\varphi^2} = \overline{v_\varphi}^2 + \sigma_\varphi^2$, necessary for the model consistency, and of $\Delta_R = \overline{v_\varphi^2} - \sigma_R^2$ and $\Delta = \overline{v_\varphi^2} - \sigma_z^2$, which are used for a well-known decomposition of $\overline{v_\varphi^2}$ into its ordered and dispersion components. Then, by discussing some axisymmetric disky and ellipsoidal (oblate and prolate) models, we apply this general procedure to some realistic case studies, understanding if and how the b-anisotropy is connected to the properties of the galaxy. We retrieve from a theoretical point of view the empirical trend such that galaxies with a more flattened stellar density profile support a larger amount of b-anisotropy, finding how this is almost independent of the specific model involved. Finally, we conduct a first, exploratory analysis of the b-anisotropy in massive, passive and very axisymmetric early-type galaxies from the TNG50 simulation. We verify that these galaxies can be modeled sufficiently well through the three-integral JEs with the b-ansatz, where b is in general greater than unity (i.e., $\sigma_R > \sigma_z$) for all the systems in the sample. However, in this case a trend between the amount of b-anisotropy and the stellar density flattening is not apparent, and no clear correlations between the spatial distribution of the b field and the properties of the galaxy emerge, suggesting that a more thorough analysis is needed. Overall, this work provides a general understanding of how the b-ansatz affects galactic kinematics, and strengthens the modeling techniques to interpret current and future observational data.

Contents

1 Overview on early-type galaxies **1**

1.1 Photometry of early-type galaxies . . . 2

1.1.1 Surface brightness profiles . . . 4

1.2 Kinematics of early-type galaxies . . . 5

1.3 Dynamical modeling of early-type galaxies . . . 7

1.3.1 The Jeans Anisotropic Modeling formalism . . . 9

1.4 Empirical trends . . . 12

1.5 Focus and motivation of our work . . . 16

1.6 Outline of the thesis . . . 19

2 The Jeans equations **23**

2.1 The distribution function . . . 24

2.1.1 The collisionless Boltzmann equation . . . 25

2.2 Derivation of the Jeans equations . . . 26

2.2.1 Dependencies of the distribution function . . . 28

2.3 The Jeans equations for axisymmetric systems . . . 29

2.3.1 Two-integral models . . . 30

2.3.2 Three-integral models . . . 33

3 The b-ansatz **35**

3.1 The Jeans equations with the b-ansatz . . . 36

3.1.1 Decompositions of azimuthal motions . . . 37
3.2 Physical constraints on the b-ansatz . . . 38
3.2.1 Positivity of $\overline{v_\varphi^2}$: the $\mathscr{B}$ region . . . 38
3.2.2 Positivity of Δ_R: the $\mathscr{D}$ region . . . 39
3.2.3 Positivity of Δ: the $\mathscr{C}$ region . . . 40
3.3 General considerations . . . 41
3.3.1 Models with $[\rho_*, \Phi] > 0$ . . . 41
3.3.2 Models with $[\rho_*, \Phi] = 0$ . . . 42
3.3.3 Models with $[\rho_*, \Phi] < 0$ . . . 43

4 Axisymmetric models **45**
4.1 One-component models . . . 46
4.1.1 Miyamoto & Nagai disk . . . 46
4.1.2 Satoh disk . . . 53
4.1.3 Ellipsoidal Sérsic models . . . 57
4.1.4 Ellipsoidal γ-models . . . 64
4.1.5 Effects of flattening and shape . . . 71
4.2 Two-component models . . . 76
4.2.1 Miyamoto & Nagai disk in a dominant Binney logarithmic halo . . . 76
4.2.2 de Vaucouleurs profile in a singular isothermal sphere halo . . . 79
4.2.3 Effects of a dark matter halo . . . 83
4.3 Models with $[\rho, \Phi] < 0$ . . . 87
4.3.1 Binney logarithmic halo . . . 88
4.3.2 Power-law ellipsoid in a dominant singular isothermal sphere . . . 92
4.3.3 Comparison with models with $[\rho, \Phi] > 0$ . . . 98

5 The b-ansatz for the Jeans modeling of TNG50 galaxies **105**
5.1 The TNG50 simulation: sample and selection criteria . . . 106
5.2 Structural and kinematic analysis . . . 107
5.2.1 Structural analysis of the stellar component . . . 107
5.2.2 Kinematic analysis of the stellar component . . . 111
5.2.3 Dynamical analysis . . . 111

5.3 Results of the analysis . . . 112
5.3.1 Comparison with theoretical and empirical results . . . 115

6 Summary and conclusions **121**
6.1 Effects of the b-ansatz on the stellar kinematics . . . 122
6.2 Results from axisymmetric models . . . 123
6.3 The b-anisotropy in TNG50 galaxies . . . 125
6.4 Perspectives . . . 126

A Mathematical background **133**
A.1 Gamma-related functions . . . 133
A.2 Hypergeometric functions . . . 135
A.3 Bessel functions . . . 135

B The μ-ansatz for the axisymmetric Jeans equations **137**

C The *Wolfram Mathematica* code **139**
C.1 Steps of the code . . . 141
C.2 Two-integral multi-component models . . . 144

D The one-component Binney logarithmic halo **147**

E A new deprojection formula for the Sérsic law **155**
E.1 Overview on the Sérsic law . . . 156
E.1.1 Approaches for the deprojection . . . 157
E.2 The asymptotically matched deprojection formula . . . 160
E.2.1 The $n \leq 1$ case . . . 164
E.2.2 Generalization to ellipsoidal density distributions . . . 166
E.3 Accuracy of the new formula . . . 166

F Ellipsoidal power-law models **171**
F.1 Power-law density profile in a dominant logarithmic potential . . . 171
F.2 Power-law profile in a singular isothermal sphere . . . 173
F.3 Power-law profile in a monopole potential . . . 186

G Technical results **193**

G.1 Relations between the $\mathscr{B}$, $\mathscr{C}$ and $\mathscr{D}$ regions 193

G.1.1 Results for $[\rho_*, \Phi] \geq 0$ 194

G.1.2 Results for $[\rho_*, \Phi] < 0$ 194

G.2 Relations between the limits for b 194

G.2.1 Results for $[\rho_*, \Phi] \geq 0$ 195

G.2.2 Results for $[\rho_*, \Phi] < 0$ 196

H Kinematic maps of the selected TNG50 galaxies **197**

CHAPTER 1

A BRIEF OVERVIEW ON EARLY-TYPE GALAXIES AND THEIR KINEMATICS

This thesis is focused on a widely-used approach to model the stellar dynamics in elliptical galaxies, and to retrieve information from observations about the structure and the nature of these astrophysical objects. To start this discussion, however, it is useful first to make an overview on what an elliptical galaxy actually is, and why astrophysicists have developed theoretical models and numerical techniques to try to interpret the observational data. The beginning of this field is referable to the works of the American astronomer Edwin Hubble (1889-1953), which almost a century ago convincingly demonstrated that galaxies are extragalactic objects. Today, we know that galaxies are fundamental building blocks of the Universe, cosmic structures containing billions of stars with sizes and masses comparable to our galaxy, the Milky Way (Figure 1.1).

Extending earlier, more rudimentary approaches (see Sandage 2005 for a historical review), Hubble (1926) proposed a well-defined scheme for visually classifying galaxies based on optical images. Two major classes emerged: (i) Early-Type Galaxies (ETGs), characterized by their smooth, elliptical or lenticular shapes without spiral arms, and (ii) spiral galaxies, defined by the presence of spiral arms traced by patchy dust and clumpy star-forming regions. In our current paradigm of galaxy formation, galaxies and the Supermassive Black Holes (SMBHs) at their center grow hierarchically, increasing in mass over time (see e.g. White and Rees 1978; Blumenthal

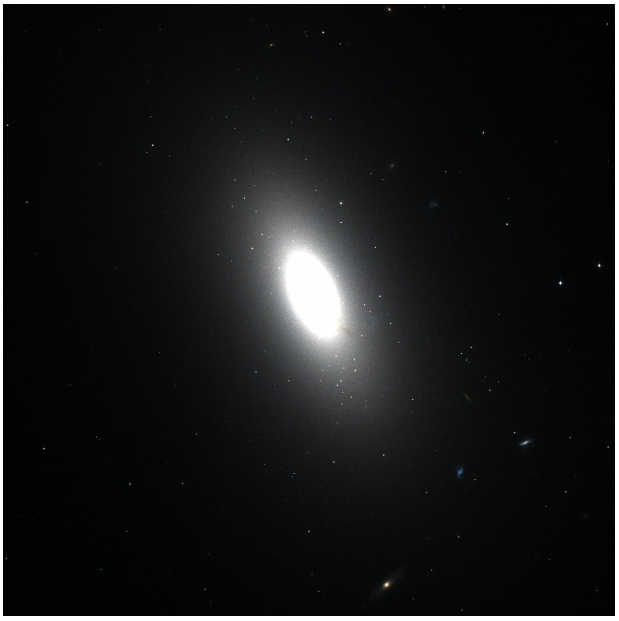


Figure 1.1. The elliptical galaxy NGC 3377 in the Leo constellation, one of the many galaxies reported in Hubble's "Atlas of galaxies" (Sandage 1961), as observed by the Hubble Space Telescope. Credits: NASA

et al. 1984). This suggests that ETGs represent the end-point of galaxy and SMBH evolution, and this motivates why they are ideal objects to test our understanding of galaxy formation and evolution. By examining ETGs properties such as their stellar populations, kinematics, and chemical abundances, astrophysicists can reconstruct their formation and evolutionary histories. Moreover, ETGs offer a unique laboratory for investigating how galaxies evolve through interactions with other systems: rarer but stronger processes like galaxy mergers, or more common but rapid encounters between galaxies can significantly impact ETGs properties, providing clues about how the environment shape their evolution through billions of years.

1.1 Photometry of early-type galaxies

The term "early" for ETGs was inspired to Hubble by the evolutionary sequence proposed by Jeans (1928), who also presented a fork-like diagram to visually arrange morphological classes. In the first published version of his classification, Hubble (1926) referred to all ETGs as "elliptical" galaxies; later, he introduced S0 galaxies as a "hypothetical class" intermediate between elliptical and spiral galaxies (Hubble 1936). At the time, the apparent shape of the galaxy on the plane of the sky was almost the only information available: hence, Hubble classified the ETGs based on their apparent axial ratio, defining the ellipticity $\varepsilon = 1 - b/a$, where b and a are the major and minor semiaxes of the (elliptical) galaxy isophotes. However, he later recognized that variations

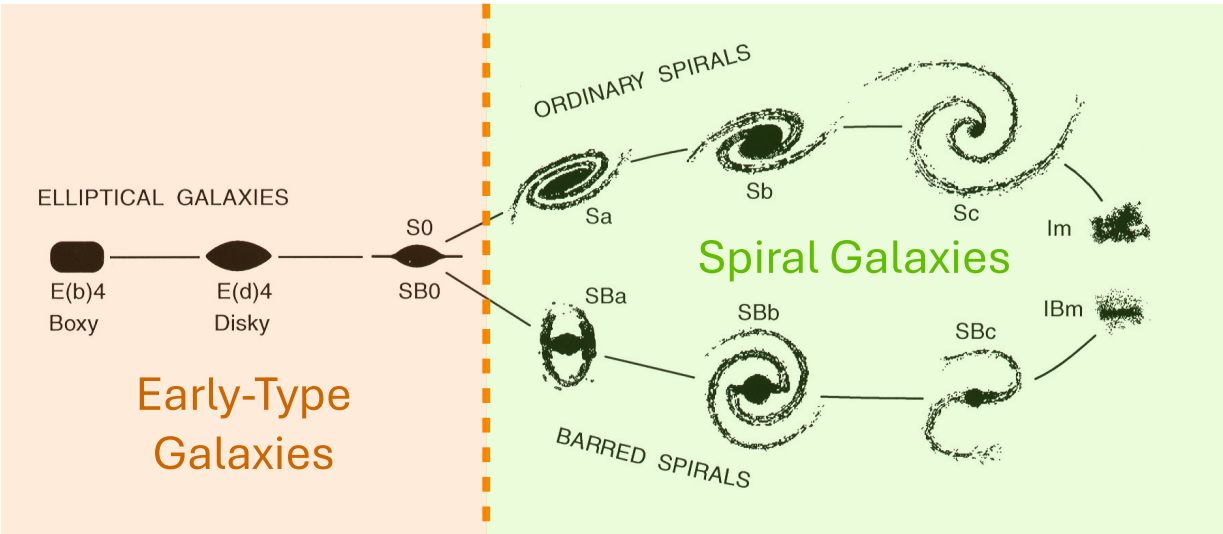


Figure 1.2. Hubble's tuning-fork diagram for galaxy classification. Early-type galaxies (E) populates the "handle", which then splits into two "prongs" representing spiral galaxies. The top prong depicts normal spirals (S), ranging from tightly wound, bulge-dominated types (Sa) to loosely wound, bulge-less types (Sc). The bottom prong shows barred spirals (SB), characterized by a bar-shaped structure and similar subclasses. Lenticular galaxies (S0), located at the fork's split, bridge the gap between elliptical and spiral galaxies, featuring a central bulge and disk but lacking prominent spiral arms. This version of the diagram was modified by Kormendy and Bender (1996) to include boxy E(b) and disky E(d) elliptical galaxies, as well as irregular galaxies (Im). Credits: Cappellari (2026)

in elliptical galaxies could not be described by ellipticity alone, and he proposed an additional separation into (i) ellipticals (E), with elliptical isophotes, and (ii) S0 galaxies, with lenticular shapes flatter than E7 but no evidence of spiral arms. Figure 1.2 presents Hubble's tuning fork, with the ETGs part of the diagram modified by Kormendy and Bender (1996) to account for key differences in the elliptical class.

Spiral galaxies are instead characterized by the presence of a stellar disk and spiral arms. However, at the center of the disk, they contain a stellar spheroid (or "bulge") which resembles a very flattened E galaxy. Hubble classified spiral galaxies as Sa, Sb, and Sc according to the prominence of the bulge, with Sa being the most bulge-dominated. He also noted that more bulge-dominated spirals have more closely coiled spiral arms and used this as an additional criterion in his classification. Although the distinction between early-type and spiral galaxies is based on visual images alone, the two types differ by various other characteristics, indicating that the classification is physically meaningful. ETGs appear smooth because they have lower amounts of gas and star formation than spiral galaxies. Therefore, their stellar population is generally older and they have redder colors. However, a separation based on color or ages is not fully equivalent to one based on morphology and cannot be used interchangeably (Strateva et al. 2001).

1.1.1 Surface brightness profiles

Early quantitative measurements of the surface brightness profiles of ETGs initially suggested that they could be universally described by an $R^{1/4}$ function (de Vaucouleurs 1948, hereafter dV). However, later observations suggested that these profiles were not universal, and they required a more general function proposed by Sérsic (1968):

$$I(R) = I_0 \mathrm{e}^{-b\,\eta^{1/n}}, \quad \eta \equiv \frac{R}{R_\mathrm{e}}, \tag{1.1}$$

where n is a shape parameter (best known as Sérsic index), I_0 is the central surface brightness, R is the radius in the projection plane, R_e is the effective radius (i.e., the radius in the projection plane enclosing half of the total luminosity of the profile), and b is a dimensionless parameter depending on n (see Appendix E.1). Qualitatively, as n increases, the galaxy light at radii around R_e is redistributed to both smaller and larger radii; a large n indicates a galaxy with both (i) a more concentrated light distribution in the central regions and (ii) a more extended stellar halo at larger radii. Most importantly, it was found that the Sérsic index n changes with the galaxy properties, as it increases with increasing total galaxy luminosity. This result was confirmed by a number of authors (see e.g. D'Onofrio, Capaccioli, and Caon 1994, Bertin, Ciotti, and Del Principe 2002, A. W. Graham and Guzmán 2003, Kormendy, Fisher, et al. 2009). The reported correlations were interpreted as due to a systematic change in the intrinsic properties of elliptical galaxies with luminosity, although this discussion is out of the present work (see e.g. A. W. Graham and Guzmán 2003).

Finally, we mention that with the advent of CCD detectors in the 1980s, it became possible to analyze the detailed shape of the isophotes of elliptical galaxies. It was discovered that some of these galaxies were not well approximated by pure ellipses, but they had more disky, or almond-shaped, isophotes. This was interpreted as indicating the presence of stellar disks, which were not as prominent as the disks of S0 galaxies and could only be detected as deviations of their isophotes from ellipses (Bender 1988). Bright galaxies, unlike fainter ones, lacked disky isophotes, and contained cores in their inner profiles: this was considered significant enough to propose a revision of Hubble's tuning-fork diagram. Kormendy and Bender (1996) suggested that there was a continuous sequence from S0 galaxies to disky ellipticals, while brighter ETGs with cores constituted a distinct class of objects. There was a crucial practical issue with the proposed

classification: the presence of stellar disks in ellipticals could only be revealed by the shape of their isophotes when galaxies were close to edge-on, and this limitation prevented the application of the proposed scheme on a galaxy-by-galaxy basis. A solution to the inclination dependence of photometric classification schemes is provided by stellar kinematics obtained with integral-field spectroscopic observations.

1.2 Kinematics of early-type galaxies

The photometric approaches to recognize different types of elliptical galaxies suffer from two limitations: (i) measuring density profiles require sub-arcsec spatial resolution, and (ii) deviations from elliptical isophotes are only visible near edge-on orientations. This prevents the applicability of either technique to the large galaxy samples at significant distances. A solution to both limitations is provided by Integral-Field Spectroscopy (IFS). In fact, IFS observations of the stellar kinematics allow to recognize the presence of stellar disks at virtually any inclination; this is illustrated in Figure 1.3, where, by using dynamical models (see Section 1.3), it is shown how two nearly edge-on galaxies, the disky NGC 821 and the S0 galaxy NGC 5308, would appear when seen close to face-on. From the Figure, we see that both the centrally concentrated disk of a disky E, and the extended dick of an S0 galaxy, produce clear observable signatures in the kinematics at nearly all inclinations. In both cases, the velocity fields display extended ordered rotation; in contrast, measurable effects on the shape of the isophotes are practically absent.

A breakthrough came with the SAURON survey (de Zeeuw et al. 2002), due to the dramatic improvement of the instrument data quality with respect to previous prototypes. It was the first project to map the two-dimensional stellar kinematics, ionized gas, and stellar population of a significant sample of 48 nearby ETGs with total absolute magnitudes $M_B < -18$. From a simple visual inspection of the kinematic maps of the sample galaxies (see Emsellem, Cappellari, Peletier, et al. 2004), two distinct classes of ETGs emerge (Figure 1.4): one class of galaxies is consistent with the models of Figure 1.3 (right panel), i.e. with stellar disks seen at various inclinations, whereas the other class is clearly inconsistent with simple disks (other panels), exhibiting a more irregular (if any) pattern of stellar motions. In two companion papers from the survey, this initial insight led to the proposal of a quantitative kinematic classification of ETGs, virtually independent of inclination effects (Emsellem, Cappellari, Krajnović, van de Ven, et al. 2007, Cappellari, Emsellem, Bacon, et al. 2007).

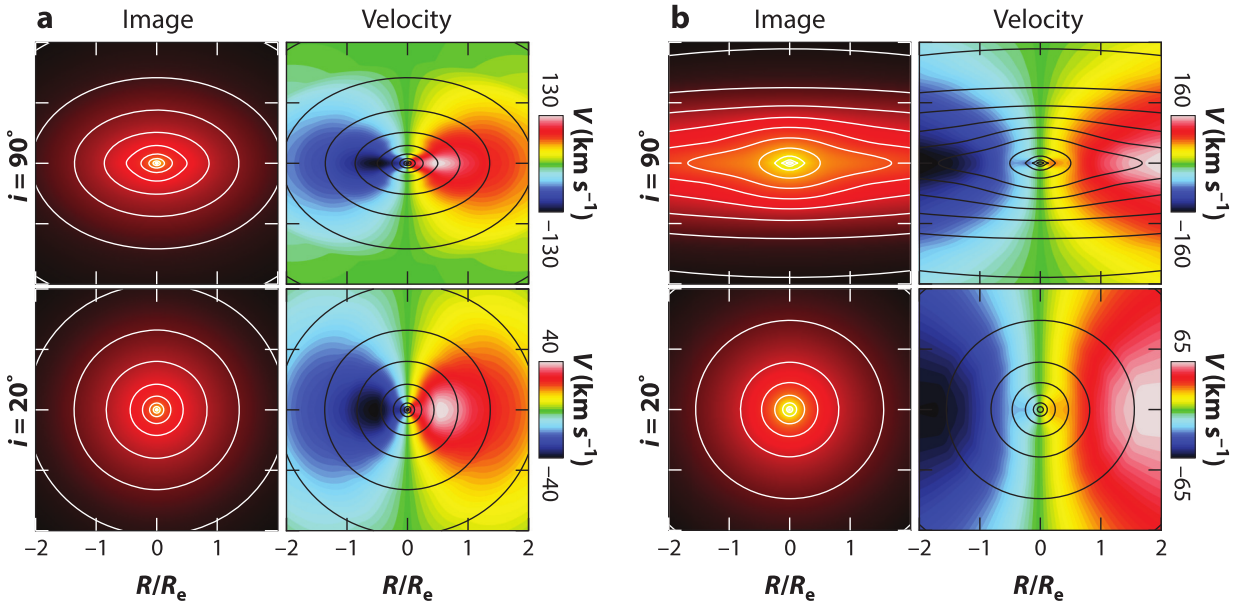


Figure 1.3. Recognizing stellar disks from the observed kinematics. Left panel: Photometric models for the disky elliptical galaxy NGC 821, projected at two inclinations. The rainbow-colored panels show the corresponding stellar velocity field predicted by the Jeans anisotropic models (see Section 1.3.1). Right panel: Same as in the left panel, but for the S0 galaxy NGC 5308. The presence of a disk can be visually recognized from the kinematics even near face-on inclination, although the photometric evidence disappears. Credits: Cappellari (2016)

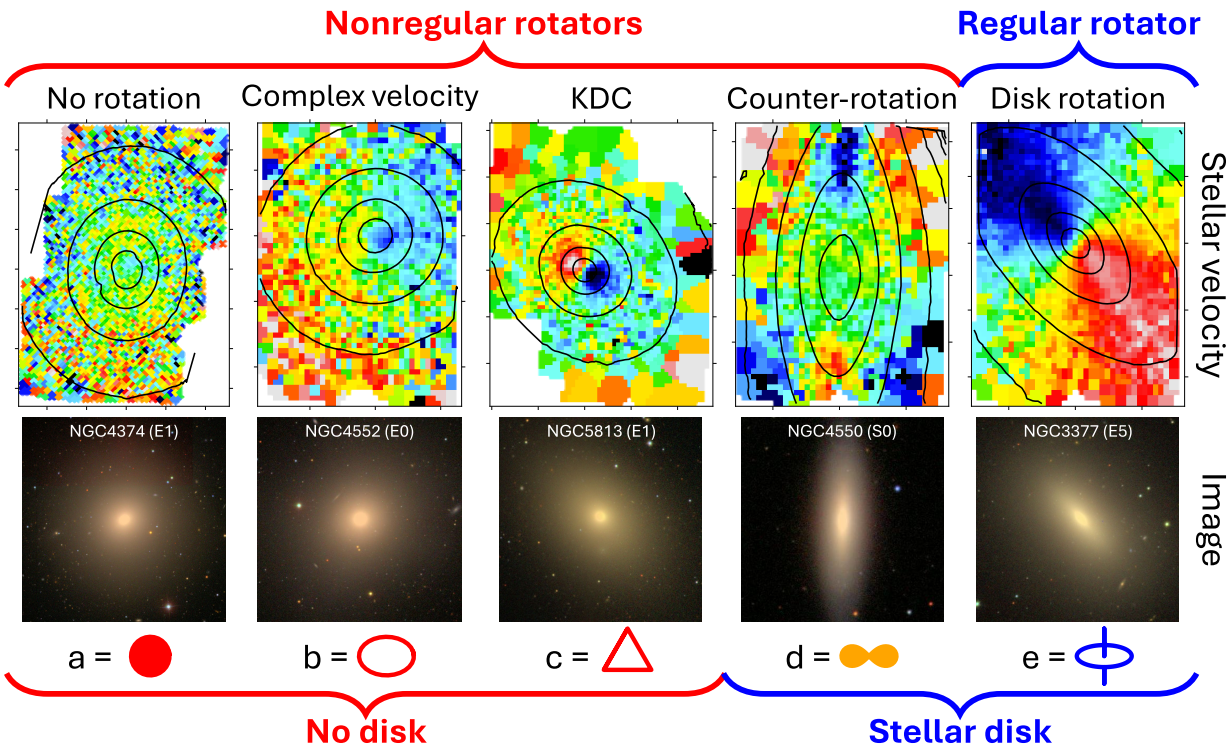


Figure 1.4. Morphological classifications based on stellar kinematics. The kinematic features in large samples of ETGs can be qualitatively described by five distinct classes (from left to right): (i) no clearly detectable rotation (NGC 4374), (b) clear but non-regular rotation (NGC 4552), (c) kinematically distinct cores (KDCs) (NGC 5813), (d) counter-rotating disks (NGC 4550), and (e) regular, extended, disk-like rotation (NGC 2974). The symbols above the maps correspond to the different morphological classes. Credits: Cappellari (2026)

The SAURON survey was then followed by the ATLAS3D project (Cappellari, Emsellem, Krajnović, et al. 2011), which was a multi-wavelength (from radio to millimeter and optical) survey combined with a theoretical modeling effort. It targeted a complete sample of 260 ETGs, extracted from a volume-limited sample of 871 galaxies brighter than $M_K < -21.5$, within 42 Mpc; the survey includes galaxies with a minimum stellar mass of $M_* \gtrsim 6 \times 10^9\,\mathrm{M}_\odot$. ATLAS3D confirmed the striking visual distinction between the kinematics of regular and non-regular rotators (Krajnović et al. 2011), proposing additional subclasses for the latter. Non-regular rotators were found to (a) either not rotate at all, (b) show clear but not symmetric rotation, (c) present Kinematically Decoupled Cores (KDC), or (d) have two counter-rotating disks (such as the prototypical S0 NGC 4550 discovered by Rubin, J. A. Graham, and Kenney 1992).

1.3 Dynamical modeling of early-type galaxies

In order to extract information from the maps obtained through IFS observations, the dynamical modeling of the stellar kinematics is needed. A key assumption of the models is that the galaxies are in a steady state, and they are assumed to have simple spherical, axisymmetric, or triaxial shapes. Under the steady-state assumption, the galaxy dynamics is fully specified by (i) the six-dimensional stellar Distribution Function (DF), which describes the distribution of the positions and velocities of stars in the galaxy (see Section 2.1), and (ii) the gravitational potential, or equivalently the total mass distribution, which may include a stellar contribution as well as a Dark Matter (DM) halo and a SMBH.

Three main techniques have been used to model the stellar dynamics of ETGs, to understand their orbital distribution and the distribution of their mass content:

- Jeans modeling: First applied by Jeans (1922), it relies on the solution of the so-called Jeans Equations (JEs), which model stars like an incompressible fluid in the six-dimensional phase space moving under the influence of gravity, and whose solutions are the velocity moments of the DF, which are then fitted to the observed kinematics.

- Orbit-superposition technique: Proposed by Schwarzschild (1979), it computes all the possible orbits in a fixed gravitational potential, and then finds the linear combination of those orbits that best fits the galaxy kinematics and photometry.

- Made-to-measure technique: Introduced by Syer and Tremaine (1996), it tries to nudge a non-steady-state N-body model towards fitting the observed kinematics. For a fixed gravitational potential, it is conceptually similar to the orbit-superposition technique, but less efficient.

The first method has the advantage that it is sufficiently flexible, as the stellar density distribution of the model can be chosen at the beginning to be in good agreement with the observational data (e.g. by using specific density profiles, or by multi-component modeling), and it has predictive power. In contrast, the latter two methods have the advantage of generality, which is required for unbiased results; however, they cannot make true predictions, and the results they yield depend on the details of how the methods are implemented. Other possibilities rely on deriving all the model properties from the DF, assuming that the gravitational potential is produced by the stars alone (e.g. King 1963, Stiavelli and Bertin 1985, Bertin and Varri 2008), or using a DF built from actions (e.g. J. Binney 2010; see also Posti et al. 2015, J. Binney and Vasiliev 2023), but we do not explore these approaches in more detail here; however, all of them are not always well suited for exploratory works, as in general the solution of the problem requires non-trivial numerical work.

We stress also that the recovery of the DF and the mass distribution using only line-of-sight quantities is an intrinsically degenerate or ill-posed problem, and consequently with a not unique solution. This is because the DF can be expressed as a function of three isolating integrals of motion (Jeans 1915, see also Section 2.1.1), and one cannot expect to uniquely constrain both the three-dimensional DF and the three-dimensional mass distribution using only a three-dimensional observable, namely the line-of-sight velocity distribution at every location on the plane of the sky). Moreover, the deprojection of the stellar surface brightness into an intrinsic stellar luminosity density is mathematically non-unique, even when assuming axisymmetry, unless the galaxy is edge-on. This degeneracy increases rapidly at lower inclinations (see e.g. Gerhard and J. J. Binney 1996, Romanowsky and Kochanek 1997, F. C. van den Bosch 1997), and it represents a natural, but fundamental barrier to model galaxies. Empirical explorations of model degeneracies using IFS data have revealed that, even in an ideal case in which one (i) uses mock noiseless two-dimensional data, (ii) artificially removes the deprojection degeneracy, and (c) assumes that the gravitational potential is produced by the stars alone (i.e., the self-gravitating case), basic parameters such as galaxy inclination or shape are virtually unconstrained (see e.g. R. C. E. van

den Bosch and van de Ven 2009).

With the previous caveats in mind, key results were obtained using dynamical models fitted to stellar kinematics. As DM appears to play a minor role within one effective radius (see Section 4.2.2 of Cappellari 2026), implying that at those radii the shape of the total mass density is close to that of the luminous density, the availability of the first set of IFS data from the SAURON survey (de Zeeuw et al. 2002) opened up the possibility for more thorough modeling of ETGs. To quantify this large amount of information, some anisotropy parameters were defined, where with the term "anisotropy" we refer to the ratio between the velocity dispersion measured along different directions by a hypothetical observer in the galaxy moving with the average stellar velocity. In particular, in Cappellari, Emsellem, Bacon, et al. (2007) the two quantities[1]

$$\beta_z = 1 - \frac{\Pi_{zz}}{\Pi_{RR}}, \quad \gamma_\varphi = 1 - \frac{\Pi_{\varphi\varphi}}{\Pi_{RR}}, \quad \Pi_{kk} \equiv \int \rho_* \, \sigma_k^2 \, d^3\mathbf{x} \tag{1.2}$$

are introduced, where ρ_* is the stellar density, σ_k^2 is the (squared) stellar velocity dispersion along the direction k (see Section 2.1), and the integral is performed over all the volume of the galaxy; in practical applications, however, the numerical integral typically extends to the region covered by the IFS observations. In practice, β_z describes the global shape of the velocity dispersion tensor in the $(v_R - v_z)$ plane, while γ_φ describes the global shape of the velocity dispersion tensor in a plane orthogonal to v_z. If the anisotropy is spatially constant, then $\beta_z = 1 - \sigma_z^2/\sigma_R^2$ and $\gamma_\varphi = 1 - \sigma_\varphi^2/\sigma_R^2$. Finally, for an isotropic system (i.e., a spherical velocity dispersion ellipsoid), $\beta_z = \gamma_\varphi = 0$. Calculation of these anisotropy parameters for 25 axisymmetric galaxies from the SAURON sample showed that, on average, (i) the velocity dispersion on the equatorial plane is higher on the equatorial plane than along the z-direction, (ii) the velocity dispersion ellipsoid (i.e., the ellipsoid in the velocity space with semiaxes proportional to σ along that direction) is oblate, i.e. $\sigma_R \approx \sigma_\varphi$ (or, equivalently, $\gamma_\varphi \approx 0$, and (iii) $\sigma_R > \sigma_z$ (or, equivalently, $\beta_z \gtrsim 0$).

1.3.1 The Jeans Anisotropic Modeling formalism

Motivated by the finding that the anisotropy of fast-rotator ETGs is on average best approximated as $\sigma_R > \sigma_z$, Cappellari (2008) developed an accurate and efficient method to solve the axisymmetric JEs, allowing for a velocity dispersion ellipsoid with generic axial ratios $\sigma_R \neq \sigma_z \neq \sigma_\varphi$, and which is aligned to the cylindrical coordinates. As discussed in detail in Sections 2.3 and 2.4 of

[1] From now on we will use standard cylindrical coordinates (R, φ, z), where z is along the symmetry axis.

that paper, the assumption on the alignment is just an approximation, as it cannot be accurately satisfied in real galaxies. This is the so-called Jeans Anisotropic Modeling (JAM) formalism (the results of which are referred to as JAM models), i.e. the anisotropic generalization of the semi-isotropic ($\sigma_R = \sigma_z$) formalism presented in Emsellem, Monnet, and Bacon (1994). Due to the linearity of the JEs, the JAM approach uses the Multi-Gaussian Expansion (MGE; Emsellem, Monnet, and Bacon 1994, Cappellari 2002) to parameterize the observed galaxy surface brightness, allowing an arbitrary number of Gaussians to reproduce all features of a galaxy image. In particular, one can describe in detail multiple photometric components, including bulges, disks, inner disks, and general ellipticity variations.

The comparison between the JAM models and the IFS observations of ETGs confirms the expectations from the Schwarzschild models. It shows that, assuming a spatially constant anisotropy with a cylindrically aligned velocity ellipsoid, one can predict the kinematics of stars with remarkable accuracy. This is shown in Figure 1.5 where the second velocity moment $V_{\rm rms} \equiv \sqrt{V^2 + \sigma^2}$ maps of regular-rotators are properly captured by this simple class of JAM models. Once the photometry of the galaxies is given as input, the models are fully specified by the single anisotropy parameter β_z and by the inclination i, as well as by the overall total mass-to-light ratio (M/L).

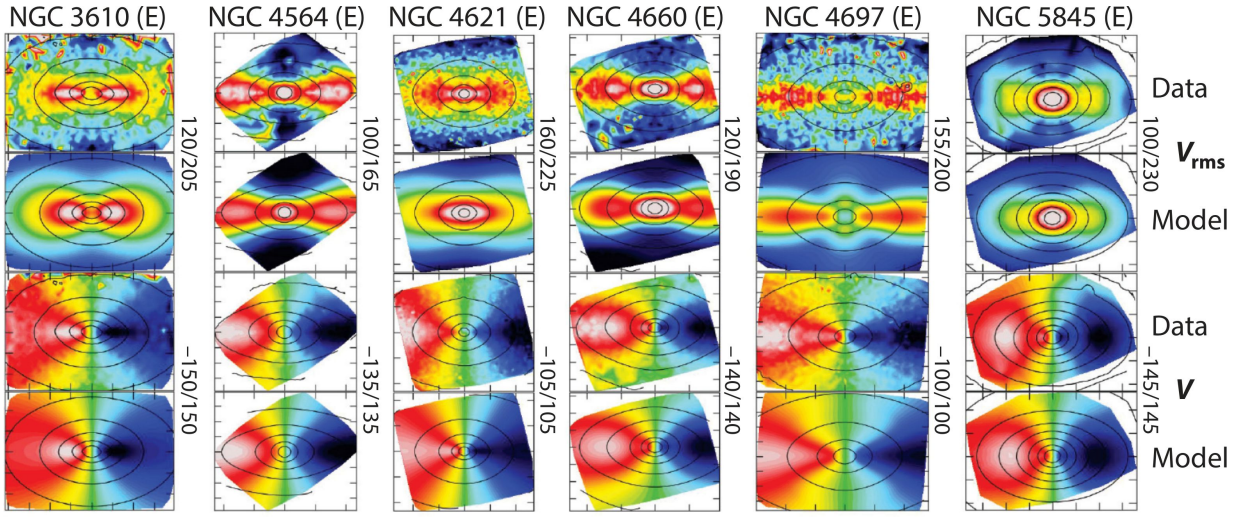


Figure 1.5. Jeans anisotropic models of regular rotators. The columns refer to six elliptical (E) galaxies from the SAURON survey (see Emsellem et al. 2004, Cappellari et al. 2011a). The rows show (from top to bottom): the symmetrized stellar $V_{\rm rms} \equiv \sqrt{V^2 + \sigma^2}$, the best fit to $V_{\rm rms}$, the observed mean stellar velocity V, and the best fit to V obtained by keeping the best-fitting anisotropy parameter (β_z), inclination, and mass-to-light ratio from the fit to $V_{\rm rms}$. Credits: Cappellari (2016)

The JAM method allows for the implementation of the other anisotropy parameter γ_φ, shown in equation (1.2). However, if one makes the simplest assumption of an oblate velocity ellipsoid

(i.e. $\gamma_\varphi = 0$), the shape of the mean stellar velocity field can also be quite accurately predicted without the need to invoke extra parameters. In a more quantitative way, if one takes the mean projected velocity field V predicted by JAM with a perfectly oblate velocity dispersion ellipsoid as a reference, the overall scaling factor (κ) required to best fit the observed velocity field $V_{\rm obs}$ is remarkably close to unity, with a very small scatter - which includes also the effect of measurement errors in β_z, i and M/L (Figure 1.6). No statistically significant difference is observed in the distribution of the elliptical and S0 regular rotators, while the non-regular rotators have a completely different distribution, which peaks at $\kappa = 0$ and has a broad tail. The result is also confirmed for the larger sample of galaxies from the final sample of ~ 10000 galaxies of the IFS survey MaNGA (Zhu et al. 2023; see Figure 9 of Cappellari 2026), whose unprecedented size and data quality establish it as the current benchmark for global galaxy property studies. This demonstrates a clean dichotomy, rather than a continuity, between the two classes of ETGs, and confirms that an oblate velocity ellipsoid provides a good approximation to the observed galaxy dynamics within $R_{\rm e}$.

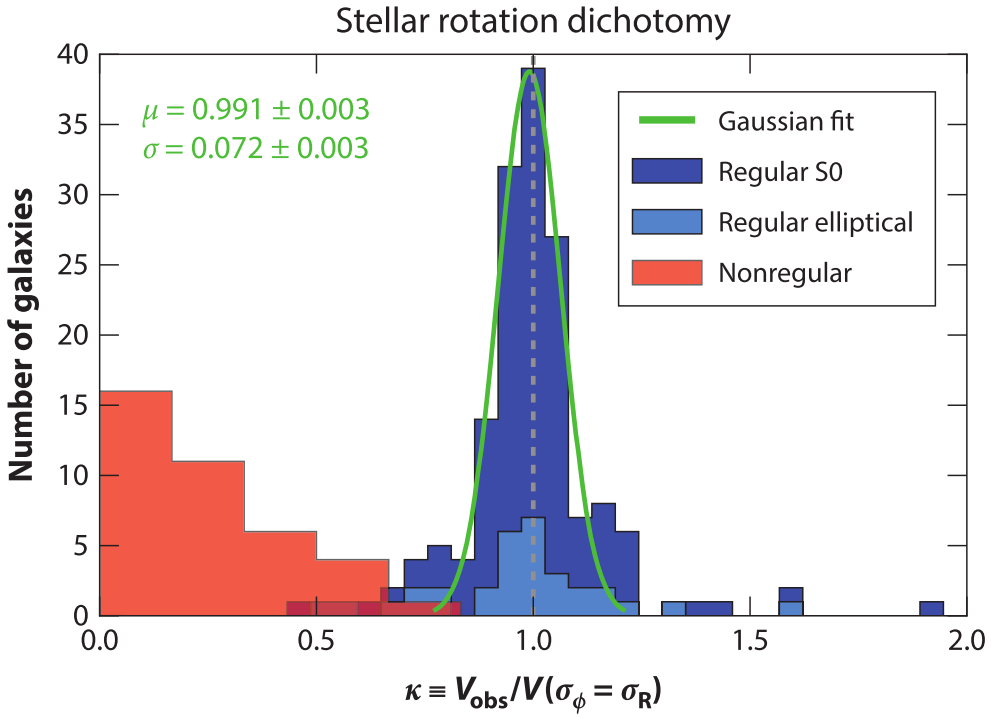


Figure 1.6. Histogram of the ratio κ between the observed velocity V_{obs} and the velocity $V(\sigma_R = \sigma_\varphi)$ predicted by a Jeans anisotropic model with an oblate velocity ellipsoid. The values are extracted from Cappellari, Scott, et al. (2013), and refers to the ATLAS3D survey sample. The green line is a Gaussian fit to the histogram, for the regular rotators only. Credits: Cappellari (2016)

1.4 Empirical trends

By applying Schwarzschild modeling to galaxies from the SAURON sample (Cappellari, Emsellem, Bacon, et al. 2007), the anisotropy parameters β_z of the regular rotators was found to be related to their intrinsic axial ratios $\varepsilon_{\rm intr}$, defined as (see e.g. Cappellari 2016)

$$\varepsilon_{\rm intr} = 1 - \sqrt{1 + \varepsilon\,(\varepsilon - 2)/\sin^2 i}, \tag{1.3}$$

where i denotes the galaxy inclination, with $i = \pi/2$ being the edge-on case. As shown in J. Binney (2005), the tensor virial theorem (see e.g. J. Binney and Tremaine 2008, hereafter BT08; Ciotti 2021, hereafter C21) already sets an upper limit for β_z as a function of $\varepsilon_{\rm intr}$, which is obtained by assuming a oblate velocity dispersion ellipsoid and considering the case with $V/\sigma = 0$ (see the dashed line in Figure 1.7). However, the observed values do not span the full space allowed by virial equilibrium, and in particular they are found to lie approximately below the linear relation (Cappellari, Emsellem, Bacon, et al. 2007):

$$\beta_z \approx 0.7\,\varepsilon_{\rm intr}, \tag{1.4}$$

with the range of possible values increasing with $\varepsilon_{\rm intr}$; this is found to be particularly true for regular rotators, while non-regular rotators tend to have $\sigma_R = \sigma_z$ ($\beta_z = 0$) in their central regions (see the left panel of Figure 1.7). These results, obtained from detailed dynamical models of a small set of galaxies, are fully consistent with those inferred by applying JAM to the much larger sample of ETGs from the ATLAS3D (see the right panel of Figure 1.7) and MaNGA (see Figure 8 in Cappellari 2026) surveys, assuming a velocity dispersion ellipsoid aligned in cylindrical coordinates. The application of JAM also show that this trend is not due to anisotropic disks embedded in isotropic bulges: in fact, the best fits to the kinematics are obtained with a constant anisotropy for both components.

The different kinematical behavior of regular and non-regular rotators is also caught by the empirical ($V/\sigma - \varepsilon$) diagram, showing the ratio between the stellar (average) ordered (V) and dispersion (σ) motions as a function of the apparent (i.e., on the plane of the sky) ellipticity of the galaxy. In particular, the first quantity (squared) is computed as

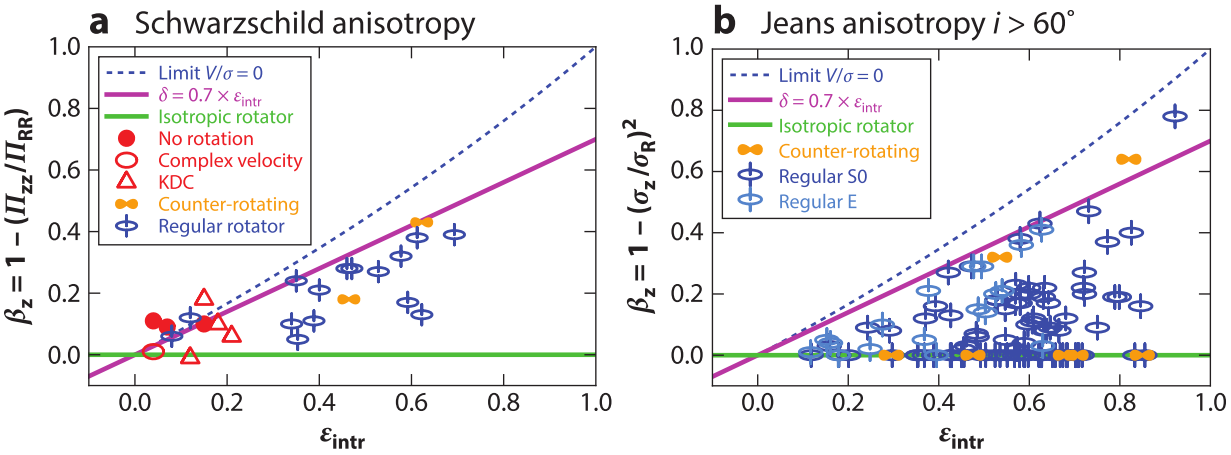


Figure 1.7. Anisotropy parameter β_z as a function of the intrinsic ellipticity $\varepsilon_{\rm intr}$ of the galaxies, from Schwarzschild modeling of SAURON galaxies in Cappellari, Emsellem, Bacon, et al. (2007) (left panel), or by applying JAM to ATLAS3D galaxies in Cappellari, Scott, et al. (2013) (right panel); in the latter case, only galaxies with $i > 60$ were included. In both the panels, the magenta line correspond to the curve in equation (1.4). The green line refers to the semi-isotropic case ($\sigma_R = \sigma_z$), and the dashed line is the limit to β_z as a function of $\varepsilon_{\rm intr}$ set by the tensor virial theorem (see e.g. BT08, C21), assuming an oblate velocity dispersion ellipsoid. The symbols denote the different galaxy classes, and are the same as those in Figure 1.4. Credits: Cappellari (2016)

$$\left(\frac{V}{\sigma}\right)^2 \equiv \frac{\sum_{n=1}^{N} F_n V_n^2}{\sum_{n=1}^{N} F_n \sigma_n^2}, \tag{1.5}$$

where V_n and σ_n are the stellar average velocity and velocity dispersion within a given spatial bin, F_n is the flux enclosed within that bin, and the sum is usually performed over all bins falling within the ellipse containing half of the total light of the galaxy. In Figure 1.8, we plot the $(V/\sigma - \varepsilon)$ diagram for the 260 ETGs from the ATLAS3D survey (Emsellem, Cappellari, Krajnović, Alatalo, et al. 2011), where the symbols denote the different galaxy classes as in Figure 1.4. We see that regular rotators are broadly distributed within the envelope defined by equation (1.4) (the magenta line) and all its projection at different inclinations (the thin dotted lines, see Cappellari, Emsellem, Bacon, et al. 2007), a region known in literature as the "magenta leaf". Therefore, regular rotators are broadly consistent with a population of randomly oriented axisymmetric galaxies with oblate velocity dispersion ellipsoids ($\gamma_\varphi = 0$), and an anisotropy satisfying the condition in equation (1.4). We also see that the anisotropy of regular rotators spans a range of values which is larger than that of the non-regular rotators; the former are generally not close to isotropic, but they often fall close to the edge-on isotropic line (the thick green line) due to projection effects. Finally, the green dashed line is the relation $(V/\sigma)^* = 1/3$, where $(V/\sigma)^* \equiv (V/\sigma)/(V/\sigma)_{\rm iso}$ is the ratio between V/σ and the corresponding theoretical value for an isotropic galaxy with the same ε; in

fact, in Cappellari, Emsellem, Bacon, et al. (2007) it had been shown that a value of $(V/\sigma)^* \approx 0.4$ approximately separated the regular and non-regular rotators extracted from the SAURON survey on the diagram, and this value was then refined for larger sample of galaxies.

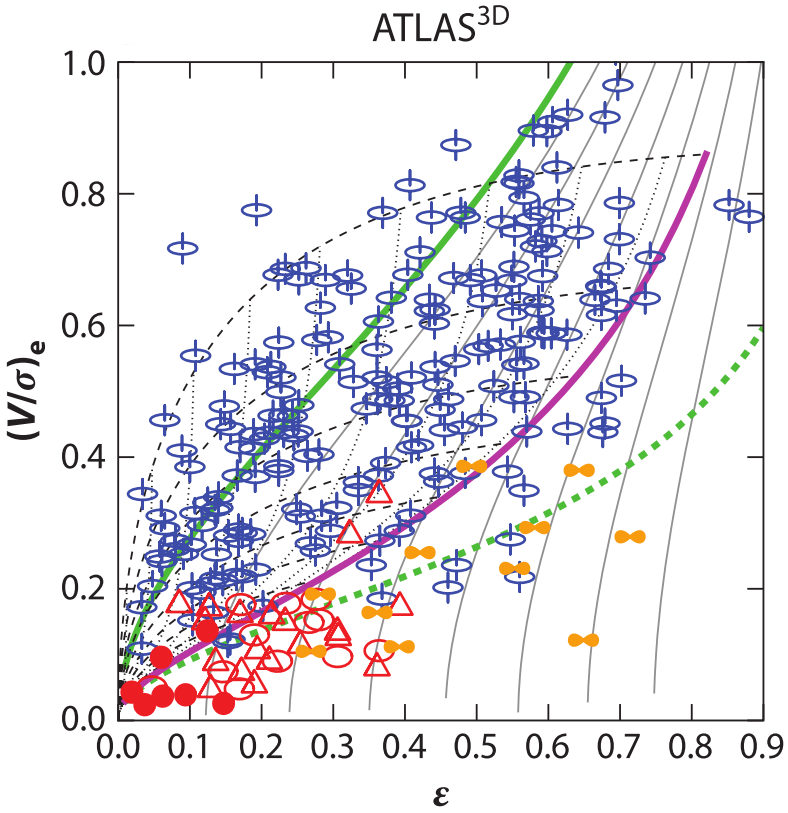


Figure 1.8. Average ratio V/σ inside the half-light ellipse as a function of the observed galaxy ellipticity ε, for the 260 ATLAS3D galaxies (Emsellem, Cappellari, Krajnović, Alatalo, et al. 2011). The magenta line is the edge-on projection of equation (1.4), and the thin dotted lines indicate how this relation transforms at different, equally spaced ($\Delta i = 10$) inclinations. The black dashed lines trace how galaxies with a particular $\varepsilon_{\rm intr}$ at $i = 90$ move with changing inclination (see Cappellari 2016). The solid green line is the prediction for an edge-on isotropic rotator, and the black thin lines refers to differences of $\beta = 0.1$ in the anisotropy parameter. The dashed green line refers to the case $(V/\sigma)^* = 1/3$. The symbols denote the different galaxy classes, as in Figure 1.4. Credits: Cappellari (2016)

Another quantitative way of distinguishing between regular and non-regular rotators is to look at the specific angular momentum parameter λ_R, introduced in Cappellari, Emsellem, Bacon, et al. (2007) to separate these two kinematic classes using IFS kinematics in a simple and reproducible way. This parameter is defined as

$$\lambda_R \equiv \frac{\sum_{n=1}^{N} F_n R_n |V_n|}{\sum_{n=1}^{N} F_n R_n \sqrt{V_n^2 + \sigma_n^2}}, \tag{1.6}$$

where F_n represents the fluxes within the N spatial bins where the mean stellar velocities V and velocity dispersions σ are measured. The summation extends to a specific finite radius within

a galaxy's isophote, usually R_e (and so the parameter is denoted as λ_{R_e}). The λ_R parameter is closely related to the V/σ parameter mentioned above, which we saw to be useful to analyze the interplay between shape, rotation, and anisotropy in ETGs; however, a significant distinction lies in the fact that λ_R is more sensitive to the spatial distribution of velocities. Similarly to what done for the V/σ parameter, it is possible to build the $(\lambda_R - \varepsilon)$ diagram, which has been systematically applied to growing samples of ETGs: Emsellem, Cappellari, Krajnović, van de Ven, et al. (2007) pioneered its use for 48 ETGs in the SAURON survey, Emsellem, Cappellari, Krajnović, Alatalo, et al. (2011) extended it to 260 galaxies in ATLAS3D, M. T. Graham et al. (2018) to 2,300 galaxies in MaNGA, Falcón-Barroso et al. (2019) to 600 galaxies in CALIFA, and van de Sande et al. (2021) to 3,000 galaxies in SAMI. The largest application to date leverages the final MaNGA survey sample of 10,000 galaxies (Zhu et al. 2023), whose unprecedented size and data quality establish it as the current benchmark for global galaxy property studies; in the left panel of Figure 1.9, we show the $(\lambda_R - \varepsilon)$ diagram for the latter dataset, adopting the kinematic classification of ETGs as in Figure 1.5. The magenta line represents the edge-on projection of equation 1.4, appropriately converted into λ_R (see Cappellari 2016); as in Figure 1.8, the magenta leaf constitutes the envelope in which regular rotators (and spiral galaxies, in this case) are located. The bulge-free disks and spiral galaxies populate the top of the region, while more bulge-dominated systems having lower ellipticity are found near the bottom of the magenta leaf. The black trapezium, instead, defines the new empirical separation boundary between the two kinematic classes, and it is defined as (see Cappellari 2016):

$$\lambda_{R_e} < 0.08 + \varepsilon_e/4, \quad \varepsilon_e < 0.4, \tag{1.7}$$

where again all of the quantities are measured inside the half-light ellipse. We see that most of the non-regular rotators visually classified with the scheme of Figure 1.5 fall within the slow-rotator region; more quantitatively, in the right panel of the Figure the histogram of the λ_{R_e} values is shown, which clearly reveals a double-peaked structure with the secondary peak within the trapezium region. A sharp transition in stellar masses is also observed between galaxies inside and outside the region, with galaxies inside it generally having larger masses than regular rotators of similar ε_e (see Figure 13 in Cappellari 2026).

Having established the physical distinction between regular and non-regular rotators, it is instructive to compare this classification against Hubble's classic morphological classification. One

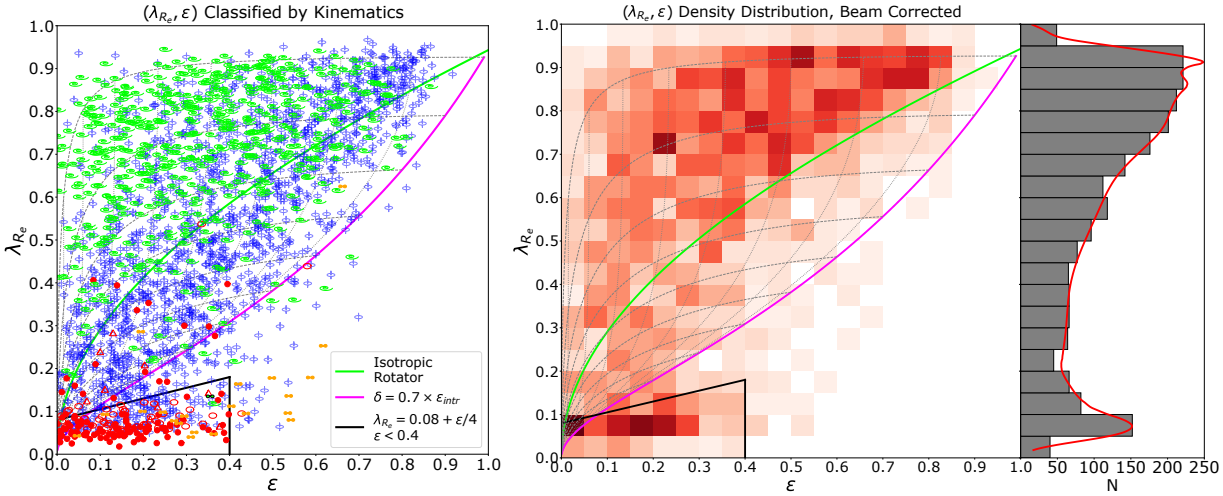


Figure 1.9. Left panel: Average specific angular momentum inside the half-light ellipse λ_{R_e} as a function of the observed galaxy ellipticity ε, for 2286 galaxies from the MaNGA IFS survey. The solid green line is the prediction for an edge-on isotropic rotator from J. Binney (2005), approximately converted into λ_{R_e} (see Emsellem, Cappellari, Krajnović, Alatalo, et al. 2011). The magenta line is the converted edge-on projection of equation (1.4), and the thin dotted lines indicate how this relation transforms at different, equally spaced ($\Delta i = 10$) inclinations. The black dashed lines trace how galaxies with a particular $\varepsilon_{\rm intr}$ at $i = 90$ move with changing inclination (see Cappellari 2016). The black trapezium in the lower-left corner define the region in equation (1.7). Right panel: Same as in the left panel, but with the distribution of galaxies shown as a two-dimensional histogram, and as a one-dimensional histogram on the right. The symbols denote the different galaxy classes, as in Figure 1.4, and spiral galaxies (included in the survey) are marked in green. Credits: Cappellari (2026)

finds that just about 1/3 of galaxies morphologically classified as ellipticals are slow rotators (see Emsellem, Cappellari, Krajnović, Alatalo, et al. 2011). This implies that Hubble's classification of elliptical galaxies is in general not comprehensive, because in the vast majority of cases it selects fast rotator ETGs. These are inclined galaxies with disks, which would be classified as either S0 or disky ellipticals if seen edge-on. This highlights the usefulness of using the new kinematic classification of ETGs.

1.5 Focus and motivation of our work

The kinematic properties of galaxies, as the ones discussed above, are nowadays recovered for samples of ever-growing size and increasing quality, thanks to the recent large IFS surveys such as ATLAS3D (Cappellari et al. 2013), SAMI (Scott et al. 2015) and MaNGA (H. Li et al. 2018), and more sophisticated data analysis and modeling techniques. In this framework, as seen in the previous Sections, the JEs are one of the standard tools for studying the stellar dynamics of galaxies, and to extract physically relevant information from observations (e.g. Cappellari 2016, Zhu et al. 2023, Surti et al. 2024). However, the JEs suffer in general from a mathematical

"closure problem", namely there are more equations than unknown fields, and to solve them several approaches are possible. In the case of axisymmetric systems, the simplest and most common choice is to use the JEs obtained under the assumption that the velocity dispersion ellipsoid is aligned in cylindrical coordinates, although alternative assumptions on the alignment of the velocity dispersion ellipsoid are also possible, as with spherical coordinates (see e.g. Cappellari 2020); moreover, the underlying DF is often assumed to depend just on the stellar orbital energy and angular momentum along the symmetry axis. A well-known consequence of this choice is the resulting identity of the vertical (σ_z) and radial (σ_R) components of the velocity dispersion tensor, known as the semi-isotropic (or two-integral) case. However, as shown in Section 1.4, data often seem to require that σ_z and σ_R are not equal, and so a relationship between σ_z and σ_R in the JEs the introduction of a phenomenological, but observationally motivated relation between σ_z and σ_R to close the JEs is favored. A widely used choice is the so-called b-ansatz, introduced in Cappellari (2008) and then implemented into the JAM approach (see Section 1.3.1), for which $\sigma_R^2 = b\,\sigma_z^2$, with a suitably assigned positive value of b (linked to the anisotropy parameter β_z as $\beta_z = 1 - 1/b$). The solution of the resulting JEs proved to capture the main properties of the stellar orbits distribution inferred from extensive three-integrals Schwarzschild modeling of integral-field stellar kinematics, and to model adequately the observations, in particular those of axisymmetric galaxies classified as regular rotators and stellar disks (see Cappellari 2016 for a review). Also, more recently, this ansatz has been used to model data relative to dwarf spheroidal galaxies, in order to study the DM profiles at their centers, and understand the effect of galaxy inclination on the inferred kinematics (see e.g. Hayashi, Chiba, and Ishiyama 2020, Vitral, van der Marel, et al. 2024).

However, albeit phenomenologically satisfactory, the b-ansatz affects the solution of the JEs in a non-trivial way. In particular, as also noticed in Cappellari (2020), the azimuthal velocity field $\overline{v_\varphi^2}$ can become negative for some values of b, therefore making the entire model unphysical. For this reason, the properties of the solutions are usually studied numerically for a given b in a "trial-and-error" approach, which however can be quite time expensive. Therefore, it is useful to have a general framework able to predict the qualitative features of the kinematic fields that will be produced by given choices of b before solving the JEs. In this way, as a function of the structural properties of the model under investigation, one can constrain the values of b that assure the positivity of $\overline{v_\varphi^2}$, and produce the features of the azimuthal and radial velocity dispersion fields

that eventually match the observational data.

Also, Wang, Cappellari, and Peng (2021) recently showed that, by applying JAM to realistic mock galaxies, the empirical limits on the anisotropy parameter β_z as a function of the intrinsic ellipticity, as the collocation of the regular rotators of the so-called magenta leaf in the $(V/\sigma - \varepsilon)$ and $(\lambda_R - \varepsilon)$ diagrams, can be attributed to an approximate limit to equilibrium solutions for the stellar orbits in galaxies with a nearly-oblate ($\gamma_\varphi \approx 0$) velocity dispersion ellipsoid. In the left panel of Figure 1.10, we show the anisotropy upper limit ($\beta_{\rm ul}$) of the mock galaxies as a function of their intrinsic ellipticity ($\varepsilon_{\rm intr}$), obtained by applying JAM with a spatially constant β_z and both cylindrically and spherically aligned velocity dispersion ellipsoids; given the density profile of a galaxy, chosen to be realistic compared to the ATLAS3D survey data, the β_z parameter is computed by checking right the positivity of the $\overline{v_\varphi^2}$ field, which becomes negative (and so the model unphysical) for too large β_z. We clearly see a similarity between these plots and the ones in Figure 1.7, as all the galaxies stand below the relation in equation (1.4) (the magenta line). Moreover, in the right panel of Figure 1.10 we see that the same galaxies are also located inside the magenta leaf in the $(V/\sigma - \varepsilon)$ and $(\lambda_R - \varepsilon)$ diagrams, meaning that they are representative of the observed regular rotators shown in Figures 1.8 and 1.9. Therefore, these results suggest that a thorough investigation about how the b-ansatz affect the stellar kinematics, as on the limits on the b-anisotropy supported by a stellar systems, may reveal important information on the connection between orbital anisotropy and the other properties of ETGs.

Finally, given the outstanding progresses in numerical simulations of galaxy formation and evolution (see e.g. Crain and van de Voort 2023 for a very recent review on the topic), it would be interesting to extend the comparison of our results to the galaxies obtained by high-resolution numerical simulations of galaxy formation in a cosmological setting, such as the IllustrisTNG suite (see e.g. Pillepich, Springel, et al. 2018, Pillepich, Nelson, Springel, et al. 2019, Nelson, Springel, et al. 2019). The spatial resolution of such simulations is large enough to check whether the b-ansatz can be applied (for example, whether the velocity dispersion ellipsoid is aligned with the local basis of coordinates), how well the b-anisotropy (e.g., with a spatially dependent b) can describe the kinematic fields, and whether the values of b are related with the properties of the galaxies, as their flattening or shape, or their environment.

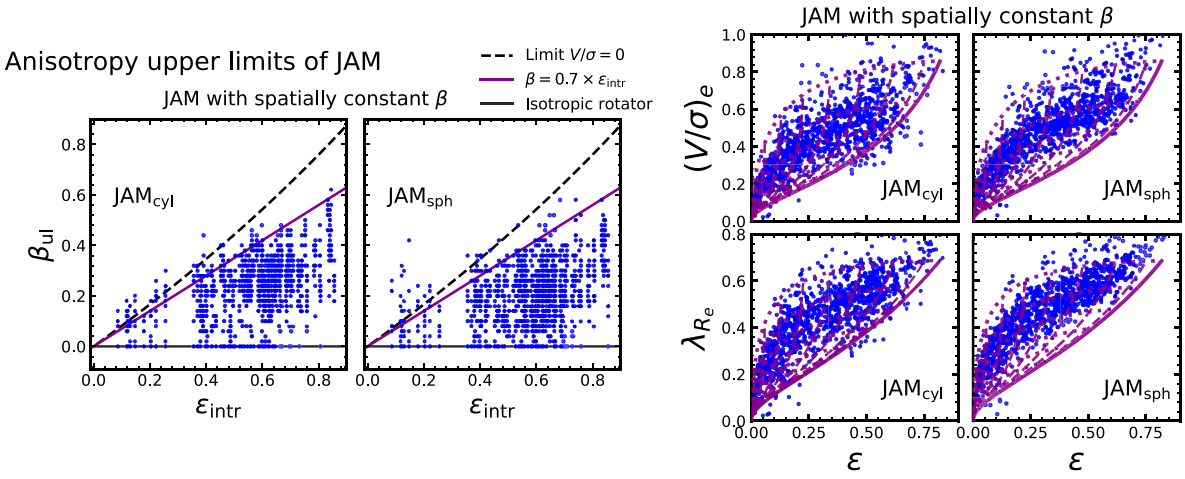


Figure 1.10. Left panel: Anisotropy upper limit βul as a function of intrinsic ellipticity $\varepsilon_{\rm intr}$ of mock galaxies modeled with JAM, by assuming spatially constant β_z and cylindrically ($\rm JAM_{cyl}$) or spherically ($\rm JAM_{sph}$) aligned velocity dispersion ellipsoids. The magenta line is the relation in equation (1.4), while the black dashed line is the limit to β_z as a function of $\varepsilon_{\rm intr}$ set by the tensor virial theorem (see e.g. BT08, C21) assuming an oblate velocity dispersion ellipsoid. Right panel: for the same mock galaxies of the left panel, ratio V/σ (top row) and specific angular momentum λ_R (bottom row) averaged inside the half-light ellipse as a function of the apparent ellipticity ε. The anisotropy parameter β_z of each model is restricted by the corresponding βul. The magenta line is the edge-on projection of equation (1.4), and the dashed lines indicate how this relation transforms for other inclinations. Credits: Wang, Cappellari, and Peng (2021)

1.6 Outline of the thesis

This thesis is structured as follows. In Chapter 2, we provide the general theoretical framework in which the JEs are used and implemented in the different dynamical models. We will derive the JEs fro axisymmetric systems from a more general equation which regulate the properties of the underlying DF, and then discuss how the possible dependencies of the DF on the integrals of motion of the system affects the form of the equations. Finally, we will show how the solution of the two-integral ($\sigma_z = \sigma_R$) JEs differ from that in the more general case with $\sigma_z \neq \sigma_R$, as suggested by observational data.

Then, in Chapter 3 we will introduce the b-ansatz as a way of mathematically solve the axisymmetric three-integral JEs. We will discuss the problem of the positivity of the kinematic fields $\overline{v_\varphi^2}$, which is necessary to ensure the consistency of the model, and Δ_R and Δ, required to apply a certain decomposition of the stellar motions in the azimuthal direction. The problem will be addressed in a very general way in the case of a b function depending on z (including the constant b case), providing formal criteria to find limits on the anisotropy parameter which guarantee the positivity of the fields. Also, we will provide a general understanding of how the kinematic fields are affected by more or less b-anisotropy, depending on some structural quantities

of the adopted model.

The results of our general procedure will be illustrated through two distinct classes of axisymmetric models: one-component models, in which a self-gravitating disky or ellipsoidal stellar density profile is considered, and two-component models, in which an external DM halo is added. This will allow to properly understand how the prescribed limits on b and the general behavior of the kinematic fields vary with respect to the galaxy flattening and shape, or the presence of the additional halo. In particular, for the more realistic (e.g., Sérsic 1968) galaxy models representative of the population of "regular rotators" we will address quantitatively a few natural questions: (i) Is there any behavior of the critical b values specifically associated with oblate shape and realistic density profiles, and that is missed by the analysis based on disky galaxy models? (ii) How are the kinematic fields affected by the b-anisotropy, especially in the galaxy regions where the gravitational field switches from being stellar dominated to DM dominated? (iii) Can we obtain some robust and sufficiently general indications about the dependence of the critical values of b on the flattening and the density profile of the stellar component of the galaxy? Moreover, we will also extend our analysis to a particular class of models which is representative of prolate galaxies, found to exist in both observations and simulations at high redshifts (see e.g. Pandya et al. 2024, Vega-Ferrero et al. 2024, Wang, Peng, et al. 2024).

Also, in Chapter 5 we will apply our framework to the stellar kinematics of simulated elliptical galaxies resembling realistic regular rotators. Our sample will be extracted from the TNG50-1 simulation, one of state-of-the-art cosmological magnetohydrodynamical simulations of galaxy formation and evolution (see Pillepich, Nelson, Springel, et al. 2019, Nelson, Pillepich, Springel, Pakmor, et al. 2019 for a full description of the simulation). In particular, we will check whether they can be modeled sufficiently well through the axisymmetric, three-integral Jeans equations addressed in the previous Sections, and we will analyze if there is any correlation between the shape and values of the $b = \sigma_R^2/\sigma_z^2$ field and the properties of the system (e.g., the stellar density flattening) and its environment.

Finally, in Chapter 6 the main results of the thesis will be summarized, and possible future research perspectives will be illustrated. In the Appendices at the end of the text, additional material is presented.

Publications

This thesis is based on the scientific works developed during the period of my PhD, which led to the following scientific publications:

- De Deo L., Ciotti L., Pellegrini S. (2024). "Anisotropy ansatz for the axisymmetric Jeans equations". In: *Monthly Notices of the Royal Astronomical Society* 530, pp.1796-1811
- Ciotti L., De Deo L., Pellegrini S. (2025), "An accurate and simple asymptotically matched deprojection of the Sérsic law". In: *Astronomy & Astrophysics*, Volume 694, A118
- De Deo L., Ciotti L., Pellegrini S. (2025). "Anisotropy ansatz for the Jeans equations: oblate galaxies". In: *Monthly Notices of the Royal Astronomical Society* 544, pp.2200-2213
- De Deo L., Baes M., Gebek A., Ciotti L., Pellegrini S. (2026) "Anisotropy ansatz for the Jeans modeling of axisymmetric TNG50 galaxies". In: *Astronomy & Astrophysics* (to be submitted)

CHAPTER 2

The Jeans equations

The JEs are one of the standard tools for the modeling of stellar systems, and the main focus of this thesis. For this reason, it is important to understand the general framework in which JEs are derived, as moments of a more general equation which regulates the behavior of the DF of the system; from this, the JEs in the case of axisymmetric galaxies will naturally come as a particular scenario, which is clearly of our interest. Also, different physical dependencies of the DF affect the resulting velocity fields in a different way: this leads to corresponding simplifications on the resulting equations, which turn out to be crucial in the modeling procedure.

This Chapter is organized as follows. In Section 2.1, we will introduce the DF for a generic system, and write the general equation that regulates the behavior of the DF in the phase-space of positions and velocities (Section 2.1.1). In Section 2.2, we will derive the general form of the JEs, and discuss the effects of the physical dependencies of the DF on the kinematic fields in the well-known case of two-integral systems (Section 2.2.1). Finally, in Section 2.3 we will explicitly write the JEs in the axisymmetric case, the one of our interest, considering systems which are supported by a two-integral (Section 2.3.1) or a more realistic three-integral (Section 2.3.2) DF.

2.1 The distribution function

When modeling a system such an elliptical galaxy, it is neither practical nor useful to follow the orbit of each star. As the comparison with observations is made on mean velocities, it is useful to define the DF f, non-negative everywhere, such that $f(\mathbf{w},t)\,\mathrm{d}^6\mathbf{w}$ is the probability that, at a given time t, a star of the galaxy has position and velocity in a volume $\mathrm{d}^6\mathbf{w} \equiv \mathrm{d}^3\mathbf{x}\,\mathrm{d}^3\mathbf{v}$ around $\mathbf{w} \equiv (\mathbf{x},\mathbf{v})$, in the six-dimensional phase-space. By definition, at any time t,

$$\int f(\mathbf{x},\mathbf{v},t)\,\mathrm{d}^3\mathbf{x}\,\mathrm{d}^3\mathbf{v} = N, \tag{2.1}$$

where N is the total number of stars in the galaxy, and the integral is computed over the whole phase-space.

Of course, the DF is connected with observable quantities. At any fixed position $\mathbf{x}$, the integral

$$n(\mathbf{x}) \equiv \int f(\mathbf{x},\mathbf{v})\,\mathrm{d}^3\mathbf{v}, \tag{2.2}$$

gives the number density of stars at $\mathbf{x}$ regardless of their velocity; this quantity can in principle be derived from the luminosity density of a galaxy. Analogously, the mean velocity of stars around the position $\mathbf{x}$ is defined as

$$\overline{\mathbf{v}}(\mathbf{x}) = \frac{1}{n(\mathbf{x})}\int f(\mathbf{x},\mathbf{v})\,\mathbf{v}\,\mathrm{d}^3\mathbf{v}, \tag{2.3}$$

and the spread of the stellar velocities around $\overline{\mathbf{v}}(\mathbf{x})$ at each point in the galaxy is characterized by the stellar velocity dispersion tensor

$$\sigma_{ij}^2(\mathbf{x}) \equiv \frac{1}{n(\mathbf{x})}\int f(\mathbf{x},\mathbf{v})\,(v_i-\overline{v}_i)\,(v_j-\overline{v}_j)\,\mathrm{d}^3\mathbf{v} = \overline{v_i v_j} - \overline{v}_i\overline{v}_j, \tag{2.4}$$

where the indices refer to the components of the tensor in the adopted coordinate system (e.g., x, y and z in Cartesian coordinates). From equation (2.4), we clearly see that the velocity dispersion tensor is symmetric for exchanges of the indices; therefore, from linear algebra, we know that there exists a set of orthogonal axes in which this tensor is diagonal, i.e.

$$\sigma_{ij}^2(\mathbf{x}) = \delta_{ij}\,\sigma_{ii}^2(\mathbf{x}), \tag{2.5}$$

where $\delta_{ij} = 1$ for $i = j$ and zero otherwise. The ellipsoid which have the diagonalizing coordinate axes as its principal axes, and σ_{11}, σ_{22} and σ_{33} as the lengths of its semiaxes is called the velocity dispersion ellipsoid at the position $\mathbf{x}$.

2.1.1 The collisionless Boltzmann equation

As a galaxy evolves with time, each star moves across the phase-space, and so the probability of finding it around any given point $(\mathbf{x}, \mathbf{v})$ changes accordingly. However, the total probability in the phase-space of the system must be conserved, in the same way that the total mass is conserved in a fluid flow. This latter case is described by the continuity equation

$$\frac{\partial \rho}{\partial t} + \frac{\partial}{\partial \mathbf{x}} \cdot (\rho \dot{\mathbf{x}}) = 0, \tag{2.6}$$

where $\rho(\mathbf{x})$ is the mass density of the fluid, and $\dot{\mathbf{x}} = \mathbf{v}$. Analogously, the equation for the conservation of the total probability in the phase-space is

$$\frac{\partial f}{\partial t} + \frac{\partial}{\partial \mathbf{w}} \cdot (\rho \dot{\mathbf{w}}) = 0, \tag{2.7}$$

best-known as the Collisionless Boltzmann Equation (hereafter CBE). The CBE is a partial differential equation for the DF as a function of the (six-dimensional) phase-space coordinates and time. For stars moving in a total gravitational potential $\Phi(\mathbf{x}, t)$, in Cartesian coordinates, the CBE reads:

$$\frac{\partial f}{\partial t} + \mathbf{v} \cdot \frac{\partial f}{\partial \mathbf{x}} - \frac{\partial \Phi}{\partial \mathbf{x}} \cdot \frac{\partial f}{\partial \mathbf{v}} = 0. \tag{2.8}$$

There exist some theorems related to the CBE, known as Jeans theorems because they were first stated in Jeans (1915), which involve the integrals of motion of a system, i.e. quantities $I(\mathbf{x}, \mathbf{v})$, independent explicitly on time, such that

$$\frac{dI}{dt} = \mathbf{v} \cdot \frac{\partial I}{\partial \mathbf{x}} - \frac{\partial \Phi}{\partial \mathbf{x}} \cdot \frac{\partial I}{\partial \mathbf{v}} = 0, \tag{2.9}$$

along any orbit in the phase-space. Comparing equation (2.9) with equation (2.8), we see that the condition for I to be an integral of motion is analogous with the condition for f to be a solution of the CBE. Therefore, we can prove the following:

Theorem 2.1.1. *Any steady-state solution of the CBE depends on the phase-space coordinates only through integrals of motion in the given potential, and any function of the integrals of motion gives a solution of the CBE.*

Proof. Suppose f is a solution of the CBE. Then, from equation (2.9), f is an integral of motion, and so the first part of the Theorem is proved. On the other hand, if $I_1, ..., I_n$ are n independent integrals of motion of the system and f depends on them, we have

$$\frac{d}{dt} f(I_1, ..., I_n) = \sum_{i=1}^{n} \frac{\partial f}{\partial I_i} \frac{dI_i}{dt} = 0, \tag{2.10}$$

and so f turns out to satisfy the CBE. □

In summary, the Jeans theorem tells us that if $I_1, ..., I_n$ are n independent integrals of motion of the system within a given gravitational potential, then any DF depending on one, some or all of these integrals of motion will be a solution of the CBE. A "stronger" version of Jeans theorem exists too (see e.g. BT08, C21): if the time-independent potential of a galaxy is such that almost all orbits are regular, then, for all practical purposes, the properties of the galaxy can be described by a DF of the form $f(I_1, I_2, I_3)$, where I_1, I_2, I_3 are three independent, isolating integrals of motion.

2.2 Derivation of the Jeans equations

As already said, the comparison between theoretical models and observations is mainly made on mean quantities, as $\overline{\mathbf{v}}$ and $\boldsymbol{\sigma}^2$, which formally are moments of the DF. Calculating these moments is easy if one knows the DF, but finding a DF that is compatible with a given stellar density distribution $\rho(\mathbf{x})$ is not straight-forward; moreover, even if a DF can be recovered, it could be not unique. To solve this problem, the JEs allow to infer moments of the DF without actually recovering the DF itself, but just from the knowledge of the stellar density and total gravitational potential. First, integrating equation (2.8) over all the velocities gives

$$\int \frac{\partial f}{\partial t} \, \mathrm{d}^3\mathbf{v} + \int v_i \frac{\partial f}{\partial x_i} \, \mathrm{d}^3\mathbf{v} - \frac{\partial \Phi}{\partial x_i} \int \frac{\partial f}{\partial v_i} \, \mathrm{d}^3\mathbf{v} = 0, \tag{2.11}$$

where, from now on, the summation over the repeated indices i is implicit. As the range of velocities over which we integrate is independent of time, the partial derivative of the first term

can be taken outside the integral sign. Moreover, as v_i does not depend on x_i, the partial derivative in the second term can be taken outside the integral sign as well. Finally, by applying the divergence theorem and given that $f = 0$ for sufficiently large $\|\mathbf{v}\|$ (i.e., there are no stars moving infinitely fast), the last term goes to zero. Therefore, recalling equations (2.2) and (2.3), we obtain the first Jeans equation:

$$\frac{\partial n}{\partial t} + \frac{\partial}{\partial x_i}(n\overline{v_i}) = 0, \tag{2.12}$$

where n is the number density of stars, and $\overline{v_i}$ is the mean stellar velocity along the coordinate i.

The first moment of the CBE is instead obtained by multiplying equation (2.8) by the velocity component v_j, and integrating over all the velocities:

$$\frac{\partial}{\partial t}\int f\, v_j \,\mathrm{d}^3\mathbf{v} + \int v_i\, v_j \,\frac{\partial f}{\partial x_i}\,\mathrm{d}^3\mathbf{v} - \frac{\partial \Phi}{\partial x_i}\int v_j\,\frac{\partial f}{\partial v_i}\,\mathrm{d}^3\mathbf{v} = 0. \tag{2.13}$$

Similarly to what done for equation (2.11), by applying the divergence theorem and from the fact that f vanishes for infinitely large $\|\mathbf{v}\|$, the last term becomes:

$$\int v_j\,\frac{\partial f}{\partial v_i}\mathrm{d}^3\mathbf{v} = \int \frac{\partial}{\partial v_i}(v_j f)\,\mathrm{d}^3\mathbf{v} - \int \frac{\partial v_j}{\partial v_i}\, f\,\mathrm{d}^3\mathbf{v} = -\delta_{ij}\, n(\mathbf{x}), \tag{2.14}$$

so that equation (2.13) can be rewritten as

$$\frac{\partial(n\overline{v_j})}{\partial t} + \frac{\partial(n\overline{v_i v_j})}{\partial x_i} + n\,\frac{\partial \Phi}{\partial x_j} = 0. \tag{2.15}$$

Expanding the first derivative and using equation (2.12), we get

$$n\,\frac{\partial \overline{v_j}}{\partial t} - \overline{v_j}\,\frac{\partial(n\overline{v_i})}{\partial x_i} + \frac{\partial(n\overline{v_i v_j})}{\partial x_i} = -n\,\frac{\partial \Phi}{\partial x_j}, \tag{2.16}$$

and by recalling the definition of σ_{ij}^2 in equation (2.4), we obtain the final form of the second Jeans equation:

$$n\,\frac{\partial \overline{v_j}}{\partial t} + n\overline{v_i}\,\frac{\partial \overline{v_j}}{\partial x_i} = -n\,\frac{\partial \Phi}{\partial x_j} - \frac{\partial(n\sigma_{ij}^2)}{\partial x_i}. \tag{2.17}$$

The left-hand side and the first term on the right-hand side of the equation are analogous to those present in the so-called Euler equation of fluid dynamics (see e.g. BT08, C21), where the mass

density and the fluid velocity are replaced, respectively, by the number density of stars and the mean stellar velocity. The last term on the right-hand side, instead, is the physical analogous of a "pressure" gradient, where however the "pressure" is not uniform in every direction of space, but it is described by the tensor $n\sigma_{ij}^2$.

Equations (2.12) and (2.17) are useful in dynamical modeling of galaxies because, in fact, they relate observationally accessible quantities, as the stellar density or mean velocity and velocity dispersion, to the mass distribution of the galaxy, which is implicit in the gravitational force term. However, even if we knew the density profile and the gravitational potential of the system, we would have nine unknown functions (i.e., the three components of $\overline{\mathbf{v}}$ and the six independent components of $\boldsymbol{\sigma}^2$) and just four equations (i.e., the first Jeans equation and the three components of the second Jeans equation). Therefore, the two JEs do not constitute a closed system of equations, and even higher-order momenta of the CBE, obtainable for example by multiplying equation (2.8) for $v_i v_k$ and integrating over velocities, would not provide sufficient information to close the system. For this reason, an additional ansatz - usually driven by observations - on the specific dependencies of the DF or on its momenta is needed to solve the JEs.

2.2.1 Dependencies of the distribution function

For some stellar systems, as those with spherical or cylindrical symmetry, the dependencies of the DF on specific integrals of motion lead to a simplification of the JEs, and therefore to their solution (see e.g. BT08, C21). Considering our case of study, in the paragraph below we just present the "classical" case of systems with cylindrical symmetry whose DF depend on two integrals of motion; the more realistic case of axisymmetric systems with the DF depending even on a third integral of motion will be addressed in Section 2.3.2.

If the system is axisymmetric, then the component of the total angular momentum along the symmetry axis (in standard cylindrical coordinates) is $L_z = R\,v_\phi$; this is an integral of motion which can be included in the dependencies of the DF, together with the total energy $E = (v_R^2 + v_z^2 + v_\varphi^2)/2 + \Phi(R, z)$. Therefore, the three components of mean velocity are

$$\overline{v}_R = \frac{1}{n(R,z)} \int v_R \, dv_R \int dv_z \int f(E, L_z) \, dv_\varphi = 0,$$

$$\overline{v}_z = \frac{1}{n(R,z)} \int dv_R \int v_z \, dv_z \int f(E, L_z) \, dv_\varphi = 0, \tag{2.18}$$

$$\overline{v}_\varphi = \frac{1}{n(R,z)} \int dv_R \int dv_z \int v_\phi \, f(E, L_z) \, dv_\varphi,$$

where the first two fields are equal to zero because the integrand functions are odd, respectively, in v_R and v_z; on the other hand, if the DF is not even in v_φ, $\overline{v}_\phi(R,z) \neq 0$ describes the mean rotation velocity around the z-axis.

Similarly to the previous case, the velocity dispersion tensor is diagonal in the (v_R, v_φ, v_z) reference frame, and its components are

$$\begin{aligned} \sigma_R^2 = \sigma_z^2 &= \frac{1}{n(R,z)} \int v_R^2 \, dv_R \int dv_z \int f(E, L_z) \, dv_\varphi, \\ \sigma_\varphi^2 &= \frac{1}{n(R,z)} \int dv_R \int dv_z \int (v_\varphi - \overline{v}_\varphi)^2 \, f(E, L_z) \, dv_\phi, \end{aligned} \tag{2.19}$$

where the equality $\sigma_R^2 = \sigma_z^2$ comes from the fact that the same dependencies of the DF on v_R and v_z are the same. If $\sigma_\varphi^2 = \sigma_R^2$ too, then the velocity dispersion tensor is isotropic, although the system is not spherically symmetric due to the presence of rotation.

2.3 The Jeans equations for axisymmetric systems

We first recall that the usual coordinate change between Cartesian and cylindrical coordinates is

$$x = R\cos\varphi, \quad y = R\sin\varphi, \quad z = z, \tag{2.20}$$

where $R = \sqrt{x^2 + y^2}$, and φ is the azimuthal angle between the projection of the position vector on the equatorial plane and the x-axis. To write the JEs for an axisymmetric system in standard cylindrical coordinates, we just need to apply the coordinate change in equation (2.20) to equations

(2.12) and (2.17). Because the system is axisymmetric, all the partial derivatives with respect to φ vanish, and so the first equation becomes

$$\frac{\partial n}{\partial t} + \frac{1}{R}\frac{\partial}{\partial R}\left(R\, n\overline{v}_R\right) + \frac{\partial}{\partial z}\left(n\overline{v}_z\right) = 0, \tag{2.21}$$

while the three components of the second equation are

$$\begin{aligned}
&\frac{\partial(n\overline{v_R})}{\partial t} + \frac{\partial}{\partial R}\left(n\overline{v_R^2}\right) + \frac{\partial(n\overline{v_R v_z})}{\partial z} + n\left(\frac{\overline{v_R^2} - \overline{v_\varphi^2}}{R} + \frac{\partial \Phi}{\partial R}\right) = 0,\\
&\frac{\partial(n\overline{v_z})}{\partial t} + \frac{\partial}{\partial R}\left(n\overline{v_R v_z}\right) + \frac{\partial}{\partial z}\left(n\overline{v_z^2}\right) + n\left(\frac{\overline{v_R v_z}}{R} + \frac{\partial \Phi}{\partial z}\right) = 0,\\
&\frac{\partial(n\overline{v_\varphi})}{\partial t} + \frac{\partial}{\partial R}\left(n\overline{v_R v_\varphi}\right) + \frac{\partial}{\partial z}\left(n\overline{v_\varphi v_z}\right) + \frac{2n}{R}\,\overline{v_R v_\varphi} = 0.
\end{aligned} \tag{2.22}$$

As noticed in Section 2.2, even if we knew the stellar density and the total gravitational potential of the system, we would remain with more unknown fields than equations; therefore, an ansatz on the dependencies of the DF is needed to close and solve the system of equations.

2.3.1 Two-integral models

If the DF is of the form $f = f(E, L_z)$, as shown in Section 2.2.1, and the stellar density distribution does not change with time, then $\partial n/\partial t = 0$ and $\overline{v_R} = \overline{v_z} = 0$, and so equation (2.21) cancels out. Instead, equation (2.22) become (see e.g. BT08, C21)

$$\begin{cases}
\dfrac{\partial \rho_* \sigma_z^2}{\partial z} = -\rho_* \dfrac{\partial \Phi}{\partial z}, \\[2ex]
\dfrac{\partial \rho_* \sigma_z^2}{\partial R} - \dfrac{\rho_* \Delta}{R} = -\rho_* \dfrac{\partial \Phi}{\partial R}, \quad \Delta \equiv \overline{v_\varphi^2} - \sigma_z^2,
\end{cases} \tag{2.23}$$

where $\rho_*(R, z)$ and $\Phi(R, z)$ are, respectively, the stellar density (obtained by multiplying the number density n for a reference mass) and the total (e.g., stars plus DM) gravitational potential. In particular, we recall that $\overline{v_\varphi^2} = \overline{v_\varphi}^2 + \sigma_\varphi^2$, where $\overline{v_\varphi}$ and σ_φ^2 are, respectively, the mean velocity and velocity dispersion along the azimuthal direction; notice also that, due to the assumptions on

the DF, $\sigma_R^2 = \sigma_z^2$.

The solutions of equations (2.23), assuming null boundary conditions at infinity, are

$$\begin{cases} \rho_* \sigma_z^2 = \displaystyle\int_z^\infty \rho_* \frac{\partial \Phi}{\partial z'}\, dz', \\ \\ \dfrac{\rho_* \Delta}{R} = \dfrac{\partial \rho_* \sigma_z^2}{\partial R} + \rho_* \dfrac{\partial \Phi}{\partial R} = [\rho_*, \Phi]\,, \end{cases} \tag{2.24}$$

where we have defined the commutator-like operator (see e.g. Barnabè et al. 2006, C21)

$$[\rho_*, \Phi] \equiv \int_z^\infty \left(\frac{\partial \rho_*}{\partial R} \frac{\partial \Phi}{\partial z'} - \frac{\partial \rho_*}{\partial z'} \frac{\partial \Phi}{\partial R} \right) dz', \tag{2.25}$$

From the second of equation (2.24), we see that Δ can be obtained or by differentiation of $\rho_* \sigma_z^2$, or by computation of $[\rho_*, \Phi]$, as in equation (2.25). This latter approach is to be preferred, as it usually reveals important properties of the solutions that are not apparent in the first approach based on differentiation; for example, it is immediate to show that the commutator vanishes for a spherical density in a spherical total potential, and in case of ellipsoidal densities in ellipsoidal potentials, the commutator is everywhere positive (negative) when the density shape is flatter (rounder) than the potential (see e.g. C21). Of course, when computing $[\rho_*, \Phi]$, the radial derivative of $\rho_* \sigma_z^2$ is obtained as a byproduct:

$$D \equiv \frac{\partial \rho_* \sigma_z^2}{\partial R} = [\rho_*, \Phi] - \rho_* \frac{\partial \Phi}{\partial R}, \tag{2.26}$$

an identity we will use in the following. Once σ_z^2 and Δ are known, one has

$$\overline{v_\varphi^2} = \Delta + \sigma_z^2 = \frac{[R\rho_*, \Phi]}{\rho_*}, \tag{2.27}$$

where the second identity involves another commutator-like operator, and it can be proved from equations (2.24) and (2.25).

Notice that a model with $\overline{v_\varphi^2} < 0$ somewhere is physically inconsistent, but $\overline{v_\varphi^2} \geq 0$ everywhere is not a sufficient condition for consistency: in fact, there are models which are consistent at the level of the JEs, but they have a negative (unphysical) DF (see e.g. Ciotti and Pellegrini 1992).

Decomposition of azimuthal motions

For axisymmetric models with $\Delta \geq 0$ everywhere, the widely used Satoh (1980) decomposition of $\overline{v_\varphi^2}$ into its ordered and dispersion components reads:

$$\overline{v_\varphi} = k\sqrt{\Delta}, \quad \sigma_\varphi^2 = \sigma_z^2 + (1-k^2)\Delta, \tag{2.28}$$

where $0 \leq k^2 \leq 1$. If $k = 0$, then $\overline{v_\varphi} = 0$ and no net rotation is present, while if $k^2 = 1$, then $\sigma_\varphi^2 = \sigma_z^2$, and so the velocity dispersion tensor is isotropic; moreover, if $\Delta = 0$ (as for self-gravitating spherical systems), then $\overline{v_\varphi} = 0$, and $\boldsymbol{\sigma}^2$ is isotropic independently of k. As shown in Ciotti and Pellegrini (1996), the decomposition in equation (2.28) can be easily generalized to a spatially dependent $k(R, z)$, provided that

$$k^2(R, z) \leq \frac{\overline{v_\varphi^2}}{\Delta}, \tag{2.29}$$

where the upper limit is obtained from equation (2.28) by imposing $\sigma_\varphi^2 = 0$ everywhere, i.e. as for maximally rotating models with no net velocity dispersion in the azimuthal direction. Of course, k is not required to be positive, thus allowing the modeling of counter-rotating structures with negative $\overline{v_\varphi}$ (see e.g. Negri, Pellegrini, and Ciotti 2013).

For systems with $\Delta < 0$, the Satoh (1980) decomposition is not possible (apart from the trivial case of $k = 0$ everywhere). However, provided that $\overline{v_\varphi^2} \geq 0$ everywhere, another decomposition is possible: we refer to this as the λ-decomposition, and it is of the very general form

$$\overline{v_\varphi} = \lambda\sqrt{\overline{v_\varphi^2}} \ , \ \ \sigma_\varphi^2 = (1-\lambda^2)\overline{v_\varphi^2}, \tag{2.30}$$

where $0 \leq \lambda^2(R, z) \leq 1$, and negative values of λ correspond to regions of counter-rotation. Two limit cases are hence possible: $\lambda = 0$ corresponds to zero net rotation in the azimuthal direction, and $\lambda^2 = 1$ to a maximally rotating system. The value of λ corresponding to the isotropic rotator ($\lambda_{\rm I}$) is obtained by imposing $\sigma_\varphi^2 = \sigma_z^2$ in the second of equation (2.30), so that

$$\lambda_{\rm I}^2(R, z) \equiv \frac{\Delta}{\overline{v_\varphi^2}}, \tag{2.31}$$

where $\Delta \geq 0$. Notice that, being equation (2.30) the most general decomposition of $\overline{v_\varphi^2}$, any other decomposition must descend from it. For example, if $\Delta \geq 0$, the following relation between λ and

k holds:

$$\lambda = k\sqrt{\frac{\Delta}{\overline{v_\varphi^2}}}; \tag{2.32}$$

this shows how, except for the case with $\overline{v_\varphi} = 0$, a spatially constant k does not necessarily correspond to a spatially constant λ, and vice versa.

2.3.2 Three-integral models

Having assessed the case of axisymmetric systems supported by a two-integral DF, we now turn to the more realistic case of systems supported by a three-integral DF, where the third integral of motion (in addition to E and L_z) is unknown. In particular, for simplicity, we assume that this third integral is an even function of v_z and v_R, so that the JEs in equation (2.22) become:

$$\begin{cases} \dfrac{\partial \rho_* \sigma_z^2}{\partial z} = -\rho_* \dfrac{\partial \Phi}{\partial z}, \\ \\ \dfrac{\partial \rho_* \sigma_R^2}{\partial R} - \dfrac{\rho_* \Delta_R}{R} = -\rho_* \dfrac{\partial \Phi}{\partial R}, \quad \Delta_R \equiv \overline{v_\varphi^2} - \sigma_R^2; \end{cases} \tag{2.33}$$

Notice that the first equation, as all the quantities depending on ρ_* and Φ alone (such as the commutator $[\rho_*, \Phi]$, or the radial derivative of $\rho_* \sigma_z^2$), are the same of the two-integral case; the definition of Δ_R is instead different, as now $\sigma_R \neq \sigma_z$.

Due to this last inequality, in this case an ansatz is needed to solve the second of equation (2.33), which is independent of the vertical velocity dispersion, and contains the two unknown functions $\overline{v_\varphi^2}$ and σ_R^2. As already anticipated in Chapter 1, in this thesis we study in detail the so-called "b-ansatz" introduced in Cappellari (2008), which is adopted in the JAM of regular rotators and stellar disks (see e.g. Cappellari 2016). The corresponding solution of the JEs, implying the alignment of the velocity dispersion ellipsoid with the local basis of cylindrical coordinates, was presented as an efficient modeling able to capture the main properties of the velocity dispersion ellipsoid inferred from extensive three-integrals Schwarzschild modeling of integral-field stellar kinematics, under the mass-follows-light hypothesis (Cappellari 2008). Of course, from a very theoretical point of view, the b-ansatz is not the only possible, and in Appendix B we discuss another ansatz (the "μ-ansatz") which leads to a nice closure of the JEs.

CHAPTER 3

THE b-ANSATZ

For axisymmetric systems supported by a three-integral DF, the b-ansatz is a closure relation which allow to solve the JEs. While its form is widely motivated by observational results, how the different values of its b parameter condition the resulting kinematics lacks of a general understanding. Moreover, numerical results showed that the field $\overline{v_\varphi^2}$ can become negative (and so the model inconsistent) for too large values of b, and currently a numerical exploration of the parameter space is the only choice to solve this issue. Therefore, it would be useful to have a general procedure which allow to understand how the kinematic fields resulting from the solution of the JEs are affected by different amount of b-anisotropy, and at the same time to constrain the values of the anisotropy parameter in order to ensure the positivity of the fields.

This Chapter is organized as follows. In Section 3.1, we will present the form of JEs with the b-ansatz, and discuss a generalized version of the Satoh (1980) decomposition in presence of b-anisotropy (Section 3.1.1). Then, in Section 3.2 we will discuss how to find, a priori from solving the JEs, the limits for b which guarantee the positivity of the kinematic fields $\overline{v_\varphi^2}$ (Section 3.2.1), Δ_R (Section 3.2.2) and Δ (Section 3.2.3) over some critical regions of the (R, z)-plane. Finally, in Section 3.3 we will discuss how the kinematic fields change by changing the value of b, and which are the relations between the different limits and between the critical regions, distinguishing between the cases of systems with a positive (Section 3.3.1), zero (Section 3.3.2) or negative (Section 3.3.3) commutator-like operator.

3.1 The Jeans equations with the b-ansatz

In the *b-ansatz*, σ_R^2 is linked to σ_z^2 through the choice of a function $b(R,z) \geq 0$, as

$$\sigma_R^2 = b(R,z)\,\sigma_z^2; \tag{3.1}$$

when $b = 0$, the system has no radial velocity dispersion, while $b = 1$ gives the two-integral case. Inserting equation (3.1) in the second of equation (2.33), and recalling the definition of D in equation (2.26), we obtain:

$$\frac{\rho_* \Delta_R}{R} - \rho_* \sigma_z^2 \frac{\partial b}{\partial R} = bD + \rho_* \frac{\partial \Phi}{\partial R} = b\,[\rho_*, \Phi] + (1-b)\,\rho_* \frac{\partial \Phi}{\partial R}, \tag{3.2}$$

where for the last equality we have used again equation (2.26); notice how b multiplies functions that are independent of the adopted ansatz. Once Δ_R is known, if we restrict to a b function that depends only on z (including the widely used constant b case), we have

$$\overline{v_\varphi^2} = \Delta_R + b\,\sigma_z^2 = \; b\,B + R\frac{\partial \Phi}{\partial R} = b\,\frac{[R\rho_*, \Phi]}{\rho_*} + (1-b)\,R\frac{\partial \Phi}{\partial R}, \tag{3.3}$$

where, from equation (2.26), we define the ansatz-independent function

$$B \equiv \frac{R\,D}{\rho_*} + \sigma_z^2 = \frac{[R\rho_*, \Phi]}{\rho_*} - R\frac{\partial \Phi}{\partial R}. \tag{3.4}$$

Only $b(z)$ functions leading to $\overline{v_\varphi^2} \geq 0$ everywhere are physically acceptable, and Section 3.2.1 deals with this request. Finally, from equation (3.3), we obtain:

$$\Delta = \overline{v_\varphi^2} - \sigma_z^2 = \Delta_R + (b-1)\,\sigma_z^2 = b\,B + C, \tag{3.5}$$

where, from equations (2.26) and (3.4), we define another ansatz-independent function

$$C \equiv R\frac{\partial \Phi}{\partial R} - \sigma_z^2 = \frac{R\,[\rho_*, \Phi]}{\rho_*} - B. \tag{3.6}$$

Notice that, with the introduction of the b-ansatz, the values of Δ are not the same of the two-

integral case, because σ_z^2 remains unaltered, but $\overline{v_\varphi^2}$ changes. From equation (3.5), we immediately see that if $\Delta_R \geq 0$ and $b(z) \geq 1$, then $\Delta \geq 0$, and if $\Delta_R < 0$ and $b(z) \leq 1$, then $\Delta < 0$. A complete discussion on the positivity of Δ_R and Δ is given in Sections 3.2.2 and 3.2.3.

3.1.1 Decompositions of azimuthal motions

Models with $\Delta_R \geq 0$ allow for a decomposition of $\overline{v_\varphi^2}$ similar to that in equation (2.28), namely (see Cappellari 2008):

$$\overline{v_\varphi} = k\sqrt{\Delta_R}, \quad \sigma_\varphi^2 = \sigma_R^2 + (1-k^2)\,\Delta_R. \tag{3.7}$$

The velocity dispersion tensor is tangential anisotropic ($\sigma_\varphi > \sigma_R$) for $k^2 < 1$, while radial anisotropy ($\sigma_\varphi < \sigma_R$) is present for $k^2 > 1$; in two-integral systems, $k = 0$ corresponds to the isotropic case. Of course, if $\Delta \geq 0$ everywhere the decomposition in equation (2.28) can also be applied, where now Δ is given in equation (3.5).

A different decomposition for the azimuthal motions can be given by using the parameter γ_φ in equation (1.2) for a spatially constant anisotropy, namely

$$\overline{v_\varphi}^2 = \Delta_R + \gamma_\varphi\,\sigma_R^2, \quad \sigma_\varphi^2 = (1-\gamma_\varphi)\,\sigma_R^2 \tag{3.8}$$

where, by requiring the positivity of $\overline{v_\varphi}^2$ and σ_φ^2,

$$-\frac{\Delta_R}{\sigma_R^2} \leq \gamma_\varphi \leq 1. \tag{3.9}$$

Tangential anisotropy is reproduced by $\gamma_\varphi < 0$, while $\gamma_\varphi > 0$ gives radial anisotropy; in two-integral systems, $\gamma_\varphi = 0$ corresponds to the isotropic case. Notice that, from equation (3.9), γ_φ can be either positive or negative if $\Delta_R > 0$; if $\Delta_R < 0$, instead, γ_φ cannot be taken negative, and so the velocity dispersion tensor can only be radially anisotropic. In Section 4.1.5, some findings based on the use of this decomposition to interpret recent empirical results (Wang, Cappellari, and Peng 2021) are discussed. Of course, once the necessary condition $\overline{v_\varphi^2} \geq 0$ is satisfied, also the most general λ-decomposition described in Section 2.3.1 is possible.

3.2 Physical constraints on the b-ansatz

Equations (2.33) can be solved only with the introduction of some closure ansatz, as the b-ansatz in equation (3.1); however, arbitrary ansatz functions can lead to unphysical solutions of the JEs. In practice, being $\sigma_z^2 \geq 0$ independent of the ansatz, the positivity of σ_R^2 is guaranteed by equation (3.1), and so problems od consistency can arise from the sign of $\overline{v_\varphi^2}$ only. Information on the positivity of Δ and Δ_R is also relevant for the modeling because, although not directly related to model consistency, it is necessary to decompose $\overline{v_\varphi^2}$ as in equations (2.28) and (3.7).

In the following, we restrict for simplicity to models with $\partial\Phi/\partial R \geq 0$ everywhere (the most common situation), and we again limit to consider $b = b(z)$; finally, we indicate with $\mathrm{P} = (R, z)$ a generic point in the (R, z)-plane.

3.2.1 Positivity of $\overline{v_\varphi^2}$: the $\mathscr{B}$ region

We discuss here the positivity of $\overline{v_\varphi^2}$, a condition necessary for model consistency. Introducing the ansatz-independent sets

$$\mathscr{B}^{\pm} = \{(R, z) : B \gtrless 0\}\,, \quad \mathscr{B}^{0} = \{(R, z) : B = 0\}\,, \tag{3.10}$$

from equation (3.3) we see that $\overline{v_\varphi^2} \geq 0$ over the region $\mathscr{B}^{+0} = \mathscr{B}^{+} \cup \mathscr{B}^{0}$ independently of b; instead, the behavior of B over $\mathscr{B}^{-}$ constrains the possible choices of $b(z)$. As illustrated in Figure 3.1, we indicate with $\mathrm{Pr}(\mathscr{B}^{\pm})$ the projection of $\mathscr{B}^{\pm}$ on the z-axis, and with $\mathscr{B}_z^{\pm} = \{R : B \gtrless 0,\, z \in \mathrm{Pr}(\mathscr{B}^{\pm})\}$ the radial section at fixed z of $\mathscr{B}^{\pm}$.

As we restrict to systems which are symmetric about the equatorial plane, in the following we limit the discussion to points with $z \geq 0$. From equation (3.3), the condition $\overline{v_\varphi^2} \geq 0$ over $\mathscr{B}^{-}$ is guaranteed provided that, at each $z \in \mathrm{Pr}(\mathscr{B}^{-})$,

$$b(z) \leq b_{\mathrm{M}}(z) \equiv \min_{\mathscr{B}_z^{-}} \frac{R}{|B|}\frac{\partial\Phi}{\partial R} = \min_{\mathscr{B}_z^{-}} \left(1 + \frac{R\,[\rho_*, \Phi] + \rho_* \sigma_z^2}{\rho_* |B|}\right), \quad z \in \mathrm{Pr}(\mathscr{B}^{-}), \tag{3.11}$$

where the last equality has been obtained by using equation (3.6). Notice that the independence of b from R implies that the upper limit $b_{\mathrm{M}}(z)$, determined over $\mathscr{B}_z^{-}$, applies also to points in the complementary section $\mathscr{B}_z^{+}$; therefore, the function $b_{\mathrm{M}}(z)$ provides a constraint over the whole rectangular strip defined by $R \geq 0$ and $z \in \mathrm{Pr}(\mathscr{B}^{-})$, which from now on we will refer to as the "strip $\mathrm{Pr}(\mathscr{B}^{-})$". In the special case of a spatially constant b, the condition in equation (3.11)

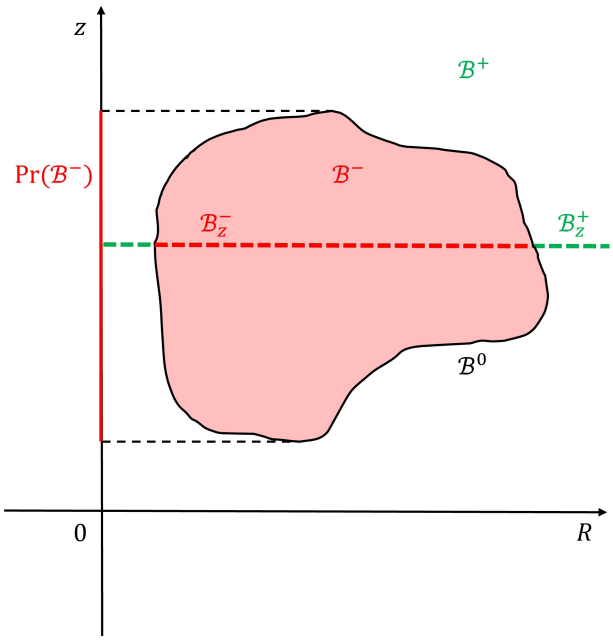


Figure 3.1. Cartoon of a fictitious $\mathscr{B}^-$ region (red area), bounded by the $\mathscr{B}^0$ curve (black line), together with its projection on the z-axis $\mathrm{Pr}(\mathscr{B}^-)$, a radial section $\mathscr{B}_z^-$ (red dashed line), and its complement $\mathscr{B}_z^+$ (green dashed line). From equation (3.10), $\mathscr{B}^+ \cup \mathscr{B}^- \cup \mathscr{B}^0$ fully covers the (R, z)-plane.

reduces to $b \leq b_\mathrm{M}$, where b_M is the minimum of $b_\mathrm{M}(z)$.

3.2.2 Positivity of Δ_R: the $\mathscr{D}$ region

As seen in Section 3.1.1, the necessary condition to apply the Satoh (1980) decomposition to $\overline{v_\varphi^2}$ is to have $\Delta_R \geq 0$ or $\Delta \geq 0$. Introducing the ansatz-independent sets

$$\mathscr{D}^\pm = \{(R, z) : D \gtrless 0\}\,, \quad \mathscr{D}^0 = \{(R, z) : D = 0\}\,, \tag{3.12}$$

where D is defined in equation (2.26), the first of equation (3.2) (with $\partial b/\partial R = 0$) shows that $\Delta_R \geq 0$ over the region $\mathscr{D}^{+0} = \mathscr{D}^+ \cup \mathscr{D}^0$ independently of $b(z)$. Instead, the condition $\Delta_R \geq 0$ over $\mathscr{D}^-$ requires

$$b(z) \leq b_0(z) \equiv \min_{\mathscr{D}_z^-} \frac{\rho_*}{|D|}\frac{\partial \Phi}{\partial R} = \min_{\mathscr{D}_z^-}\left(1 + \frac{[\rho_*, \Phi]}{|D|}\right), \quad z \in \mathrm{Pr}(\mathscr{D}^-), \tag{3.13}$$

where $\mathrm{Pr}(\mathscr{D}^\pm)$ is the projection of $\mathscr{D}^\pm$ on the z-axis, $\mathscr{D}_z^\pm = \{R : D \gtrless 0, z \in \mathrm{Pr}(\mathscr{D}^\pm)\}$, and the last equality follows from equation (2.26). Again, due to the independence of b from R, the condition in equation (3.13) must be verified over the whole strip $\mathrm{Pr}(\mathscr{D}^-)$. In the special case of a constant b, then $\Delta_R \geq 0$ for $b \leq b_0$, where b_0 is the minimum of $b_0(z)$.

Notice that, as proved in Theorem G.1.1, the strip $\Pr(\mathscr{B}^-)$ is contained in the strip $\Pr(\mathscr{D}^-)$; moreover, as proved in Theorem G.2.1, in this common region $b_0(z) \leq b_{\rm M}(z)$.

3.2.3 Positivity of Δ: the $\mathscr{C}$ region

The determination of the positivity of Δ as a function of $b(z)$ is more complicated, as it depends on the sign of both the B and C functions in equation (3.5). Similarly to what done before, we introduce the sets

$$\mathscr{C}^{\pm} = \{(R,z) : C \gtrless 0\}\,, \quad \mathscr{C}^{0} = \{(R,z) : C = 0\}\,, \tag{3.14}$$

with $\mathscr{C}^{\pm}_z = \{R : C \gtrless 0, z \in \Pr(\mathscr{C}^{\pm})\}$, and $\mathscr{C}^{+0} = \mathscr{C}^{+} \cup \mathscr{C}^{0}$. The sign of Δ at a point P depends on its position in the (R,z)-plane, as follows:

- $\Delta \geq 0$ independently of $b(z)$ over $\mathscr{B}^{+0} \cap \mathscr{C}^{+0}$. Moreover, $\Delta \geq 0$ over $\mathscr{B}^{+} \cap \mathscr{C}^{-}$ for

$$b(z) \geq b_1(z) \equiv \max_{\mathscr{B}^+_z \cap \mathscr{C}^-_z} \frac{|C|}{B} = \max_{\mathscr{B}^+_z \cap \mathscr{C}^-_z} \left(1 - \frac{R\,[\rho_*, \Phi]}{\rho_* B}\right), \quad z \in \Pr(\mathscr{B}^+ \cap \mathscr{C}^-), \tag{3.15}$$

  and over $\mathscr{B}^- \cap \mathscr{C}^+$ for

$$b(z) \leq b_2(z) \equiv \min_{\mathscr{B}^-_z \cap \mathscr{C}^+_z} \frac{C}{|B|} = \min_{\mathscr{B}^-_z \cap \mathscr{C}^+_z} \left(1 + \frac{R\,[\rho_*, \Phi]}{\rho_* |B|}\right), \quad z \in \Pr(\mathscr{B}^- \cap \mathscr{C}^+). \tag{3.16}$$

- $\Delta < 0$ independently of $b(z)$ over $(\mathscr{B}^- \cap \mathscr{C}^-) \cup (\mathscr{B}^0 \cap \mathscr{C}^-) \cup (\mathscr{B}^- \cap \mathscr{C}^0)$[1]. Moreover, $\Delta < 0$ over $\mathscr{B}^+ \cap \mathscr{C}^-$ for $b(z) < b_1(z)$, and over $\mathscr{B}^- \cap \mathscr{C}^+$ for $b(z) > b_2(z)$.

For a spatially constant b, the previous inequalities hold replacing $b_1(z)$ and $b_2(z)$ with b_1 and b_2, which are respectively the maximum of $b_1(z)$, and the minimum of $b_2(z)$.

Summarizing, we have found that, independently of $b(z)$, $\overline{v_\varphi^2} \geq 0$ over $\mathscr{B}^{+0}$, $\Delta_R \geq 0$ over $\mathscr{D}^{+0}$, $\Delta \geq 0$ over $\mathscr{B}^{+0} \cap \mathscr{C}^{+0}$ and $\Delta < 0$ over $(\mathscr{B}^- \cap \mathscr{C}^-) \cup (\mathscr{B}^0 \cap \mathscr{C}^-) \cup (\mathscr{B}^- \cap \mathscr{C}^0)$. Instead, equations (3.11), (3.13), (3.15) and (3.16) set the constraints on $b(z)$ required for the positivity of $\overline{v_\varphi^2}$ over $\mathscr{B}^-$, Δ_R over $\mathscr{D}^-$, and Δ over the intersection regions $\mathscr{B}^+ \cap \mathscr{C}^-$ and $\mathscr{B}^- \cap \mathscr{C}^+$.

[1] This region is the complementary of $\mathscr{B}^{+0} \cap \mathscr{C}^{+0}$ minus the regions in equations (3.15) and (3.16), as can be proved with the De Morgan's law.

3.3 General considerations

The properties of the kinematic fields resulting from a given choice for $b(z)$ are determined by the relations between the ansatz-independent regions $\mathscr{B}^{\pm}$, $\mathscr{C}^{\pm}$ and $\mathscr{D}^{\pm}$, and the functions defined over them. As each of these regions is made by two disjoint parts fully covering the (R, z)-plane, the determination of $\mathscr{B}^{-}$, $\mathscr{C}^{-}$ and $\mathscr{D}^{-}$ is sufficient for investigating a given model.

We now discuss the qualitative effects of increasing b (assumed for simplicity as spatially constant) on the fields σ_R^2, $\overline{v_\varphi^2}$, Δ_R and Δ. Suppose that a given model is assigned, and the regions $\mathscr{B}^{\pm}$, $\mathscr{C}^{\pm}$ and $\mathscr{D}^{\pm}$ have been determined. Therefore, from equations (3.2), (3.3) and (3.5), we clearly see that, as b becomes higher, $\overline{v_\varphi^2}$ and Δ increase in $\mathscr{B}^{+}$ and decrease in $\mathscr{B}^{-}$, while Δ_R increase in $\mathscr{D}^{+}$ and decrease in $\mathscr{D}^{-}$. The positivity of the fields in these regions, instead, depend on the sign of $[\rho_*, \Phi]$, which determine the relative disposition of the limits for b; therefore, in the remainder of this Section we will discuss the three cases of positive, zero or negative commutator. The only two results which are independent of the sign of $[\rho_*, \Phi]$ are that $\mathscr{B}^{-}$ is always contained in $\mathscr{D}^{-}$ (Theorem G.1.1), and $b_0(z) \leq b_{\mathrm{M}}(z)$ for $z \in \mathrm{Pr}(\mathscr{B}^{-})$ (Theorem G.2.1).

3.3.1 Models with $[\rho_*, \Phi] > 0$

If $[\rho_*, \Phi] > 0$ everywhere (as for self-gravitating oblate ellipsoids), then from Theorem G.1.2 we have $\mathscr{B}^{-} \subseteq \mathscr{C}^{+}$ and $\mathscr{C}^{-} \subseteq \mathscr{B}^{+}$; notice that the relative position of the regions in not completely determined, as nothing general can be said about $\mathscr{C}^{\pm}$ and $\mathscr{D}^{\pm}$. Moreover, from Theorems G.2.2 and G.2.4, we have:

$$\begin{cases} b_1(z) \leq 1 \quad \forall z \in \mathrm{Pr}(\mathscr{C}^{-}), \\ \\ 1 \leq b_0(z) \leq b_2(z) \leq b_{\mathrm{M}}(z) \quad \forall z \in \mathrm{Pr}(\mathscr{B}^{-}). \end{cases} \tag{3.17}$$

Notice that, from the considerations above, $\mathscr{B}^{-}$ and $\mathscr{C}^{-}$ are two disjoint regions, but this does not mean that their projections in equation (3.17) are disjoint too: in fact, as for all the models discussed here, they may coincide with the z-axis.

We start considering the case of $b = 0$ (i.e., $\sigma_R^2 = 0$ everywhere): as 0 is smaller than b_0 and b_{M}, then $\overline{v_\varphi^2}$ and Δ_R are positive everywhere, while $\Delta < 0$ somewhere in $\mathscr{C}^{-}$ (because $0 < b_1$), and $\Delta \geq 0$ everywhere in $\mathscr{C}^{+}$ (because $0 < b_2$). For increasing b, σ_R^2 increases everywhere, $\overline{v_\varphi^2}$

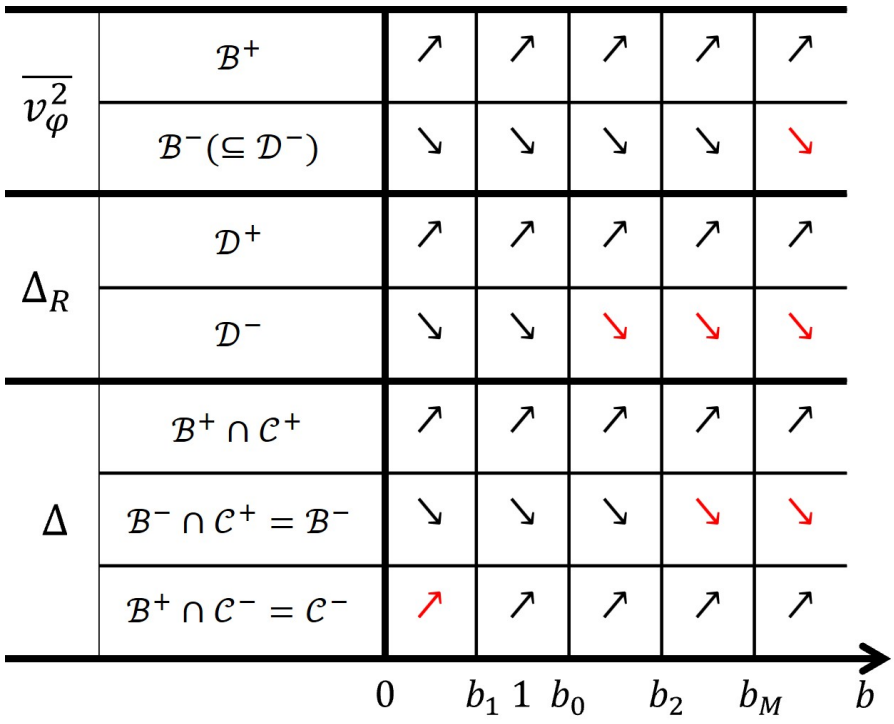


Figure 3.2. For models with $[\rho, \Phi] > 0$, behavior of the kinematic fields $\overline{v_\varphi^2}$, Δ_R and Δ over the regions $\mathscr{B}^\pm$, $\mathscr{C}^\pm$ and $\mathscr{D}^\pm$, as a function of b. Each row refers to a specific ansatz-independent region. For increasing b (from left to right), arrows point upwards if the field is increasing, and downwards if the field is decreasing; black arrows indicate that the field is positive, red arrows that it is negative. For $b > b_{\mathrm{M}}$, the model becomes unphysical.

decreases over $\mathscr{B}^-$ and increases over $\mathscr{B}^+$, while Δ_R decreases over $\mathscr{D}^-$ and increases over $\mathscr{D}^+$. When $b > b_1$, Δ becomes positive over $\mathscr{C}^-$. Then, for $b > b_0$, Δ_R becomes negative somewhere over $\mathscr{D}^-$, and for $b > b_2$, Δ becomes negative somewhere over $\mathscr{B}^-$. Finally, for $b > b_{\mathrm{M}}$, $\overline{v_\varphi^2} < 0$ somewhere in $\mathscr{B}^-$, and the model becomes unphysical. These behaviors are shown in Figure 3.2.

3.3.2 Models with $[\rho_*, \Phi] = 0$

If $[\rho_*, \Phi] = 0$ everywhere, then from Theorem G.1.2 we have $\mathscr{B}^- = \mathscr{C}^+$ and $\mathscr{B}^+ = \mathscr{C}^-$. Moreover, from equation (2.26), $\mathscr{D}^{-0}$ coincides with the whole (R, z)-plane; therefore, differently from systems with $[\rho_*, \Phi] > 0$, the relative position of the regions is univocally determined. Finally, from equations (3.13), (3.15) and (3.16), equation (3.17) becomes:

$$\begin{cases} b_1(z) = 1 \quad \forall z \in \mathrm{Pr}(\mathscr{C}^-), \\ \\ 1 = b_0(z) = b_2(z) \leq b_{\mathrm{M}}(z) \quad \forall z \in \mathrm{Pr}(\mathscr{B}^-). \end{cases} \tag{3.18}$$

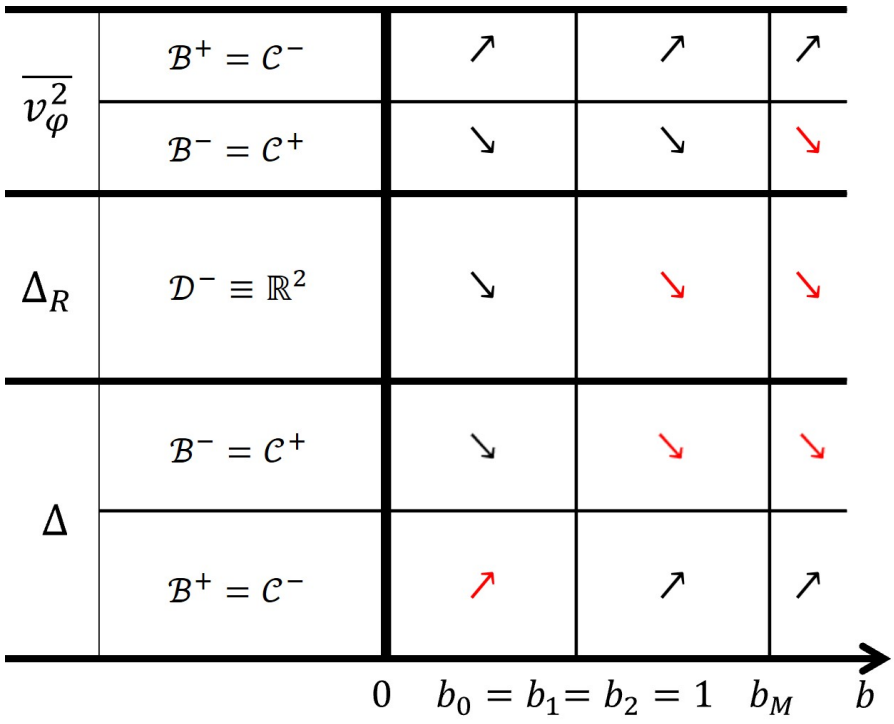


Figure 3.3. Same as Figure 3.2, but for models with $[\rho, \Phi] = 0$.

The behavior of the main kinematic fields for increasing b is analogous to that for systems with $[\rho_*, \Phi] > 0$, but considering the different relative position of the regions, and the identity between b_0, b_1 and b_2. In practice, increasing b above 1, Δ becomes positive over $\mathscr{C}^- = \mathscr{B}^+$, Δ_R becomes negative somewhere over the (R, z)-plane, and Δ becomes negative somewhere over $\mathscr{B}^- = \mathscr{C}^+$. Finally, for $b > b_{\rm M}$, $\overline{v_\varphi^2} < 0$ somewhere in $\mathscr{B}^- = \mathscr{C}^+$, and the model becomes unphysical. These behaviors are shown in Figure 3.3, and one example of these models is shown in Appendix F.1.

3.3.3 Models with $[\rho_*, \Phi] < 0$

If $[\rho_*, \Phi] < 0$ everywhere, from Theorem G.1.3 we have $\mathscr{B}^+ \subseteq \mathscr{C}^-$ and $\mathscr{C}^+ \subseteq \mathscr{B}^-$. Moreover, from equation (2.26), $\mathscr{D}^-$ coincides with the whole (R, z)-plane; therefore, as for models with $[\rho_*, \Phi] = 0$, the relative position of the regions is univocally determined, i.e. $\mathscr{C}^+ \subseteq \mathscr{B}^- \subseteq \mathscr{D}^-$. Moreover, from the Theorems in Appendix G.2.2, we have:

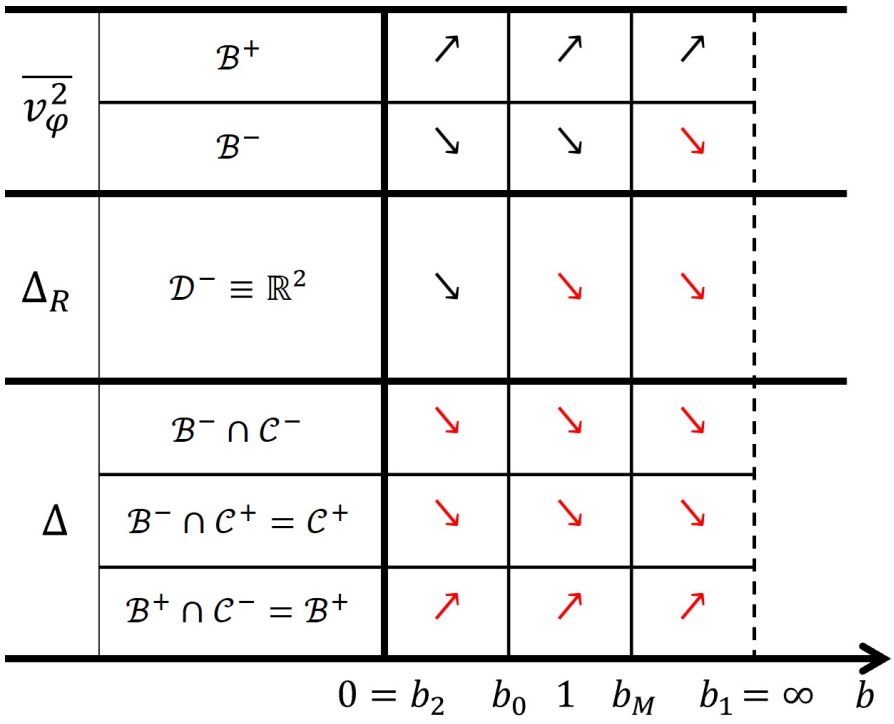


Figure 3.4. Same as Figure 3.2, but for models with $[\rho, \Phi] < 0$, and $[R\rho_*, \Phi] > 0$ (i.e., $b_{\rm M} > 1$).

$$\begin{cases} b_0(z) \leq 1 \quad \forall z \in \Pr(\mathscr{D}^-), \\ b_1(z) = +\infty \quad \forall z \in \Pr(\mathscr{B}^+), \\ b_2(z) = 0 \quad \forall z \in \Pr(\mathscr{C}^+). \end{cases} \tag{3.19}$$

Notice that, although from Theorem G.2.1 we know that $b_{\rm M}(z) \leq b_0(z)$, the relative position of $b_{\rm M}(z)$ with respect to unity remains undetermined; however, if the commutator $[R\,\rho_*, \Phi] \equiv R\,[\rho_*, \Phi] + \rho_* \sigma_z^2 < 0$ as well, from equation (3.11) we have $b_{\rm M}(z) < 1$.

In Figure 3.4, we summarize the behavior of the kinematic fields as a function of b; for simplicity, although this is not always true, we assume that $b_{\rm M} > 1$. The general trends with b are the same to those for models with $[\rho_*, \Phi] \geq 0$, but the regions have different relative position, and b_1 and b_2 have no finite values. In practice, the positivity of $\overline{v_\varphi^2}$ is identical, while $\Delta_R < 0$ somewhere on the (R, z)-plane even for $b < 1$, and Δ is never non-negative everywhere. Therefore, in the two-integral case, $\Delta_R = \Delta < 0$; also, if $b_{\rm M} < 1$ (i.e. when $[R\,\rho_*, \Phi] < 0$), $\overline{v_\varphi^2} < 0$ as well.

CHAPTER 4

Axisymmetric models

After having set a general procedure to understand the behavior of the solutions of the JEs as a function of the b parameter, and to constrain the values of b to ensure the positivity of the fields, it is useful to apply this procedure to some sufficiently simple axisymmetric models, for which all the critical regions and the limits for b can be easily found analytically or numerically. This also allows to understand if there is some connection between the properties of the galaxy, as its shape or the presence of a DM halo, and the behavior previously discussed, recalling for example that the empirical results shown in Chapter 1 clearly show a connection between the maximum amount of b-anisotropy and the flattening of the stellar density distribution. The numerical solution of the JEs for the following models, as all the kinematic maps shown in the Figures, are made with a *Wolfram Mathematica* code specifically written for this work, and illustrated in Appendix C.

This Chapter is structured as follows. In Chapter 4.1, we will analyze some self-gravitating disky and ellipsoidal models, i.e. the Miyamoto and Nagai (1975) (hereafter MN) disk (Section 4.1.1), the Satoh (1980) disk (Section 4.1.2), the ellipsoidal Sérsic (1968) models (see Section 4.1.3) and the ellipsoidal γ-models (see Section 4.1.4); we will investigate if the flattening and the shape of the stellar density profile have some appreciable effects on the behavior of the critical regions and the limits for b (Section 4.1.5). Then, in Section 4.2 we will discuss a couple of models with an additional DM halo, i.e. a MN disk in a dominant Binney logarithmic halo (Section 4.2.1) and an ellipsoidal dV profile in a Singular Isothermal Sphere (SIS) DM halo (Section 4.2.2); our purpose

will be to understand whether the DM halo has some relevant effects on the behaviors previously discussed (Section 4.2.3). Finally, in Section 4.3 we will repeat our analysis for two simple models with $[\rho_*, \Phi] < 0$, i.e. the one-component Binney logarithmic halo (Section 4.3.1), and power-law ellipsoids in a dominant SIS (Section 4.3.2), comparing the results with those obtained from the previous models (Section 4.3.3).

4.1 One-component models

In light of the results in Section 3.3, we now explore the behavior of some well-known self-gravitating galaxy models, following a fully analytical treatment when possible. The models could be divided into two main "families": the disky models, i.e. the MN and Satoh (1980) disks, and the ellipsoidal models, i.e the Sérsic (1968) and γ-models. In the former case, the systems are more idealized, but their analysis is useful to understand if our general results are verified, and how the critical regions and the limits for b change by changing the flattening of the stellar density profile. In the latter case, instead, the chosen models are more realistic and representative of the population of regular rotators observed through IFS surveys (see e.g. Cappellari 2016); in this way, we intend to study in a more quantitative way if there are any additional effects linked to the density flattening and shape, which are missed by the disky galaxy models. Finally, from our findings we will derive some more stringent conclusions on the relations between our determined limits for b and the empirical results of Wang, Cappellari, and Peng (2021), concerning the distribution of realistic mock galaxies on the $(V/\sigma - \varepsilon)$ and $(\lambda_R - \varepsilon)$ diagrams.

For our discussion, it is important to notice that, from equation (2.24), a sufficient condition to have $D \leq 0$ over the whole (R, z) plane is that $\partial\rho_*/\partial R \leq 0$ and $\partial^2\Phi/\partial R\partial z \leq 0$ everywhere. For the ellipsoidal models, this condition is verified for any $\rho_*(m_*)$ in the potential produced by an ellipsoidal $\rho_{\rm h}(m_{\rm h})$ (independently of the flattenings of the two distributions) if $d\rho_*(m_*)/dm_* \leq 0$ and $d\rho_{\rm h}(m_{\rm h})/dm_{\rm h} \leq 0$. From this conditions, we derive that $[\rho_*, \Phi] \geq 0$ and $D \leq 0$ everywhere for all models considered in this Section.

4.1.1 Miyamoto & Nagai disk

The potential-density pair of the MN disk of total mass M_*, and scale lengths a_* and b_* can be written as:

$$\begin{cases} \Phi_* = -\dfrac{GM_*}{b_*\,\xi}, \quad \xi \equiv \sqrt{R^2 + (s+\zeta)^2}, \\ \\ \rho_* = \dfrac{M_*}{b_*^3}\dfrac{s\,\xi^2 + 3\,\zeta\,(s+\zeta)^2}{4\pi\,\zeta^3\xi^5}, \end{cases} \tag{4.1}$$

where $\zeta \equiv \sqrt{1+z^2}$, and $s \equiv a_*/b_*$ is a measure of the flattening of the disk; for $a_* = 0$, the MN model reduces to the Plummer (1911) sphere, while for $b_* = 0$ to the razor-thin Kuzmin disk (Kuzmin 1956, Toomre 1963). In the formulae above and in the remainder of this Section, R and z are assumed to be normalized to $b_* \neq 0$. From equations (2.24) and (2.25), we have

$$\rho_*\sigma_z^2 = \frac{GM_*^2}{b_*^4}\frac{(s+\zeta)^2}{8\pi\,\zeta^2\xi^6}, \quad [\rho_*, \Phi_*] = \frac{GM_*^2}{b_*^5}\frac{s\,R}{4\pi\,\zeta^3\xi^6}, \tag{4.2}$$

from which we see that $[\rho_*, \Phi_*] \geq 0$ everywhere, vanishing in the spherical case ($s = 0$); therefore, all the considerations made at the end of Section 3.3 apply. For reference, in the top panels of Figure 4.1 we show the 2D maps of the ansatz-independent fields σ_z^2, $R\,[\rho_*, \Phi_*]\,/\rho_*$ (i.e., Δ in the two-integral case) and $R\,\partial\Phi/\partial R$ for $s = 1$; we see that σ_z^2 present an hourglass-like shape with higher values close to the z-axis, while the other two fields peak close to the equatorial plane. For increasing s (see Figure 4.2), all the fields decrease, and the maxima of both $R\,[\rho_*, \Phi_*]\,/\rho_*$ and $R\partial\Phi/\partial R$ move towards larger radii.

To analyze the behavior of the kinematic fields as a function of b, our first task is the identification of the ansatz-independent $\mathscr{B}$, $\mathscr{C}$ and $\mathscr{D}$ regions; remarkably, equation (4.2) allows for an analytical expression for all of them. In particular, we have

$$\mathscr{B}^- = \left\{(R,z) : \sqrt{5}\,R - (s+\zeta) > 0\right\} : \tag{4.3}$$

therefore, $\mathscr{B}^-$ is the portion of the (R,z)-plane at the right of the curve $\mathscr{B}^0$, i.e. the hyperbola with vertex located at $R = (1+s)/\sqrt{5}$ and $z = 0$, and asymptotes $z = \pm\sqrt{5}R$, and $\Pr(\mathscr{B}^-)$ coincides with the z-axis. In the top panels of Figure 4.3, we show the $\mathscr{B}^-$ regions (to the right of the $\mathscr{B}^0$ lines) of the MN model for three representative values of s; we see that $\mathscr{B}^-$ becomes smaller as s increases, i.e. for more flattened models.

Moreover, the radial derivative of the first of equation (4.2) shows that, independently of s, $\mathscr{D}^-$ fully covers the (R,z)-plane, with $D = 0$ for $R = 0$; therefore, $\Pr(\mathscr{D}^-)$ coincides with the

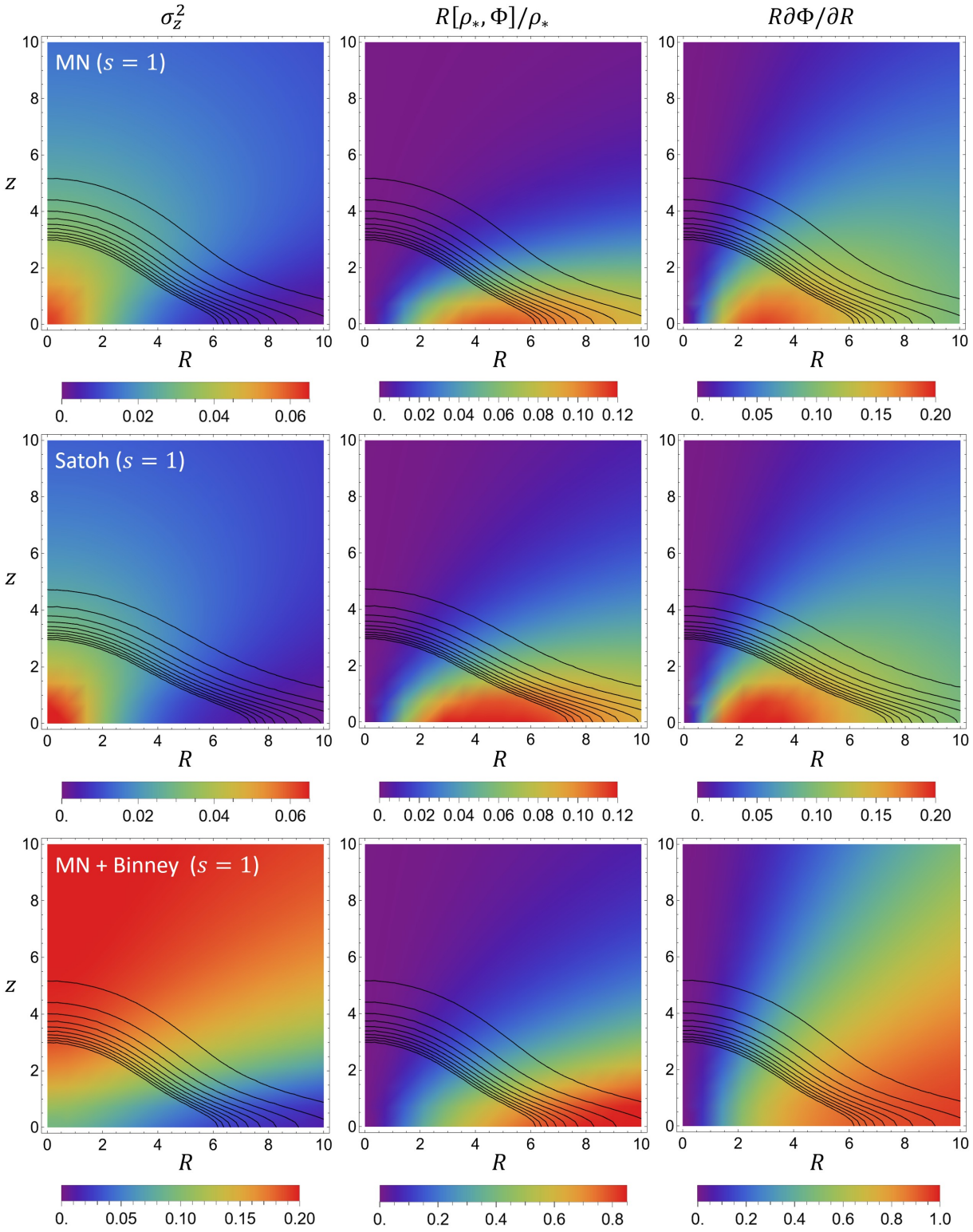


Figure 4.1. Maps in the (R, z)-plane of σ_z^2 (left column), $R\,[\rho_*, \Phi]\,/\rho_*$ (central column) and $R\,\partial\Phi/\partial R$ (right column), in units of GM_*/b_*, for the MN disk with $s = 1$ (top row), the Satoh disk with $s = 1$ (central row), and the MN stellar disk with $s = 1$ in a dominant ($\Phi = \Phi_{\rm h}$) spherical ($q_{\rm h} = 1$) Binney logarithmic DM halo with $b_{\rm h} = 2$ (bottom row). Black solid lines show equally spaced isodensity contours.

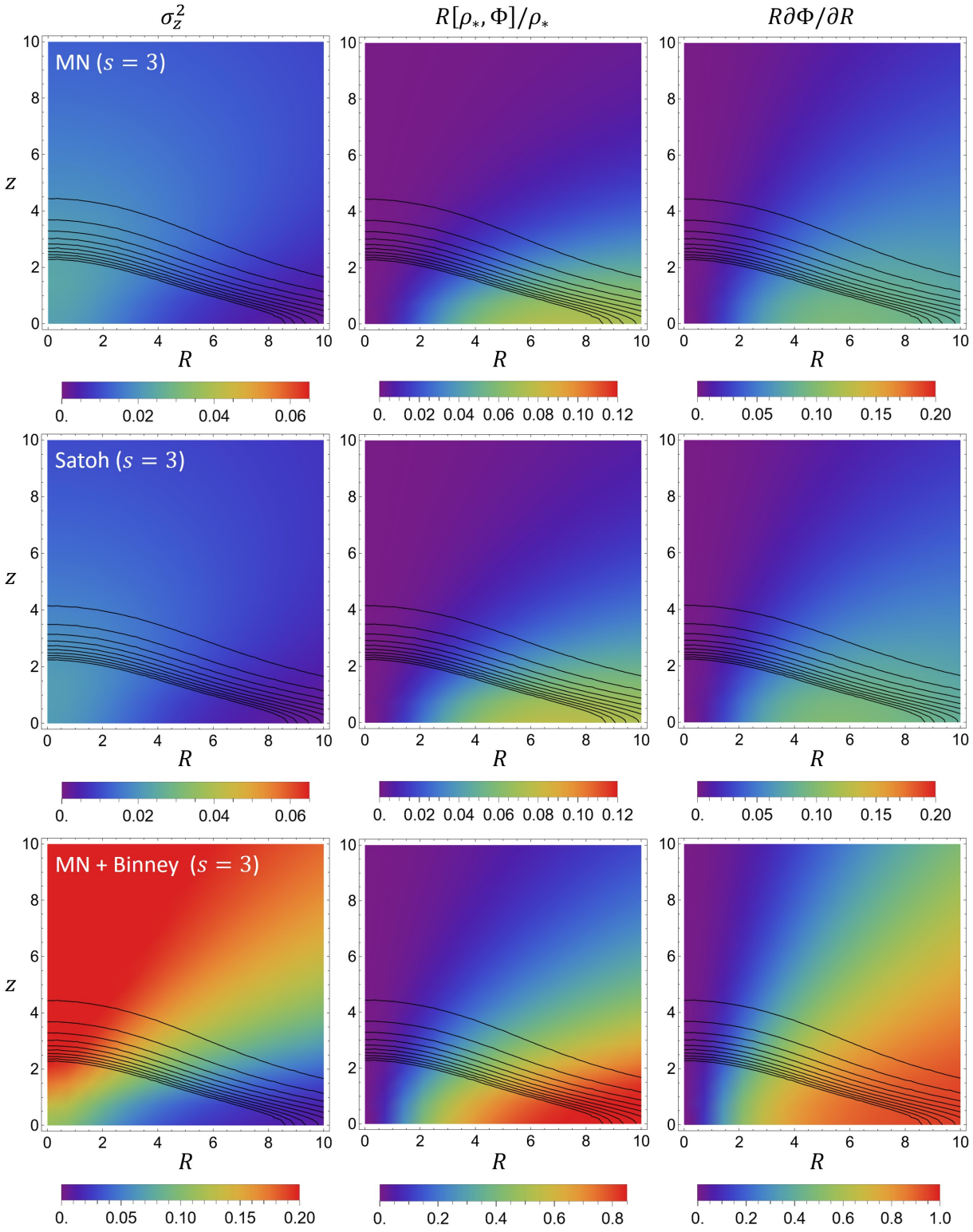


Figure 4.2. Same as Figure 4.1, but for the MN disk with $s = 3$ (top row), the Satoh disk with $s = 3$ (central row), and the MN stellar disk with $s = 3$ in a dominant ($\Phi = \Phi_{\rm h}$) spherical ($q_{\rm h} = 1$) Binney logarithmic DM halo with $b_{\rm h} = 2$.

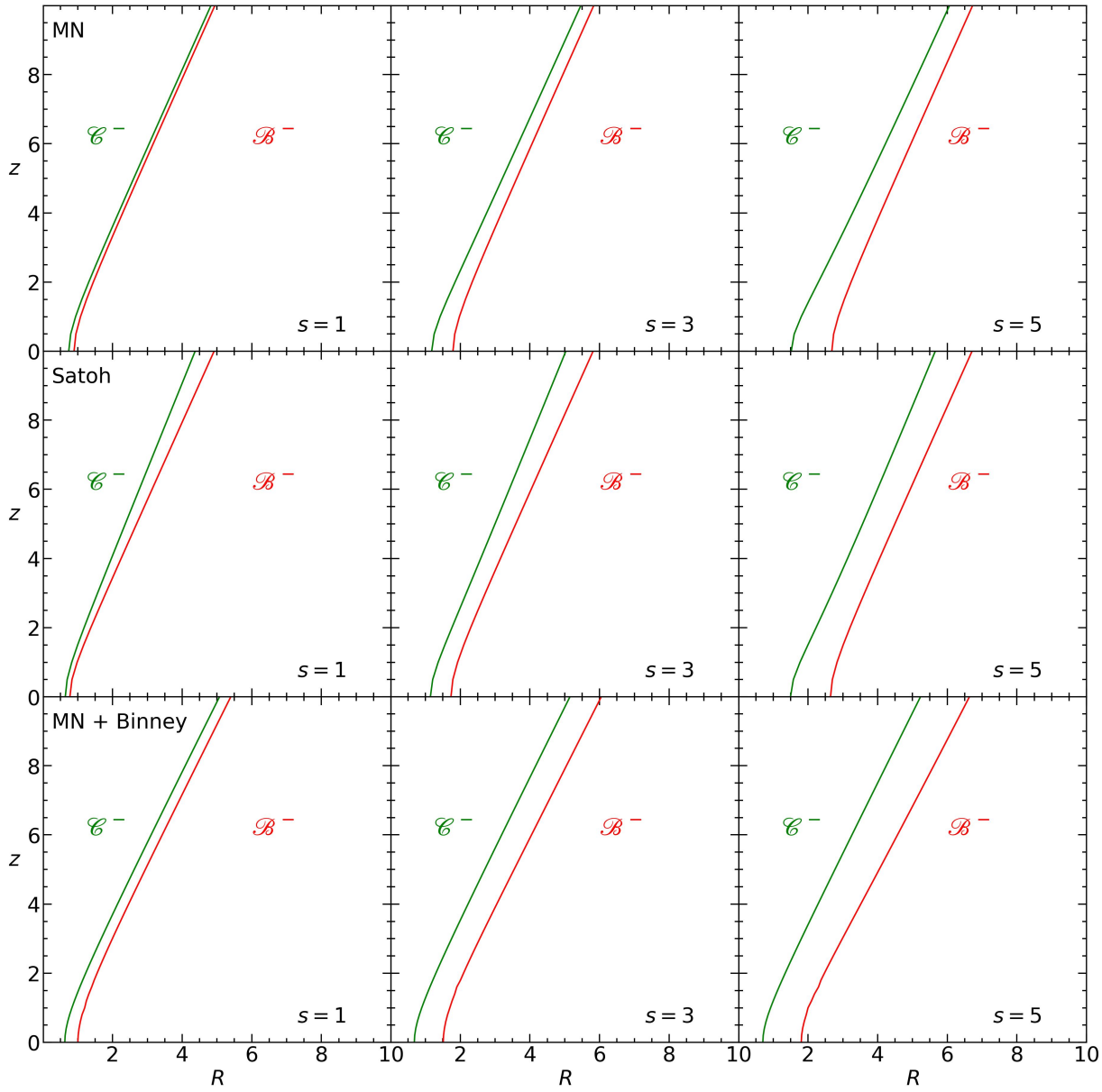


Figure 4.3. The ansatz-independent regions $\mathscr{B}$, $\mathscr{C}$ and $\mathscr{D}$ of the MN disk (top row), the Satoh disk (central row) and the MN disk in a dominant ($\Phi = \Phi_{\rm h}$) spherical ($q = 1$) Binney logarithmic halo with $b_{\rm h} = 2$ (bottom row), for different values of s; from left to right, the stellar density profiles becomes more flattened. The $\mathscr{B}^-$ and $\mathscr{C}^-$ regions are, respectively, to the right of the red curves ($\mathscr{B}^0$) and to the left of the green curves ($\mathscr{C}^0$), and Pr($\mathscr{B}^-$) and Pr($\mathscr{C}^-$) coincide with the z-axis. For all the models, $\mathscr{D}^-$ fully covers the (R, z)-plane, with $\mathscr{D}^0$ coinciding with the z-axis. The values of R and z are normalized to $b_{\rm h}$ for the Binney model, and to b_* for the other models.

z-axis, and $\mathscr{D}^+$ is empty. Finally, from the second of equation (3.5), we get

$$\mathscr{C}^- = \Big\{(R,z):\ 2s\,R^4 + (s+\zeta)^2\,(2s+5\zeta)\,R^2 - (s+\zeta)^4\,\zeta < 0\Big\}, \tag{4.4}$$

a biquadratic expression in R which has a positive discriminant, and a permanence and a variation of signs in the coefficients. It follows that $\mathscr{C}^-$ is the portion of the (R,z)-plane contained between the z-axis and the (positive) square root of the (positive) solution of the biquadratic, which we do not report here for simplicity, and $\mathrm{Pr}(\mathscr{C}^-)$ coincides with the z-axis. In the top panels of Figure 4.3, we show the $\mathscr{C}^-$ regions (to the left of the $\mathscr{C}^0$ line) of the MN model for three representative values of s; we see that the trend is opposite to that for $\mathscr{B}^-$, i.e. $\mathscr{C}^-$ becomes larger as s increases. Again from Figure 4.3, it is apparent that, independently of s, $\mathscr{B}^- \subseteq \mathscr{C}^+$ and $\mathscr{C}^- \subseteq \mathscr{B}^+$, as expected from the general considerations in Section 3.3.1; notice also how the separation between $\mathscr{B}^-$ and $\mathscr{C}^-$, i.e. the region $\mathscr{B}^+ \cap \mathscr{C}^+$, becomes larger as s increases. Moreover, in the spherical case ($s = 0$) we would have $\mathscr{B}^- = \mathscr{C}^+$ and $\mathscr{C}^- = \mathscr{B}^+$, with $\mathscr{B}^0 = \mathscr{C}^0$.

Recalling the procedure in Section 3.2, we now determine the limits for $b(z)$ that guarantee the positivity of $\overline{v_\varphi^2}$, Δ_R and Δ. Remarkably, all the computations in equations (3.11), (3.13), (3.15) and (3.16) can be carried out explicitly, and we have:

$$b_{\mathrm{M}}(z) = \frac{6}{5} + \frac{14\,s + 4\sqrt{s\,(6s+15\zeta)}}{25\,\zeta}, \tag{4.5}$$

$$b_0(z) = 1 + \frac{s}{3\,\zeta}, \tag{4.6}$$

$$b_1(z) = 1, \quad b_2(z) = 1 + \frac{\left(14 + 4\sqrt{6}\right)\,s}{25\,\zeta}. \tag{4.7}$$

In the top-left panel of Figure 4.4, we show the four functions above for three different values of s (for simplicity, b_2 is shown only for the model with $s = 3$); we see that all the limits (except for b_1, which is always equal to 1) increase for increasing s, and the chain of inequalities in equation (3.17) holds, considering that both $\mathrm{Pr}(\mathscr{B}^-)$ and $\mathrm{Pr}(\mathscr{C}^-)$ coincide with the z-axis. If one restricts to the case of a spatially constant b, we have

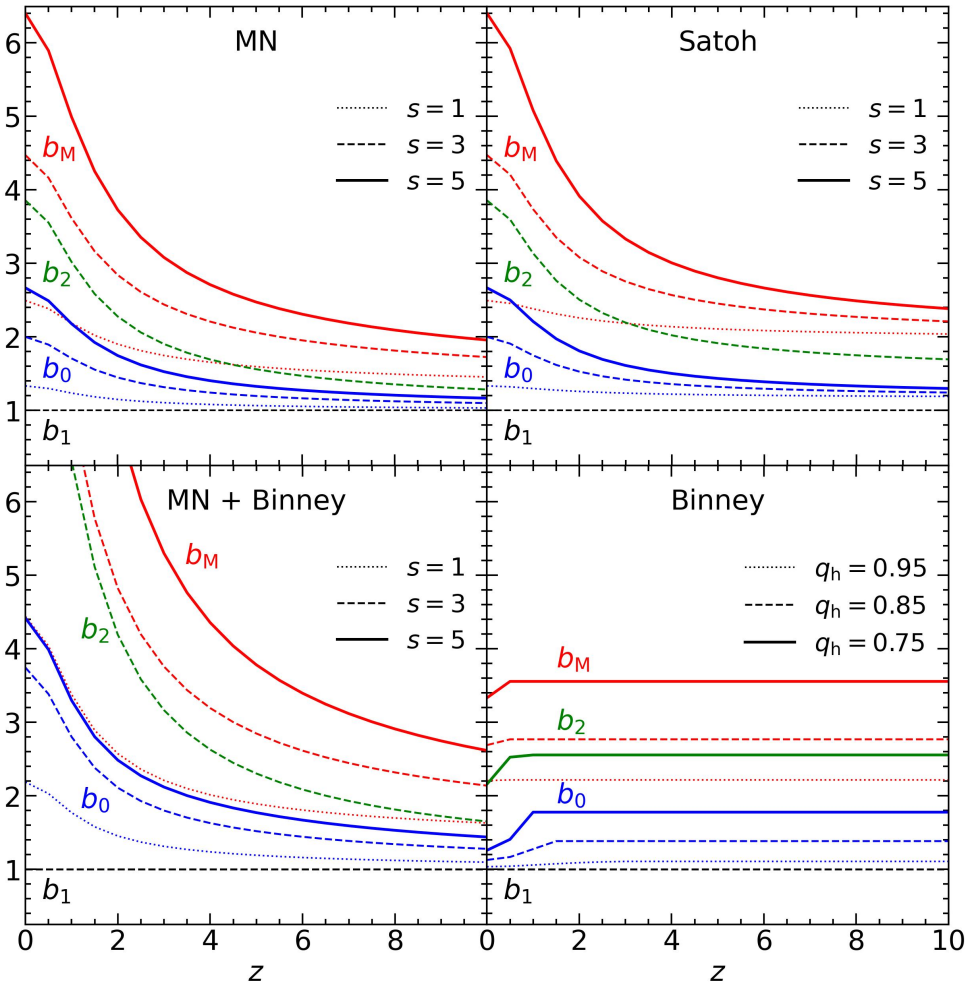


Figure 4.4. Profiles of $b_1(z)$ (black dashed curves), $b_0(z)$ (blue curves), $b_2(z)$ (green curves) and $b_{\rm M}(z)$ (red curves) for the MN disk (top-left panel), the Satoh disk (top-right panel) and the MN disk in a dominant ($\Phi = \Phi_{\rm h}$) spherical ($q = 1$) Binney logarithmic halo with $b_{\rm h} = 2$ (bottom-left panel), for different values of s, and for the one-component Binney logarithmic halo for different values of $q_{\rm h}$ (bottom-right panel). The values of z are normalized to $b_{\rm h}$ for the Binney model, and to b_* for the other models.

$$1 = b_1 = b_0 = b_2 < b_{\rm M} = \frac{6}{5}, \tag{4.8}$$

independently of s, where all the minima of the functions are reached for $z \to \infty$.

In Figure 4.5, we illustrate the behavior of $\overline{v_\varphi^2}$, Δ_R and Δ for the MN disk with $s = 1$, and for three values of constant b. For $b = 0.5$, $\overline{v_\varphi^2}$ and Δ_R are everywhere positive, while Δ is negative over some region in $\mathscr{B}^+ \cap \mathscr{C}^- = \mathscr{C}^-$, being $0.5 < b_1$, and positive over $\mathscr{B}^- \cap \mathscr{C}^+ = \mathscr{B}^-$, being $0.5 < b_2$. For $b = 1$ (i.e., the two-integral case), the fields are everywhere positive, in agreement with equation (4.8), and the increase of b from 0.5 to 1 produces the expected changes summarized in Figure 3.2: $\overline{v_\varphi^2}$ and Δ decreases over $\mathscr{B}^-$ and increases over $\mathscr{B}^+$, and Δ_R decreases over $\mathscr{D}^-$ (i.e. everywhere). Finally, the three right panels of Figure 4.5 correspond to the (unphysical) model

with $b = 2 > b_{\rm M}$, for which $\overline{v_\varphi^2}$ becomes negative inside $\mathscr{B}^-$; increasing further b would increase the size of this negativity region up to the whole $\mathscr{B}^-$, while $\overline{v_\varphi^2}$ would continue to increase in $\mathscr{B}^+$. As $2 > b_0$, Δ_R becomes negative over a region of the (R, z)-plane, which would become larger up to the entire (R, z)-plane by increasing further b. Also, being $2 > b_2$, the negativity region of Δ has now switched to the $\mathscr{B}^-$ region.

In Figure 4.6, we discuss the effects of increasing the disk flattening to $s = 3$. Notice that the trends with increasing b are the same, but since the limits for b are now higher, the negativity regions for the fields when b exceeds these limits are smaller.

4.1.2 Satoh disk

We now discuss the case of the Satoh (1980) disk, another model representative of flattened stellar density distributions, and also taken as an example in Cappellari (2020). Its potential-density pair, with total mass M_*, and scale lengths a_* and b_*, can be written as:

$$\begin{cases} \Phi_* = -\dfrac{GM_*}{b_*\xi}, \quad \xi \equiv \sqrt{R^2 + (s+\zeta)^2 - 1}, \\ \\ \rho_* = \dfrac{M_*}{b_*^3} \dfrac{s\,\xi^2 + 3\,s\,\zeta\,(s+2\zeta)}{4\pi\,\zeta^3\xi^5}, \end{cases} \tag{4.9}$$

where again $\zeta \equiv \sqrt{1+z^2}$, $s \equiv a_*/b_*$ is a measure of the disk flattening, and from now on all lengths are assumed to be normalized to $b_* \neq 0$. Notice that, contrary to the MN model, the spherical limit of the Satoh model (i.e. $s = 0$) reduces to the case of a point mass of no practical interest. From equations (2.24) and (2.25), one has:

$$\rho_*\sigma_z^2 = \frac{GM_*^2}{b_*^4} \frac{s\,(s+2\zeta)}{8\pi\,\zeta^2\xi^6}, \quad [\rho_*, \Phi_*] = \frac{GM_*^2}{b_*^5} \frac{s\,R}{4\pi\,\zeta^3\xi^6}; \tag{4.10}$$

similarly to the MN disk, $[\rho_*, \Phi_*] \geq 0$ everywhere, and so all the considerations in Section 3.3.1 apply. In the middle panels of Figure 4.1, the 2D maps of σ_z^2, $[\rho_*, \Phi]$ and $R\partial\Phi/\partial R$ are shown for $s = 1$: they are very similar to those of the MN model with same disk flattening, and the behavior of the fields for increasing s is identical as well (see the middle panels of Figure 4.2).

The $\mathscr{B}$, $\mathscr{C}$ and $\mathscr{D}$ regions can again be determined analytically. In particular,

$$\mathscr{B}^- = \left\{(R, z) : 5\,R^2 - (s+\zeta)^2 + 1 > 0\right\}, \tag{4.11}$$

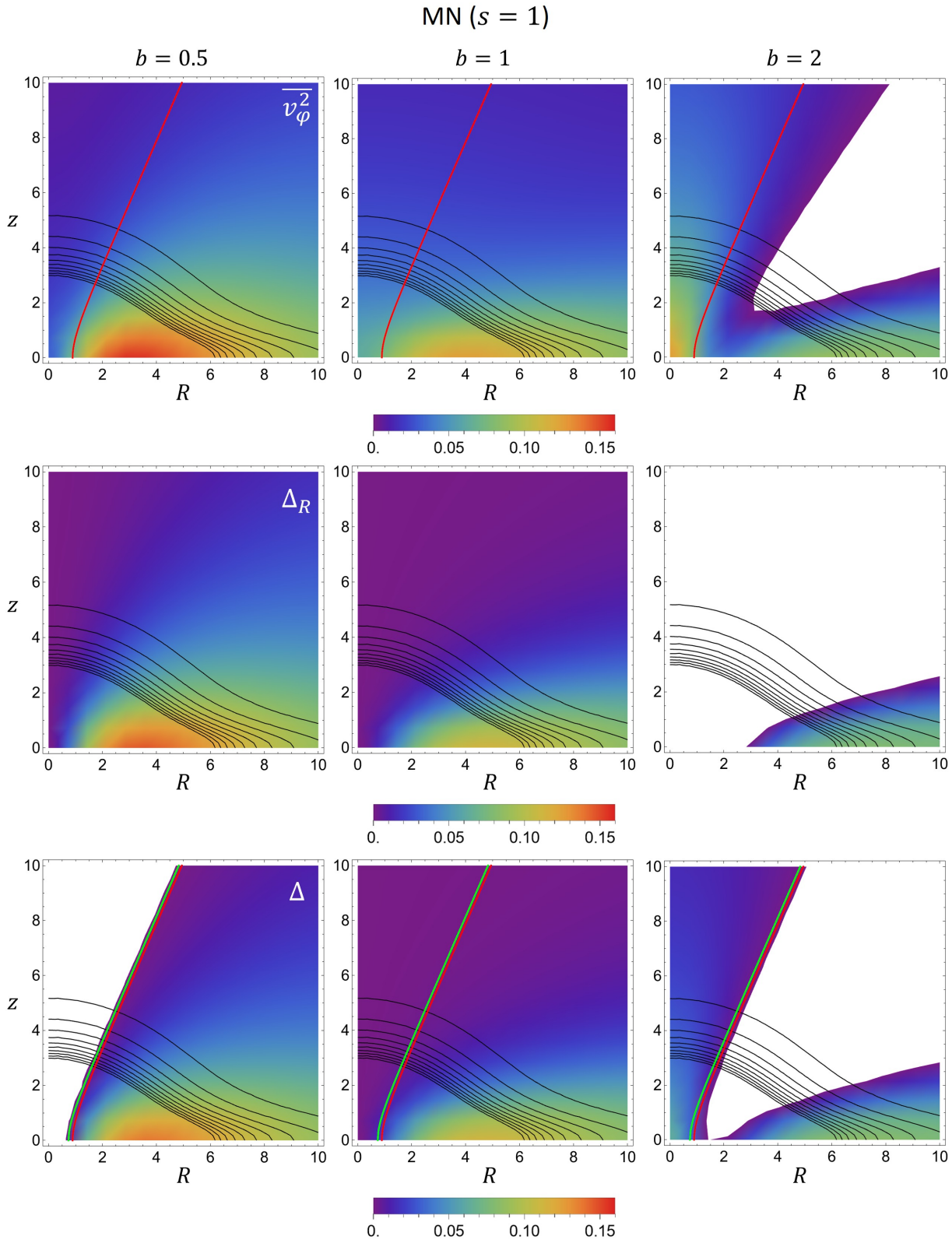


Figure 4.5. Maps in the (R, z)-plane of $\overline{v_\varphi^2}$ (top row), Δ_R (central row) and Δ (bottom row), in units of GM_*/b_*, for the MN disk with $s = 1$, and constant $b = 0.5$ (left column), $b = 1$ (central column) and $b = 2$ (right column). The red and green lines show, respectively, the $\mathscr{B}^0$ and $\mathscr{C}^0$ curves, while $\mathscr{D}^0$ coincides with the z-axis. Black solid lines show equally spaced isodensity contours. White regions correspond to negative values of the fields.

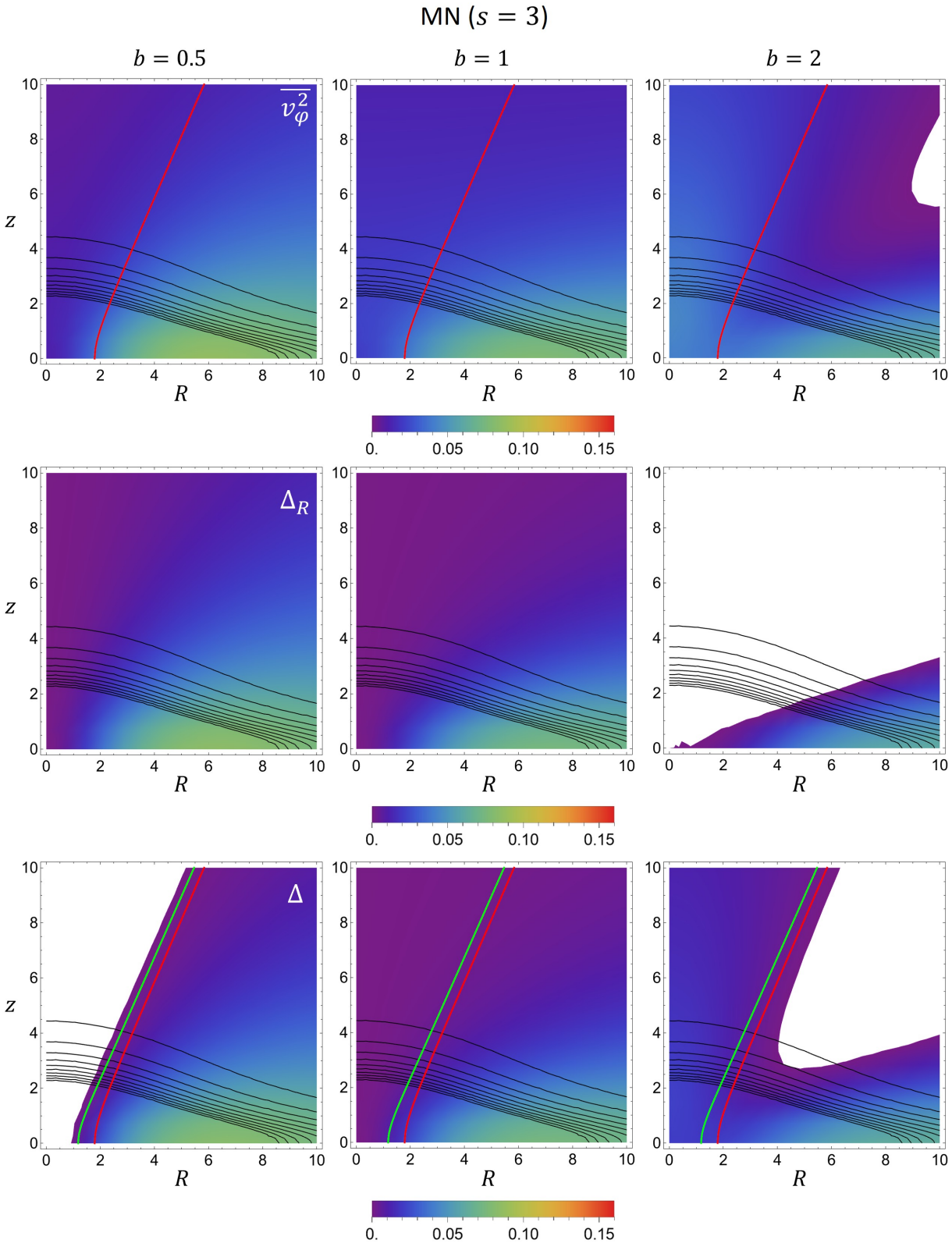


Figure 4.6. Same as in Figure 4.5, but for $s = 3$.

so that $\mathscr{B}^-$ is the portion of the (R,z)-plane to the right of the curve $\mathscr{B}^0$, i.e. the hyperbola with vertex coordinates $R=\sqrt{s\,(s+2)/5}$ and $z=0$, and asymptotes $z=\pm\sqrt{5}\,R$; again, $\mathrm{Pr}(\mathscr{B}^-)$ coincides with the z-axis. In the middle panels of Figure 4.3, we show the $\mathscr{B}^-$ regions (to the right of the $\mathscr{B}^0$ lines) of the Satoh model for three representative values of s; as for the MN model, $\mathscr{B}^-$ becomes smaller as s increases, i.e. for more flattened models.

The radial derivative of the first of equation (4.10) shows that $D<0$ everywhere, and $D=0$ on the z-axis; therefore, $\mathrm{Pr}(\mathscr{D}^-)$ coincides with the z-axis. Finally, from the second of equation (3.5), we get

$$\mathscr{C}^- = \Big\{(R,z) : 2\,R^4 + (12\,\zeta^2 + 9s\,\zeta + 2s^2 - 2)\,R^2 - (\zeta+s+1)\,(\zeta+s-1)(s+2\,\zeta)\,\zeta < 0\Big\}, \tag{4.12}$$

a biquadratic in R with two real solutions. Again, from the fact that $\zeta\geq 1$, the coefficients present a permanence and a variation of their sign, so that $\mathscr{C}^-$ is the region between the z-axis and the (positive) square root of the (positive) solution of the biquadratic. In the middle panels of Figure 4.3, we show the $\mathscr{C}^-$ regions (to the left of the $\mathscr{C}^0$ lines) for three representative values of s; the trend is opposite to that of $\mathscr{B}^-$, namely $\mathscr{C}^-$ becomes larger as the disk flattening increases. Again, all the results summarized in Section 3.3.1 about the relative position of the regions apply, i.e. $\mathscr{B}^-\cap\mathscr{C}^+=\mathscr{B}^-$ and $\mathscr{B}^+\cap\mathscr{C}^-=\mathscr{C}^-$.

As for the MN model, the limits for $b(z)$ can all be obtained analytically. From equations (3.11), (3.13), (3.15) and (3.16),

$$b_{\mathrm{M}}(z)=\frac{6}{5}+\frac{14\,\zeta_*^2+2\,\zeta_*\,\sqrt{24\,\zeta_*^2+60\,\zeta\,(s+2\zeta)}}{25\,\zeta\,(s+2\zeta)}, \tag{4.13}$$

$$b_0(z)=1+\frac{\zeta_*^2}{3\,\zeta\,(s+2\zeta)}, \tag{4.14}$$

$$b_1(z)=1,\quad b_2(z)=1+\frac{\left(14+4\sqrt{6}\right)\,\zeta_*^2}{25\,\zeta\,(s+2\zeta)}, \tag{4.15}$$

where we have defined $\zeta_*\equiv\sqrt{(s+\zeta)^2-1}$. In the top-right panel of Figure 4.4, we show the four

functions above for three values of s (for simplicity, b_2 is shown only for the $s = 3$ case). We see that, as for the MN disk, all the constraints increase for increasing disk flattening; moreover, considering that $\Pr(\mathscr{B}^-)$ and $\Pr(\mathscr{C}^-)$ both coincide with the z-axis, they fulfill the inequalities in equation (3.17). In the constant b case, we have

$$b_1 = 1 < b_0 = \frac{7}{6} < b_2 = \frac{32 + 2\sqrt{6}}{25} < b_{\mathrm{M}} = \frac{49}{25}, \tag{4.16}$$

independently of s, where all the minima are reached for $z \to \infty$.

In Figures 4.7 and 4.8, we show $\overline{v_\varphi^2}$, Δ_R and Δ of the Satoh disk for different values of constant b, analogously to Figures 4.5 and 4.6 for the MN disk. Given that the behavior of the fields with b is always the same, the shape of the critical and negativity regions are very similar between the two models; the only appreciable difference is that, for the Satoh disk, $b_1 \neq b_0 \neq b_2$, while for the MN disk they are all equal to 1. Interestingly, when $b > b_{\mathrm{M}}$, the shape and the position of the negativity region for $\overline{v_\varphi^2}$ is very close to that shown in Figure 10 of Cappellari (2020), where the numerically evaluated $\overline{v_\varphi^2}$ for the same model (with $b = 4/3$) goes to zero.

4.1.3 Ellipsoidal Sérsic models

We now want to consider a class of more realistic ellipsoidal density profiles, in order to investigate the behavior of the b-anisotropy with respect to other galaxy properties, such as its shape. As shown in Section 1.1.1, the Sérsic (1968) model fits very well the surface brightness distribution of real ETGs. Its edge-on projected surface density profile with index n, considering a stellar total mass M_* and minor-to-major axial ratio q is

$$\Sigma_*(R, z) = \frac{M_*}{R_{\mathrm{e}}^2} \frac{b_n^{2n}\, e^{-b\, l^{1/n}}}{\pi\, q\, \Gamma(2n + 1)}, \quad l = \sqrt{\frac{R^2}{R_{\mathrm{e}}^2} + \frac{z^2}{q^2 R_{\mathrm{e}}^2}}, \tag{4.17}$$

where Γ is the Euler complete gamma function (see Appendix A.1),

$$b = 2n - \frac{1}{3} + \frac{4}{405\, n} + \frac{46}{25515\, n^2} + O(n^{-3}), \tag{4.18}$$

as shown in equation (E.3), and R_{e} is the semimajor axis of the isophotal ellipse enclosing half of the total mass (or light) of the system; notice that, for $n = 4$, we obtain the well-known dV profile. Unfortunately, the deprojection $\rho_*(m)$ of equation (4.17), required to compute the gravitational force and then solve the JEs, cannot be obtained in terms of elementary functions

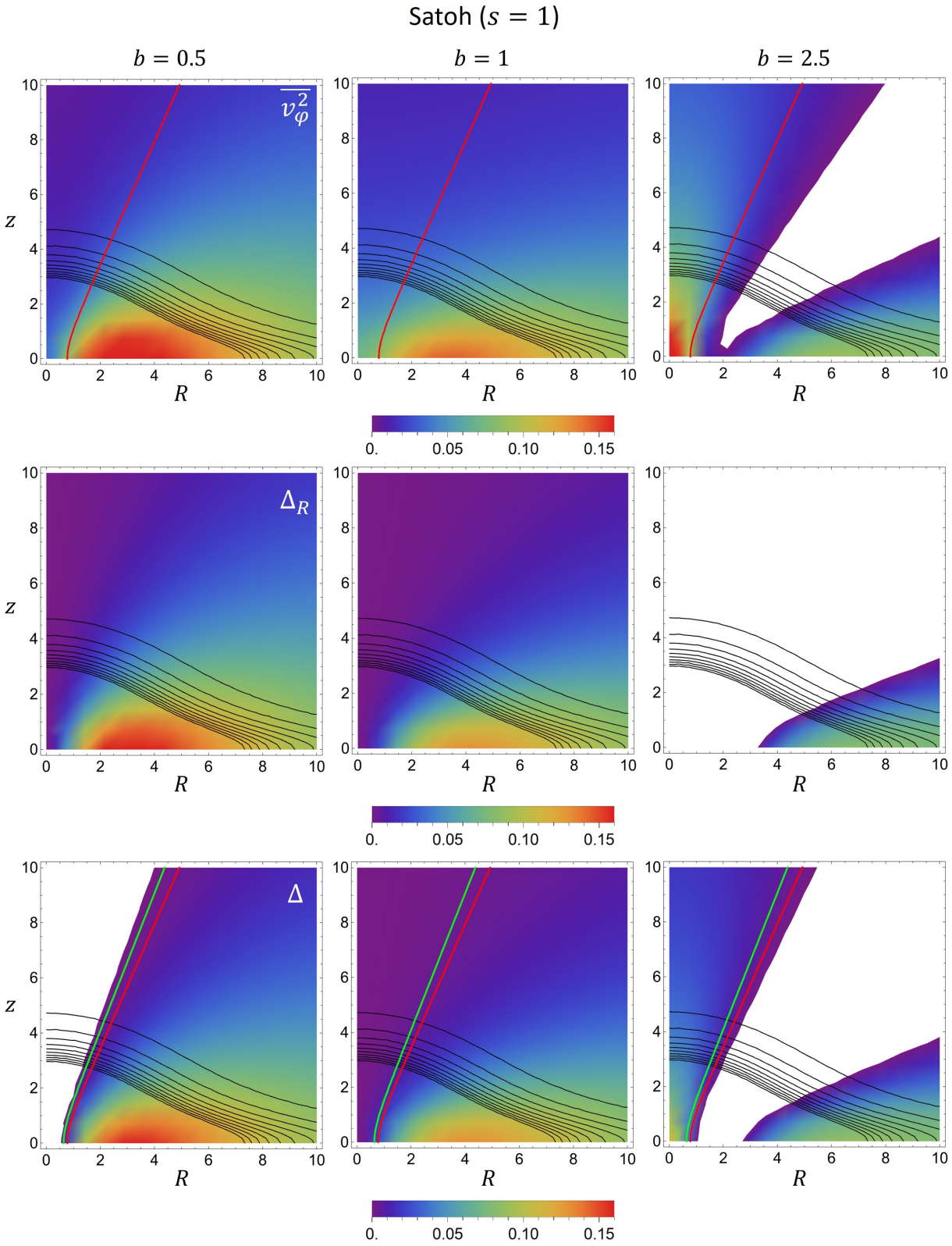


Figure 4.7. Maps in the (R, z)-plane of $\overline{v_\varphi^2}$ (top row), Δ_R (central row) and Δ (bottom row), in units of GM_*/b_*, for the Satoh disk with $s = 1$, and constant $b = 0.5$ (left column), $b = 1$ (central column) and $b = 2$ (right column). The red and green lines show, respectively, the $\mathscr{B}^0$ and $\mathscr{C}^0$ curves, while $\mathscr{D}^0$ coincides with the z-axis. Black solid lines show equally spaced isodensity contours. White regions correspond to negative values of the fields.

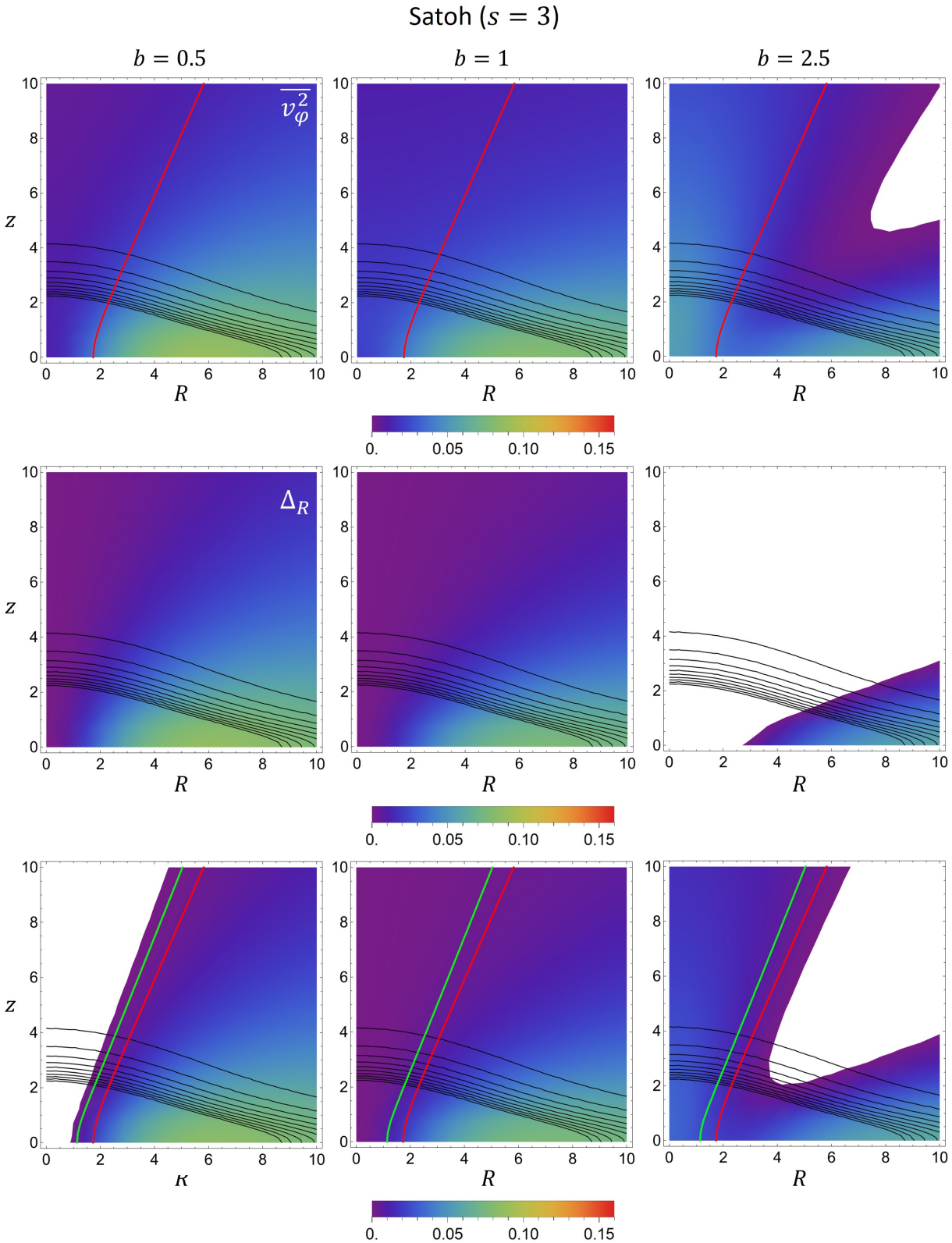


Figure 4.8. Same as in Figure 4.7, but for $s = 3$.

for generic values of n. Analytical approximations of the deprojection of the Sersic profile are known in literature, and some of them are reported in Appendix E.1.1; here, we adopt the very accurate expression reported in Appendix E.2:

$$\rho_*(m) = \frac{M_*}{q\,R_\mathrm{e}^3}\frac{c_1\,\mathrm{e}^{-b\,m^{1/n}}m^{1/n-1}}{\left[1+c_2^{p_n}\,m^{p_n/(2n)}\right]^{1/p_n}},\quad m=\sqrt{\frac{R^2}{R_\mathrm{e}^2}+\frac{z^2}{q^2R_\mathrm{e}^2}} \tag{4.19}$$

where

$$c_1 = \frac{b_n^{2n+1}}{4\pi^2\,n^2\,\Gamma(2n)}\,\mathrm{B}\left(\frac{1}{2},\frac{n-1}{2n}\right),\quad c_2=\sqrt{\frac{b}{2\pi n}}\,\mathrm{B}\left(\frac{1}{2},\frac{n-1}{2n}\right), \tag{4.20}$$

B is Euler complete beta function (see Appendix A.1), and the values of p_n as a function of n are provided in Table E.1.

For reference, in the top panels of Figure 4.9 we show the 2D maps of σ_z^2, $[\rho_*,\Phi]$ and $R\,\partial\Phi/\partial R$ for the dV model with $q=0.5$. Notice that the fields are quite similar to the ones of the disky models in Figure 4.1, apart from the fact that the maxima of $[\rho_*,\Phi]$ and $R\,\partial\Phi/\partial R$ are reached closer to the center. The effects of the shape and stellar density flattening are shown in the top panels of the analogous Figures 4.10 and 4.11. The only relevant effect of decreasing q is to slightly increase the value of $[\rho_*,\Phi]$ and $R\,\partial\Phi/\partial R$ close to the equatorial plane; increasing n has a similar effects, but it also increases σ_z^2 close to the center.

Differently from the models previously investigated, the $\mathscr{B}^\pm$, $\mathscr{C}^\pm$ and $\mathscr{D}^\pm$ regions can not be derived analytically; however, with the numerical code presented in Appendix C, their numerical determination is straightforward. In Figure 4.12, we show the $\mathscr{B}^-$ (to the right of the $\mathscr{B}^0$ lines) and $\mathscr{C}^-$ (to the left of the $\mathscr{C}^0$ lines) regions for different values of q and n; the stellar density flattening increases from left to right. Decreasing q makes both $\mathscr{B}^-$ and $\mathscr{C}^-$ smaller, so that the region $\mathscr{B}^+\cap\mathscr{C}^+$ becomes larger, while increasing n makes $\mathscr{B}^-$ smaller and $\mathscr{C}^-$ larger; the effects of increasing flattening are is in accordance to what observed for the disky models in Figure 4.3, and dominant over that of changing the density shape. As expected from the general discussion in Section 3.3, given that $[\rho_*,\Phi]\geq 0$ everywhere, we see that $\mathscr{B}^-\subseteq\mathscr{C}^+$ and $\mathscr{C}^-\subseteq\mathscr{B}^+$, and in the spherical case ($q=1$) we would have the regions would coincide (with $\mathscr{B}^0=\mathscr{C}^0$). Finally, it should be noted how $\mathscr{B}^0$ and $\mathscr{C}^0$ are almost straight lines for all n and q. All these properties can be understood by using the simple power-law models described in Appendix F: in particular, the left panels of Figures F.6 and F.12 illustrate the dependence of the $\mathscr{B}^0$ and $\mathscr{C}^0$ curves on the

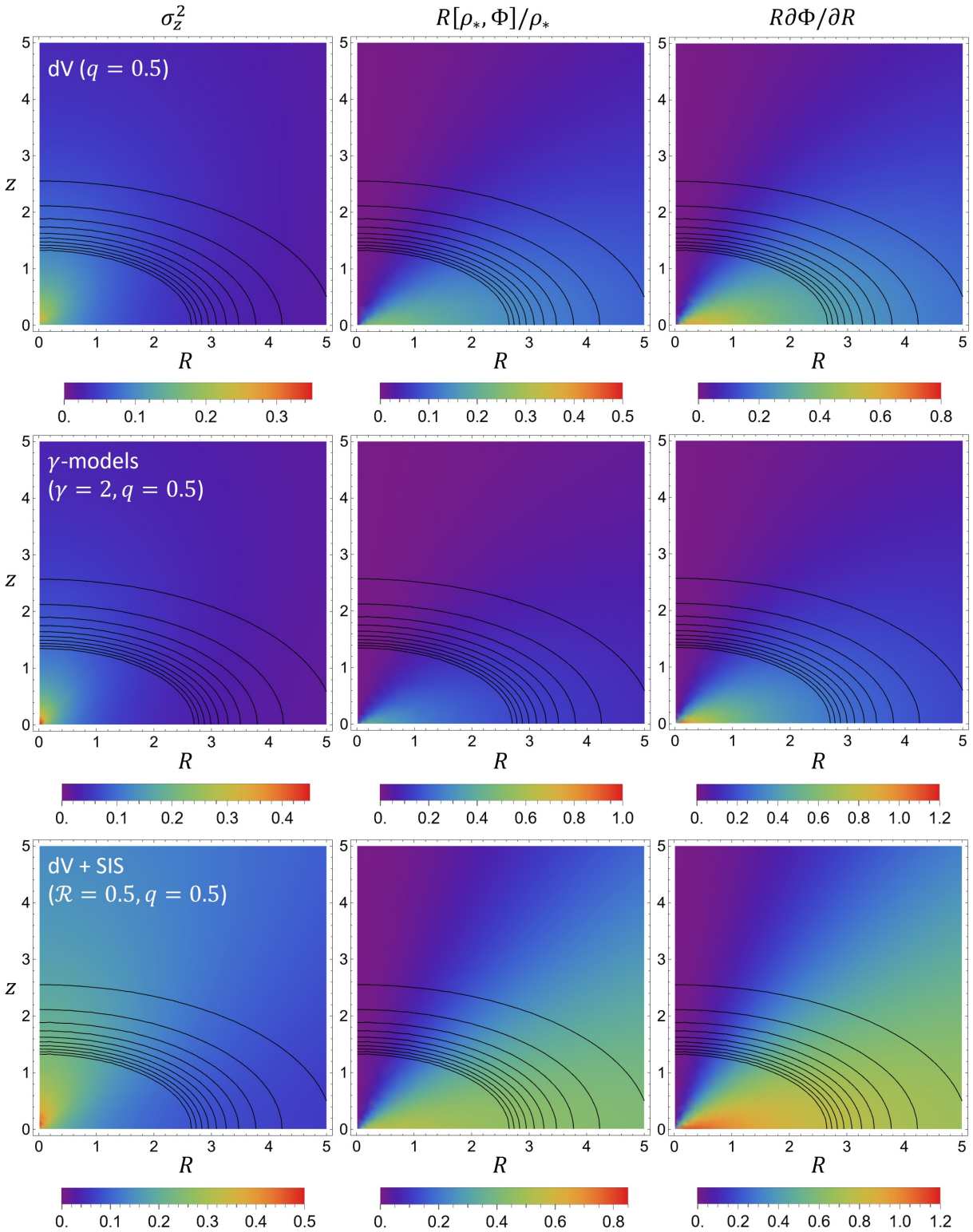


Figure 4.9. Maps in the (R, z)-plane of σ_z^2 (left column), $R\,[\rho_*, \Phi]\,/\rho_*$ (central column), and $R\,\partial\Phi/\partial R$ (right column) for the ellipsoidal dV model with $q = 0.5$ (top row), the ellipsoidal γ-model with $\gamma = 2$ and $q = 0.5$ (central row), and the ellipsoidal dV model ($q = 0.5$) in a SIS with $\mathcal{R} = 0.5$. The fields are in units of GM_*/a_* for the γ-models, and of GM_*/R_e for the other two models. Black solid lines show equally spaced isodensity contours.

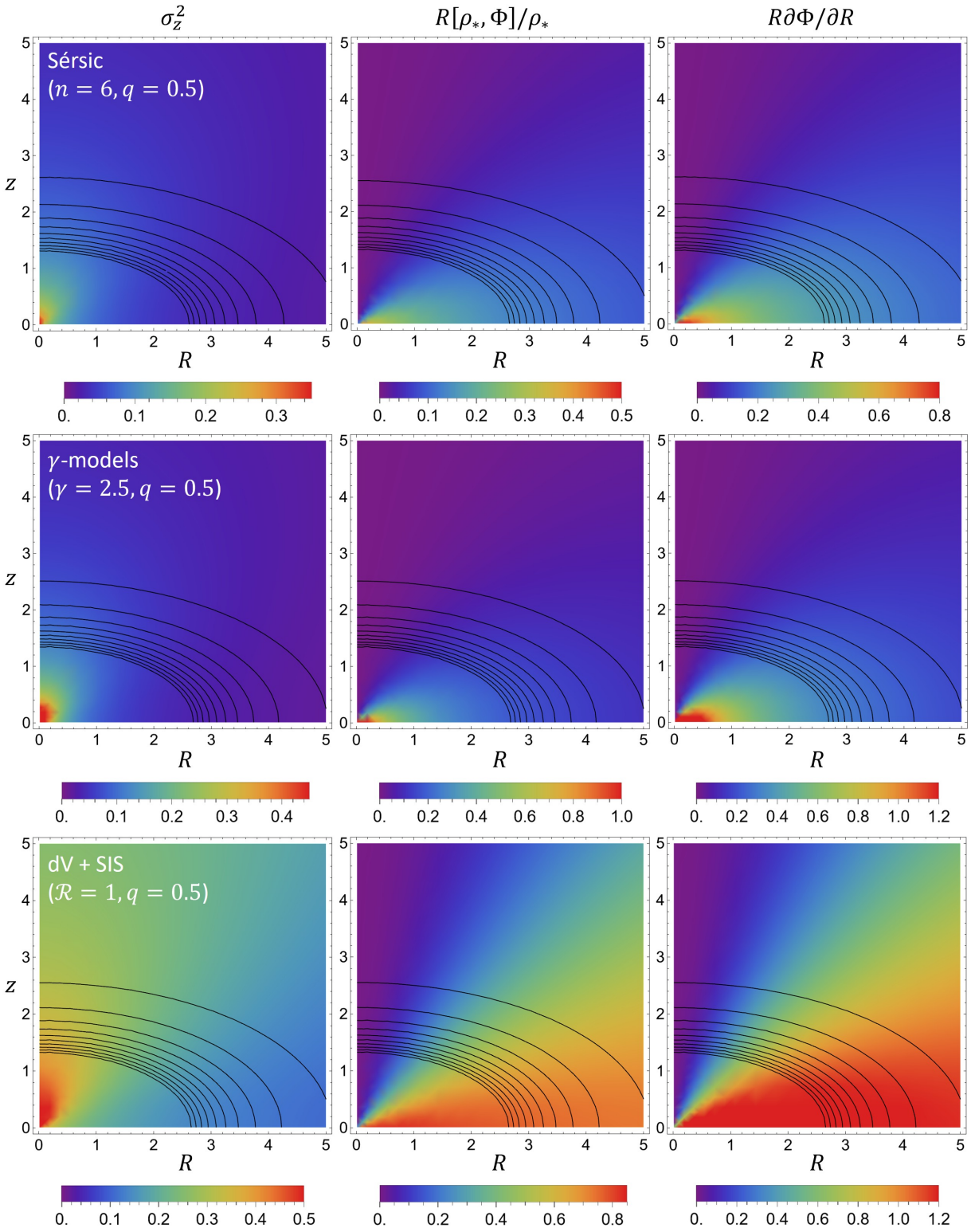


Figure 4.10. Same as in Figure 4.9, but for the ellipsoidal Sérsic model with $n = 6$ and $q = 0.5$ (top row), the ellipsoidal γ-model with $\gamma = 2.5$ and $q = 0.5$ (central row), and the ellipsoidal dV model with $q = 0.5$ in a SIS with $\mathcal{R} = 1$.

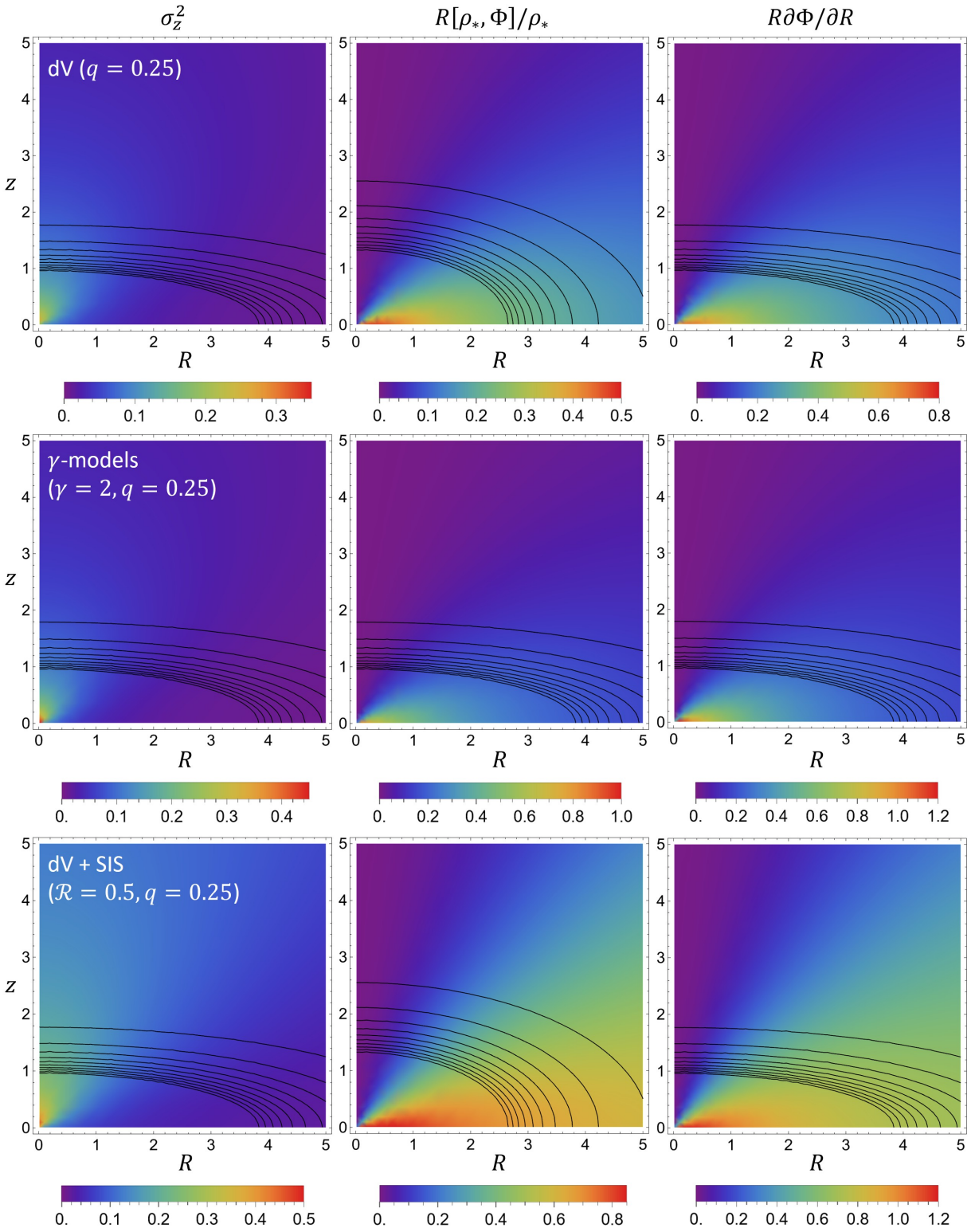


Figure 4.11. Same as in Figure 4.9, but for the ellipsoidal dV model with $q = 0.25$ (top row), the ellipsoidal γ-model with $\gamma = 2$ and $q = 0.25$ (central row), and the ellipsoidal dV model with $q = 0.25$ in a SIS with $\mathcal{R} = 0.5$.

model flattening, which is qualitatively identical to that of these models.

The limits for b for this model can be obtained numerically, and in the top-left panel of Figure 4.13 we show the profiles of $b_{\rm M}$, b_0, b_1 and b_2 (in the constant b case) as a function of q, for three different values of n (for simplicity, the b_2 curve is shown only for the dV model). Notice that, apart from $b_1 = 1$ for all the models, all the values of the constraints become higher as the stellar density flattening increase, in analogy to what observed in Figure 4.4 for the disky models. Moreover, as for the shape and the size of the $\mathscr{B}^-$ and $\mathscr{C}^-$ regions, also these limits depend much more on q than on the specific density profile, as we can see from the small variation of the curves with n. Again, these results can be interpreted with the the models in Appendix F, whose critical b can be expressed in a fully analytical way, and are shown in the bottom-right panel of Figure 4.13; in particular, the comparison should be carried out with the curves corresponding to power-law models in a monopole potential, a situation that naturally holds at intermediate or large radii in finite-mass models. Notice that not only qualitatively, but also quantitatively, the curves are very similar, although Sérsic models are not power-law profiles.

In Figure 4.14, we show the fields $\overline{v_\varphi^2}$, Δ_R and Δ of the one-component dV model with $q = 0.5$, for three different values of constant b. Apart from the different shape of the $\mathscr{B}^-$ and $\mathscr{C}^-$ regions, the behavior of the fields for increasing b is analogous to what observed in Sections 4.1.1 and 4.1.2 for disky models, given that for all of these models $[\rho_*, \Phi] \geq 0$ everywhere, and $\mathscr{D}^-$ covers all the (R, z)-plane; in particular, $\overline{v_\varphi^2}$ and Δ increase in $\mathscr{B}^+$ and decrease in $\mathscr{B}^-$, and Δ_R decreases everywhere. The effect of increasing the stellar density flattening is shown in Figure 4.15, where we show the same model with $q = 0.25$. In line with our expectations, the effects are quite significant: in fact, we see that $\overline{v_\varphi^2}$ and Δ are now positive over all $\mathscr{B}^-$ for $b = 3.5$, given that $b_{\rm M}$ and b_2 have become both higher, and the negativity region of Δ_R has become smaller in size. In Figure 4.16, instead, we show the same fields for a Sérsic model with $n = 6$ and $q = 0.5$. We see that the effects of increasing n, thus changing the specific density profile, has a very minor effect compared to that of the stellar density flattening, apart from a slight increase of Δ_R and Δ close to the equatorial plane for low values of b.

4.1.4 Ellipsoidal γ-models

Another family of realistic ellipsoidal models is that of the so-called γ-models (see Dehnen 1993, BT08); their density profile, assuming total stellar mass M_*, minor-to-major axial ratio q and

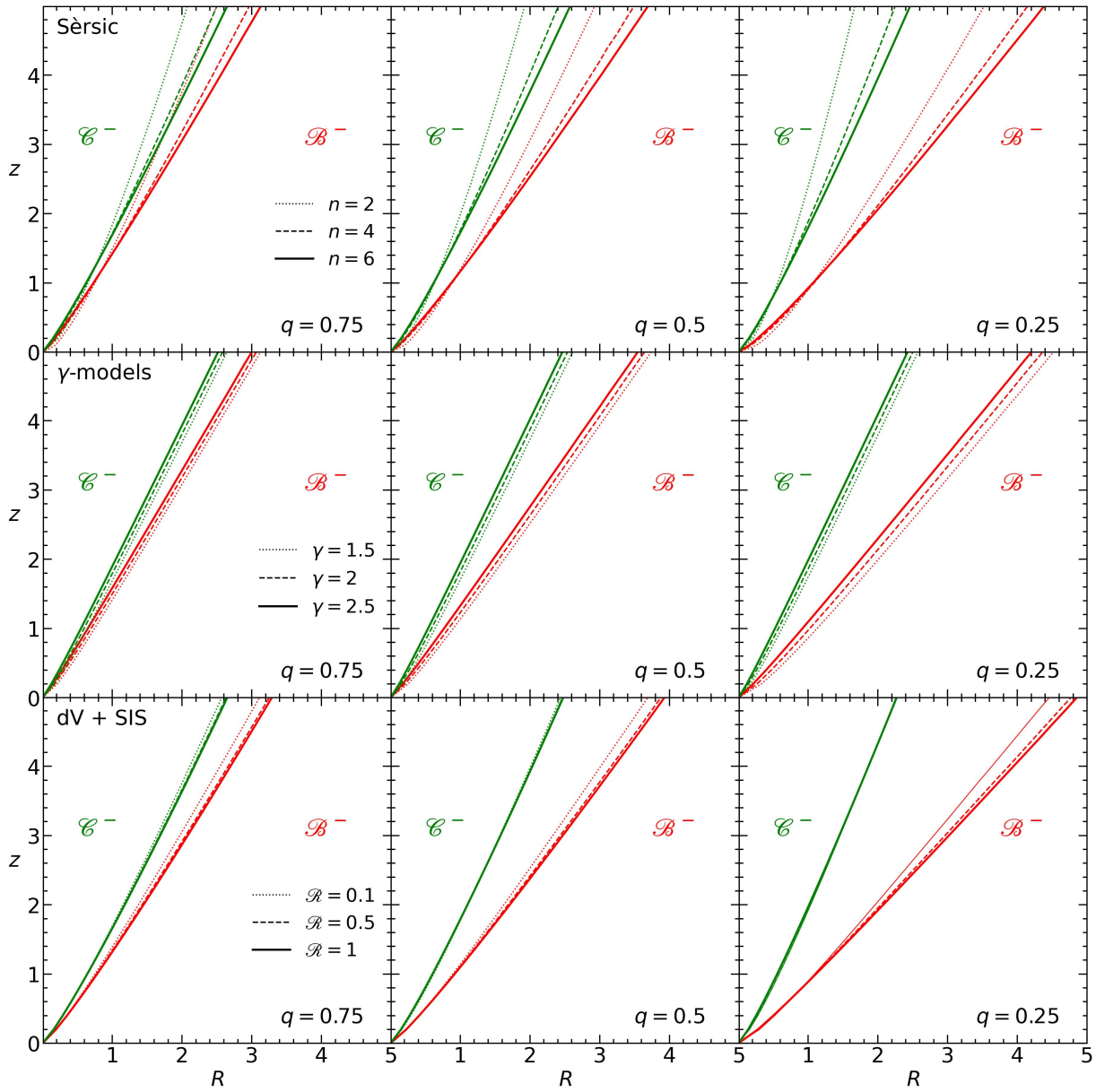


Figure 4.12. The ansatz-independent regions $\mathscr{B}$, $\mathscr{C}$ and $\mathscr{D}$ of the ellipsoidal Sérsic model with different values of q and n (top row), the ellipsoidal γ-model with different values of q and γ (central row), and the ellipsoidal dV model in a SIS with different values of $\mathcal{R}$ (bottom row); from left to right, the stellar density profile becomes more flattened. The $\mathscr{B}^-$ and $\mathscr{C}^-$ regions are, respectively, to the right of the red curves ($\mathscr{B}^0$) and to the left of the green curves ($\mathscr{C}^0$), and $\mathrm{Pr}(\mathscr{B}^-)$ and $\mathrm{Pr}(\mathscr{C}^-)$ coincide with the z-axis. For all the models, $\mathscr{D}^-$ fully covers the (R, z)-plane, with $\mathscr{D}^0$ coinciding with the z-axis. The values of R and z are normalized to a_* for the γ-models, and to R_e for the other models.

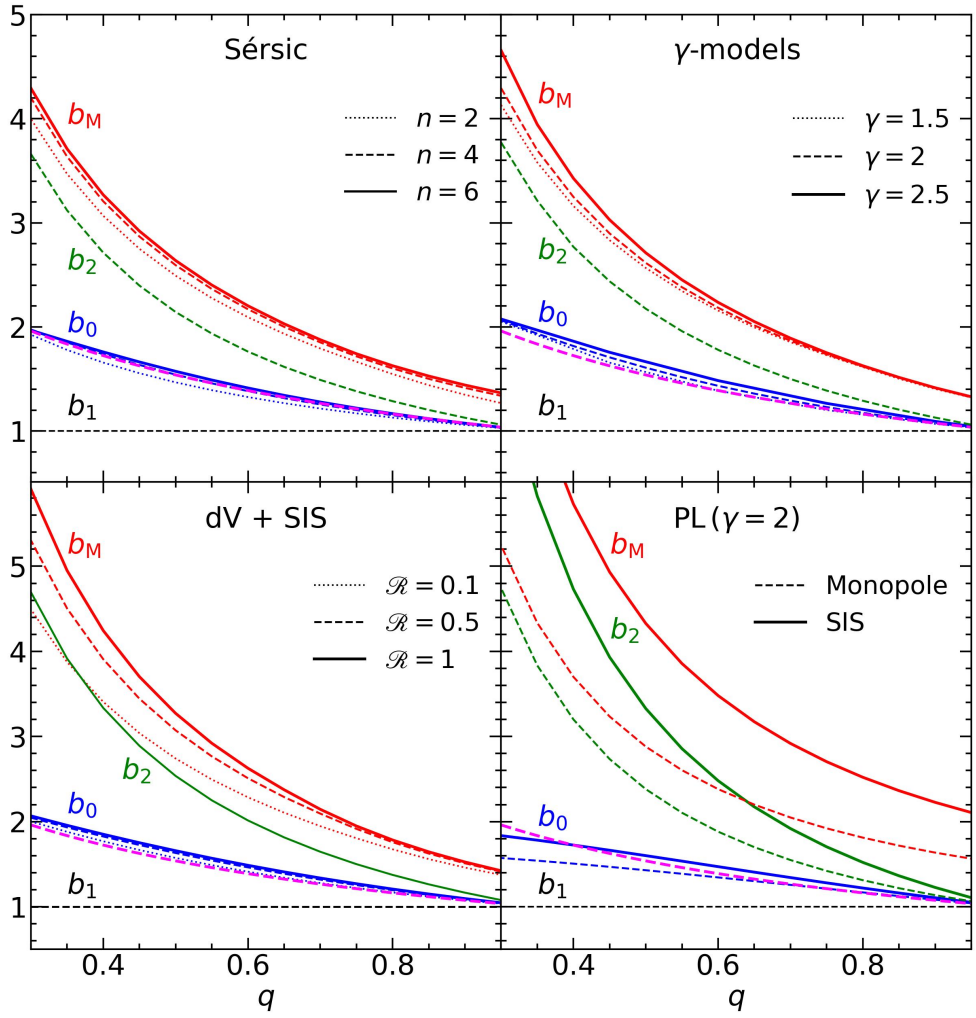


Figure 4.13. Profiles of b_1 (black dashed curves), b_0 (blue curves), b_2 (green curves) and $b_{\rm M}$ (red curves) as a function of q for the ellipsoidal Sérsic model with different n (top-left panel), the ellipsoidal γ-model with different values of γ (top-right panel), the ellipsoidal dV models in a SIS with different values of $\mathcal{R} = v_{\rm h}^2 R_{\rm e}/GM_*$ (bottom-left panel), and the ellipsoidal power-law model with $\gamma = 2$ in a dominant SIS or monopole potential (bottom-right panel). In all the panels, the magenta line is the limit on the b-anisotropy as a function of the stellar density flattening reported in Cappellari, Emsellem, Bacon, et al. (2007) (see Section 1.4).

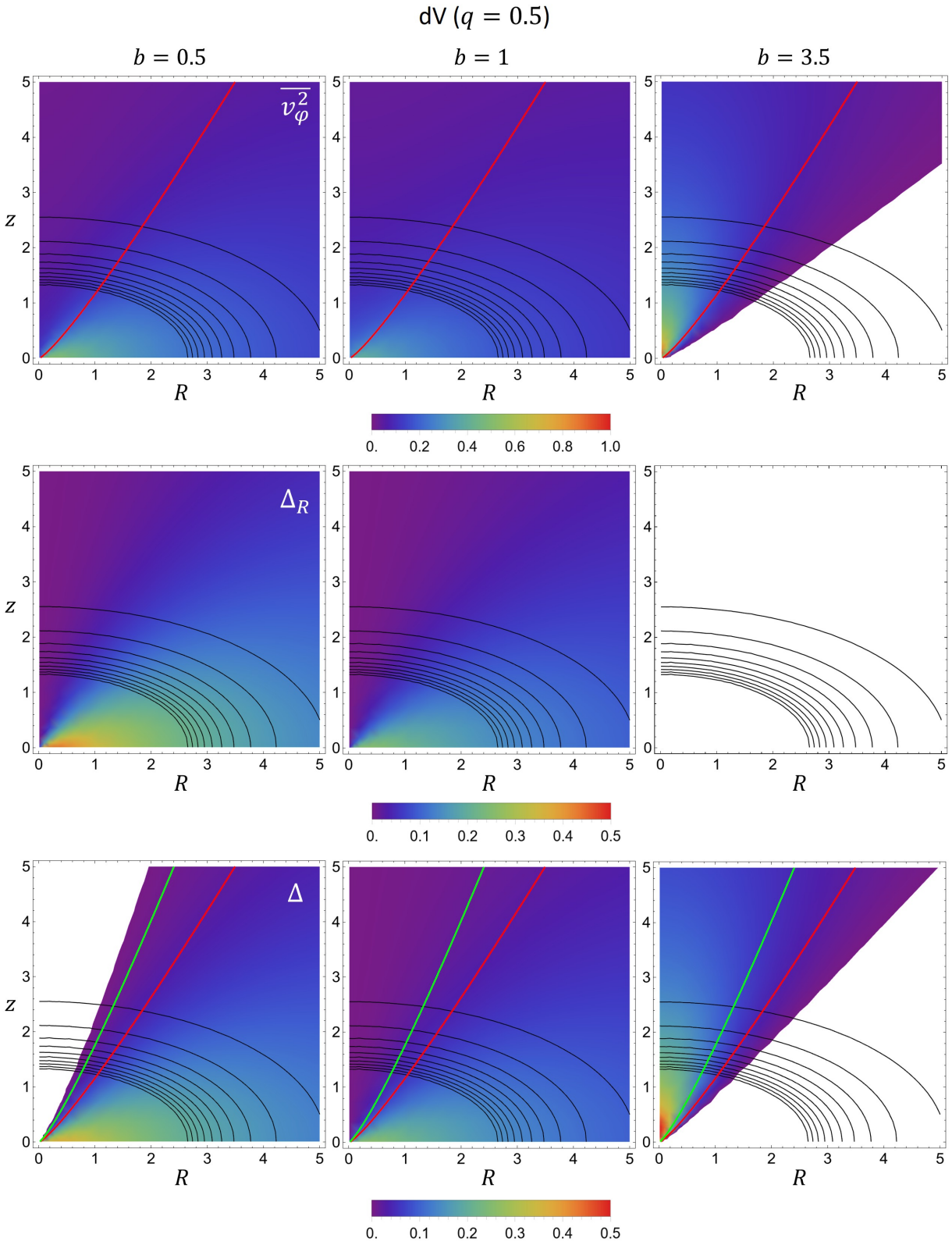


Figure 4.14. Maps in the (R, z)-plane of $\overline{v_\varphi^2}$ (top row), Δ_R (central row) and Δ (bottom row), in units of GM_*/R_e, for the ellipsoidal dV model with $q = 0.5$, and constant $b = 0.5$ (left column), $b = 1$ (central column) and $b = 2$ (right column). The red and green lines show, respectively, the $\mathscr{B}^0$ and $\mathscr{C}^0$ curves, while $\mathscr{D}^0$ coincides with the z-axis. Black solid lines show equally spaced isodensity contours. White regions correspond to negative values of the fields.

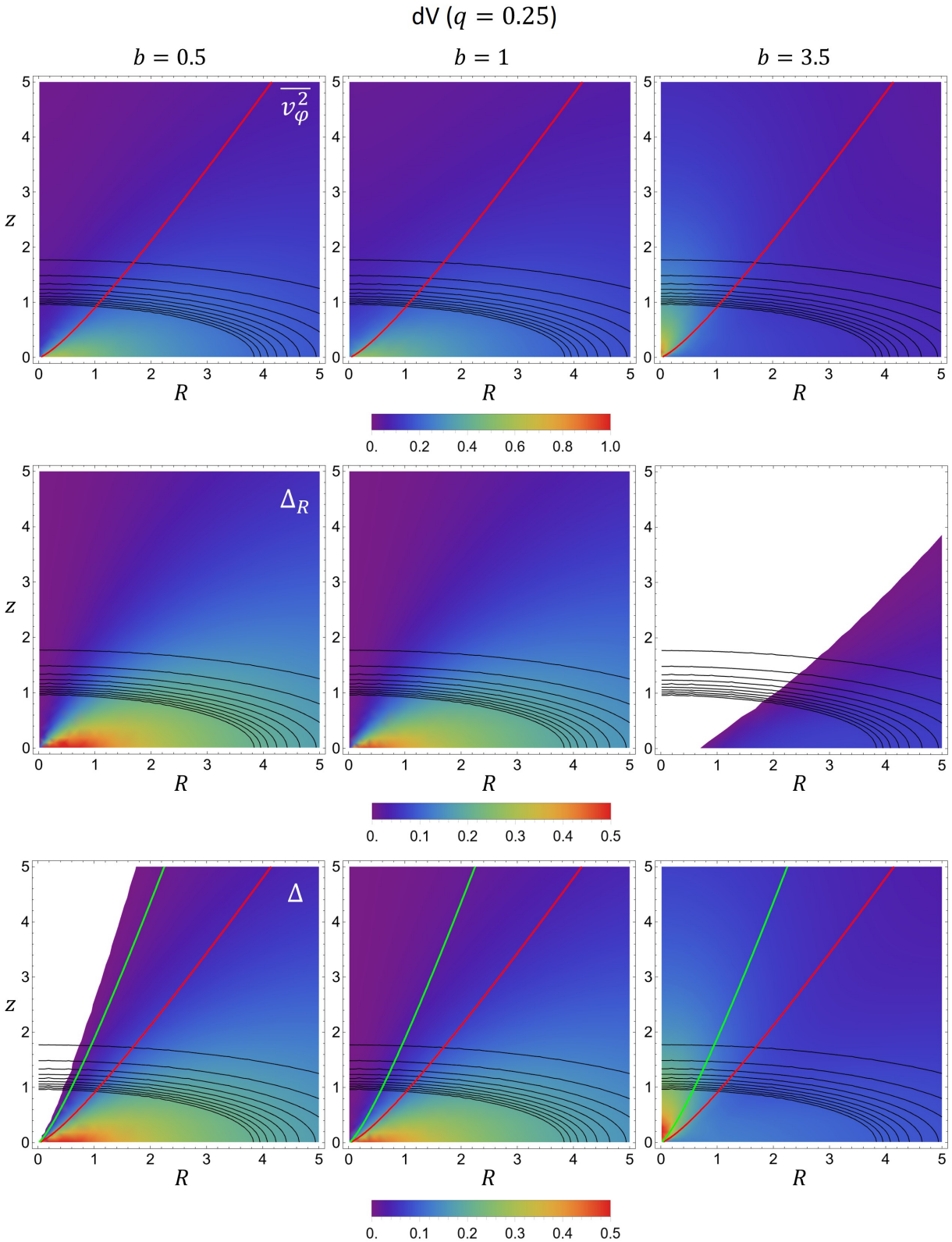


Figure 4.15. Same as in Figure 4.14, but for $q = 0.25$.

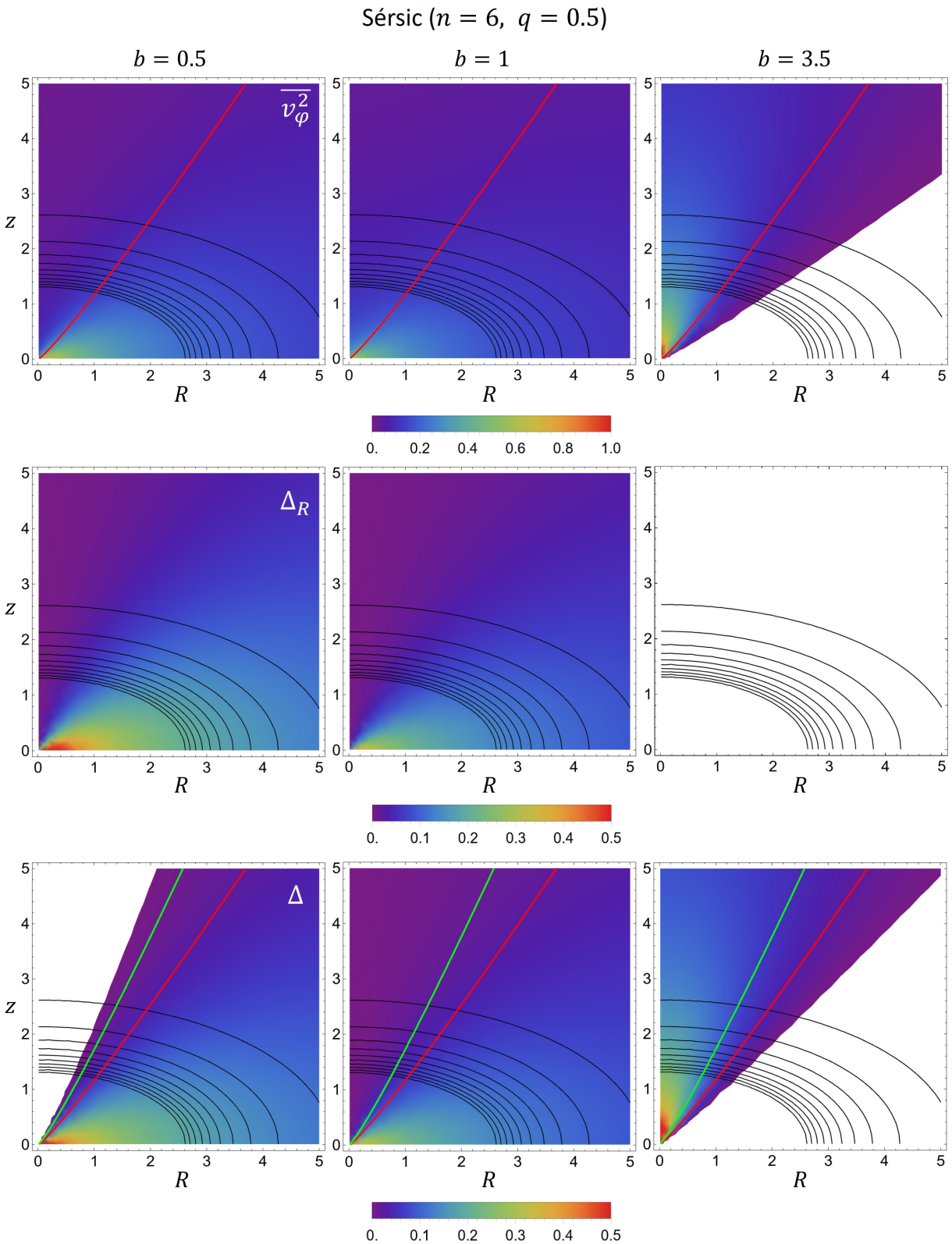


Figure 4.16. Same as in Figure 4.14, but for an ellipsoidal Sérsic model with $n = 6$.

scale length a_*, is

$$\rho_*(m) = \frac{M_*}{a_*^3} \frac{3-\gamma}{4\pi\, q\, m^\gamma\, (1+m)^{4-\gamma}},\ m = \sqrt{\frac{R^2}{a_*^2} + \frac{z^2}{q^2\, a_*^2}}, \tag{4.21}$$

where $0 \leq \gamma < 3$. Notice that in the central regions $\rho_* \sim m^{-\gamma}$: for this reason, the γ-models are a complementary family of models with respect to the Sérsic ones, where (for $n > 1$) the density is proportional to $m^{1/n-1}$, and so it can not be so steep even for very large values of n (see equation E.12 and Ciotti 1991). Instead, in the external regions (where the density slope of Sérsic models changes as a function of the distance from the center) $\rho_* \sim m^{-4}$ independently of γ, and so we expect that their behavior is captured by the simpler power-law models in Appendix F.

For reference, in the central panels of Figure 4.9 we show the 2D maps of σ_z^2, $[\rho_*, \Phi]$ and $R\,\partial\Phi/\partial R$ for the model with $\gamma = 2$ and $q = 0.5$; the global shape of the fields is similar to that of the Sérsic models. Moreover, from Figure 4.10 we see that, for increasing γ, both $[\rho_*, \Phi]$ and $R\,\partial\Phi/\partial R$ increase close to the equatorial plane, and σ_z^2 increases close to the origin; the effect is similar to that for decreasing q, as shown in Figure 4.11.

Also for these models, the determination of the $\mathscr{B}^-$ and $\mathscr{C}^-$ regions can be carried out numerically, and in the central panels of Figure 4.12, we show the critical regions for different values of q and γ. The similarity of the behavior with that observed for the Sérsic models is apparent, with the only differences that the $\mathscr{B}^0$ and $\mathscr{C}^0$ lines outside the radius a_* are almost perfectly straight (as for power-law models in Appendix F.3, given that the stellar density distribution is more and more close to a power-law profile), and that the effect of increasing γ is the opposite of that of increasing n, i.e. the $\mathscr{B}^-$ region becomes larger and $\mathscr{C}^-$ smaller for increasing values of γ. However, the effect of increasing flattening is the dominant one, and it goes in the same direction in all the models, namely the $\mathscr{B}^-$ and $\mathscr{C}^-$ regions become smaller for decreasing q.

The limits for b, found numerically, are shown in the top-right panel of Figure 4.13 as a function of q, for three different values of γ. Again, we see a remarkable similarity with ellipsoidal Sérsic models, with models with a more flattened stellar density profile supporting a higher b-anisotropy; the effect of q is always dominant compared to that of γ, which determines just slight differences between the curves. The observed trends are explained qualitatively by the power-law models in Appendix F, and in particular by the model with monopole potential in Appendix F.3, as apparent from the bottom-right panel of Figure 4.13.

Finally, in Figure 4.17 we show the $\overline{v_\varphi^2}$, Δ_R and Δ fields for different values of constant b;

the general trends with increasing anisotropy are analogous to those of the Sérsic models. In Figure 4.18, we investigate the effect of considering a higher stellar density flattening ($q = 0.25$): again, we notice that the critical regions become smaller, and the limits for b higher, so that the negativity regions of $\overline{v_\varphi^2}$ and Δ at higher b both disappear, and that of Δ_R becomes smaller. The effects of changing the density slope γ, investigated in Figure 4.19, are instead much less relevant concerning the trends with b, although for increasing γ the fields become higher close to the origin.

4.1.5 Effects of flattening and shape

After having discussed some general considerations about the behavior of kinematic fields of our interest with respect to the amount of b-anisotropy (see Section 3.3), we applied our procedure on some one-component galaxy models for which the analysis can be carried out analytically or numerically with sufficient ease. In these models, apart from the b parameter, the only galaxy parameters which are free to change are connected to the flattening (i.e., s for the disky models and q for the ellipsoidal models) and the shape (i.e., the Sérsic index n and the inner density slope γ) of the stellar density distribution. In all the analyzed models, which are representative of observed disky galaxies and regular rotators, we found that the general behavior of the fields with b is always the same, as expected from our considerations, but the flattening parameter has the most relevant effect on determining the shape of the critical regions where the fields can become negative, and the values of the limits for b which guarantee their positivity. Therefore, for an increasing stellar density flattening, the following results hold:

- The profile of σ_z^2 shrinks along the symmetry axis and assumes an hourglass-like shape, slightly decreasing close to the equatorial plane, while the commutator $[\rho_*, \Phi]$ increases close to the equatorial plane;

- The critical regions $\mathscr{B}^-$, where $\overline{v_\varphi^2}$ become negative for $b > b_\mathrm{M}$, and $\mathscr{C}^-$, where Δ become negative for $b < b_1$, become both smaller, so that the region $\mathscr{B}^+ \cap \mathscr{C}^+$ (where Δ is always positive, independently of b) becomes larger;

- Apart from b_1, which is equal to 1 independently of the model parameters, all the critical values of b increases, meaning that the fields $\overline{v_\varphi^2}$, Δ_R and Δ remain positive in the respective critical regions ($\mathscr{B}^-$, $\mathscr{D}^-$ and $\mathscr{B}^-$, respectively) for higher values of b;

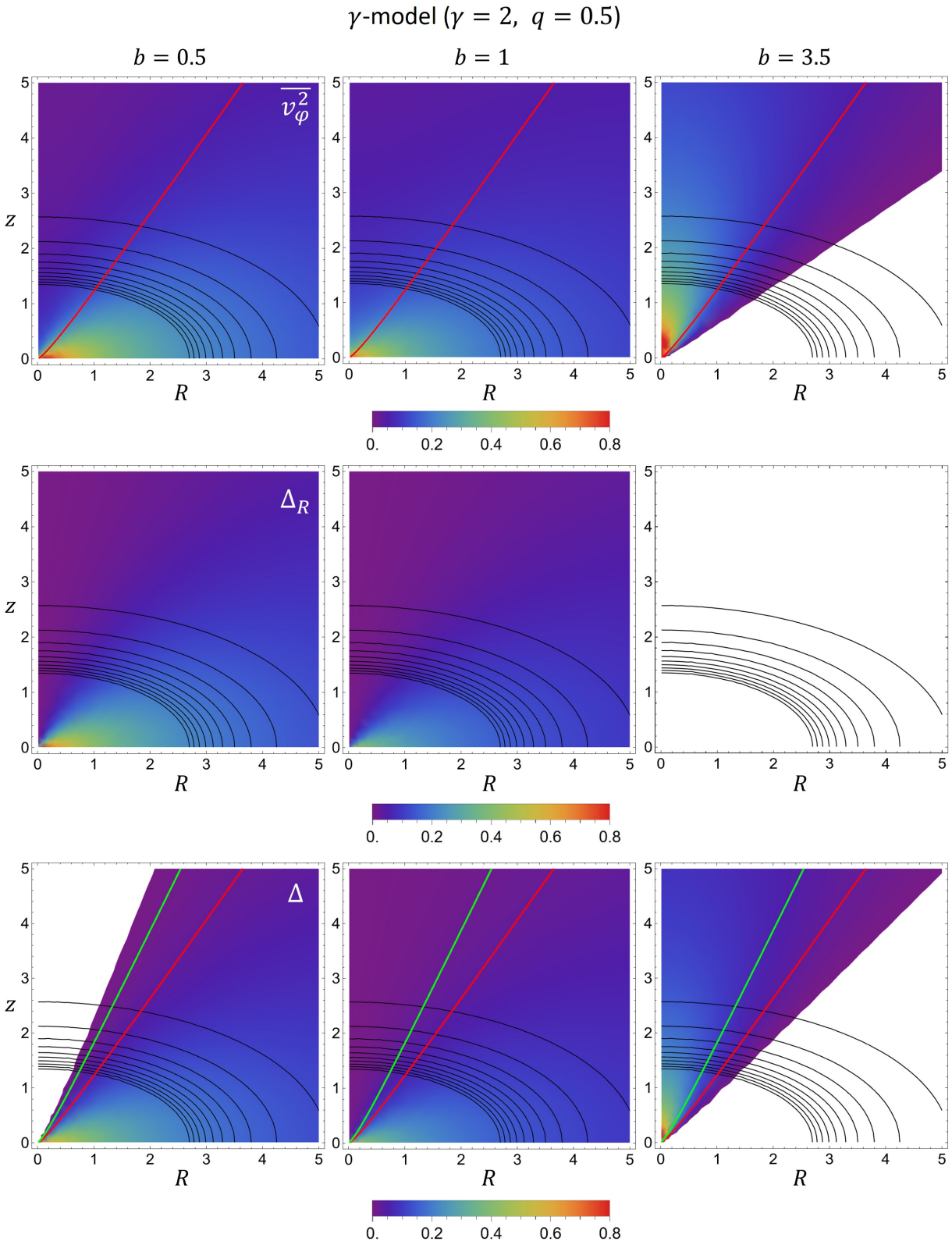


Figure 4.17. Maps in the (R, z)-plane of $\overline{v_\varphi^2}$ (top row), Δ_R (central row) and Δ (bottom row), in units of GM_*/a_*, for the ellipsoidal γ-model with $\gamma = 2$ and $q = 0.5$, and constant $b = 0.5$ (left column), $b = 1$ (central column) and $b = 2$ (right column). The red and green lines show, respectively, the $\mathscr{B}^0$ and $\mathscr{C}^0$ curves, while $\mathscr{D}^0$ coincides with the z-axis. Black solid lines show equally spaced isodensity contours. White regions correspond to negative values of the fields.

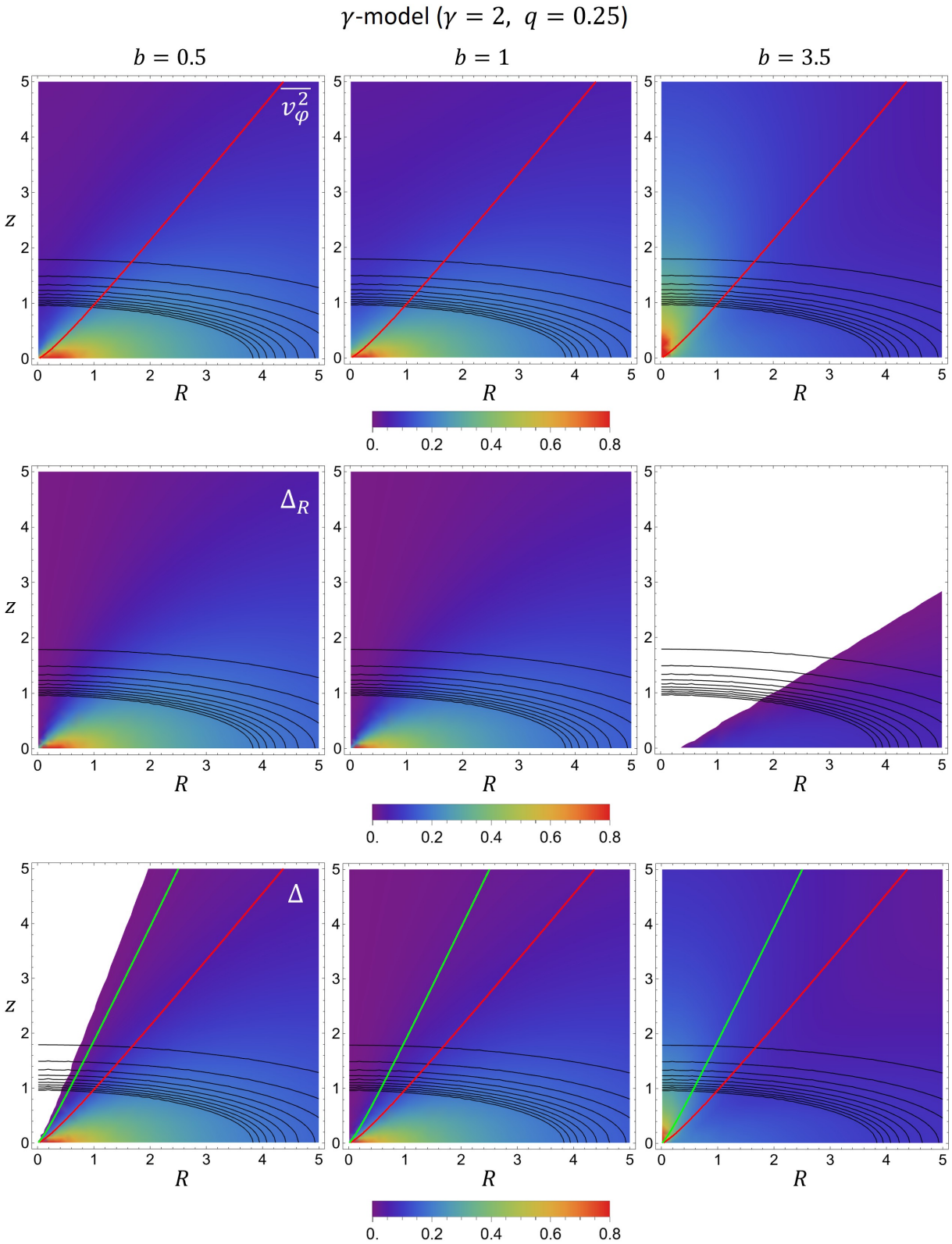


Figure 4.18. Same as in Figure 4.17, but for $q = 0.25$.

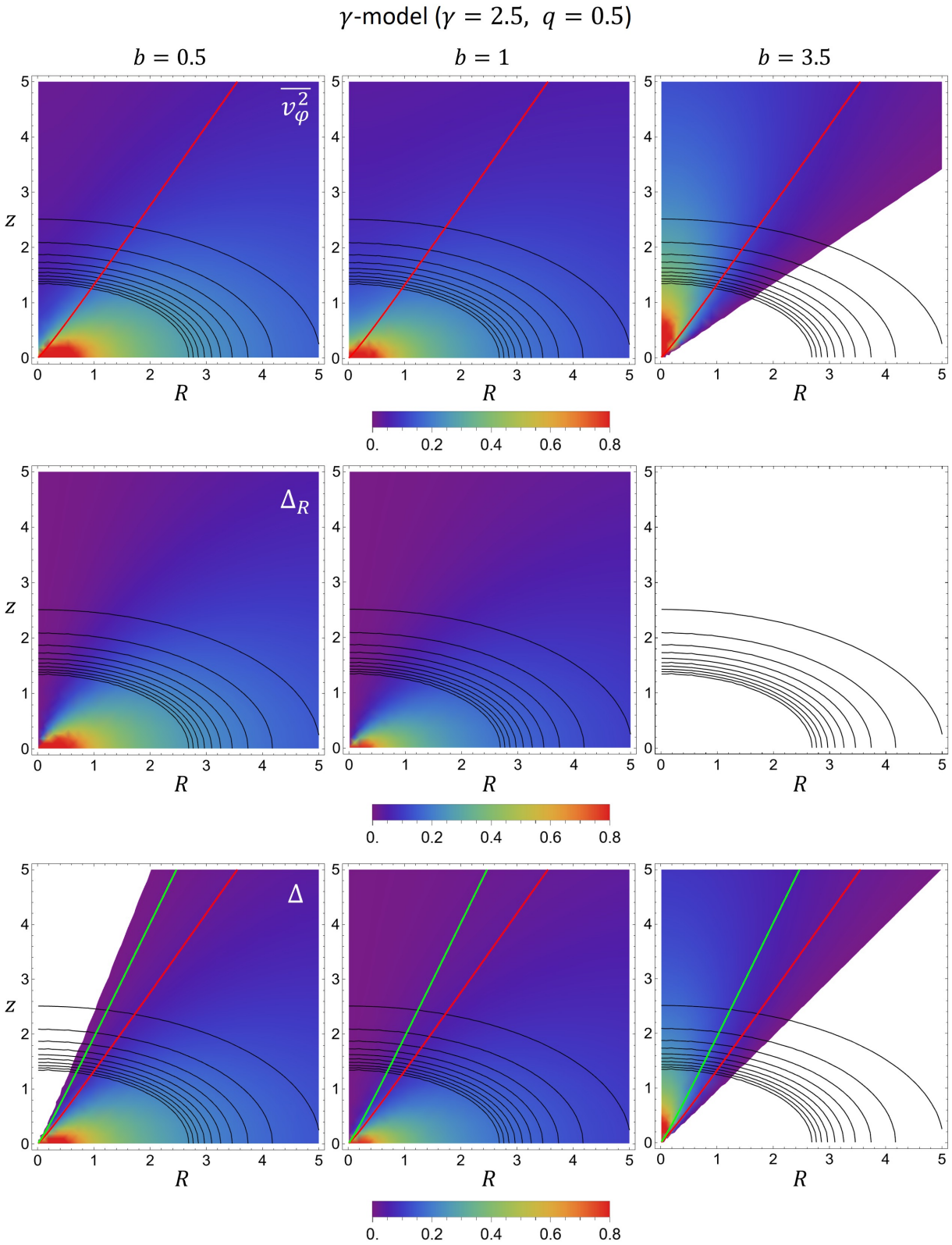


Figure 4.19. Same as in Figure 4.17, but for $\gamma = 2.5$.

- The $\overline{v_\varphi^2}$, Δ_R and Δ fields generally increase close to the equatorial plane, and their negativity regions for sufficiently high values of b become smaller or even disappear.

Taken all together, these results clearly indicate that systems with a more flattened stellar density distribution support a larger amount of b-anisotropy, before they become inconsistent at the level of the JEs (i.e., when $\overline{v_\varphi^2} < 0$ somewhere in $\mathscr{B}^-$), or a generalized Satoh (1980) decomposition can not be applied anymore (i.e., when $\Delta_R < 0$ somewhere in $\mathscr{D}^-$, or $\Delta < 0$ somewhere in $\mathscr{B}^-$). Moreover, we stress that changing the specific density profile, as well as the shape or slope parameters, has a very minor effect on these trends, suggesting that their effect is overall secondary in the Jeans modeling of three-integral galaxies with the b-ansatz.

Our findings are in accordance with the empirical results discussed in Section 1.4, namely the general trend of increasing b-anisotropy for more flattened galaxies that was found for samples of both regular rotators and axisymmetric mock galaxies resembling the ones observed in the most recent integral-field spectroscopic surveys. In the latter case (see Wang, Cappellari, and Peng 2021), the authors found that the upper limit on the anisotropy parameter $\beta_z = 1 - 1/b$ correlates positively with the intrinsic ellipticity ε of the galaxies, with all the galaxies staying below the empirical "magenta line" in equation (1.4) (see the left panels of Figure 1.10). More specifically, their approach was to build models with $\gamma \approx 0$ (i.e. $\sigma_R \approx \sigma_\varphi$) as found in observations (see e.g. Cappellari 2016), and then to numerically compute the value of β_z for which $\overline{v_\varphi}^2 = \Delta_R + \gamma\,\sigma_R^2 \approx \Delta_R$ became negative in a sufficiently large portion of the galaxy. In our framework, this translates into the condition $b \leq b_0$, where b_0 right increase with increasing stellar density flattening. Given also the fact that $b_0(q)$ is almost independent of the specific stellar density profile, as shown by the almost identical b_0 lines for the different models in the four panels of Figure 4.13, this could provide a natural explanation for the existence of the empirical limit on b; in fact, in the same Figure we see that there is a remarkable similarity between the magenta line and the different $b_0(q)$ curves.

We conclude with a comment about the relation between our findings and the decomposition for the azimuthal motions based on the parameter γ_φ, already presented in equation (1.2) and them illustrated in Section 3.1.1. We recall that $\gamma_\varphi > 0$ corresponds to radial anisotropy, $\gamma_\varphi < 0$ to tangential anisotropy, and in two-integral systems $\gamma_\varphi = 0$ to the isotropic case. From the condition in equation (3.9), based on the positivity of both $\overline{v_\varphi}^2$ and σ_φ^2, γ_φ can be either positive or negative where $\Delta_R > 0$, but it can only be positive where $\Delta_R < 0$; in particular, in order to

have galaxies with $\sigma_\varphi = \sigma_R$ (i.e., $\gamma_\varphi = 0$), Δ_R must be positive everywhere (i.e., $b \leq b_0$). As for increasing flattening b_0 increases, it follows that systems with a more flattened stellar density profile can have $\sigma_\varphi = \sigma_R$, and at the same time a higher σ_R (compared to σ_z) than less flattened stellar densities, as the critical limit for b increases.

4.2 Two-component models

Having investigated the relation between the amount of b-anisotropy and the properties of the stellar density profile of a galaxy, as its flattening and shape, we can now discuss the effect of considering an external DM halo, under the form of an additional contribution to the total gravitational potential. Following the qualitative classification between disky and more idealized, and ellipsoidal and more realistic galaxy models, we will focus on two case studies: the MN stellar disk in a dominant ($\Phi = \Phi_\mathrm{h}$) Binney logarithmic DM halo, and the dV stellar profile in a SIS DM halo for different DM-to-stellar mass ratios. These two models allow to quantify if and in which measure the critical regions and the limits for b ensuring the positivity of the kinematic fields are affected by the presence of this additional contribution, and if there are any differences between the case in which the halo is dominant and the one in which there is a transition region between the stellar-dominated and the DM-dominated regimes; in the latter case, it will be interesting to show if additional properties emerge in this transition region. Of course, given that the gravitational field increases, we expect that the values of all the kinematic fields of our interest increase in general; however, as also seen for the one-component models in Section 4.1, their behavior with respect to the change of b-anisotropy is not trivial, therefore deserving a deeper investigation.

4.2.1 Miyamoto & Nagai disk in a dominant Binney logarithmic halo

We now consider the two-component model made by a stellar MN disk embedded in a DM Binney logarithmic DM halo; in order to better understand the specific properties of the halo, in Appendix D we also solve the JEs with the b-ansatz for the case of a self-gravitating Binney logarithmic halo, finding in a full analytical way all the critical regions and limits for b. We adopt this model because σ_z^2 and the commutator for the stellar density distribution can be given in closed form for arbitrary values of the disk flattening s and the halo potential flattening q_h (see Smet, Posacki, and Ciotti 2015, hereafter S15). However, the resulting expressions are sufficiently complicated to exclude the possibility of an analogous analytical study of the $\mathscr{B}$, $\mathscr{C}$ and $\mathscr{D}$ regions, which

are therefore determined numerically from the expressions in S15. By using the normalizations adopted for the MN model in Section 4.1.1, i.e. $b_* \neq 0$ for lengths and GM_*/b_* for potentials and squared velocities, the total potential of this model is

$$\Phi = \Phi_* + \mathcal{R}\,\Phi_\mathrm{h}, \quad \mathcal{R} \equiv \frac{v_\mathrm{h}^2 b_*}{GM_*}, \tag{4.22}$$

in which the dimensionless stellar potential is $\Phi_* = -1/\xi$, as given in equation (4.1), and from equation (D.1) the dimensionless halo potential is

$$\Phi_\mathrm{h} = \frac{1}{2}\ln\left(1 + \frac{R^2}{b_\mathrm{h}^2} + \frac{z^2}{q_\mathrm{h}^2\, b_\mathrm{h}^2}\right), \tag{4.23}$$

where b_h is the scale length of the halo, now in units of b_*; for $\mathcal{R} = 0$, the model reduces to the self-gravitating MN disk discussed in Section 4.1.1, while for $\mathcal{R} \gg 1$ we obtain the "halo-dominated" case of our interest, in practice equivalent to considering $\Phi = \Phi_\mathrm{h}$ in the JEs. Notice that at sufficiently large $r = \sqrt{R^2 + z^2}$ the model is always halo-dominated, independently of the value of $\mathcal{R}$.

In the two-integral case, σ_z^2 can be obtained by adding equations (10) and (17) of S15, while $[\rho_*, \Phi]$ can be obtained from equation (27) of S15. It can be shown that, while $\sigma_z^2 \geq 0$ regardless of the model parameters, the sign of $[\rho_*, \Phi]$ depends on the value of q_h, and if $q_\mathrm{h} < 1$ there are regions at large r where $[\rho_*, \Phi] < 0$; instead, if $q_\mathrm{h} \geq 1$, then $[\rho_*, \Phi] \geq 0$ everywhere. An asymptotic analysis of the solutions of the JEs also shows that, in the two-integral case and independently of s and $\mathcal{R}$, $\overline{v_\varphi^2}$ becomes negative at large r for $q_\mathrm{h} \lesssim 0.85$, while $\overline{v_\varphi^2} \geq 0$ everywhere for $q_\mathrm{h} \gtrsim 0.85$. Therefore, to avoid additional effects due to the sign of the commutator (as discussed in Section 4.3), for simplicity we now consider a spherical ($q = 1$) halo; also, given that the halo-dominated models are expected to be the most different compared to the one-component MN disk, in the following analysis we assume $\Phi = \Phi_\mathrm{h}$. For reference, in the bottom panels of Figure 4.1, we show the ansatz-independent fields σ_z^2, $R\,[\rho_*, \Phi]/\rho_*$ and $R\,\partial\Phi/\partial R$ for the halo-dominated model with $s = 1$ and $b_\mathrm{h} = 2$. By comparison with the top panels in the same Figure, referred to the one-component MN model with same s, we see that all the fields have now increased, and the maxima of σ_z^2 and the other two fields have moved, respectively, to higher z and R; in particular, the latter effect is expected from the flat rotation curve of the halo at large radii. In the more central regions, instead, the self-gravitating effects of the disk are not visible, as in this model

its gravitational field of the disk is neglected everywhere. Also, by comparison with the same fields in Figure D.1, we see that, qualitatively, the profile of σ_z^2 is more similar to that of the one-component Binney logarithmic halo than to that of the MN disk, while $R\left[\rho,\Phi\right]/\rho$ is more conditioned by the stellar density profile. Finally, in the bottom panels of Figure 4.2, we show the same fields for a higher value of s: the increase of the stellar density flattening slightly changes the profile of σ_z^2, which now assumes a more hourglass-like shape, while $R\left[\rho_*,\Phi\right]/\rho_*$ remains almost unchanged, and $R\,\partial\Phi/\partial R$ is by construction the same.

Even though the gravitational potential is dominated by the halo, the stellar density profile enters in the definition of the ansatz-independent B, C and D functions: therefore, we expect that the $\mathscr{B}$, $\mathscr{C}$ and $\mathscr{D}$ regions, determined numerically, are not coincident with those of the one-component Binney halo shown in Figure D.2. Indeed, in the bottom panels of Figure 4.3 we show the $\mathscr{B}^-$ and $\mathscr{C}^-$ regions of the two-component model with $b_\mathrm{h}=2$ and three different values of s; we see that the shape of the regions, although qualitatively similar among all the models, resembles more that of the one-component MN disk than that of the self-gravitating Binney logarithmic halo. Also, we see that the effect of the DM halo is to make both $\mathscr{B}^-$ and $\mathscr{C}^-$ smaller (i.e., the $\mathscr{B}^+\cap\mathscr{C}^+$ region larger), similarly to what happens for increasing s; however, the effect produced by the change of the stellar density flattening is dominant over the other. Finally, as for the MN disk, $\mathscr{D}^-$ coincides with the (R,z)-plane, with $D=0$ on the z-axis, and both $\mathrm{Pr}(\mathscr{B}^-)$ and $\mathrm{Pr}(\mathscr{C}^-)$ coincide with the z-axis.

Due to the numerical determination of the ansatz-independent regions, the different limits for b are computed numerically as well. In the bottom-left panel of Figure 4.4, we show them for the model with $b_\mathrm{h}=2$, and different values of the disk flattening s (for simplicity, the b_2 curve is shown only for the model with $s=3$); reassuringly, being $[\rho_*,\Phi]\geq 0$ everywhere, the inequalities presented in Section 3.3.1 hold. Notice that, also in this case, a more flattened stellar density profile allow to support a larger amount of b-anisotropy, confirming the empirical trends already discussed in Section 4.1.5. Moreover, similarly to the ansatz-independent regions, we see that the shapes of the functions are more similar to those for the MN disk (see the top-left panel in the same Figure), than those for the self-gravitating Binney logarithmic halo (see the bottom-right panel of the same Figure). However, compared to the limits of the one-component MN disk, the presence of the DM halo increases the values of all of them (except for b_1, that remains equal to 1), especially at lower z. In case of a spatially constant b case, we find that $b_1=b_0=b_2=1$ and

$b_{\rm M} = 5/4$, a result which is very similar to that for the one-component model.

In Figure 4.20, we show the 2D maps of $\overline{v_\varphi^2}$, Δ_R and Δ for the halo-dominated model with $s = 1$, and for the three values of constant b already used in Figure 4.5 for the one-component MN disk. Apart from their higher values, due to the presence of the additional halo, we see that the fields are qualitatively more similar to those of the one-component MN disk than to those of the self-gravitating Binney model, shown in Figure D.3 for a halo with $q_{\rm h} = 0.85$; this happens even though the MN disk is halo-dominated, suggesting that the stellar density profile has the most relevant effect in determining the kinematical trends with b. In Figure 4.21, we show the same fields for a higher value of s: analogously to what seen in Figure 4.6 for the one-component MN model, increasing the stellar density flattening makes the negativity regions smaller or even disappear for sufficiently high values of b. Therefore, we conclude that a DM halo has clearly an effect on globally increasing the values of the kinematic fields, but it does not alter appreciably the qualitative behavior of these fields under the b-ansatz, even when the halo is dominant.

4.2.2 de Vaucouleurs profile in a singular isothermal sphere halo

With this model, we go beyond the simplistic case of a dominant, external potential in which a disky stellar density profile is embedded; in this sense, the effects of a DM halo in the transition between the stellar-dominated region and the halo-dominated region can be studied. In particular, or model is made by an ellipsoidal dV stellar density profile of total mass M_*, effective radius $R_{\rm e}$ and flattening $q_{\rm h}$, described by equation (4.17) with $n = 4$, embedded in DM halo described by a SIS of circular velocity $v_{\rm h}$ and potential

$$\Phi_{\rm h} = v_{\rm h}^2 \ln \frac{r}{R_{\rm e}}, \quad r = \sqrt{R^2 + z^2}, \tag{4.24}$$

where the normalization of the spherical radius r to $R_{\rm e}$ has been introduced to make the argument of the logarithm dimensionless. At variance with the models where the stellar component of the galaxy is assumed to be a tracer in a dominant DM potential, here the total potential is

$$\Phi = \Phi_* + \mathcal{R} \ln r, \quad \mathcal{R} \equiv \frac{v_{\rm h}^2 R_{\rm e}}{G M_*}, \tag{4.25}$$

where Φ is normalized to $GM_*/R_{\rm e}$, and the lengths to $R_{\rm e}$; the dimensionless coefficient $\mathcal{R}$ measures the importance of the DM potential relative to the stellar one, and so it is crucial to understand

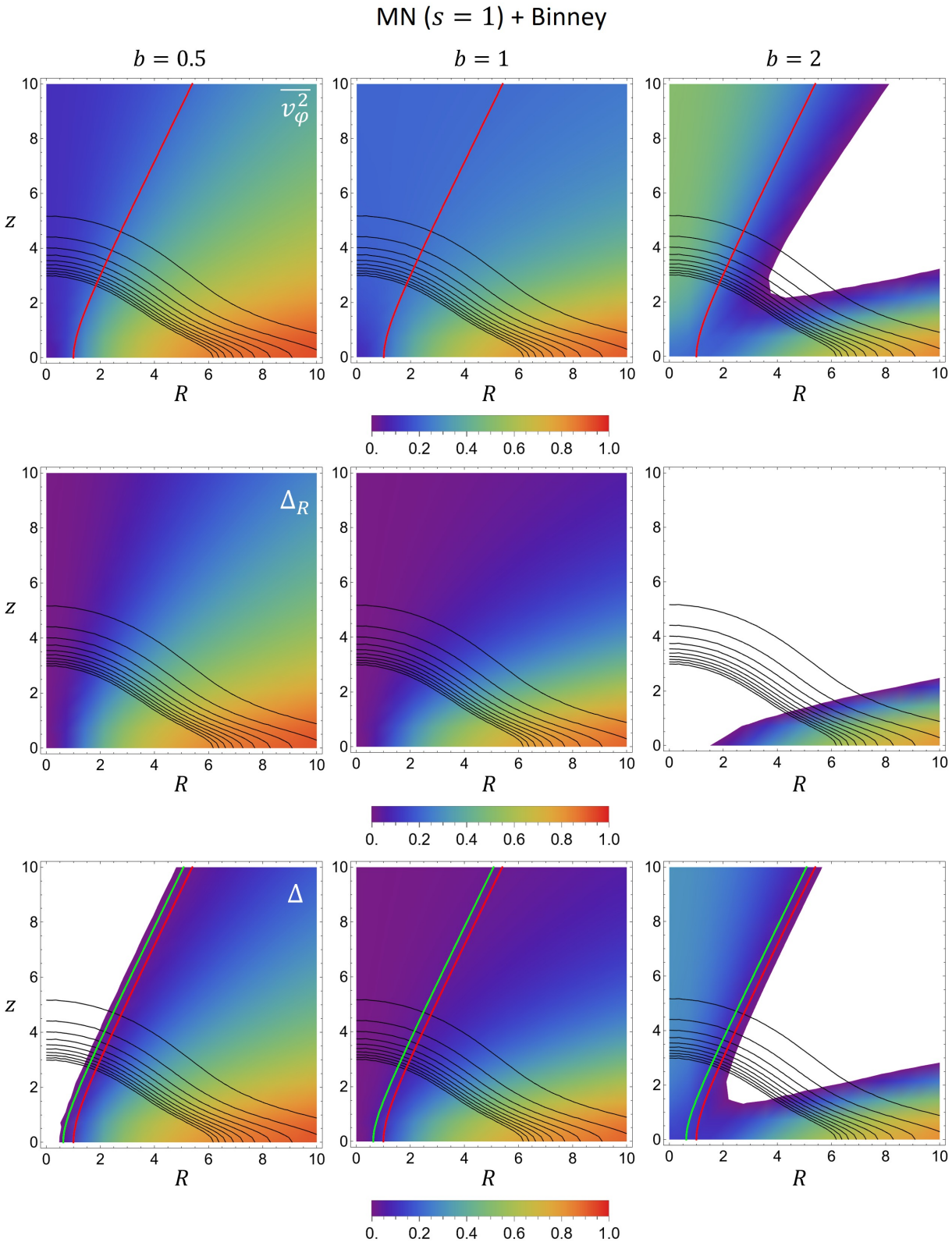


Figure 4.20. Maps in the (R, z)-plane of $\overline{v_\varphi^2}$ (top row), Δ_R (central row) and Δ (bottom row), in units of GM_*/b_*, for the MN disk with $s = 1$ in a dominant ($\Phi = \Phi_\mathrm{h}$) spherical ($q_\mathrm{h} = 1$) Binney logarithmic halo with $b_\mathrm{h} = 2$, and constant $b = 0.5$ (left column), $b = 1$ (central column) and $b = 2$ (right column). The red and green lines show, respectively, the $\mathscr{B}^0$ and $\mathscr{C}^0$ curves, while $\mathscr{D}^0$ coincides with the z-axis. Black solid lines show equally spaced isodensity contours. White regions correspond to negative values of the fields.

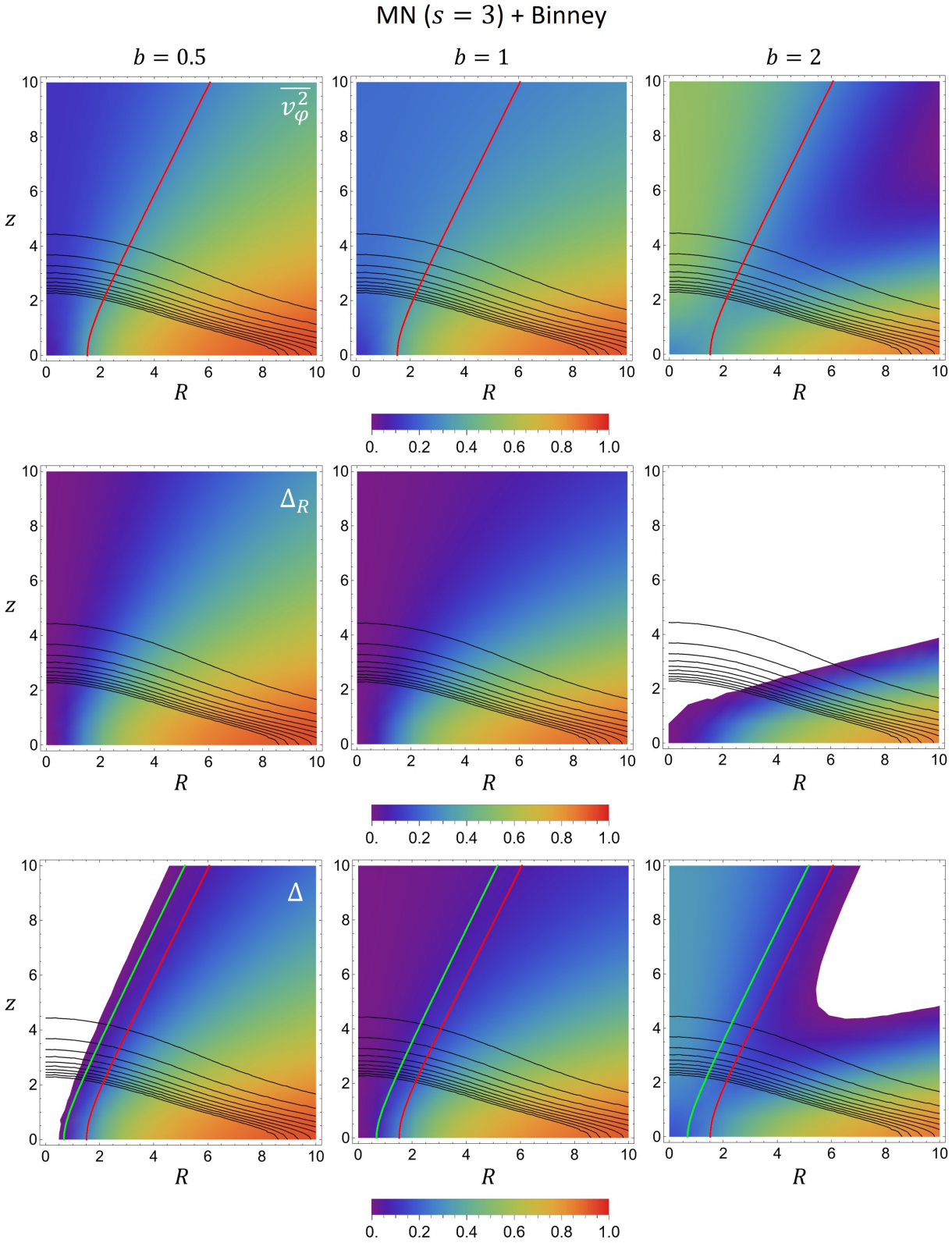


Figure 4.21. Same as in Figure 4.20, but for $s = 3$.

the relative effects of the halo with respect to the stellar component. In order to fix a realistic value for $\mathcal{R}$, we consider the (projected) DM-to-stellar mass ratio inside R_e for the case of a spherical dV stellar component:

$$\frac{M_{\mathrm{p,DM}}(R_\mathrm{e})}{M_{\mathrm{p},*}(R_\mathrm{e})} = \pi\mathcal{R}; \tag{4.26}$$

of course, from the definition of R_e, equation (4.26) applies also to a spherical Sérsic profile of index n in a SIS halo. In our analysis, we consider the range $0 \leq \mathcal{R} \leq 1$, although realistic values for $\mathcal{R}$ would be $\mathcal{R} \approx 0.15$.

For reference, in the bottom panels of Figure 4.9 we show the ansatz-independent fields σ_z^2, $R\left[\rho_*, \Phi\right]/\rho_*$ and $R\,\partial\Phi/\partial R$ for the model with $q = 0.5$ and $\mathcal{R} = 0.5$. Compared to the case without the DM halo (see the top panels in the same Figure), we see that the shape of the fields is very similar, although (as for the models in Section 4.2.1) their values are globally higher, and in particular at larger distances from the center; as shown in the bottom panes of Figure 4.10, increasing $\mathcal{R}$ makes all the fields even higher, but their shapes do not change significantly from the lower $\mathcal{R}$ case. In the bottom panels of Figure 4.11, instead, we show the effects of increasing the stellar density flattening: as for the models previously discussed, decreasing q makes σ_z^2 shrink along the z-axis, and the other two fields increase close to the equatorial plane.

Of course, the B, C and D functions can be computed only numerically, and so the $\mathscr{B}^\pm$, $\mathscr{C}^\pm$ and $\mathscr{D}^\pm$ regions; however, from the general considerations at the beginning of Section 4.1, we already know that $D < 0$ everywhere. In the bottom panels of Figure 4.12, instead, we show the $\mathscr{B}^-$ (to the right of the $\mathscr{B}^0$ curves) and $\mathscr{C}^-$ (to the left of the $\mathscr{C}^0$ curves) regions of the model, for different values of q and $\mathcal{R}$. Qualitatively, the behavior of these two-component models is analogous to that of the corresponding one-component models, shown as the $n = 4$ case in the top panels of the same Figure. In particular, the increase of the stellar density flattening always makes both $\mathscr{B}^-$ and $\mathscr{C}^-$ smaller, while the only detectable effects of the additional DM halo is to moderately reduce the size of the $\mathscr{B}^-$ region at fixed q; however, the entity of this effect does not change significantly even for a dominant halo, and the most significant parameter of the problem in determining the shape and size of the $\mathscr{B}^-$ and $\mathscr{C}^-$ regions results to be always q.

The limits for b can be determined only numerically as well, and in the bottom-left panel of Figure 4.13 we show them (in the constant b case) as a function of q, and for the three values of $\mathcal{R}$. As for the corresponding one-component models (see the $n = 4$ case in the top-left panel of the

same Figure), more flattened stellar density distributions are able to support more b-anisotropy; also, similarly as for the behavior of the $\mathscr{B}^-$ region, the effect of the additional halo is just to slightly increase the range of admissible values for b, even though this effect do not change too much with $\mathcal{R}$. These findings are qualitatively confirmed by looking at the critical b curves for the halo-dominated power-law stellar models (see Appendix F) in the bottom-right panel of the same Figure, and comparing them to the curves for the one-component γ-model with $\gamma = 2$ (see the top-right panel of the same Figure); of course, due to the shape of the potential, the SIS halo mimics an increase of the DM halo effects over the monopole case.

Finally, in Figure 4.22 we show $\overline{v_\varphi^2}$, Δ_R and Δ for the model with $q = 0.5$ and $\mathcal{R} = 0.5$, and for the same (constant) values of b used in Figure 4.14 for the corresponding one-component model. Comparing the two figures, we see that the effects of the DM halo are to increase the values of the fields, and to reduce the size of the negativity regions (in particular those of $\overline{v_\varphi^2}$ and Δ) for sufficiently high values of b; these effects are of course larger for increasing values of $\mathcal{R}$, as apparent in Figure 4.23 for the $\mathcal{R} = 1$ case. In Figure 4.24, instead, we show the same fields for a lower value of q: as the limits for b have increased significantly, for $b = 3.5$ the negativity regions of both $\overline{v_\varphi^2}$ and Δ disappear, and the one of Δ_R becomes smaller. Again, comparing the effects of the DM halo and the stellar density flattening with respect to an increasing b-anisotropy, we see that the latter are always dominant over the others, confirming the results already obtained for the models in Section 4.2.1.

4.2.3 Effects of a dark matter halo

In this Section, we investigated the effects that an additional DM halo has on the solutions of the JEs with the b-ansatz, particularly with respect to the shape and size of the ansatz-independent regions, and the values of the critical limits for b. In particular, we first considered the idealized case of a MN disk embedded in a dominant Binney logarithmic halo, where we could see the effect of an external potential on a disky density distribution, and then we repeated the analysis for a more realistic dV stellar density profile in a SIS halo, even for cases when the halo is not dominant anymore; this latter case allowed to understand if and how different DM-to-stars mass ratios affect the results, and if additional effects appeared in the transition between the stellar-dominated and the halo-dominated regions. In summary, by including an external DM halo in the models, the following results hold:

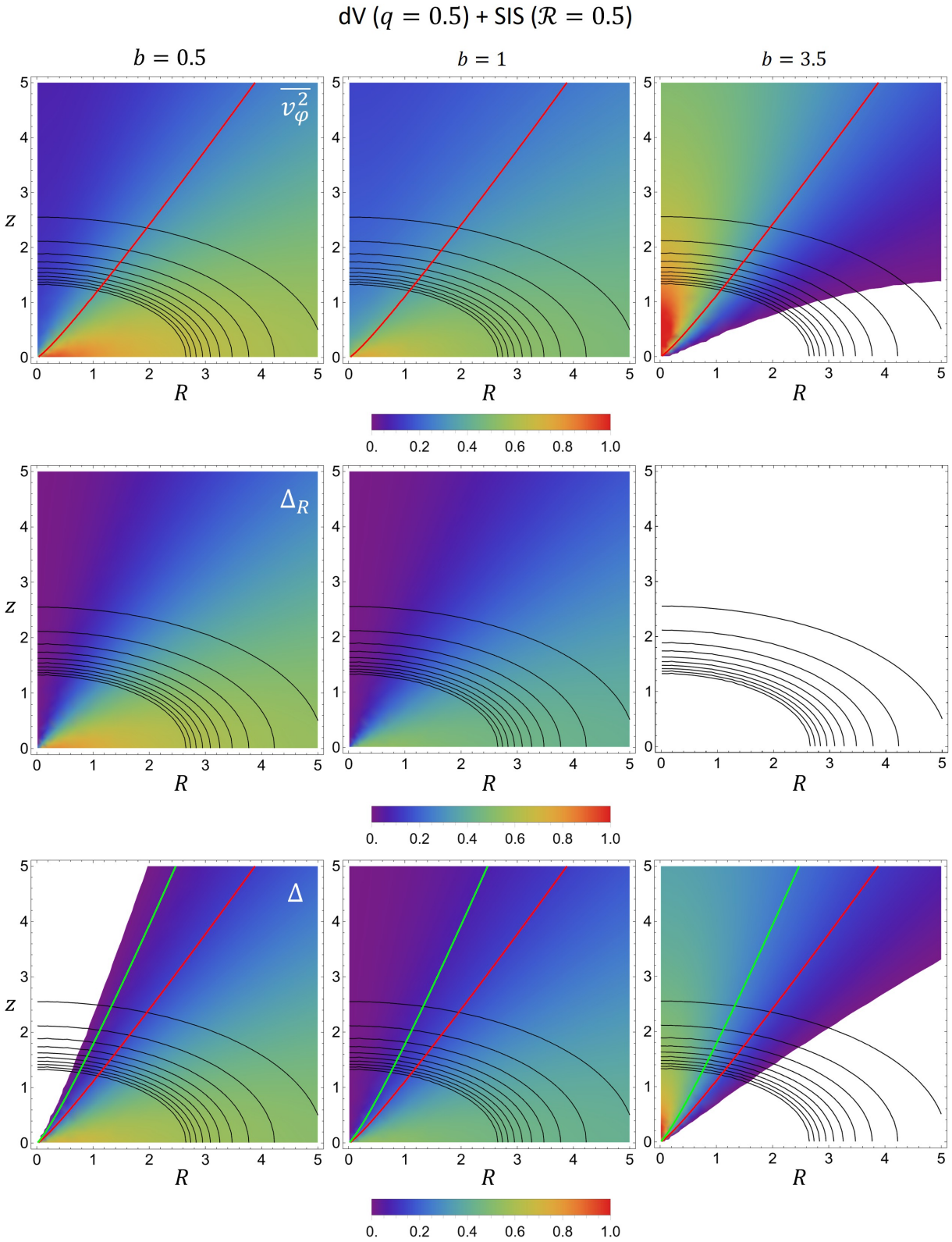


Figure 4.22. Maps in the (R, z)-plane of $\overline{v_\varphi^2}$ (top row), Δ_R (central row) and Δ (bottom row) in units of GM_*/a_*, for the ellipsoidal dV model with $q = 0.5$ in a SIS with $\mathcal{R} = 0.5$, and constant $b = 0.5$ (left column), $b = 1$ (central column) and $b = 2$ (right column). The red and green lines show, respectively, the $\mathscr{B}^0$ and $\mathscr{C}^0$ curves, while $\mathscr{D}^0$ coincides with the z-axis. Black solid lines show equally spaced isodensity contours. White regions correspond to negative values of the fields.

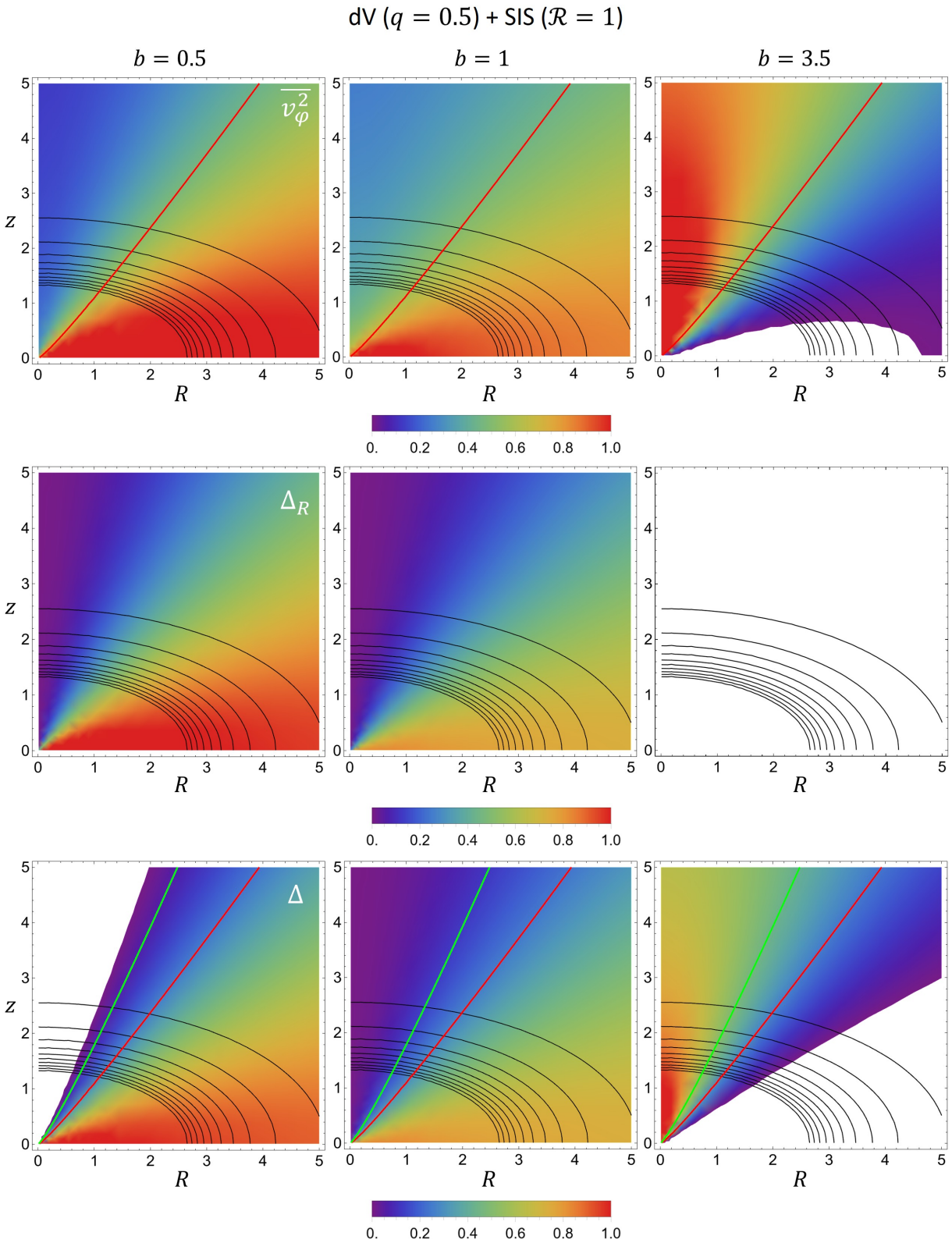


Figure 4.23. Same as in Figure 4.22, but for $\mathcal{R} = 1$.

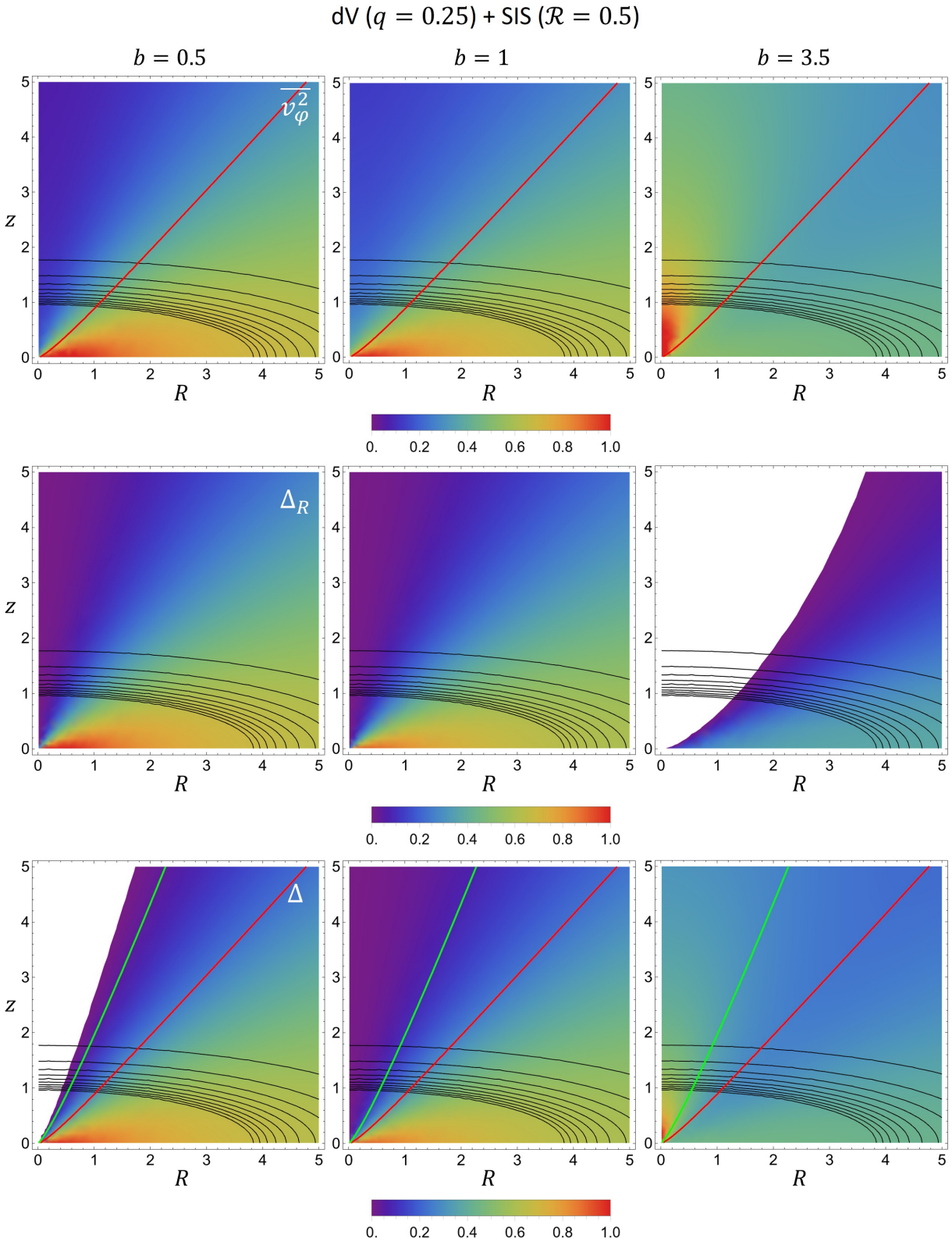


Figure 4.24. Same as in Figure 4.22, but for $q = 0.25$.

- In general, due an additional gravitational field, all the ansatz-independent fields increase, and the effect is larger for increasing values of $\mathcal{R}$ (up to the halo-dominated case);
- The $\mathscr{C}^-$ region remains almost unchanged in size, while $\mathscr{B}^-$ becomes smaller (and so $\mathscr{B}^+ \cap \mathscr{C}^+$ larger) for increasing values of $\mathcal{R}$;
- All the critical limits for b (except for b_1, which remains equal to 1) increase, and the effect is larger for increasing $\mathcal{R}$;
- The kinematic fields $\overline{v_\varphi^2}$, Δ_R and Δ increase in general everywhere, and their negativity regions for sufficiently high values of b become smaller as $\mathcal{R}$ increases.

Taken together, these results suggest that the presence of an additional DM halo globally increases the values of all the kinematic fields, and produces effects on the critical regions and limits for b which in general go in the same direction as for an increasing flattening of the stellar density distribution. However, the latter effects are always dominant over the former ones, to the point that, even in the halo-dominated case, the negativity regions of the fields for b exceeding the corresponding limits become much smaller or even disappear.

These results are also visible in the very simple, but useful models in Appendix F.2, where we consider power-law ellipsoids in the dominant external potential of a SIS. In that case, due to the scale-free nature of the model, the critical regions are all bound by straight lines, and we see that the $\mathscr{B}^-$ region is smaller than that of the corresponding one-component γ-model with $\gamma = 2$ (see Figure F.6 and the central panels of Figure 4.12 for comparison). Also, when looking at the limits for b, it is apparent how the presence of an external halo increases their values (see the top-right and the bottom-right panels of Figure 4.13); however, as for the critical regions, this effect is less important than that driven by the variation of the stellar density flattening.

4.3 Models with $[\rho, \Phi] < 0$

In this Section, we explore a different class of models which has not been addressed in our previous discussion, i.e. those with a negative $[\rho_*, \Phi]$. In fact, from the general considerations in Section 3.3.3, we already know that for this class of models the relations between the different critical regions and the limits for b are different compared to those valid for models with $[\rho_*, \Phi] \geq 0$. Therefore, it is interesting to investigate whether the trends with the stellar density flattening

and the presence of an additional DM halo hold in this case as well, or whether significative differences distinguishing between the two classes of models are found. This goes also in the direction of looking for specific kinematic properties to differentiate between oblate and prolate galaxies, the latter being found both observationally and in simulations of galaxy formation and evolution (see e.g. Pandya et al. 2024, Vega-Ferrero et al. 2024, Wang, Peng, et al. 2024). An extensive study on this topic is presented in Congera (2025), where two-integral JEs are used to study the kinematic fields and the consistency of different one-component prolate models, all presenting a negative commutator. Here we do not enter in the very specific treatment of that work, which also investigates how the gravitational field of these models differs from that of the oblate counterparts, or how their global equilibrium is possible. Instead, here we follow a more general approach based on the b-ansatz which addresses the consistency problems already found in the above-mentioned work, and investigate the behavior of the models with respect to the amount of b-anisotropy.

In order to do this, we will focus on two simple case studies which allow for a fully analytical treatment, but which are useful enough for our purpose. First, we will discuss the case of the self-gravitating Binney logarithmic halo (shown in Appendix D for the case with $[\rho_*, \Phi] \geq 0$) for $q > 1$, a regime in which the commutator is negative everywhere; this model will allow to show the behavior of the regions and the limits for b as the stellar density profile becomes more and more elongated, extending in some sense the considerations made in Section 4.1.5 for an increasing flattening. Second, we will address the case of a prolate power-law ellipsoidal stellar density profile in a dominant SIS DM halo (shown in Appendix F.2 for the case with $[\rho_*, \Phi] \geq 0$), in which the effects of adding an external potential will be considered. More complete and realistic models, such as the equivalent of the one presented in Section 4.2.2, are out of the scope of this thesis, but they could be addressed in future work.

4.3.1 Binney logarithmic halo

We now consider the Binney logarithmic halo described in Appendix D, whose potential-density pair is given in equation (D.1); again, the lengths are assumed normalized to the scale-length $b_\mathrm{h} \neq 0$, and potential and squared velocities to v_h^2. From equation D.2, we see that the commutator becomes negative for $q_\mathrm{h} > 1$, so this range will be assumed hereafter. Notice that, as proved in Evans (1993) and already mentioned in the Appendix, the DF of the model becomes negative

(and so the model inconsistent) already for $q_{\rm h} \gtrsim 1.08$; however, as the purpose of this discussion is to show the effects of the b-anisotropy as the commutator becomes more and more negative, we will also consider values of $q_{\rm h}$ above this value, limiting in checking the consistency of the model just at the level of the JEs. For reference, in the top panels of Figure 4.25 we show the 2D maps of σ_z^2, $R\left[\rho_{\rm h}, \Phi_{\rm h}\right]/\rho_{\rm h}$ and $R\,\partial\Phi_{\rm h}/\partial R$ for $q_{\rm h} = 1, 25$. Compared to the analogous fields in Figure D.1, where $q_{\rm h} < 1$ and so the commutator is positive, we see that the maximum of σ_z^2 is now close to the R-axis, as the density profile is now more compressed along that direction, while $R\left[\rho_{\rm h}, \Phi_{\rm h}\right]/\rho_{\rm h}$ has a more similar shape to that of the models with $q_{\rm h} < 1$, but with negative values (see the different color scale). In the bottom panels of the same Figure, we show the fields for a higher value of $q_{\rm h}$, i.e. for an higher potential (and stellar) flattening along the z-axis. We see that $R\left[\rho_{\rm h}, \Phi_{\rm h}\right]/\rho_{\rm h}$ becomes more negative close to the equatorial plane, similarly (in absolute value) to what happens in the model with positive commutator by decreasing $q_{\rm h}$, while σ_z^2 increase and assumes a hourglass-like shape in the same region, again analogously to what observed for the other models along the z-axis.

Given the simplicity of the model, the $\mathscr{B}^{\pm}$, $\mathscr{C}^{\pm}$ and $\mathscr{D}^{\pm}$ regions can be determined in a fully analytical way. In particular, by solving equation (D.4) with $q_{\rm h} > 1$, in Figure 4.26 we show the $\mathscr{B}^{-}$ regions (to the right of the $\mathscr{B}^{0}$ curves) of the model for three different values of $q_{\rm h}$. As for the models with $q_{\rm h} < 1$, we see that $\mathscr{B}^{-}$ becomes larger as $q_{\rm h}$ increases, i.e. as the commutator becomes more negative; moreover, $\Pr(\mathscr{B}^{-})$ always coincides with the z-axis. Also, from the considerations in Appendix D, $\mathscr{D}^{-}$ covers the whole (R, z)-plane (with $D = 0$ on the z-axis) independently of $q_{\rm h}$, and $\Pr(\mathscr{D}^{-})$ coincides with the z-axis. Finally, from equation (D.6), we see that in the range $1 < q < \sqrt{2}$ the biquadratic has a positive discriminant and admits a positive and a negative solution, so that $\mathscr{C}^{-}$ is the region between the z-axis and the (positive) square root of the (positive) solution. Moreover, there exists a critical value $q_{\rm h} \simeq 1.74$, obtainable numerically, such that the discriminant of the biquadratic is always negative, and so $\mathscr{C}^{-}$ covers the whole (R, z)-plane. Finally, for $\sqrt{2} < q_{\rm h} \lesssim 1.74$, the biquadratic admits two positive solutions up to a specific z (depending on $q_{\rm h}$), and no solutions above it: therefore, in this range of potential flattening $\mathscr{C}^{0}$ is a closed curve shape adjacent to the equatorial plane, resulting from the conjunction of the (positive) square roots of the two solutions in the region where they exist. This behavior is apparent in Figure 4.26, where $\mathscr{C}^{-}$ is to the left of the $\mathscr{C}^{0}$ curve in the left panel, and outside the closed $\mathscr{C}^{0}$ curve in the central panel; in the right panel, as $q_{\rm h}$ is greater than the

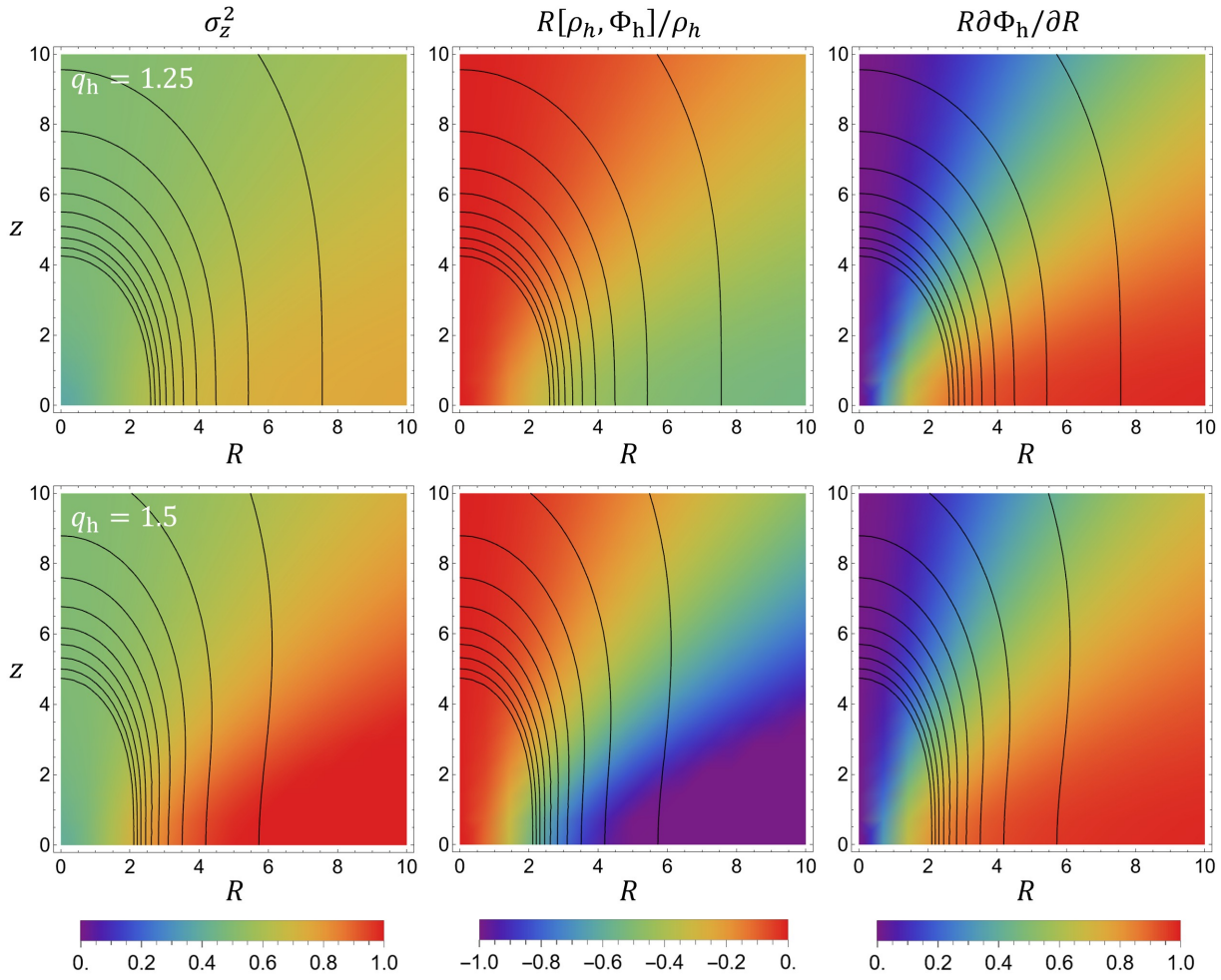


Figure 4.25. Maps in the (R, z)-plane of σ_z^2 (left column), $R\left[\rho_{\rm h}, \Phi_{\rm h}\right]/\rho_{\rm h}$ (central column) and $R\,\partial\Phi_{\rm h}/\partial R$ (right column), in units of $v_{\rm h}^2$, for the Binney logarithmic halo with $q_{\rm h} = 1.25$ (top row) and $q_{\rm h} = 1.5$ (bottom row). Black solid lines show equally spaced isodensity contours.

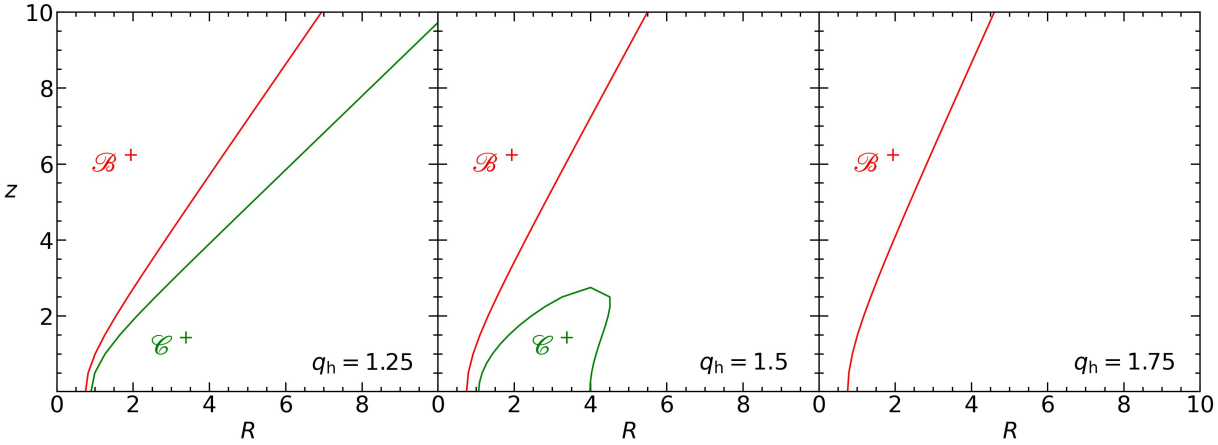


Figure 4.26. The ansatz-independent regions $\mathscr{B}$, $\mathscr{C}$ and $\mathscr{D}$ of the Binney logarithmic halo, for different values of q_h; from left to right, the stellar density profile becomes more elongated along the z-axis (and the commutator more negative). The $\mathscr{B}^-$ regions are to the right of the red curves ($\mathscr{B}^0$), while $\mathscr{C}^-$ is to the left of the green curve ($\mathscr{C}^0$) for $q_h = 1.25$, outside the same curve for $q_h = 1.5$, and it fully covers the (R, z)-plane for $q_h = 1.75$. For all the models, $\mathscr{D}^-$ fully covers the (R, z)-plane, with $\mathscr{D}^0$ coinciding with the z-axis, and $\mathrm{Pr}(\mathscr{B}^-)$ and $\mathrm{Pr}(\mathscr{C}^-)$ coincide with the z-axis. The values of R and z are normalized to b_h.

critical value discussed above, $\mathscr{C}^-$ covers the entire (R, z)-plane. As expected from our general considerations in Appendix 3.3.3, we also see that $\mathscr{B}^- \subseteq \mathscr{D}^-$, and $\mathscr{B}^+ \subseteq \mathscr{C}^-$ and $\mathscr{C}^+ \subseteq \mathscr{B}^-$; moreover, $\mathscr{B}^+ \cap \mathscr{C}^+ = \emptyset$, and the region $\mathscr{B}^- \cap \mathscr{C}^-$ becomes larger as q_h increases, i.e. as the commutator becomes more negative.

Concerning the limits on b, from the general considerations we have $b_1 = \infty$, and $b_2 = 0$, the latter for the models in which $\mathscr{C}^+$ exists. Moreover, from equations (3.11) and (3.13), we have

$$b_M = \frac{2}{q_h^2}, \quad b_0 = \frac{1}{q_h^2}, \tag{4.27}$$

independently of z, where both the minima are reached for $R \to \infty$; in the spherical limit ($q = 1$), in accordance to equations (D.8) and (D.9), $b_M = 2$ and $b_0 = 1$. Some considerations can be made at this point: first, as expected from the general considerations, $b_0 < 1$, and $b_M < 1$ for $q_h > \sqrt{2}$, the range in which the commutator $[R\,\rho_h, \Phi_h]$ (i.e., $\overline{v_\varphi^2}$ in the two-integral case) becomes negative. Second, as proved in the very general Theorem G.2.1, $b_M \geq b_0$ independently of q_h. Finally, both b_M and b_0 decrease for increasing q_h: in a certain sense, this extends with continuity the trend of lower amounts of supported b-anisotropy for increasing values of q (see Section 4.1.5), in this case going beyond the spherical limit.

In Figure 4.27, we show the 2D maps of $\overline{v_\varphi^2}$, Δ_R and Δ for $q_h = 1.25$, and three values of (constant) b. The behavior of the fields with b is analogous to that illustrated for the previous

models, i.e. $\overline{v_\varphi^2}$ and Δ decreases in $\mathscr{B}^-$ and increase in $\mathscr{B}^+$, and Δ_R decreases in $\mathscr{D}^-$ (i.e., everywhere); however, given the negativity of the commutator, the relative position of the $\mathscr{B}^\pm$ and $\mathscr{C}^\pm$ regions is now different, as shown in Figure 4.26. In particular, notice that $\Delta_R = \Delta$ is negative everywhere in the two-integral case ($b = 1$), as $b_0 < 1$, and Δ is never everywhere positive in $\mathscr{B}^+$ (as $b_1 = \infty$) and $\mathscr{C}^+$ (as $b_2 = 0$). The effect of changing the potential flattening is investigated in Figure 4.28, where the same fields are shown for $q_\mathrm{h} = 1.5$. We see that all the fields decrease close to the equatorial plane, and a negativity region for $\overline{v_\varphi^2}$ and Δ_R appear for lower values of b; in particular, as b_M and b_0 are smaller than 1, both the fields are somewhere negative in the two-integral case. Notice also that the $\mathscr{C}^+$ region is now delimited by a close curve; for $b = b_2 = 0$, Δ would be non-negative inside it.

4.3.2 Power-law ellipsoid in a dominant singular isothermal sphere

As an ellipsoidal model, we now consider a power-law stellar density profile, as in equation (F.1), in a dominant ($\Phi = \Phi_\mathrm{h}$) DM halo modeled as a SIS, i.e. by fixing $q_\mathrm{h} = 1$ in equation (F.2); in the following, all the lengths are normalized to a_*, densities to ρ_0, and potential and squared velocities to v_h^2. From equation (F.8), obtained for the oblate ($q < 1$) case, and by using the identity in equation A.13, it is possible to show that, for $q > 1$:

$$\begin{cases} \rho_* \sigma_z^2 = \dfrac{1}{\gamma q^{1-\gamma} (R^2 + z^2)^{\gamma/2}} \, {}_2\mathrm{F}_1 \left(\dfrac{\gamma}{2}, \dfrac{\gamma}{2}, \dfrac{2+\gamma}{2}; x \right), \\ \\ [\rho_*, \Phi_\mathrm{h}] = \dfrac{\gamma (1-q^2) q^{\gamma-1} R}{(2+\gamma) \left(R^2 + z^2\right)^{1+\frac{\gamma}{2}}} \, {}_2\mathrm{F}_1 \left(\dfrac{2+\gamma}{2}, \dfrac{2+\gamma}{2}, \dfrac{4+\gamma}{2}; x \right), \end{cases} \tag{4.28}$$

where ${}_2\mathrm{F}_1(a, b, c; x)$ is the hypergeometric function (see Appendix A.2), and

$$x \equiv \frac{(1-q^2) R^2}{R^2 + z^2} = \frac{1-q^2}{1+s^2}; \quad s \equiv \frac{z}{R}. \tag{4.29}$$

Given the scale-free nature of the model, the ansatz-independent fields σ_z^2, $R\,[\rho_*, \Phi_\mathrm{h}]\,/\rho_*$ and $R\,\partial\Phi_\mathrm{h}/\partial R$ are constant on straight lines $z = sR$, and $[\rho_*, \Phi_\mathrm{h}] < 0$ everywhere; in the spherical limit, $\sigma_z^2 = 1/\gamma$ and $[\rho_*, \Phi_\mathrm{h}] = 0$. For reference, in Figure 4.29 we show the three kinematic fields for different values of γ and q. Apart from $R\,\partial\Phi_\mathrm{h}/\partial R$, which is fixed by construction, we see that increasing γ slightly decrease the values of the fields near the equatorial plane, while increasing q, in analogy with the model in Figure 4.25, has the more apparent effects of increasing σ_z^2 and

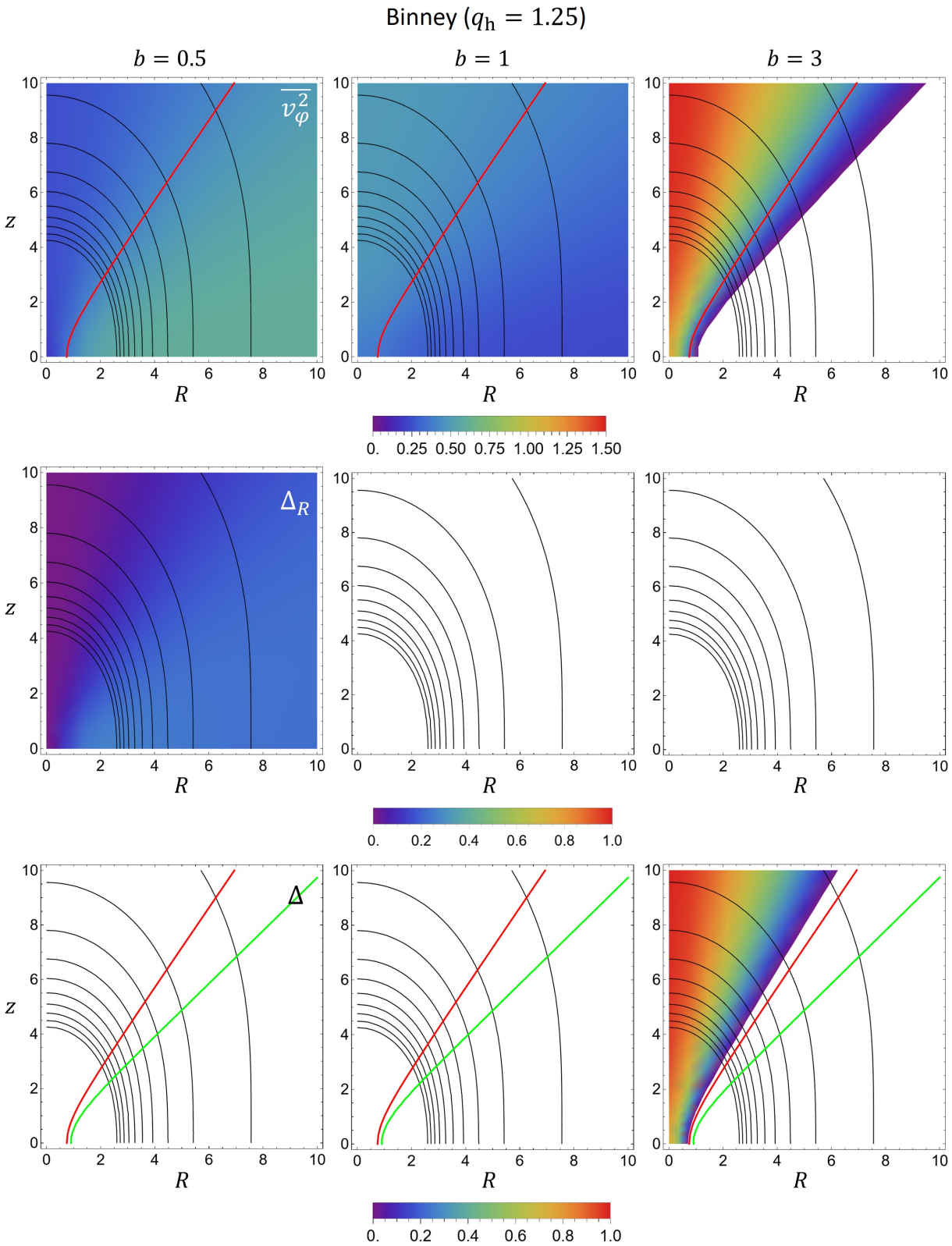


Figure 4.27. Maps in the (R, z)-plane of $\overline{v_\varphi^2}$ (top row), Δ_R (central row) and Δ (bottom row), in units of v_h^2, for the Binney logarithmic halo with $q_h = 1.25$, and constant $b = 0.5$ (left column), $b = 1$ (central column) and $b = 3$ (right column). The red and green lines show, respectively, the $\mathscr{B}^0$ and $\mathscr{C}^0$ curves, while $\mathscr{D}^0$ coincides with the z-axis. Black solid lines show equally spaced isodensity contours. White regions correspond to negative values of the fields.

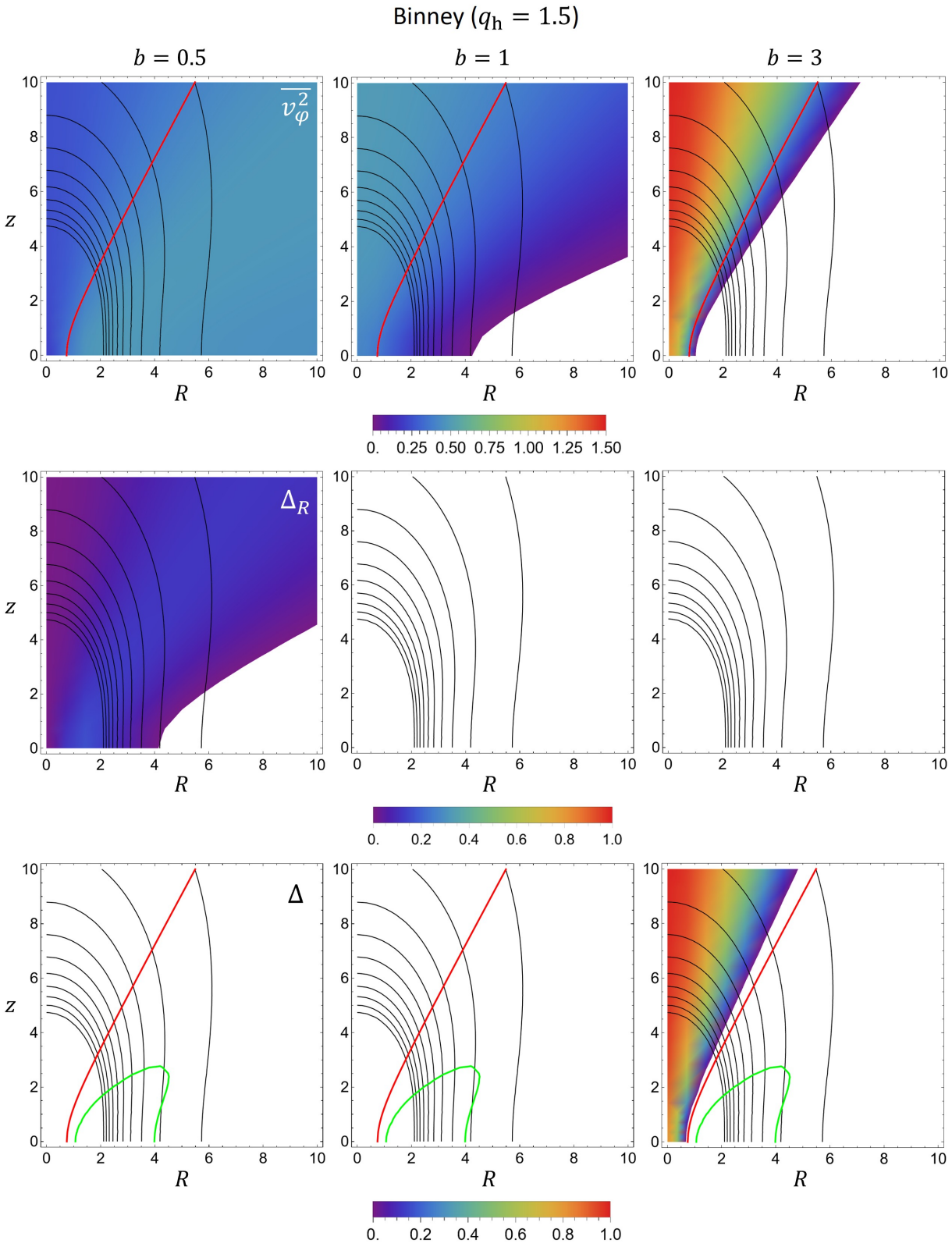


Figure 4.28. Same as in Figure 4.27, but for $q_h = 1.5$.

(in absolute value) $R\left[\rho_*, \Phi_{\rm h}\right]/\rho_*$ close to the equatorial plane.

The B, C and D functions can be determined in a fully analytical way from equations (2.26), (3.4) and (3.6), or by using equation (A.13) in equations (F.10), (F.11) and (F.12):

$$D = \frac{q^{\gamma-1}}{R^{\gamma+1}}\left[\frac{s^2(q^2+s^2)^{-\gamma/2}}{1+s^2} - \frac{1}{(1+s^2)^{\gamma/2}}\,{}_2\mathrm{F}_1\left(\frac{\gamma}{2}, \frac{\gamma}{2}, \frac{2+\gamma}{2}; x\right)\right], \tag{4.30}$$

$$B = \frac{s^2}{1+s^2} + \frac{1-\gamma}{\gamma}\left(\frac{q^2+s^2}{1+s^2}\right)^{\gamma/2}\,{}_2\mathrm{F}_1\left(\frac{\gamma}{2}, \frac{\gamma}{2}, \frac{2+\gamma}{2}; x\right), \tag{4.31}$$

$$C = \frac{1}{1+s^2} - \frac{1}{\gamma}\left(\frac{q^2+s^2}{1+s^2}\right)^{\gamma/2}\,{}_2\mathrm{F}_1\left(\frac{\gamma}{2}, \frac{\gamma}{2}, \frac{2+\gamma}{2}; x\right). \tag{4.32}$$

Notice that, as for the models in Appendix F.2, B and C are constant along straight lines, and $B \geq 0$ everywhere (i.e., the $\mathscr{B}^-$ region disappears) for $\gamma \leq 1$; also, $\mathscr{D}^-$ covers the entire (R, z)-plane, with $D = 0$ on the z-axis. In Figure 4.30, we show the $\mathscr{B}^-$ regions (to the right of the $\mathscr{B}^0$ lines) for different values of q and γ. We see that $\mathscr{B}^-$ becomes larger for increasing q and γ, namely as the commutator becomes more and more negative; moreover, for all the models, $\mathrm{Pr}(\mathscr{B}^-)$ coincides with the z-axis. Analogously, the $\mathscr{C}^-$ regions (to the left of the $\mathscr{C}^0$ curves) are shown for the same combinations of parameters, and we see that they become in general larger for increasing q and decreasing γ. However, as stated in Appendix F.2, there exists a critical value of the flattening $q_{\mathscr{C}}(\gamma)$ such that $\mathscr{C}^-$ covers the whole (R, z)-plane for $q \geq q_{\mathscr{C}}$, and this is the case for models with $\gamma = 1.5$ and $q = 2$, and with $\gamma \geq 2$ and $q = 2.5$; moreover, $\mathrm{Pr}(\mathscr{C}^-)$ always coincides with the z-axis. Notice that the trends of the $\mathscr{B}^-$ region with q and γ are in accordance with the findings in Congera (2025) for two-integral models, where consistency problems can arise in a region close to the equatorial plane.

As for the models in Appendix F.2, the constraints on $b(z)$ can be easily determined thanks to the fact that all the relevant functions are stratified on the straight lines $z = s\,R$; therefore, the problem reduces to the study of a function of one variable, and the resulting minimum will depend on γ and q, but not on z. From equation (3.11) (for $\gamma > 1$), $b_{\rm M}$ is found for $s = 0$ (i.e., on the equatorial plane) as

$$b_{\rm M} = \frac{\gamma}{q^\gamma\,(\gamma-1)\,{}_2\mathrm{F}_1\left(\frac{\gamma}{2}, \frac{\gamma}{2}, \frac{2+\gamma}{2}; 1-q^2\right)}, \tag{4.33}$$

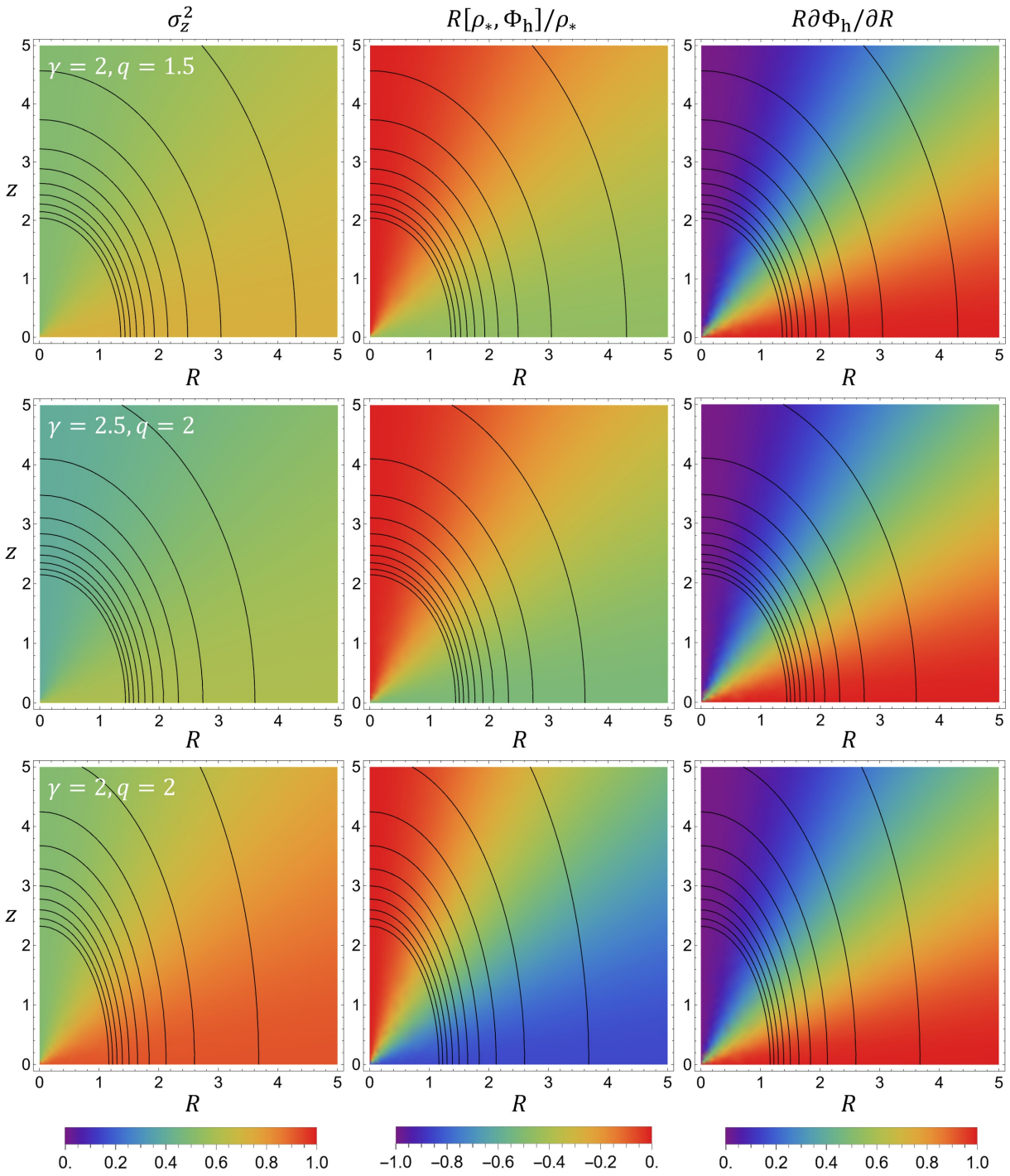


Figure 4.29. Maps in the (R, z)-plane of σ_z^2 (left column), $R\,[\rho_*, \Phi_\mathrm{h}]\,/\rho_*$ (central column), and $R\,\partial\Phi_\mathrm{h}/\partial R$ (right column), in units of v_h^2, for the power-law ellipsoid with $\gamma = 2$ and $q = 1.5$ (top row), $\gamma = 2.5$ and $q = 1.5$ (central row), and $\gamma = 2$ and $q = 2$ (bottom row). Black solid lines show equally spaced isodensity contours.

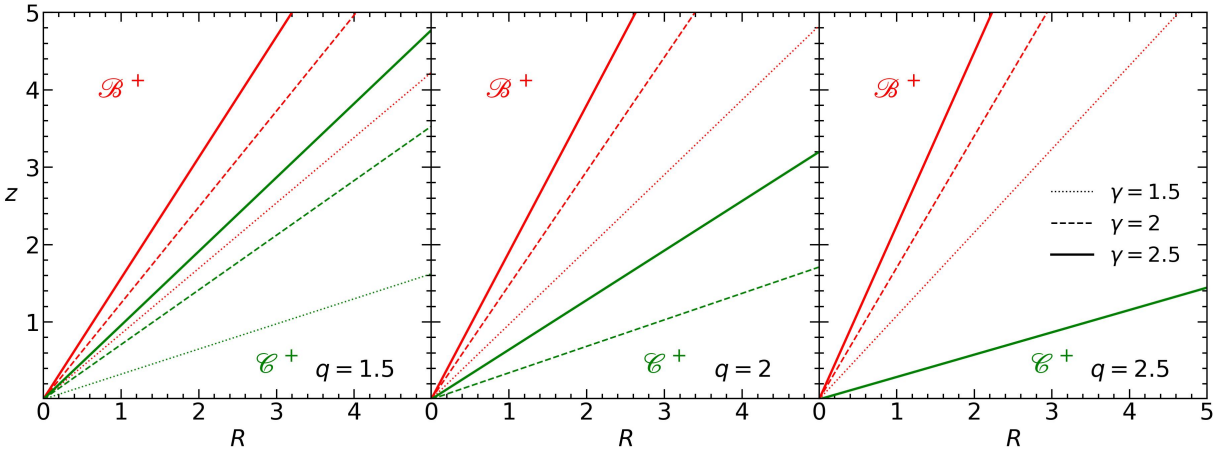


Figure 4.30. The ansatz-independent regions $\mathscr{B}$, $\mathscr{C}$ and $\mathscr{D}$ of the power-law ellipsoid in a dominant SIS, for different values of q; from left to right, the stellar density profile becomes more elongated along the z-axis (and the commutator more negative). The $\mathscr{B}^-$ regions are to the right of the red curves ($\mathscr{B}^0$), while $\mathscr{C}^-$ is to the left of the green curves ($\mathscr{C}^0$), and it fully covers the (R, z)-plane when $\mathscr{C}^0$ is not shown. For all the models, $\mathscr{D}^-$ fully covers the (R, z)-plane, with $\mathscr{D}^0$ coinciding with the z-axis, and $\mathrm{Pr}(\mathscr{B}^-)$ and $\mathrm{Pr}(\mathscr{C}^-)$ coincide with the z-axis. The values of R and z are normalized to a_*.

which decreases for increasing q and γ. From equation (3.13), given that $\mathscr{D}^-$ covers the whole (R, z)-plane, b_0 is found for $s \to \infty$ (i.e., on the z-axis) as

$$b_0 = \frac{2+\gamma}{2+q^2\gamma}; \tag{4.34}$$

analogously to b_M, b_0 decreases for increasing q and γ, and $b_0 = 1$ in the spherical limit. Notice that all the trends with the stellar density flattening are preserved, namely that less b-anisotropy is supported as q increases (even above $q = 1$); apart from the specific values of the limits, the presence of a DM halo do not alter these results. Finally, from the general considerations in Section 3.3.3, $b_1 = \infty$, and $b_2 = 0$ (for models with $\mathscr{C}^+ \neq \emptyset$).

Finally, in Figure 4.31 we show the $\overline{v_\varphi^2}$, Δ_R and Δ fields for the model with $\gamma = 2$ and $q = 1.5$, for three different values of (constant) b. Given that both the $\mathscr{B}^-$ and $\mathscr{C}^-$ regions exist, all the trends with b are identical to those of the previous models, with all the functions stratified on straight lines. Notice however that, as $b_0 < 1$, the two-integral field $\Delta_R = \Delta$ is negative everywhere, and $\Delta < 0$ independently of $b > 0$ inside $\mathscr{C}^+$ (as $b_2 = 0$), and $\mathscr{B}^+$ (as $b_1 = \infty$). For comparison, in Figure 4.32 we show the same fields for a higher q; notice that the fields globally decrease, and their negativity regions become larger, with $\Delta_R < 0$ in a large portion of the (R, z)-plane for $b = 0.5$ as well. In Figure 4.33, instead, we show the effects of increasing γ: the results are quite similar, as $\mathscr{B}^-$ becomes larger and both b_M and b_0 decrease, although Δ_R

remains positive at lower b.

4.3.3 Comparison with models with $[\rho, \Phi] > 0$

With this exploratory analysis, we tested our general procedure of determining the behavior of the solution of the JEs with the b-ansatz also for the class of models with $[\rho, \Phi] < 0$. We did not enter into particular details regarding the intrinsic structural properties of these objects (see e.g. Congera 2025 and references therein), but we succeeded in providing a full extension of the results found in the previous Sections, concerning in particular the trends of the critical regions and the limits for b with the properties of the galaxy. In summary, comparing these models to the ones with $[\rho, \Phi] > 0$, the following results hold:

- The spatial behavior of the ansatz-independent fields are very similar between the models, apart from the fact that the maxima of σ_z^2 and $R\,[\rho, \Phi]\,/\rho$ are now reached along the equatorial plane (i.e., perpendicular to the direction of the elongation), and the commutator is negative everywhere;

- The $\mathscr{D}^-$ region covers the entire (R, z)-plane, as for almost all the models with $[\rho, \Phi] > 0$, and $\mathscr{B}^- \subseteq \mathscr{D}^-$, but the relative position of the $\mathscr{B}^\pm$ and $\mathscr{C}^\pm$ regions is now different, as $\mathscr{B}^+ \subseteq \mathscr{C}^-$ and $\mathscr{C}^+ \subseteq \mathscr{B}^-$;

- The limits for b can be found in an analogous way, with $b_\mathrm{M} \geq b_0$ independently of the model parameters, but $b_0 < 1$, $b_1 = +\infty$ and $b_2 = 0$, and $b_\mathrm{M} < 1$ (i.e., $\overline{v_\varphi^2} < 0$ in the two-integral case) if the commutator $[R\,\rho, \Phi]$ is negative as well;

- The $\overline{v_\varphi^2}$, Δ_R and Δ fields have similar shapes and behave identically for increasing values of b (i.e., $\overline{v_\varphi^2}$ and Δ decrease in $\mathscr{B}^-$ and increase in $\mathscr{B}^+$, and Δ_R decreases in $\mathscr{D}^-$ and increases in $\mathscr{D}^+$), but the different relative position of the critical regions and the inequalities between the limits for b makes $\Delta_R = \Delta < 0$ in the two-integral case, and $\Delta < 0$ somewhere independently of b;

- The main trends with an increasing value of q are the same, namely that both the $\mathscr{B}^-$ and $\mathscr{C}^-$ region becomes larger, and the b_M and b_0 limits decrease. Instead, the effects of adding a DM halo are not investigated in detail, but in the two-component model $\overline{v_\varphi^2}$ stays positive

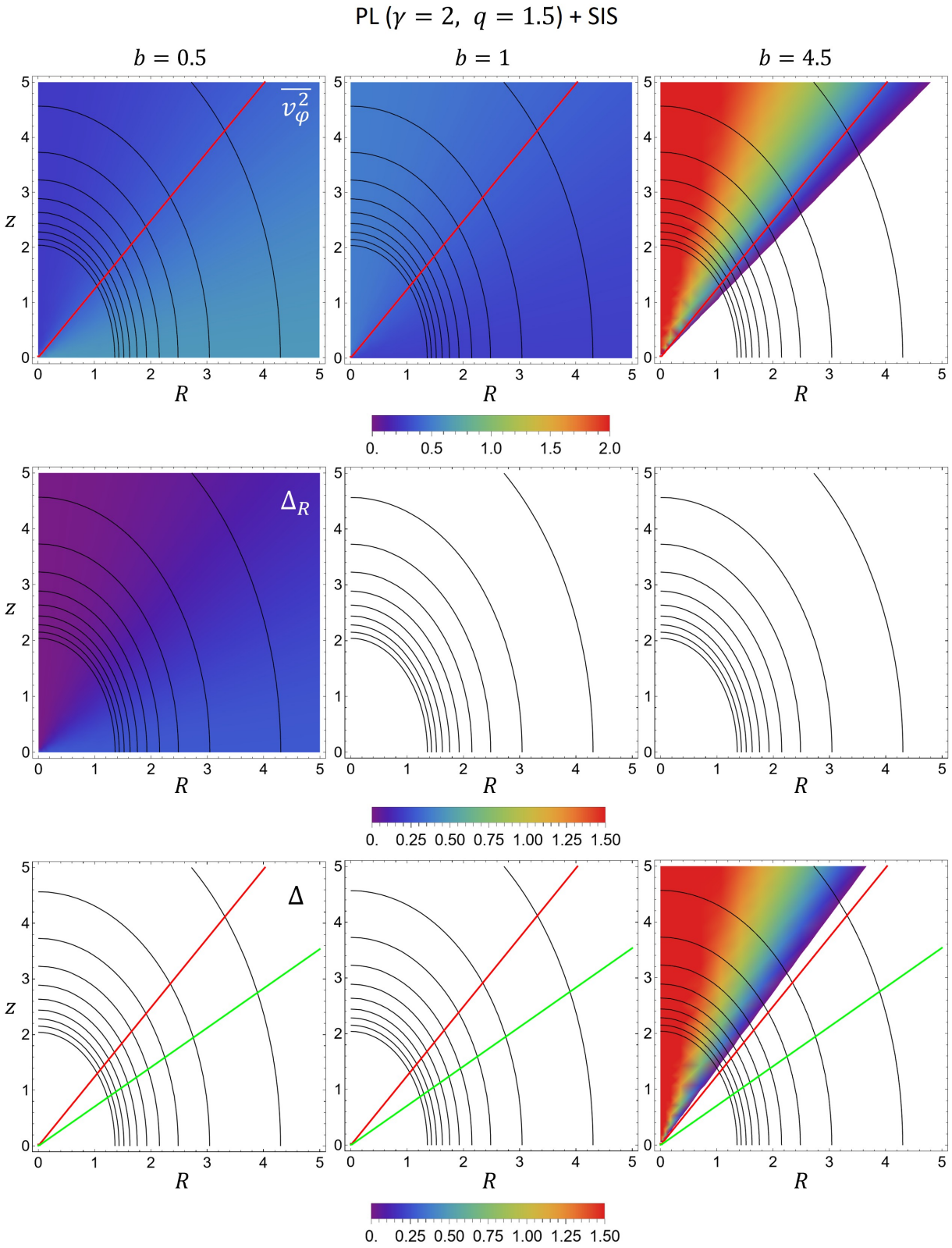


Figure 4.31. Maps in the (R, z)-plane of $\overline{v_\varphi^2}$ (top row), Δ_R (central row) and Δ (bottom row), in units of v_h^2, for the power-law ellipsoid with $\gamma = 2$ and $q = 1.5$ in a dominant SIS, for constant $b = 0.5$ (left column), $b = 1$ (central column) and $b = 4.5$ (right column). The red and green lines show, respectively, the $\mathscr{B}^0$ and $\mathscr{C}^0$ curves, while $\mathscr{D}^0$ coincides with the z-axis. Black solid lines show equally spaced isodensity contours. White regions correspond to negative values of the fields.

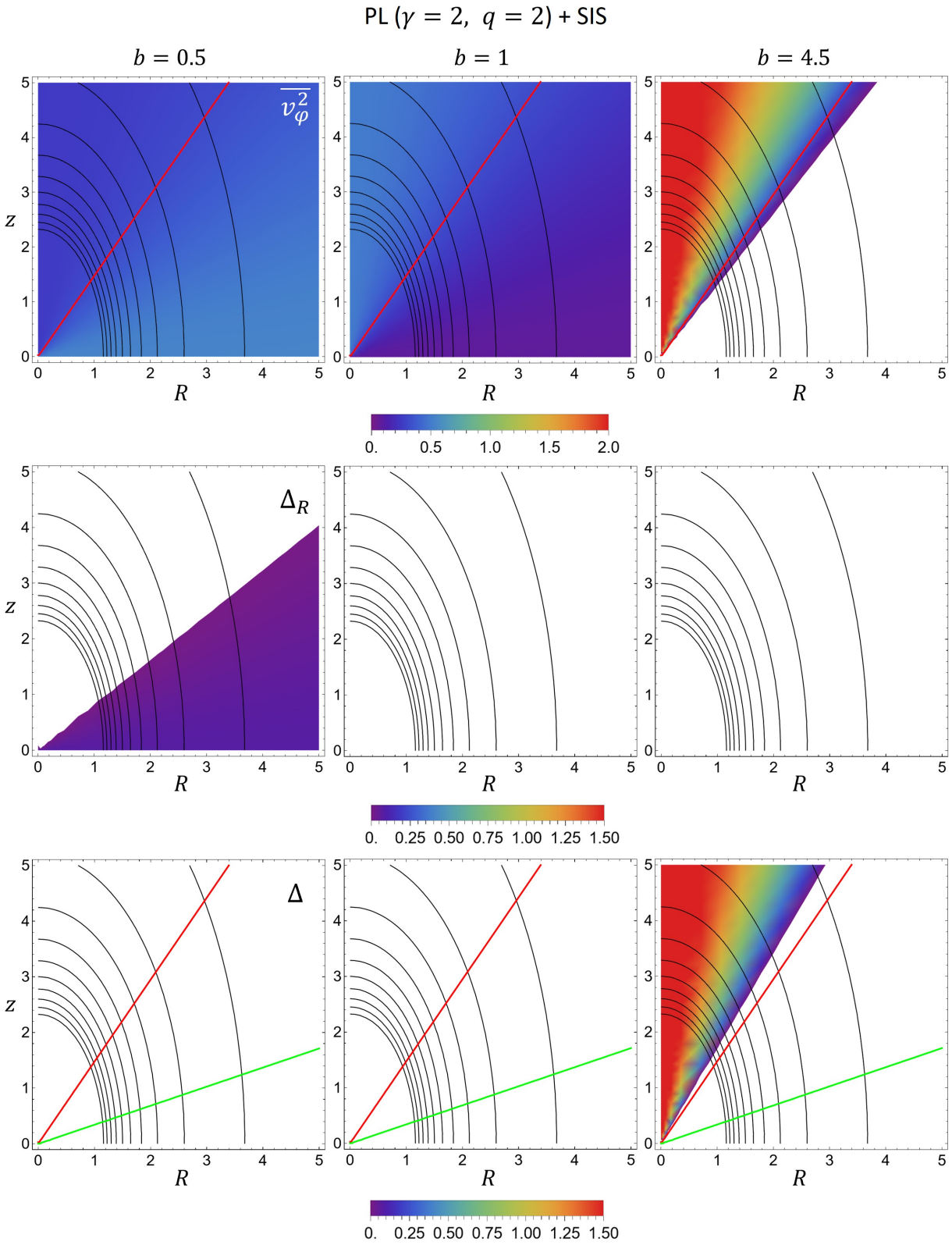


Figure 4.32. Same as in Figure 4.31, but for $q = 2$.

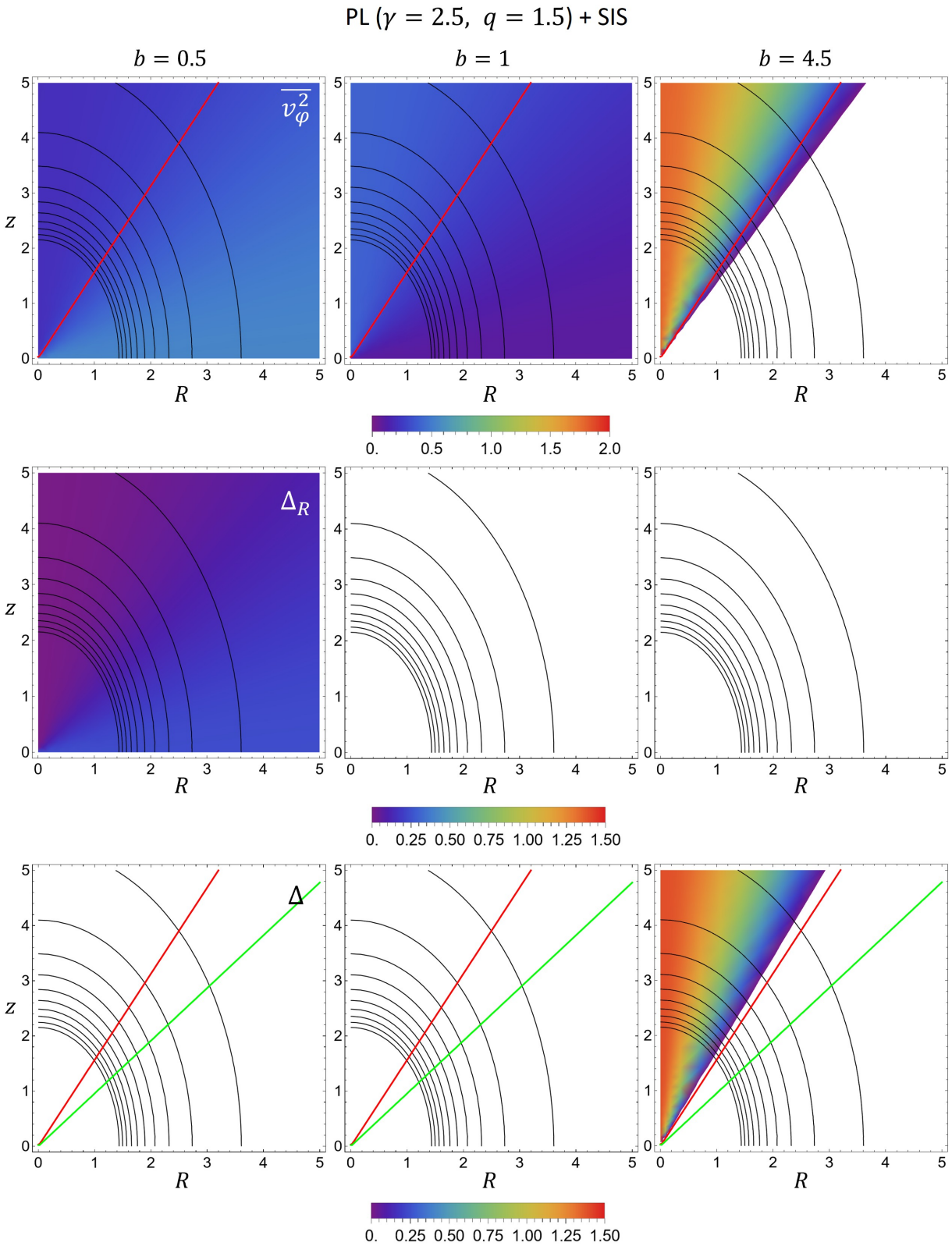


Figure 4.33. Same as in Figure 4.31, but for $\gamma = 2.5$.

for higher values of $q > 1$ (compared to the one.component model), suggesting that larger values of b-anisotropy may be allowed as well,.

Taken all together, these results clearly show that kinematic differences between models with positive and negative commutator exist, which may be useful to distinguish between the two models. In particular, although the ansatz-dependent fields have quite similar shapes and their behavior with b is the one expected from our general considerations, we stress the fact that both Δ_R and Δ are always negative in the two-integral case, and Δ is never everywhere positive; also, if $[R\,\rho, \Phi] < 0$, two-integral models can not exist, and lower values of b such that $\sigma_z > \sigma_R$ are needed to ensure their consistency. However, quite surprisingly, we also see that the trend of less supported b-anisotropy for increasing values of q naturally extends even for $q > 1$, i.e. when the stellar density profile of the galaxy elongates along the z-axis. Therefore, both for the critical regions and the limits for b, there is a continuum between models with positive, zero and negative commutator such that:

- The regions $\mathscr{B}^-$, $\mathscr{C}^-$ and $\mathscr{D}^-$ (if not already covering the entire space) become monotonically larger, overlapping in the spherical limit;
- The limits $b_{\rm M}$ and b_0 become monotonically smaller, with $b_0 = b_1 = b_2 = 1$ in the spherical limit, while b_1 and b_2 transition from 1 to, respectively, $+\infty$ and 0 as the commutator becomes negative.

These results suggest that the commutator may be reconsidered as a characterizing parameter of a model, and the behavior of the critical regions and of the $b_{\rm M}$ and b_0 limits smoothly transitions from the case of $[\rho_*, \Phi] > 0$ to the one of $[\rho_*, \Phi] < 0$, passing through the situation in which $[\rho_*, \Phi] = 0$ everywhere; the only discontinuity is in the values of b_1 and b_2, although the corresponding critical regions do not change significantly. Also, in the regime where the commutator is negative, the case with $[R\,\rho_*, \Phi] < 0$ is included, where $b_{\rm M} < 1$ and so no two-integral models exist. This important finding reveals that the behavior of the kinematic fields with respect to the amount of the b-anisotropy is general, and it depends only on quantities related to the properties of the galaxy and its environment. Among these, the flattening of the stellar density profile has the most relevant effect, followed by the presence (and dominance) of a DM halo, and last by the specific shape of the stellar profile. The sign of the commutator reveals, a priori from solving

the JEs, the relative position of the regions and the inequalities between the limits for b, but the general trends with increasing anisotropy remain the same.

CHAPTER 5

The b-ansatz for the Jeans modeling of TNG50 galaxies

In the previous Sections, we have analyzed how the b-ansatz, introduced in Cappellari (2008) and applied in the JAM approach (see Section 1.3.1), affects the stellar kinematics of axisymmetric ETGs. We provided general criteria that limit the possible values of the b-anisotropy in order to guarantee the positivity of some kinematic fields, and we discussed the connections between these limits and the properties of the galaxy, as the flattening and the shape of its stellar density distribution, or the DM-to-stellar mass ratio. In particular, we retrieved a trend between the limit on b and the flattening of the stellar density profile, as seen from both observational and mock data (see Section 1.4); we also showed that this trend is almost independent of the specific density profile, and of the presence of a (more or less dominant) DM halo, suggesting that this might be a general property of galaxies which can be properly modeled through the three-integral, axisymmetric JEs presented in Section 3.1. As a test bench of this, we now investigate whether these general trends hold also for simulated elliptical galaxies which resemble regular rotators, after testing whether their kinematics can be modeled sufficiently well by using the axisymmetric JEs with the b-ansatz. The latter result should not be taken as granted, because, even if it has been found quite successful in the modeling of real galaxies, the b-ansatz is just one over several possible choices to close the JEs. In particular, we choose the TNG50 simulation, whose high

baryonic mass resolution and large number of massive galaxies allow for an extended, spatially resolved study of the stellar kinematics of mock ETGs. Examples of Jeans modeling of TNG galaxies can be found in Loubser et al. (2020) and Shi et al. (2024), but this is the first time that an investigation of the b-ansatz is carried out for simulated elliptical galaxies.

This Chapter is structured as follows. In Section 5.1, we present the TNG50 simulation, and we describe the selection criteria for the sample of galaxies of our study. Then, in Section 5.2 we describe how all the structural (Section 5.2.1), kinematic (Section 5.2.2) and dynamical (Section 5.2.3) quantities of the galaxies related to the solution of the JEs are extracted from the simulation data. Finally, in Section 5.3 the main results of our analysis are presented, discussing whether our findings are in accordance to those found from our previous analysis (Section 5.3.1).

5.1 The TNG50 simulation: sample and selection criteria

The IllustrisTNG simulations are a suite of state-of-the-art cosmological magnetohydrodynamical simulations of galaxy formation and evolution (Marinacci et al. 2018; Naiman et al. 2018; Nelson, Pillepich, Springel, Weinberger, et al. 2018; Pillepich, Nelson, Hernquist, et al. 2018; Springel et al. 2018). Compared to the previous Illustris simulations (see e.g. Vogelsberger et al. 2014), they contain a new implementation of black hole feedback (Weinberger et al. 2017), as well as updates to the galactic wind feedback, stellar evolution and gas chemical enrichment models (Pillepich, Springel, et al. 2018). For example, the new AGN feedback model is responsible for the quenching of galaxies in massive halos and for the production of red and passive galaxies at late times, alleviating the discrepancies with observational data at the massive end of the halo mass function (Weinberger et al. 2017; Nelson, Pillepich, Springel, Weinberger, et al. 2018; Donnari et al. 2019). The faster stellar winds in IllustrisTNG reduce the star formation at all masses and all times, resulting in a suppressed galaxy stellar mass function at $z = 0$ for $M_* \lesssim 10^{10} M_\odot$, and generally smaller galaxy sizes (Pillepich, Springel, et al. 2018). Overall, the model has been demonstrated to agree satisfactorily with many observational constraints (see e.g. Genel et al. 2018; Nelson, Pillepich, Springel, Weinberger, et al. 2018), and to return a reasonable mix of morphological galaxy types (Rodriguez-Gomez et al. 2019). It is therefore of great interest to extend the analysis to the dynamical characteristics of the final galaxies.

For our analysis, we consider the simulation TNG50, which takes into account a $\simeq 50$ comoving-Mpc^3 box, and reaches mass resolutions with a target baryon mass of $8.5 \times 10^4 M_\odot$, typ-

ical of zoom-in simulations (see Pillepich, Nelson, Springel, et al. 2019, Nelson, Pillepich, Springel, Pakmor, et al. 2019 for a full description of the simulation). The cosmological parameters used in the simulation are $\Omega_{\rm m} = 0.3089$, $\Omega_{\rm b} = 0.0486$, $\Omega_\Lambda = 0.6911$ and $H_0 = 67.74\ {\rm km\,s^{-1}\,Mpc^{-1}}$, and are based on the latest Planck results (Planck Collaboration et al. 2016). The high number of galaxies with a sufficiently large M_* and baryon mass resolution allow for a more detailed study of the spatially resolved kinematics of the mock elliptical galaxies.

From the TNG50-1 cutout at redshift $z = 0$, we selected the whole sample of 81 galaxies with stellar mass $10^{10.5} \leq M_*/M_\odot \leq 10^{12}$, and specific star formation rate (sSFR) $\leq 10^{-12}\,yr^{-1}$. For all the galaxies of the sample, we considered the stellar and DM particles only, since the contributions from gas and the central black hole are negligible. An additional selection was performed by restricting to a sufficiently axisymmetric stellar density distribution, as discussed in Section 5.2.1. The list of the resulting 29 galaxies is given in Table 5.1.

5.2 Structural and kinematic analysis

In this Section, we illustrate the procedures that we used to compute the structural and kinematic quantities of our interest from the simulation data. We recall that our aims are first to test whether the massive and passive galaxies of TNG50 with a sufficiently axisymmetric stellar density distribution satisfy the three-integral JEs in equation (2.33), and then to check if there are any correlations between the shape and values of the anisotropy function $b = \sigma_R^2/\sigma_z^2$ and the properties of the galaxies and their environment.

5.2.1 Structural analysis of the stellar component

For each of the 81 galaxies selected to have sufficiently high stellar mass and low sSFR, we computed the second-order mass tensor (see e.g. Zemp et al. 2011, C21):

$$\mathcal{S}_{ij} = \frac{\sum_k m_k\, r_{ki}\, r_{kj}}{\sum_k m_k}, \tag{5.1}$$

where r_{ki} denotes the i-th component of the position vector of the k-th stellar particle, and the summation is performed over all the particles within $2\,r_{1/2}$, where $r_{1/2}$ is the stellar intrinsic half-mass radius (see Diemer et al. 2018).

As in case of an ellipsoidal density distribution, the eigenvectors of $\mathcal{S}$ give the direction of

Table 5.1: Physical properties and parameters associated to the 29 galaxies (subhalos) of the sample. From left to right: ID of the galaxy in the TNG50 simulation, total stellar mass, stellar intrinsic half-mass radius (in kpc), intermediate-to-major (Ax) and minor-to-major (q) axial ratios inside $2\,r_{1/2}$ (computed as in Section 5.2.1), mass-weighted average b (computed as in Section 5.2.2), s_R and s_z parameters related to the shape of the b field (see Section 5.3), mass-weighted average γ_φ (computed as in Section 5.2.2), number of galaxies inside the parent halo, relative positioning of the galaxy (Central/Satellite) inside the parent halo.

ID	$\log(M_*/\mathrm{M}_\odot)$	$r_{1/2}$	Ax	q	$\langle b \rangle$	s_R	s_z	$\langle \gamma_\varphi \rangle$	Rich	C/S
1	11.6	8.43	0.997	0.562	1.48	−0.297	0.203	0.095	390	S
2	11.3	7.686	0.954	0.654	1.84	−0.622	0.334	0.066	390	S
5	10.9	7.24	0.988	0.565	1.99	−0.977	0.253	0.261	390	S
9	10.8	5.47	0.993	0.506	1.85	−0.694	0.329	0.162	390	S
10	10.8	6.41	0.998	0.327	1.77	−0.136	0.293	0.212	390	S
63874	10.8	3.40	0.988	0.589	1.53	0.078	0.222	−0.074	209	S
96763	10.9	4.72	0.954	0.548	2.01	−0.085	0.320	0.094	141	S
96764	11.0	5.26	0.956	0.585	1.84	−0.197	0.257	0.114	141	S
117252	11.3	7.72	0.992	0.403	1.58	−0.405	0.267	0.203	160	S
117259	10.7	5.96	0.978	0.358	1.96	0.040	0.013	0.117	160	S
143883	11.3	4.56	0.986	0.525	1.50	−0.043	0.262	−1.02	129	S
184932	11.2	9.09	0.979	0.391	1.88	−0.209	0.113	0.113	103	S
184937	10.8	2.20	0.999	0.712	1.62	0.264	0.126	0.084	103	S
264885	11.1	3.53	0.978	0.546	1.70	0.084	0.111	0.169	47	S
313694	10.6	3.54	0.984	0.386	1.79	−0.290	0.246	0.271	33	S
319730	11.8	11.8	0.979	0.771	1.40	−0.345	0.128	0.101	18	C
390932	11.4	9.97	0.997	0.633	1.36	−0.333	0.106	−0.219	8	C
418335	11.2	8.98	0.991	0.800	1.28	−0.022	0.067	0.033	9	C
428177	11.0	4.68	0.993	0.581	1.41	0.238	0.214	−0.271	12	C
450916	11.1	7.64	0.973	0.725	1.63	−0.301	0.199	−0.112	5	C
454171	10.9	5.24	0.987	0.294	1.90	−0.372	0.286	0.231	5	C
478216	10.8	5.04	0.976	0.378	1.67	−0.419	0.250	−0.026	8	C
482155	11.1	6.58	0.969	0.341	1.81	−0.385	0.289	0.050	3	C
498522	11.0	6.81	0.984	0.407	1.83	−0.491	0.082	0.139	3	C
516101	10.7	3.25	0.973	0.582	1.56	−0.241	0.181	−0.115	4	C
543114	10.8	3.09	0.951	0.542	1.72	0.517	0.296	−1.83	1	C
546114	10.7	3.10	0.960	0.501	1.63	0.069	0.244	−0.249	2	C
563732	10.6	5.29	0.985	0.329	1.85	−0.015	0.103	0.130	2	C
572328	10.6	4.18	0.979	0.358	1.59	−0.306	0.184	0.203	2	C

the principal axes, and the eigenvalues are proportional to the squared lengths of the semiaxes (see e.g. Exercises 2.17 and 2.18 in C21). Therefore, in order to select sufficiently axisymmetric galaxies, we computed the eigenvectors and eigenvalues of $\mathcal{S}$ for each of the 81 galaxies, and we restricted the sample to the 29 systems having the ratio between the intermediate and the largest semiaxes ≥ 0.95 (i.e., a difference smaller than 5%); notice that, with this choice, only systems with almost oblate ellipsoidal (or spherical) stellar density distributions are selected. For the stellar component of each galaxy, we also estimate the minor-to-major axial ratio q inside two stellar half-mass radii. In the top row of Figure 5.1, we show the histogram of q for the 29 galaxies of the final sample, together with the histograms of their stellar masses M_*, and stellar half-mass radii $r_{1/2}$.

To proceed with the dynamical study, the stellar and DM particles of each of the selected

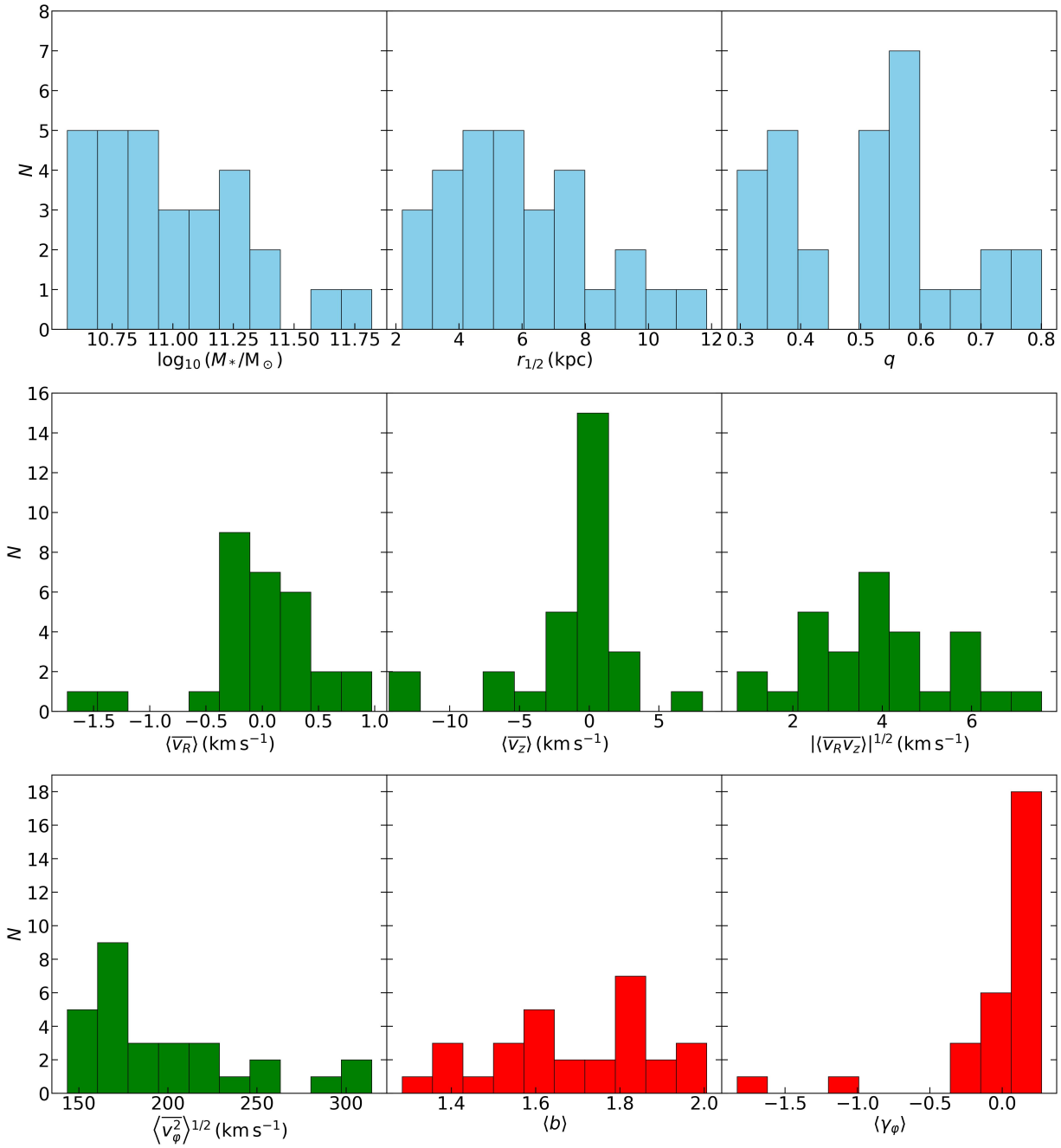


Figure 5.1. From left to right, histograms for the 29 galaxies in our sample of: (top row) total stellar mass, stellar half-mass radius, minor-to-major axial ratio of the stellar density distribution inside two stellar half-mass radii; (central row) mass-weighted average inside two stellar half-mass radii of $\overline{v_R}$, $\overline{v_z}$, and $\overline{v_R v_z}$ (in absolute value and square root); (bottom row) mass-weighted average inside two stellar half-mass radii of $\overline{v_\varphi^2}$ (in absolute value and square root), $b = \sigma_R^2/\sigma_z^2$ and $\gamma_\varphi = 1 - \sigma_\varphi^2/\sigma_R^2$.

galaxies are re-oriented such that the z-axis is aligned with the symmetry axis of the stellar density distribution, i.e. with the third eigenvector of the tensor; moreover, for each particle, the cartesian coordinates are easily converted to cylindrical coordinates (R, φ, z) as

$$R = \sqrt{x^2 + y^2}, \quad \varphi = \arctan(y/x). \tag{5.2}$$

In order to compute the kinematic quantities of our interest, the (R, z)-plane is then subdivided into a (regular) grid of pixels with fixed $\Delta R = \Delta z = 100\,\mathrm{pc}$ sides, extending radially from 0 to $2\,r_{1/2}$, and vertically from $-r_{1/2}$ to $r_{1/2}$; the spatial resolution of the grid was established following Harborne et al. (2024), to reach an amount of particles-per pixel ($\gtrsim 200$ in general) sufficient to compute robust average kinematical fields.

After this procedure, we are ready to compute the stellar density profile ρ_* of each galaxy. For a generic, continuous $\rho_*(R, \varphi, z)$, the equivalent axisymmetric $\overline{\rho_*}(R, z)$ at the point (R, z) is found by azimuthal averaging the density distribution over a ring at fixed (R, z), i.e.

$$\overline{\rho_*}(R, z) = \frac{1}{2\pi} \int_0^{2\pi} \rho_*(R, \varphi, z)\, d\varphi. \tag{5.3}$$

In our case, being the numerical ρ_* made by discrete particles, for the pixel centered at (R, z) we sum the mass of all the particles belonging to it, independently of their φ coordinate, and then we divide the total pixel mass $\sum_k m_k$ by the volume of the rectangular torus of section $\Delta R \Delta z$, i.e.

$$\rho_*(R, z) = \frac{\sum_k m_k}{2\pi R\, \Delta R\, \Delta z}; \tag{5.4}$$

these maps are shown for all the galaxies in the sample[1] in the top panels of the Figures in Appendix H. We stress that, given our strict selection criteria, the systems are highly axisymmetric, and so their density distribution only slightly differs from the angle-averaged one; therefore, in the following we identify $\rho_*(R, z)$ with $\overline{\rho_*}(R, z)$.

[1] For the TNG117252 galaxy, we noticed the presence an overdense region above the equatorial plane, possibly due to previous interactions with other galaxies. However, we also checked that it does not significantly affect the results on the kinematics, and so we decided to keep this galaxy in the sample.

5.2.2 Kinematic analysis of the stellar component

We computed the values of the stellar kinematic fields with the same "particle-in-pixel" approach used to compute ρ_*. For each particle, the velocity components in cylindrical coordinates are given by

$$\begin{cases} v_R = v_x \cos\varphi + v_y \sin\varphi, \\ v_\varphi = -v_x \sin\varphi + v_y \cos\varphi, \\ v_z = v_z. \end{cases} \tag{5.5}$$

and then, by assigning each particle to a pixel of the grid, we compute the angle averaged mean velocity ($\overline{v_i}$), mean squared velocity ($\overline{v_i^2}$) and velocity dispersion (σ_i^2) in the i-th direction as

$$\overline{v_i} = \frac{\sum_k m_k\, v_{i,k}}{\sum_k m_k}, \quad \overline{v_i^2} = \frac{\sum_k m_k\, v_{i,k}^2}{\sum_k m_k}, \quad \sigma_i^2 = \overline{v_i^2} - (\overline{v_i})^2, \tag{5.6}$$

where the sum is performed over all the stellar particles in the pixel centered at (R, z), and all the quantities are normalized to appropriate units. In an analogous way, we also compute $\overline{v_R v_z}$ (which we recall to be zero in case of a cylindrically-aligned velocity dispersion tensor), and the ansatz function $b \equiv \sigma_R^2/\sigma_z^2$, which is the focus of our study. The maps of these fields for the galaxies in our final sample are shown in the second, third and fourth rows of the Figures in Appendix H.

Finally, for a generic angle-averaged function g, we compute its mass-weighted average inside two stellar half-mass radii as

$$\langle g \rangle \equiv \frac{\sum_n m_n\, g_n}{\sum_n m_n}, \tag{5.7}$$

where the sum is performed over all the pixels inside that region; however, to avoid excessive numerical noise, we empirically chose to compute this average on a grid with larger pixels ($\Delta R = \Delta z = 500\,\mathrm{pc}$). In the central and bottom rows of Figure 5.1, we show the histograms of $\langle \overline{v_R} \rangle$, $\langle \overline{v_z} \rangle$, $\langle \overline{v_R v_z} \rangle$, and of the two mass-weighted average b and γ_φ parameters for the 29 galaxies in our sample.

5.2.3 Dynamical analysis

Finally, in order to get the z and R components of the gravitational field which appear at the right-hand side of the JEs, we compute the total (i.e., stars plus DM) gravitational potential of

each galaxy as

$$\Phi(\mathbf{x}) = -G \sum_n \frac{m_n}{\sqrt{(x_n - x)^2 + (y_n - y)^2 + (z_n - z)^2 + \epsilon^2}}, \tag{5.8}$$

where $\mathbf{x} = (x, y, z)$, and the sum goes over all the stellar and DM particles within the subhalo (i.e., the galaxy); the softening length ϵ is set equal to the pixel scale. Assuming that the system is sufficiently axisymmetric, we compute equation (5.8) for all the points of the (R, z)-plane at $y = 0$, i.e. the (positive) (x, z)-plane. Therefore, we take the central position $(R, z) = (x, z)$ of each pixel in this plane, and we calculate the contribution of all the particles to the potential at that point. Numerical differentiation of equation (5.8) finally allows to compute the right-hand sides of the JEs in equation (2.33). The maps of these quantities are shown in the bottom panels of the Figures in Appendix H, for all the 29 galaxies in our sample.

5.3 Results of the analysis

The first point of our study is to investigate whether the selected galaxies obey the JEs in equation (2.33), meaning that they are stationary, axisymmetric three-integral systems with a cylindrically-aligned velocity dispersion ellipsoid. First, by visual inspection of the kinematic maps (see Appendix H), wee see that for all the selected galaxies $\overline{v_R} \approx \overline{v_z} \approx 0$, and $\overline{v_R v_z}$ is significantly lower than the other velocity fields; this is also confirmed by looking at the histograms in the middle row of Figure 5.1, which show that the mass-weighted average of $\overline{v_R v_z}$ is significantly smaller (less than percent) than the mass-weighted average of $\overline{v_\varphi^2}$. Furthermore, for the majority of the galaxies $\sigma_R^2 > \sigma_z^2$ for almost all the points of the (R, z)-plane, as also confirmed by the histogram of $\langle b \rangle$ in Figure 5.1, meaning that these systems are not supported by a two-integral DF. Finally, a qualitative comparison between the numerically computed left and right-hand sides of the JEs (see the bottom panels of the Figures in Appendix H) shows that the two are similar. All these results together suggest that the selected systems are well modeled by the axisymmetric, three-integral JEs in equation (2.33).

Concerning their orbital anisotropy, in Figure 5.2, we show the maps of $b = \sigma_R^2/\sigma_z^2$ for the 29 galaxies in our sample, ordered by decreasing stellar density flattening: by a simple visual inspection, is apparent that the the anisotropy parameter is in general greater than unity (i.e., $\sigma_R > \sigma_z$), as also confirmed by looking at the histogram of $\langle b \rangle$ in Figure 5.1. However, we notice

some patterns that characterize the distribution of its values: in fact, for some galaxies the highest b values extend radially even beyond the half-mass radius and keep increasing outwards (see e.g. the top left panel), while in others the values of b present a more uniform distribution (see e.g. the bottom right panel). Moreover, for the former class of systems, the largest b values extend out of the central region in a conical shape with axis on $z = 0$, with the aperture of this cone being largely different between the systems. This means that, even if σ_R^2 and σ_z^2 both decrease at high radii, their ratio (i.e., the b function) remains almost constant.

To investigate these features more quantitatively, and check possible relations with the galaxy properties, we define the two adimensional parameters s_R and s_z as

$$s_R \equiv 1 - \frac{\langle b \rangle_B}{\langle b \rangle_A}, \quad s_z \equiv 1 - \frac{\langle b \rangle_{\rm M}}{\langle b \rangle_B}, \quad \langle b \rangle_{\rm M} \equiv \frac{\langle b \rangle_C + \langle b \rangle_D}{2}, \tag{5.9}$$

where the letters denote the volumes, shown in Figure 5.3, over which the mass-weighted averages of b are computed; notice that the size of the regions are $r_{1/2}$ of width and 1 kpc of height, in order to make the analysis sufficiently general for all the galaxies. Lower (higher) values of s_R indicate that, on the equatorial plane, the mass-average b at high radii is greater (smaller) than the mass-average b at low radii. Instead, lower (higher) values of s_z indicate that, at outer radii, the mass-average b outside the equatorial plane is on average greater (smaller) than the mass-average b on the equatorial plane. In practice, s_R measures how much the b field varies along the equatorial plane, while s_z gives the indication of a wedge-like shape at outer radii; therefore, for example, galaxies with a perfectly thin "strip" of b values across the equatorial plane would therefore have $s_R = 0$ (as $\langle b \rangle_A = \langle b \rangle_B$) and s_z close to unity (as $\langle b \rangle_M < \langle b \rangle_B$).

In Figure 5.4, we show the values of s_R and s_z for all the 29 galaxies of the sample, color-coded by their stellar minor-to-major semiaxes ratio q (top-left panel), stellar mass M_* (top-right), stellar half-mass radius $r_{1/2}$ (bottom-left panel) and cluster richness, i.e. the number of galaxies in the parent halo (bottom-right panel). We see that all the galaxies have $s_z > 0$, meaning that the values of $\langle b \rangle$ on the equatorial plane are larger than outside it, and the majority of them have $s_R < 0$, namely the values of $\langle b \rangle$ are larger at outer radii than close to the origin. However, while no apparent trend with q is present, galaxies with the most massive (high M_*) and extended (large $r_{1/2}$) stellar component all support larger b-anisotropy at outer radii than close to the origin ($s_R < 0$), although the spread in s_z shows that the specific shape of the b field can vary. Moreover, galaxies with a larger b-anisotropy close to the center ($s_R > 0$) all have small stellar masses and

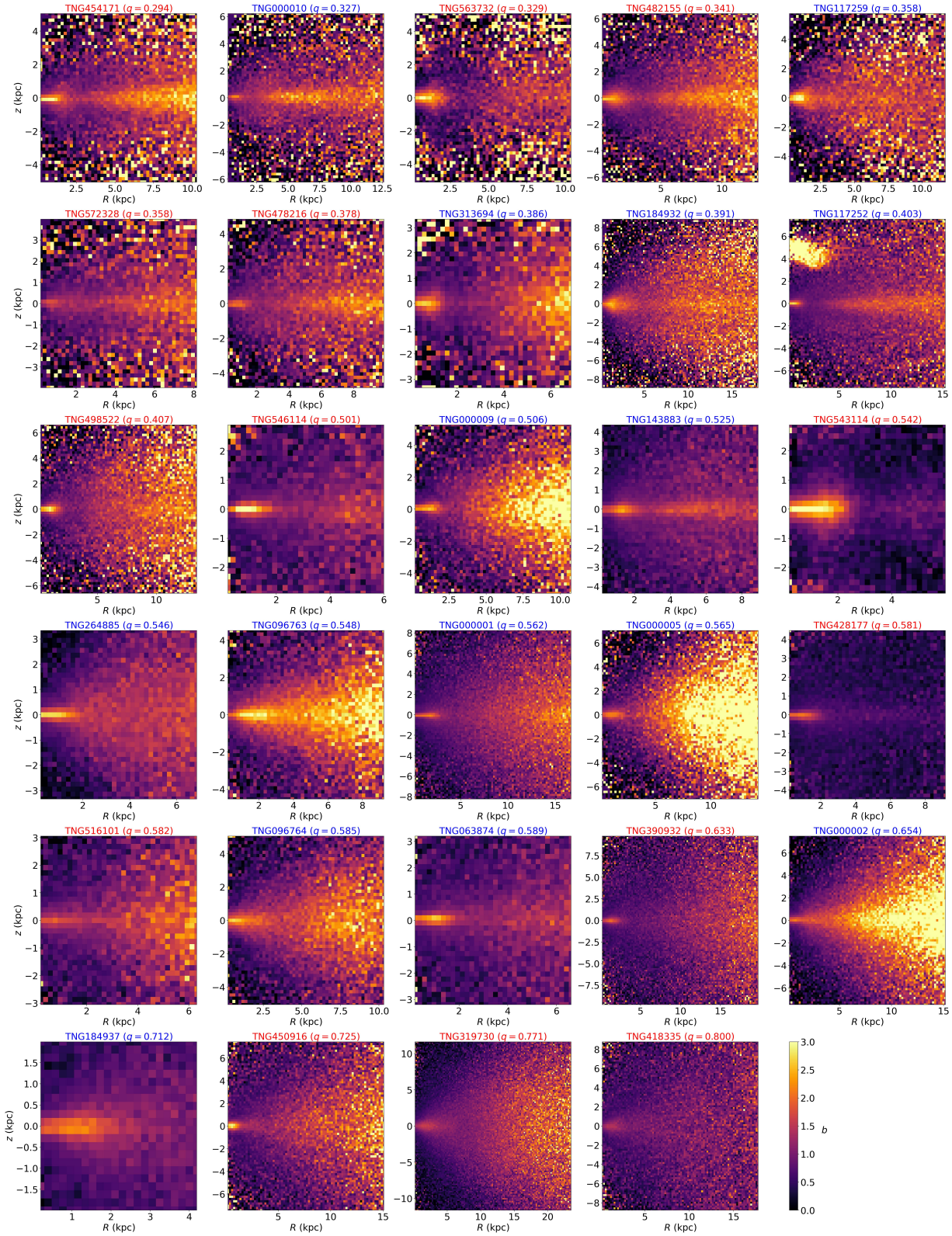


Figure 5.2. Maps on the (R, z)-plane of $b = \sigma_R^2/\sigma_z^2$ for all the 29 galaxies in our sample, sorted (from top-left to bottom-right) by their stellar minor-to-major semiaxes ratio q (written in brackets). Central galaxies have names colored in red, satellite galaxies in blue. For each galaxy, the box extends from 0 to $2r_{1/2}$ in the R direction, and from $-r_{1/2}$ to $r_{1/2}$ in the z direction.

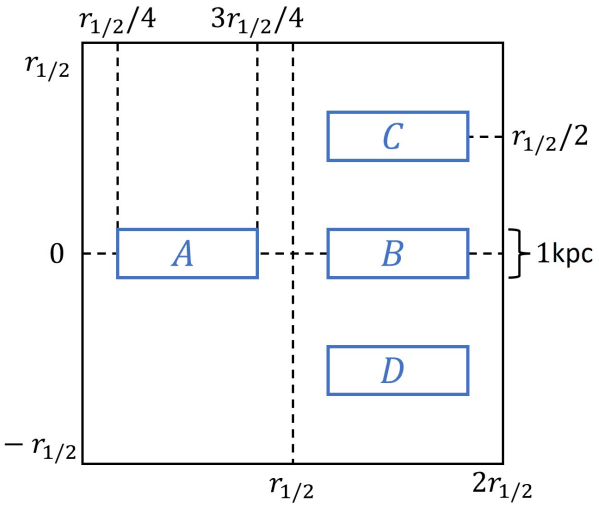


Figure 5.3. Regions A, B, C and D over a box of $2\,r_{1/2}$ side on the (R, z)-plane. The extension of all the regions is $r_{1/2}/2$ in the R direction, and 1 kpc (i.e., the dimension of two pixels) in the z-direction.

half-mass radii. Concerning possible environmental effects, we see that central (triangles) and satellite (squares) galaxies do not occupy specific regions of the diagrams, so that no correlations between the shape of the b field and the "status" of the galaxy seem to be present. However, as apparent from the bottom-right panel of the Figure, galaxies in richer halos tend to have lower values of s_R and higher values of s_z, meaning that their b is higher at outer radii, and has a strip-like shape.

5.3.1 Comparison with theoretical and empirical results

As already discussed in Section 4.1.5, starting from the analysis of the effects of the b-anisotropy in different one and two-component models, there exists a clear and general trend between the maximum value of supported b and the stellar minor-to-major axial ratio q, such that galaxies with a more flattened stellar density distribution support a larger amount of b anisotropy. As this trend has been retrieved also from Schwarzschild modeling and JAM of real elliptical galaxies (see Section 1.4), and then by applying JAM to realistic mock galaxies (Wang, Cappellari, and Peng 2021), it would be interesting to see whether the systems in our sample satisfy it as well; this may constitute an additional proof that the TNG50 galaxies (at least the most axisymmetric ones) are sufficiently close to the realistic ones, also from a dynamical point of view.

In Figure 5.5, we plot the mass-weighted average b as a function of the stellar minor-to-major axial ratio q for all the galaxies in our sample. In this case, we do not see a global trend of decreasing $\langle b \rangle$ as a function of q. By looking at the first two panels of the Figure, we also see that

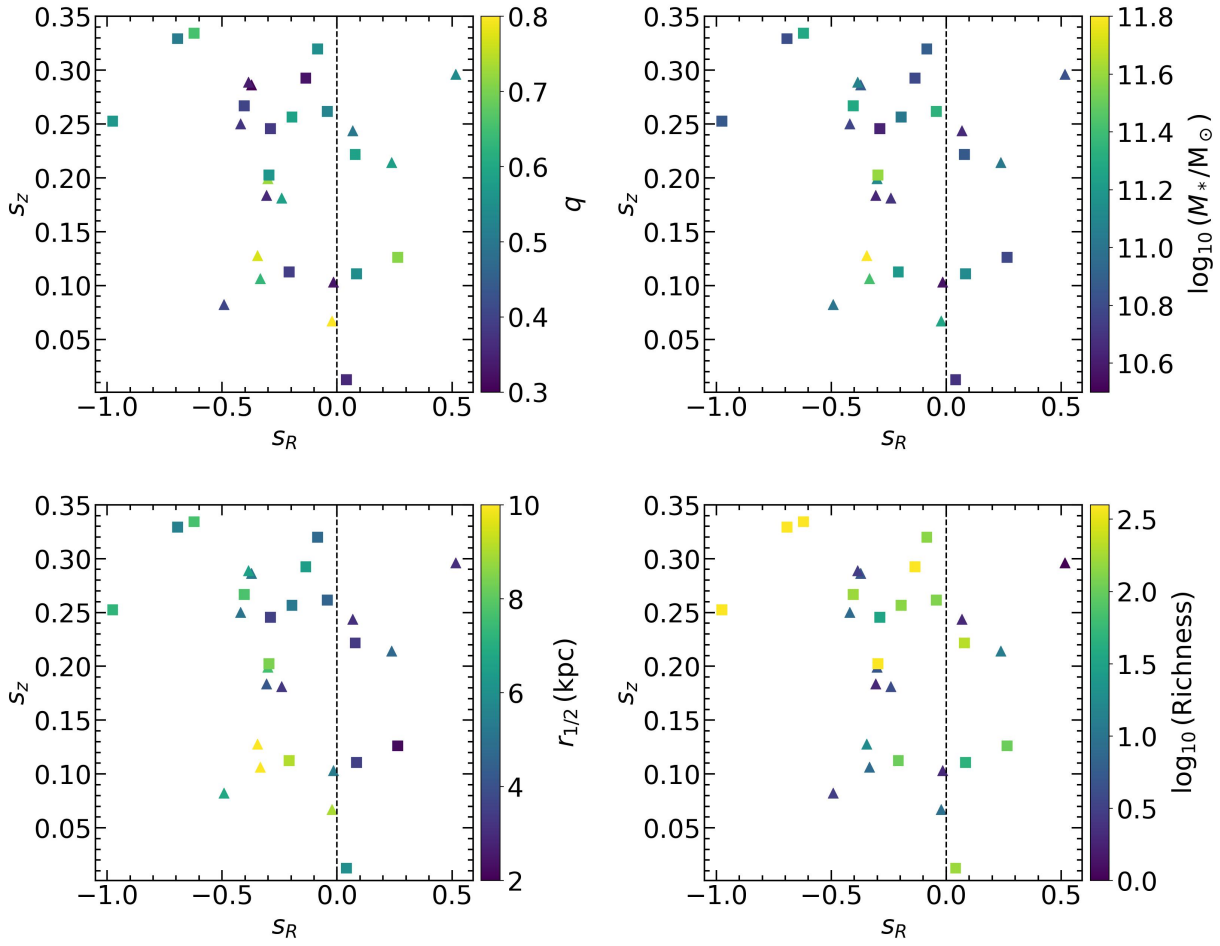


Figure 5.4. Parameters s_R and s_z for all the 29 galaxies of the sample, color-coded by their stellar minor-to-major semiaxes ratio q (top-left panel), stellar mass M_* (top-right panel), stellar half-mass radius $r_{1/2}$ (bottom-left panel) and parent cluster's richness (here in logarithmic scale, bottom-right panel). Central galaxies are identified with triangles, satellite galaxies with squares.

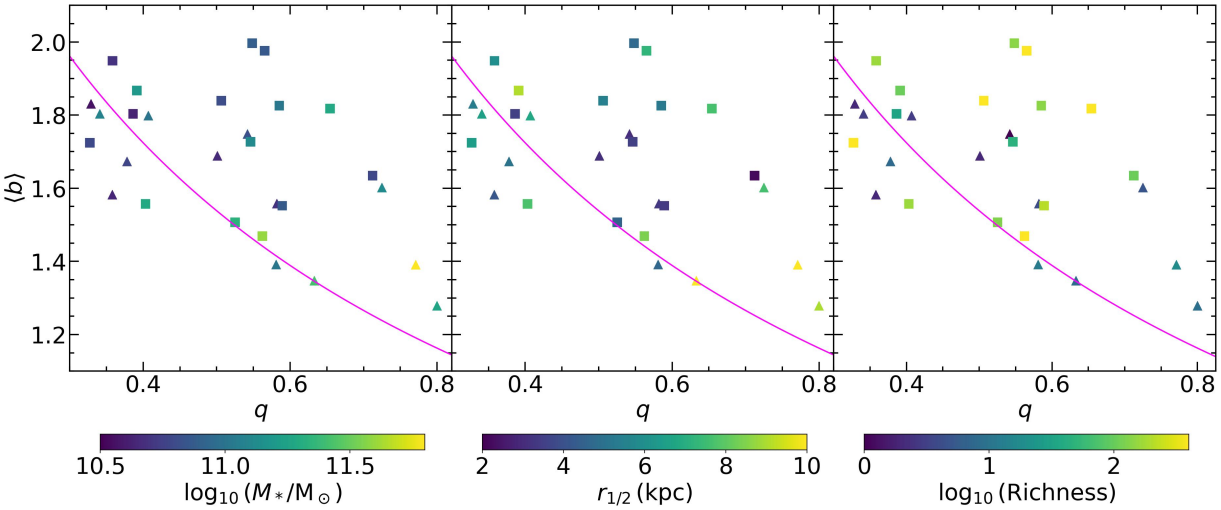


Figure 5.5. Mass-weighted average b as a function of the stellar q for the 29 galaxies in our sample. From left to right, galaxies are color-coded by stellar mass, stellar half-mass radius and cluster richness (here in logarithmic scale). In all the panels, central galaxies are represented by triangles, while satellite by squares; the magenta line is the relation $b = 1/(0.3 + 0.7\,q)$ (see Cappellari, Emsellem, Bacon, et al. 2007).

no trend with the stellar mass or the stellar half-mass radius of the galaxy is apparent, apart from the fact that the less massive and more compact galaxies have higher values of b. Concerning possible environmental effects, we see that no distinction between central and satellite galaxies is present; however, from the right panel of the Figure, we see that galaxies in richer halos have higher values of b. Another interesting point is that, apart from a few galaxies, the majority of our systems lie above the curve $b = 1/(0.3 + 0.7\,q)$ (i.e., the "magenta line"), which we recall to be originally obtained as an empirical limit on the anisotropy parameter β_z for the regular rotators in the SAURON integral-field survey (see Section 1.4). Therefore, at least from this preliminary analysis, we conclude that the selected galaxies can be properly described as three-integral axisymmetric systems with a cylindrically aligned velocity dispersion ellipsoid, but the shape of the latter, apart from being anisotropic (as $\sigma_R > \sigma_z$), remains dubious. The distribution of $\langle \gamma_\varphi \rangle$ in Figure 5.1 suggests an oblate velocity dispersion ellipsoid, as these values are not so distant from zero for almost all the systems; however, if this is the case, the deviations from the magenta line - which is obtained by assuming an oblate velocity dispersion ellipsoid - would remain unclear, so that further analysis is needed. Also, no apparent distinction between the behavior of satellite and central galaxies is present, although the former are the most subject to impactful merging events, while the latter are often characterized by a more gradual form of evolution (e.g., through "cannibalism" of other galaxies), which should affect less the distribution of the stellar orbits.

From a more theoretical point of view, in Figure 5.6 we plot the values of $\langle b \rangle$ and q of galaxies in our sample (black dots) over the critical b curves shown in Figure 4.13 for the ellipsoidal Sérsic model with different shape parameter n, and the ellipsoidal dV model in a SIS DM halo with different DM-to-stars mass ratios $\mathcal{R}$ (see Sections 4.1.3 and 4.2.2 for more details). At fixed q, we recall that $b > b_{\rm M}$ implies $\overline{v_\varphi^2} < 0$ somewhere inside $\mathscr{B}^-$, and so the model is physically inconsistent; instead, $b > b_0$ gives $\Delta_R < 0$ inside $\mathscr{D}^-$, so that the generalized Satoh (1980) decomposition in equation (3.7) can not be applied. We clearly see that $\langle b \rangle \leq b_{\rm M}$ for all the galaxies in our sample: this is reassuring, as we have already checked that the kinematics of these objects obeys well to the axisymmetric JEs of equation (2.33), and so the the positivity of $\overline{v_\varphi^2}$ should be satisfied. However, we also see that for the majority of the galaxies $\langle b \rangle \geq b_0$ as well, where the b_0 curves are almost independent of the specific properties of the models (even in those including a DM halo), and very close to the magenta line: as discussed in Section 4.1.5, these curves are very similar because galaxies with $\gamma_\varphi \approx 0$ (as constrained from observations) have $\overline{v_\varphi}^2 \geq 0$ if and only if $\Delta_R \geq 0$, a condition guaranteed by $b \leq b_0$. Therefore, given that all our galaxies are well described by the JEs in equation (2.33), we expect that Δ_R (or its mass-weighted average) is negative for the systems above the magenta line, i.e. they are mostly radially anisotropic. This point, which may reveal important details about the kinematic features of these mock axisymmetric elliptical galaxies, will be addressed in future work (see Section 6.4 for some perspectives).

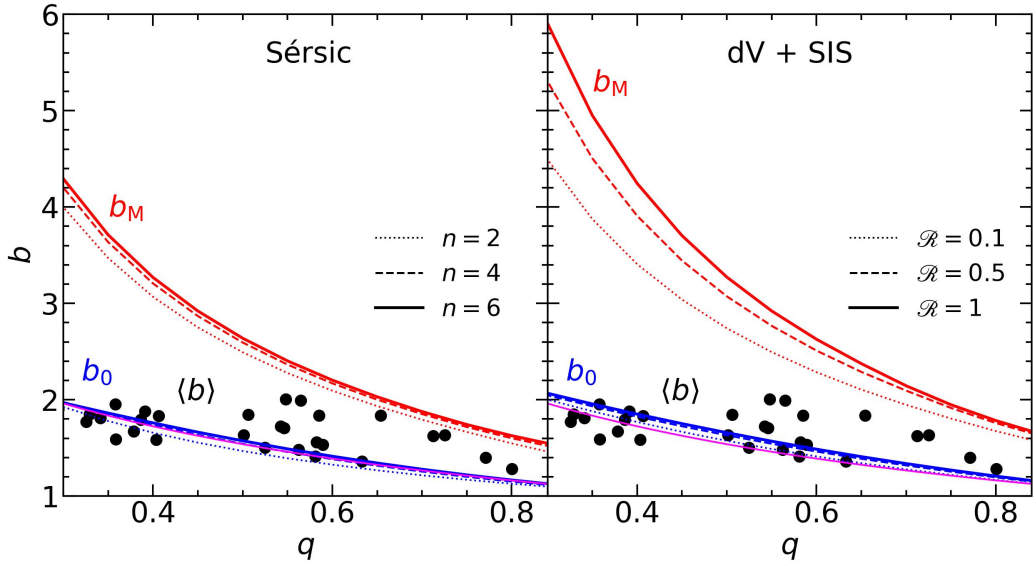


Figure 5.6. Mass-weighted average b as a function of the stellar minor-to-major semiaxes ratio q for the 29 galaxies in our sample (black dots), compared to the critical $b_{\rm M}$ and b_0 curves of the ellipsoidal Sérsic model for three different values of n (left panel), and the ellipsoidal dV model in a SIS DM halo for three different values of DM-to-stellar mass ratio $\mathcal{R}$ (see Figure 4.13). In both the panels, the magenta line $b = 1/(0.3 + 0.7\,q)$ (see Cappellari, Emsellem, Bacon, et al. 2007) is shown.

CHAPTER 6

Summary and conclusions

The kinematic properties of galaxies are recovered for samples of ever-growing size and increasing quality thanks to the recent large IFS surveys such as ATLAS3D (Cappellari et al. 2013), SAMI (Scott et al. 2015) and MaNGA (H. Li et al. 2018), and more sophisticated data analysis and modeling techniques. In this context, the JEs are one of the standard tools for studying the stellar dynamics of galaxies, and to extract physically relevant information from observations (e.g. Cappellari 2016, Zhu et al. 2023, Surti et al. 2024). In order to close the system of equations through a phenomenologically motivated relation, a widely used choice is the so-called b-ansatz, introduced in Cappellari (2008) and then used in the Jeans modeling of axisymmetric galaxies classified as regular rotators and stellar disks (see e.g. Cappellari 2016 for a review).

In this thesis, we first provided a general discussion on how the b-ansatz affects the solution of the JEs, being able to predict, a priori from solving the JEs, the qualitative features of the resulting kinematic fields for different choices of b. In this way, as a function of the structural properties of the model under investigation, we can constrain the values of b that assure the positivity of the azimuthal velocity field $\overline{v_\varphi^2}$, necessary for model consistency, and of Δ_R and Δ, which are used for the well-known Satoh (1980) decomposition of $\overline{v_\varphi^2}$ into its ordered and dispersion components. Then, by discussing some disky and ellipsoidal axisymmetric models, we applied this general procedure to some realistic case studies, understanding if and how the b-anisotropy is connected to the properties of a galaxy, as its flattening, shape, or DM-to-stellar

mass ratio. We verified that all our general results apply, being able for each model to compute (analytically or numerically) the regions of the (R, z)-plane where the kinematic fields change by varying the amount of anisotropy, and what are the constraints on b to ensure their positivity; moreover, we retrieved from a theoretical point of view the empirical trend such that galaxies with a more flattened stellar density profile support a larger amount of b-anisotropy, finding how this is almost independent of the specific model involved. Also, we extended this analysis to systems with the commutator-like operator $[\rho_*, \Phi] < 0$ (a situation which occurs for ellipsoidal prolate galaxies), proving that a fully general understanding of the effects of the b-anisotropy on the kinematics is possible for these systems too. Finally, we conducted a first, exploratory analysis of the b-anisotropy in galaxies produced by a cosmological magneto-hydrodynamical simulation, choosing TNG50 for its high baryon mass resolution and large amount of sufficiently massive galaxies (similar to the observed ETGs). Selecting a restricted sample of massive, passive and very axisymmetric galaxies from the snapshot at $z = 0$, we verified that these galaxies can be modeled sufficiently well through the three-integral JEs with a cylindrically aligned velocity dispersion ellipsoid, and $b = \sigma_R^2/\sigma_z^2$ generally greater than unity (i.e., $\sigma_R > \sigma_z$). However, we found out that a trend between the amount of b-anisotropy and the stellar density flattening is not apparent, and the shape and values of the b field do not correlate clearly with the properties of the galaxies and their environment. This suggests that the kinematics of the very axisymmetric galaxies in our sample may differ from that of the observed "regular rotators", but further analysis is need to assess the robustness of our results.

The main results of this thesis are listed below, divided for simplicity into three representative categories: general effects of the b-ansatz on the stellar kinematics (see Chapter 3), results from axisymmetric models (see Chapter 4), and properties of the b-anisotropy in simulated TNG50 galaxies (see Chapter 5).

6.1 Effects of the b-ansatz on the stellar kinematics

- We obtained the general expressions, as a function of b and of the ansatz-independent quantities, for $\overline{v_\varphi^2}$ and the related functions $\Delta_R = \overline{v_\varphi^2} - \sigma_R^2$ and $\Delta = \overline{v_\varphi^2} - \sigma_z^2$. These general expressions are fundamental to investigate the positivity of $\overline{v_\varphi^2}$, required for the model consistency, and of Δ_R and Δ, necessary for the Satoh (1980) decomposition and its variants. Also, they allow to predict, before solving the JEs, the trends of $\overline{v_\varphi^2}$, Δ and

Δ_R as a function of b throughout the galaxy, thus avoiding a time-consuming numerical exploration of the parameter space in the modeling procedure; in particular, for increasing b, $\overline{v_\varphi^2}$ and Δ increase in the region $\mathscr{B}^+$ and decrease in $\mathscr{B}^-$, while Δ_R increase in $\mathscr{D}^+$ and decrease in $\mathscr{D}^-$.

- For systems with $\partial\Phi/\partial R \geq 0$ everywhere (the common situation) and $b = b(z)$ (which includes the widely used constant b case), we discussed the positivity problem in full generality: we first showed how to determine the ansatz-independent regions of the (R, z)-plane where negativity is possible, i.e. $\mathscr{B}^-$ for $\overline{v_\varphi^2}$, $\mathscr{D}^-$ for Δ_R and a more complicate intersection of $\mathscr{B}^\pm$ and $\mathscr{C}^\pm$ for Δ. Then, we showed how to determine the limiting values of $b(z)$ that guarantee positive kinematic fields over these regions: $b_{\rm M}(z)$ for $\overline{v_\varphi^2}$, $b_0(z)$ for Δ_R, and $b_1(z)$ and $b_2(z)$ for Δ.

- For all the systems, $\mathscr{B}^- \subseteq \mathscr{D}^-$, and $b_{\rm M}(z) \geq b_0(z)$ for $z \in {\rm Pr}(\mathscr{B}^-)$. In the common case of $[\rho, \Phi] \geq 0$ everywhere (as for oblate self-gravitating systems), one has $\mathscr{B}^- \subseteq \mathscr{C}^+$ and $\mathscr{C}^- \subseteq \mathscr{B}^+$; moreover, $b_1(z) \leq 1$ for $z \in {\rm Pr}(\mathscr{C}^-)$, and $1 \leq b_0(z) \leq b_2(z) \leq b_{\rm M}(z)$ for $z \in {\rm Pr}(\mathscr{B}^-)$. If $[\rho, \Phi] = 0$ (as for spherical self-gravitating systems), then $\mathscr{B}^- \equiv \mathscr{C}^+$ and $\mathscr{C}^- \equiv \mathscr{B}^+$, and $b_0 = b_1 = b_2 = 1$ independently of z. Finally, if $[\rho, \Phi] < 0$ (as for prolate self-gravitating systems), $\mathscr{B}^+ \subseteq \mathscr{C}^-$ and $\mathscr{C}^+ \subseteq \mathscr{B}^-$; also, $b_0(z) \leq 1$ for $z \in {\rm Pr}(\mathscr{D}^-)$, $b_1 = +\infty$ for $z \in {\rm Pr}(\mathscr{B}^+)$, and $b_2 = 0$ for $z \in {\rm Pr}(\mathscr{C}^+)$.

6.2 Results from axisymmetric models

- The shape of the $\mathscr{B}^\pm$, $\mathscr{C}^\pm$ and $\mathscr{D}^\pm$ regions, where $\overline{v_\varphi^2}$, Δ_R, and Δ become negative for b values failing to satisfy the constraints, can all be obtained analytically or numerically, depending on the specific models. For the models here investigated (except for the Binney logarithmic halo, see Appendix D), $\mathscr{D}^-$ coincides with the (R, z)-plane independently of the model parameters; it is also shown that for oblate ellipsoidal systems these properties holds under quite weak and natural assumptions, so we conclude that these properties and their implications can be safely applied also to different (oblate) galaxy models. For all the models, $\mathscr{B}^-$ is adjacent to the equatorial plane, and $\mathscr{C}^-$ contains the z-axis; if $[\rho, \Phi] \geq 0$, then $\mathscr{B}^- \subseteq \mathscr{C}^+$ and $\mathscr{C}^- \subseteq \mathscr{B}^+$, while if $[\rho, \Phi] < 0$, then $\mathscr{B}^+ \subseteq \mathscr{C}^-$ and $\mathscr{C}^+ \subseteq \mathscr{B}^-$. Also, these regions have remarkably similar shapes for the different one and two-component

models here explored, meaning that the behavior of the fields by changing the b-anisotropy is practically the same independently of the specific (e.g. disky or ellipsoidal) density profile.

- By analytically or numerically solving the JEs, we illustrated how the kinematic fields change over the galaxy as a function of b, for simplicity assumed as spatially constant. The results are in agreement with the general considerations, both for their trend with b, and for the regions where they become negative, confirming the utility of our preliminary analysis. The limits on $b(z)$ (i.e., $b_{\rm M}$, b_0, b_1 and b_2) can all be determined analytically or numerically, depending on the specific model, and the relations between these limits obtained from general considerations hold.

- Among all the model parameters, the flattening of the stellar density distribution has the most relevant effect on determining both the shape of the critical regions, and the values of the limits for b. More flattened models are able to sustain larger b-anisotropy (i.e., all the critical b values increase for increasing galaxy flattening), and their $\mathscr{B}^-$ regions, where $\overline{v_\varphi^2}$ can become negative, shrink towards the equatorial plane. In two-component models, the presence of a more or less dominant DM halo clearly conditions the values of the kinematic field, making them higher (in absolute value), and in general it also allows for a larger anisotropy, increasing for increasing DM-to-stellar mass ratio; however, we found out that this latter effect is smaller than that produced by an increasing stellar density flattening, suggesting that the b-anisotropy may be more sensitive to this property of the galaxy. Finally, for all the models here discussed, the specific stellar density profile appears to have a very minor effect in determining both the overall shape of the critical regions and the critical b values.

- Models with $[\rho, \Phi] < 0$ also allow for a fully general understanding of how the b-anisotropy affects the stellar kinematic fields. All the general considerations concerning the relative position of the $\mathscr{B}^\pm$ and $\mathscr{C}^\pm$ regions hold, as well as the relations between the limits for b. Given that $b_0 < 1$, $b_1 = +\infty$ and $b_2 = 0$ independently of the model parameters, $\Delta_R < 0$ in the two-integral case, and $\Delta < 0$ somewhere independently of the values of b. Also, models with $[R\,\rho, \Phi] < 0$ (as those with too high $q > 1$) have $b_{\rm M} < 1$, so that they do not exist in the two-integral case; however, for sufficiently small values of $b < b_{\rm M}$ (i.e., by increasing σ_z with respect to σ_R) they become consistent at least at the level of the JEs.

- The sign of the commutator plays a crucial role in determining the properties of both the critical regions and the limits for b. In fact, there is a continuum between models with positive, zero and negative commutator such that the regions $\mathscr{B}^-$ and $\mathscr{C}^-$ become monotonically larger, overlapping in the spherical limit, and the limits $b_{\rm M}$ and b_0 become monotonically smaller, with $b_0 = b_1 = b_2 = 1$ in the spherical limit. Instead, b_1 and b_2 transition from 1 to, respectively, $+\infty$ and 0 as the commutator becomes negative.

6.3 The b-anisotropy in TNG50 galaxies

- For all the 29 galaxies in our sample, we find that $\overline{v_R} \approx \overline{v_z} \approx 0$, $\overline{v_R v_z}$ is significantly lower than the other velocity fields, and in general $\sigma_R \neq \sigma_z$; this means that these systems are well modeled by the axisymmetric, three-integral JEs with the velocity dispersion ellipsoid aligned in cylindrical coordinates. This result is also confirmed by visually inspecting the left- and right-hand sides of the JEs, which are computed numerically.

- The $b = \sigma_R^2/\sigma_z^2$ field is in general greater than unity, proving that our galaxies can not be described as systems supported by a two-integral DF. Also, b is not spatially constant, and in the majority of the galaxies the largest b values extend out of the central region in a conical shape around the equatorial plane. However, at least for the galaxies in our sample, the specific shape of the b field do not correlate clearly with the properties of the system and its environment. The only plausible results are that galaxies with the most massive and extended stellar component all support larger b-anisotropy at outer radii than close to the origin, as the galaxies in richer clusters.

- In general, the mass-weighted average b of the selected galaxies does not correlate with the flattening of the stellar density profile, and most of the systems are located above the empirical "magenta line" (see Cappellari, Emsellem, Bacon, et al. 2007). This contrasts with a trend that has been empirically obtained from dynamical modeling of real (see e.g. Cappellari 2016) and mock (Wang, Cappellari, and Peng 2021) galaxies, and then discussed from a more theoretical perspective for realistic ellipsoidal galaxies (see Section 4.1.5). The result seems independent of the properties of the systems, although galaxies in richer halos tend to have larger values of b-anisotropy.

- Taken all together, our findings suggest that massive, passive and axisymmetric elliptical

galaxies in TNG50 can be modeled as three-integral systems with a cylindrically aligned velocity dispersion ellipsoid, with $\sigma_R > \sigma_z$. However, the shape of the velocity dispersion ellipsoid remains dubious, as the deviations from the magenta line - obtained by assuming an oblate velocity dispersion ellipsoid - remain unclear, so that further analysis is needed. Also, no apparent distinction between the behavior of satellite and central galaxies is present, although the former are the most subject to impactful merging events, while the latter are often characterized by a more gradual form of evolution (e.g., through "cannibalism" of other galaxies), which should affect less the distribution of the stellar orbits.

- By comparison with our previous models, we see that all the values of $\langle b \rangle$ for the galaxies in our sample lie below the $b_{\rm M}$ curves: this is reassuring, as we checked that the kinematics of these objects obeys well to the axisymmetric JEs of equation (2.33), and so the the positivity of $\overline{v_\varphi^2}$ should be satisfied. However, we also see that only for some of the galaxies $\langle b \rangle \leq b_0$ as well, where the b_0 curves are almost independent of the specific properties of the models (even in those including a DM halo). Therefore, we expect that systems above the magenta line have a negative Δ_R (or its mass-weighted average), and so are mostly radially anisotropic. If confirmed, this may reveal important details about the kinematic features of these mock axisymmetric elliptical galaxies.

6.4 Perspectives

Although a general understanding of how the b-anisotropy affects the kinematical fields resulting from the solution of the JEs has been reached within this thesis, some additional aspects still need to be explored. First, the analysis based on the TNG50 simulation is just preliminary, and a thorough study of the $\Delta_R = \overline{v_\varphi^2} - \sigma_R^2$ field for the selected systems could explain why they position above the magenta line. Second, it is still to be checked whether relaxing the selection criteria on mass (i.e., $10^{10.5} \leq M_*/\mathrm{M}_\odot \leq 10^{12}$) and axisymmetry (i.e., differences between the intermediate and the major semiaxes smaller than 5%), as well as the size of the regions where all the mass-weighted averages have been computed (i.e., inside two stellar half-mass radii), may change the results significantly or not. Also, although from the analysis of two-component axisymmetric models we know that the presence of the halo increase the limits for b, the effects of the DM halo have not been investigated so far, as we limited the discussion to possible correlations between

b and the properties of the stellar components. Moreover, comparing our results with those obtained from a different simulation (e.g. TNG100), or by using a Voronoi-based tassellation to keep constant the signal-to-noise ratio in the maps (see e.g. Walo-Martín et al. 2020), may reveal if and how much different (mass and numerical) resolution and galaxy population affect the observed trends. Finally, repeating the analysis at different simulated redshifts could allow us to understand how the properties of b-anisotropy are connected to the evolutionary path of the galaxy, possibly finding some explanation of this phenomenological assumption.

Concerning the more theoretical analysis, a deep understanding of the dynamics of prolate galaxies in presence of b-anisotropy is missing, even though, at the level of the JEs, we proved that a general discussion on the behavior of the fields and the limits for b is possible. In Congera (2025), an analysis is carried out for two-integral models, but this could be extended to anisotropic models where $\overline{v_\varphi^2} > 0$ for small values of $b < 1$; this may find some applications for interpreting the kinematics of prolate galaxies observed through IFS surveys. Also, we could look for the existence of anisotropic prolate systems in cosmological simulations, discussing their different intrinsic kinematics and checking whether our theoretical predictions on orbital anisotropy are satisfied or not.

Finally, our whole analysis could be repeated for other ansatz which are able to close the system of the JEs, such as the "μ-ansatz" presented in Appendix B. We still lack an understanding of how they affect the stellar kinematics resulting from solving the equations, and what are the similarities and differences compared to the more used b-ansatz. The results of this analysis may make alternative ansatz more advantageous in dynamical modeling of galaxies, and so suggest their possible implementation in numerical codes used for the analysis of more extended samples of observed galaxies.

All these steps, addressable in future work, may shed more light on the connection between stellar dynamics and the properties of galaxies, revealing important details on the formation and evolution of these systems across cosmic time.

ACKNOWLEDGMENTS

I dedicate this thesis to the people that I met over these years, and who have shown me how science, as the other disciplines practiced by human beings, is a context for reflecting on our place in the World, and discovering ourselves.

To Mom and Dad, who believed in my choices and supported me consistently in facing the small and large challenges of life.

To Grandma Anna and my relatives, who showed me the value of simplicity and small things, and the importance of sharing.

To Federica, Gianluigi, Giovanni, Özlem, Rachele and Veronica, with whom I shared my feelings, emotions and the many, sparkling nuances of our existence.

To Ambra, Annalisa, Fabio, Franco, Guido, Paola, Luisa, Rosetta and the community of people who embody my "extended family" in Bologna, and with whom I rebuilt a dimension of everyday life.

To Alberto, Luca and Silvia, wise guides who taught me to think scientifically, and to study the phenomena of the Cosmos with passion and enthusiasm.

To Giulia and Mattia, research companions with whom I have the pleasure of collaborating, and sharing the discovery of novelty also in a human sense.

To Andrea, Maarten, Nele and the people I met in Ghent, with whom I experienced, in a family atmosphere, new cultures and approaches to live the academic and non-academic world.

To Fabrizio, Olivia and Sara, people of great cultural and human value with whom to explore new horizons of meaning, through the gaze of complexity.

To Bartolo, Elena, Gabriele and the members of the "Cosmic Roots" project, with whom I created an invisible bridge between our Planet and the Universe, appreciating the beauty of our diversity.

To Daniele, friend and adventure companion with whom I founded the "Pescara-Scienza" festival, bringing science closer to people and returning our experience to our hometown.

To those who are no longer here, who have brought me closer to the inscrutable mystery of death, and encourage me day after day to invest in the only life I am certain of.

To those who, like a comet, shine unexpectedly in my life, illuminating it with amazement

and wonder, giving me the motivation to continue growing and imagining a better future.

RINGRAZIAMENTI

Dedico questa tesi alle persone che ho incontrato nel corso di questi anni, e che mi hanno dimostrato come la scienza, al pari delle altre discipline praticate dall'uomo, sia un contesto per riflettere sul nostro posto nel Mondo, e scoprire noi stessi.

A Mamma e Papà, che hanno creduto nelle mie scelte e mi hanno sostenuto con costanza nell'affrontare le piccole e grandi sfide della vita.

A Nonna Anna e ai miei familiari, che mi hanno mostrato il valore della semplicità e delle piccole cose, e l'importanza della condivisione.

A Federica, Gianluigi, Giovanni, Özlem, Rachele e Veronica, con cui ho condiviso i miei sentimenti, le mie emozioni e le tante, scintillanti sfumature della nostra esistenza.

Ad Ambra, Annalisa, Fabio, Franco, Guido, Paola, Rosetta e la comunità di persone che a Bologna incarna la mia "famiglia allargata", e con cui sono riuscito a ricostruire una dimensione di quotidianità.

Ad Alberto, Luca and Silvia, sapienti guide che mi hanno insegnato a pensare criticamente, e a studiare i fenomeni del Cosmo con passione ed entusiasmo.

A Giulia e Mattia, compagni di ricerca con cui ho il piacere di collaborare, e condividere la scoperta della novità anche in senso umano.

A Andrea, Maarten, Nele e le persone che ho incontrato a Ghent, con cui ho sperimentato, in un clima familiare, nuove culture e approcci di vivere la realtà accademica e non.

A Fabrizio, Olivia e Sara, persone di grande valore culturale e umano con cui esplorare nuovi orizzonti di senso, attraverso lo sguardo della complessità.

A Bartolo, Elena, Gabriele e i membri del progetto "Radici Cosmiche", con cui ho creato un ponte invisibile tra il nostro Pianeta e l'Universo, apprezzando la bellezza della nostra diversità.

A Daniele, amico e compagno di avventure con cui ho fondato il festival "Pescara-Scienza", avvicinando la scienza alle persone e restituendo la nostra esperienza alla nostra città d'origine.

A chi non c'è più, che mi ha avvicinato al mistero imperscrutabile della morte, e mi sprona giorno dopo giorno a investire nell'unica vita di cui ho certezza.

A chi, come una cometa, brilla inaspettatamente nella mia vita illuminandola di stupore e meraviglia, dandomi la motivazione per continuare a crescere e immaginare un futuro migliore.

APPENDIX A

Mathematical background

In this Appendix, we give some details about the special functions which are used in the models here discussed, and may be useful for the computation of the kinematic quantities of our interest. Among the classical references on this topic, we mention Prudnikov, Brychkov, Marichev, et al. (1990), Arfken and Weber (2005) and Gradshteyn et al. (2007).

A.1 Gamma-related functions

The widely-used Euler Gamma function is defined as

$$\Gamma(x) = \int_0^\infty t^{x-1} e^{-t} dt, \quad x > 0; \tag{A.1}$$

some special values of this function are $\Gamma(1) = \Gamma(2) = 1$, and $\Gamma(1/2) = \sqrt{\pi}$. Integration by parts of equation (A.1) shows that the function satisfies the recursive relation

$$\Gamma(x+1) = x\,\Gamma(x). \tag{A.2}$$

Other important relations are

$$\frac{\Gamma(x)}{\Gamma(x/2)} = \frac{2^{x-1}}{\sqrt{\pi}} \Gamma\left(\frac{x+1}{2}\right), \tag{A.3}$$

and the so-called Stirling expansion

$$\Gamma(x) \sim \sqrt{2\pi}\, x^{x-1/2}\, e^{-x}, \quad x \to \infty. \tag{A.4}$$

Two functions associated with the Gamma function and which are quite often encountered are the incomplete left and right Gamma functions, defined as

$$\gamma(a,x) = \int_0^x t^{a-1}\, e^{-t}\, dt, \quad \Gamma(a,x) = \int_x^\infty t^{a-1}\, e^{-t}\, dt; \tag{A.5}$$

the function $\gamma(a,x)$ exists for $a > 0$, and in this case $\gamma(a,x) + \Gamma(a,x) = \Gamma(a)$. These functions also obey the following recursive relations:

$$\gamma(a+1,x) = a\,\gamma(a,x) - x^a\, e^{-x}, \quad \Gamma(a+1,x) = a\,\Gamma(a,x) + x^a\, e^{-x}. \tag{A.6}$$

The Euler Beta function is defined for real arguments $x > 0$ and $y > 0$ as

$$\mathrm{B}(x,y) = \int_0^1 t^{x-1}\,(1-t)^{y-1}\, dt, \tag{A.7}$$

from which it is possible to show that $\mathrm{B}(x,y) = \mathrm{B}(y,x)$. The link between the Beta and the Gamma functions is

$$\mathrm{B}(x,y) = \frac{\Gamma(x)\Gamma(y)}{\Gamma(x+y)}. \tag{A.8}$$

Analogously to the incomplete Gamma function, the incomplete Beta function can be defined as

$$\mathrm{B}_x(p,q) = \int_0^x t^{p-1}\,(1-t)^{q-1}\, dt, \tag{A.9}$$

where $\mathrm{B}_1(p,q;1) = \mathrm{B}(p,q)$, and the function is not symmetric under the exchange between p and q. A common expansion is

$$\mathrm{B}_x(p,q) \sim \frac{x^p}{p} + \frac{(1-q)\, x^{1+p}}{1+p}, \quad x \to 0. \tag{A.10}$$

A.2 Hypergeometric functions

Among the special functions, the Gauss hypergeometric functions have a preeminent role. They were originally introduced as the power series with convergence radius equal to 1

$$ {}_2\mathrm{F}_1(a,b;c;z) = 1 + \frac{ab}{c}z + \frac{a(a+1)b(b+1)}{c(c+1)}\frac{z^2}{2!} + \ldots \quad c \neq 0,-1,-2,..., \tag{A.11} $$

with ${}_2\mathrm{F}_1(a,b;c;0) = 0$ and ${}_2\mathrm{F}_1(a,b;c;z) = {}_2\mathrm{F}_1(b,a;c;z)$. Its integral representation, instead, is

$$ {}_2\mathrm{F}_1(a,b;c;z) = \frac{\Gamma(c)}{\Gamma(b)\Gamma(c-b)}\int_0^1 t^{b-1}\,(1-t)^{c-b-1}\,(1-zt)^{-a}\,dt, \quad c > b > 0. \tag{A.12} $$

As well known, a large part of elementary and higher transcendental functions can be expressed by using the hypergeometric functions for special values of the parameters, and an impressive umber of identities, transformations and recursive relations are known. Among these, the following connects the incomplete Beta function to ${}_2\mathrm{F}_1$:

$$ \mathrm{B}(p,q;x) = p^{-1}\,x^p\,{}_2\mathrm{F}_1(p,1-q;p+1;x), \tag{A.13} $$

Finally, the ${}_2\mathrm{F}_1$ functions are generalized to the ${}_p\mathrm{F}_q$ functions, and further to the Meijer G-functions and to the even more general family of Fox H-functions (see e.g. Mathai, Saxena, and Haubold 2009); however, we do not discuss them further in this context.

A.3 Bessel functions

The Bessel functions of the first (J_μ) and second (Y_μ) types are the two independent solutions of the following second-order, linear differential equation:

$$ \frac{1}{x}\frac{d}{dx}\left(x\frac{dU}{dx}\right) + \left(1 - \frac{\mu^2}{x^2}\right)U = 0, \quad 0 \leq x < \infty, \tag{A.14} $$

where μ is a parameter which can assume complex values. These functions are special cases of the Gauss hypergeometric functions (Appendix A.2), and so they obey an impressive number of identities. Restricting to the case of $\mu = m$, where m is an integer, the following identities hold:

$$\mathrm{J}_{m-1}(x) + \mathrm{J}_{m+1}(x) = \frac{2\,m}{x}\,\mathrm{J}_m(x), \quad \mathrm{J}_{-m}(x) = (-1)^m\,\mathrm{J}_m(x), \tag{A.15}$$

and $\mathrm{J}_m(0) = 0$ for integer $m \neq 0$, while $\mathrm{J}_0(0) = 1$. Moreover,

$$\frac{d\mathrm{J}_m(x)}{dx} = \frac{\mathrm{J}_{m-1}(x) - \mathrm{J}_{m+1}(x)}{2}, \quad \frac{d\mathrm{J}_0(x)}{dx} = -\mathrm{J}_1(x), \tag{A.16}$$

where the last identity can be proved from the general one.

Here we also recall the family of modified Bessel function of the first (I_m) and second (K_m) kinds, which are obtained from the Bessel functions evaluated for purely imaginary arguments (see e.g. Arfken and Weber 2005), or as solutions of the following modified Bessel differential equation:

$$\frac{1}{x}\frac{d}{dx}\left(x\,\frac{dU}{dx}\right) - \left(1 + \frac{\mu^2}{x^2}\right) U = 0, \quad 0 \leq x < \infty. \tag{A.17}$$

Some of the most relevant and used identities are the following:

$$\mathrm{I}_{m-1}(x) - \mathrm{I}_{m+1}(x) = \frac{2\,m}{x}\,\mathrm{I}_m(x), \quad \mathrm{I}_{-m}(x) = \mathrm{I}_m(x), \tag{A.18}$$

and $\mathrm{I_m}(0) = 0$ for integer $m \neq 0$, while $\mathrm{I}_0(0) = 1$. Moreover,

$$\frac{d\mathrm{I}_m(x)}{dx} = \frac{\mathrm{I}_{m-1}(x) + \mathrm{I}_{m+1}(x)}{2}, \quad \frac{d\mathrm{I}_0(x)}{dx} = \mathrm{I}_1(x). \tag{A.19}$$

Finally,

$$\mathrm{K}_{m-1}(x) - \mathrm{K}_{m+1}(x) = -\frac{2\,m}{x}\,\mathrm{K}_m(x), \quad \mathrm{K}_{-m}(x) = \mathrm{K}_m(x), \tag{A.20}$$

$$\frac{d\mathrm{K}_m(x)}{dx} = -\frac{\mathrm{K}_{m-1}(x) + \mathrm{K}_{m+1}(x)}{2}, \quad \frac{d\mathrm{K}_0(x)}{dx} = -\mathrm{J}_1(x). \tag{A.21}$$

APPENDIX B

The μ-ansatz for the axisymmetric Jeans equations

We consider here a second family of ansatz which is required to close the system of the axisymmetric three-integral JEs presented in Section 2.3.2. We call it the "μ-ansatz", and priority is given to the relation between Δ_R and the unknown σ_R^2 as:

$$\Delta_R = \mu\,\sigma_R^2, \quad \overline{v_\varphi^2} = (1+\mu)\,\sigma_R^2, \tag{B.1}$$

with $\mu(R,z) \geq -1$. to guarantee the positivity of $\overline{v_\varphi^2}$. Given this choice, it is possible to solve in closed form the second JE, and obtain σ_R^2; in fact, putting equation (B.1) inside the second of equation (2.33) leads to a linear, non-homogeneous differential equation prone to an explicit solution, similar to that for anisotropic spherically symmetric systems (J. Binney and Mamon 1982, C21). Assuming that $\rho_*\sigma_R^2 \to 0$ at infinity, the solution of the equation reads

$$\rho_*\sigma_R^2 = \int_R^\infty \rho_*(u,z)\,\frac{\partial\Phi(u,z)}{\partial u}\,e^{-h(u,R,z)}\,du, \tag{B.2}$$

where

$$h(u,R,z) \equiv \int_u^R \frac{\mu(v,z)}{v}\,dv; \tag{B.3}$$

if μ is independent of R, we have:

$$\rho_* \sigma_R^2 = \frac{1}{R^\mu} \int_R^\infty \rho(u,z) \, \frac{\partial \Phi(u,z)}{\partial u} \, u^\mu \, du. \tag{B.4}$$

Clearly, once the JEs are solved, each adopted ansatz can be expressed in terms of the others. For example, the μ function associated to a b-ansatz is given by

$$\mu = \frac{\Delta_R}{b \, \sigma_z^2}, \tag{B.5}$$

further reducing to $\mu = \Delta/\sigma_z^2$ in the two-integral case, i.e. when $b = 1$ and $\Delta_R = \Delta$. Of course, if one adopts the μ-ansatz, the equivalent b function is just given by equation (3.1), where now σ_R^2 is computed as in equation (B.2).

An important advantage of using the μ-ansatz is that, from equation (B.2), $\sigma_R^2 \geq 0$ for realistic potentials with $\partial\Phi/\partial R \geq 0$, and so the condition $\mu \geq 1$ in the second of equation (B.1) automatically assures the positivity of σ_R^2 and $\overline{v_\varphi^2}$, without the need for complicated analytical or numerical checks. Therefore, the combination of the μ-ansatz with the generalized Satoh (1980) decomposition, or with the most general λ-decomposition, allows for a relatively simple and flexible solution of the JEs.

APPENDIX C

THE *WOLFRAM MATHEMATICA* CODE FOR THE SOLUTION OF THE JEANS EQUATIONS WITH THE b-ANSATZ

The solution of the axisymmetric, three-integral JEs with the b-ansatz, together with the determination of the critical regions and the physical limits for the b function, can be carried out analytically just for a limited amount of very simple (and often idealized) models. In all the other cases, the analysis must be carried out numerically, and a *Wolfram Mathematica* code has been specifically created for this purpose. This software package is sufficiently flexible to perform formal algebra (e.g., with the function `FullSimplify`), solve integrals numerically (e.g., with the function `NIntegrate`), finding minima and maxima of functions (e.g., with the functions `NMinimize`/`NMaximize`), and even plot the desired kinematic fields (e.g., with the functions `DensityPlot` and `ContourPlots`).

A scheme of the basic structure of the code is shown in Figure C.1. In practice, once the density profile of the model is given as an input (together with an external potential in the case of two-component models), the code first computes some ansatz-independent quantities, also solving the first JE, and then branches into two complementary parts. The first one carries out the determination of the critical $\mathscr{B}^-$, $\mathscr{C}^-$ and $\mathscr{D}^-$ regions where the $\overline{v_\varphi^2}$, Δ_R and Δ fields can

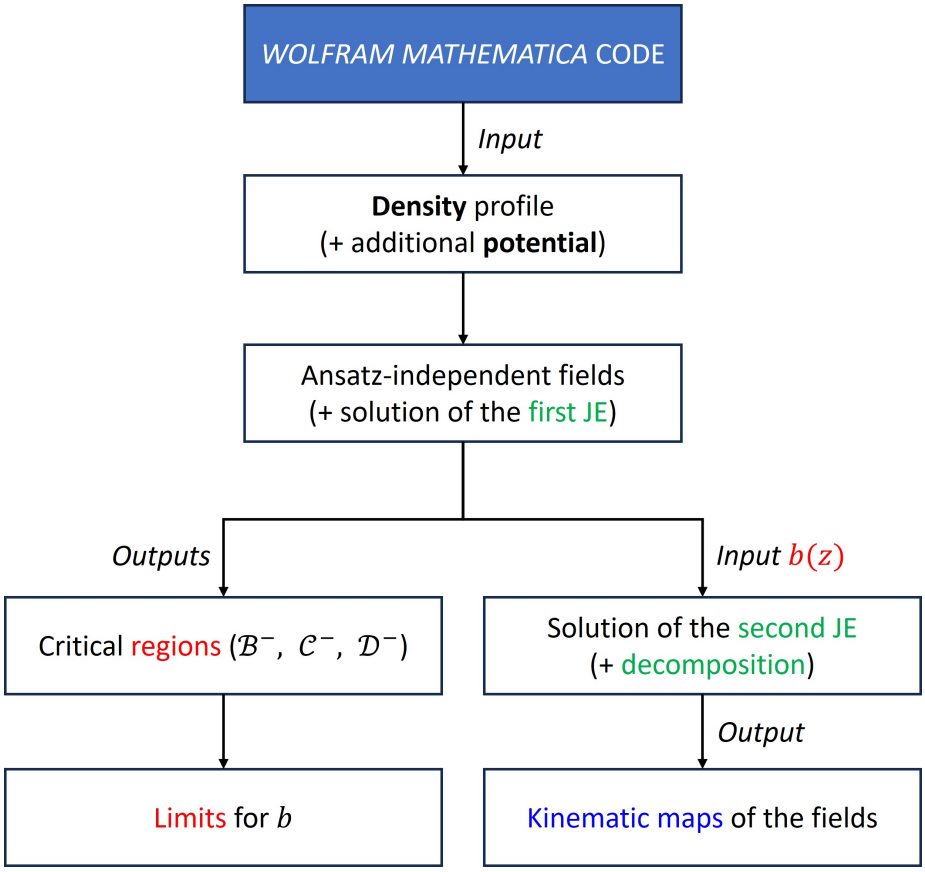


Figure C.1. Schematic representation of the structure of the *Wolfram Mathematica* code used for the numerical solution of the axisymmetric three-integral JEs with the b-ansatz.

become negative, and then it computes the limits for the b function which ensure the positivity of the fields in those regions. The second part, instead, is dedicated to the solution of the second JE with a generic $b(z)$ (or constant b) function, where the two-integral case is obtained simply by putting $b = 1$, together with the decomposition of $\overline{v_\varphi^2}$ with the approaches discussed in Sections 2.3.1 and 3.1.1; the kinematic maps of all the fields can be plotted, or exported as data files.

This Appendix is structured as follows. In Appendix C.1, we will discuss in more detail the different steps of the code; we are focusing for simplicity on a one-component stellar density profile both in the self-gravitating case, and considering an additional (more or less dominant) external gravitational potential. The case with two or more stellar density components is addressed in Appendix C.2 for two-integral systems (see also Caravita, Ciotti, and Pellegrini 2021 for more details). To get a copy of the code, or for any other information, please contact the Author.

C.1 Steps of the code

Stellar density and gravitational potential

The code takes as an input the axisymmetric stellar density profile $\rho_*(R, z)$ of the model, usually normalized to some appropriate units (e.g., mass over a scale length). If we assume an external potential $\Phi_{\rm ext}$, as that of a DM halo, the total gravitational potential of the model is

$$\Phi = \Phi_* + \Phi_{\rm ext}, \tag{C.1}$$

where all the fields can be normalized to appropriate units, with the physical dimension of a squared velocity. For some stellar density profiles, Φ_* can be given in analytical form, and so the derivatives can be explicitly computed. For finite-mass, axisymmetric ellipsoidal density distributions $\rho_*(m)$ of principal semiaxes a_*, $b_* = a_*$ and c_*, with

$$m \equiv \sqrt{\frac{R^2}{a_*^2} + \frac{z^2}{q^2\, a_*^2}}, \quad q \equiv \frac{c_*}{a_*}, \tag{C.2}$$

the gravitational potential is given by the Chandrasekhar (1969) formula (see also BT08, C21)

$$\Phi_*(R, z) = -G\,\pi\,q\,a_*^3 \int_0^\infty \frac{\Delta\Psi(\tau)}{(a_*^2 + \tau)\sqrt{q^2 a_*^2 + \tau}}\, d\tau, \tag{C.3}$$

where G is the gravitational constant, and we defined

$$\Delta\Psi(\tau) \equiv 2 \int_{\mathscr{M}(R,z,\tau)}^\infty \rho_*(t)\, dt, \quad \mathcal{M}(R, z, \tau) \equiv \sqrt{\frac{R^2}{a_*^2 + \tau} + \frac{z^2}{q^2\, a_*^2 + \tau}}. \tag{C.4}$$

Ansatz-independent fields

The z and R derivatives of equation (C.1), which enters the right-hand sides of the JEs, can be computed by direct differentiation of the (known) potential, or from equation (C.3) as

$$\frac{\partial \Phi_*}{\partial z} = -2\,\pi\,G\,q\,a_*^3 z \int_0^\infty \frac{\rho_*(\mathcal{M}_\tau)}{(a_*^2 + \tau)(q^2\, a_*^2 + \tau)^{3/2}}\, d\tau, \tag{C.5}$$

$$\frac{\partial \Phi_*}{\partial R} = -2\,\pi\,G\,q\,a_*^3\, R \int_0^\infty \frac{\rho_*(\mathcal{M}_\tau)}{(a_*^2 + \tau)^2\sqrt{q^2\, a_*^2 + \tau}}\, d\tau, \tag{C.6}$$

where for simplicity we defined $\mathcal{M}_\tau \equiv \mathcal{M}(R, z, \tau)$, as in equation (C.4). At the end, the total

(e.g., stars plus DM) gravitational field is found by summing this contribution to that of the external potential, which is also differentiated with respect to the z and R coordinates.

The solution of the first JE, which is independent on b, is then performed as in the first of equation (2.24), where the integral is solved numerically; once $\rho_*\sigma_z^2$ is found, σ_z^2 is simply obtained by dividing by ρ_*. After this step, the code computes the ansatz-independent functions

$$D = \frac{\partial \rho_* \sigma_z^2}{\partial R}, \quad B = \frac{R}{\rho_*} D + \sigma_z^2, \quad C = R\,\frac{\partial \Phi}{\partial R} - \sigma_z^2, \tag{C.7}$$

which are useful to compute the other kinematic fields depending on the ansatz, as well as the critical regions and the limits for b that guarantee the positivity of the fields.

Critical regions and limits for b

Once the ansatz-independent fields above are computed, the $\mathscr{B}^-$, $\mathscr{C}^-$ and $\mathscr{D}^-$ regions are (analytically or numerically) found by imposing the negativity of the corresponding B, C and D functions in equation (C.7); $\mathscr{B}^+$, $\mathscr{C}^+$ and $\mathscr{D}^+$ are simply the complementary of these regions on the (R, z)-plane, and $\mathscr{B}^0$, $\mathscr{C}^0$ and $\mathscr{D}^0$ are the curves separating each pair of regions.

The limits for b which guarantee the positivity of the $\overline{v_\varphi^2}$, Δ_R and Δ fields can then be found by minimizing or maximizing specific functions over those regions. In particular, as described in Section 3.2, the code computes

$$b_{\rm M}(z) = \min_{\mathscr{B}_z^-} \frac{R\,\partial\Phi/\partial R}{|B|}, \quad z \in \Pr(\mathscr{B}^-), \tag{C.8}$$

$$b_0(z) = \min_{\mathscr{D}_z^-} \frac{\rho_*\,\partial\Phi/\partial R}{|D|}, \quad z \in \Pr(\mathscr{D}^-), \tag{C.9}$$

$$b_1(z) = \max_{\mathscr{B}_z^+ \cap \mathscr{C}_z^-} \frac{|C|}{B}, \quad z \in \Pr(\mathscr{B}^+) \cap \Pr(\mathscr{C}^-), \tag{C.10}$$

$$b_2(z) = \min_{\mathscr{B}_z^- \cap \mathscr{C}_z^+} \frac{C}{|B|}, \quad z \in \Pr(\mathscr{B}^-) \cap \Pr(\mathscr{C}^+); \tag{C.11}$$

all these functions can be computed analytically or numerically depending on the model[1]. Of

[1] By default, the code computes the minimum (or the maximum) over the whole radial section of the region (i.e., usually up to $R \to \infty$), but for practical purposes it is also possible to restrict the computation to a fixed radial section, e.g. up to five effective radii.

course, in the case of a spatially constant b, the limits $b_{\rm M}$, b_0, b_1 and b_2 can be found by minimizing (or maximizing) the functions above in the corresponding range of z.

We recall that the only necessary condition for the model consistency at the level of the JEs is to have $\overline{v_\varphi^2} \geq 0$ everywhere, and this is guaranteed by $b(z) \leq b_{\rm M}(z)$ (or $b < b_{\rm M}$ in the constant b case). Instead, the conditions $b(z) \leq b_0(z)$ (or $b < b_0$), $b(z) \geq b_1(z)$ (or $b > b_1$) and $b(z) \leq b_2(z)$ (or $b < b_2$) guarantee that $\Delta_R \geq 0$ and $\Delta \geq 0$ everywhere, so that the generalized Satoh (1980) decomposition of $\overline{v_\varphi^2}$ can be applied (see Section 3.1.1).

Second Jeans equation and decomposition

To solve the second JE with the b-ansatz, the code takes any non-negative $b(z)$ function as an input, and computes

$$\sigma_R^2 = b\,\sigma_z^2; \tag{C.12}$$

for $b = 1$, we reduce to the two-integral case. Of course, given the outputs of the first branch of the code, we suggest to coherently choose a $b(z)$ function (or constant b) that ensure at least the consistency of the model, i.e. below the critical limit $b_{\rm M}(z)$ (or $b_{\rm M}$).

Once the b function is specified, the code computes all the kinematic fields of our interest by using the previously determined ansatz-independent functions:

$$\overline{v_\varphi^2} = b\,B + R\,\frac{\partial \Phi}{\partial R}, \tag{C.13}$$

$$\Delta_R = b\,D + \rho_*\frac{\partial \Phi}{\partial R}, \tag{C.14}$$

$$\Delta = b\,B + C. \tag{C.15}$$

Of course, depending on the specific model, the computation can be carried out both analytically or numerically, and the code allows to vary all the additional parameters (e.g., the flattening of the stellar density profile) as preferred. As mentioned above, one could also choose a b function which is out of the limits found in the other part of the code, but in that case the resulting fields will be negative inside the corresponding critical regions.

Once the second JE is solved, the code allows to decompose $\overline{v_\varphi^2} = \overline{v_\varphi}^2 + \sigma_\varphi^2$ into the rotation and dispersion components. This can be done by choosing one of the decompositions described in Section 3.1.1, which are all implemented in the code; we recall that the generalized Satoh (1980) decomposition can be applied if and only if $\Delta_R \geq 0$ or $\Delta \geq 0$ everywhere, while the more general λ-decomposition just requires $\overline{v_\varphi^2} \geq 0$ everywhere (i.e., the physical consistency of the model).

Finally, in the last part of the code, two-dimensional maps on the (R, z)-plane of all the kinematic fields of our interest can be produced; the contours of the stellar density profile and of the ansatz-independent regions (e.g., the $\mathscr{B}^0$, $\mathscr{C}^0$ and $\mathscr{D}^0$ curves) can be superimposed as well. The specific model parameters can be varied plot by plot, and the interface is sufficiently simple to provide the maximum flexibility.

C.2 Two-integral multi-component models

In the two-integral ($b = 1$) case, the current version of the code also allows for the implementation of a multi-component stellar density distribution. In practice, we are considering

$$\rho_* = \sum_i \rho_{*,i}, \tag{C.16}$$

where the sum is performed over all the i-th components. Therefore, the gravitational potential associated to the stellar component is

$$\Phi_* = \sum_i \Phi_{*,i}, \tag{C.17}$$

and the total (e.g., stars plus DM) gravitational potential and its derivatives with respect to a generic x_j coordinate are

$$\Phi = \sum_i \Phi_{*,i} + \Phi_{\rm ext}, \quad \frac{\partial \Phi}{\partial x_j} = \sum_i \frac{\partial \Phi_{*,i}}{\partial x_j} + \frac{\partial \Phi_{\rm ext}}{\partial x_j}; \tag{C.18}$$

of course, in the summation of the different contributions, all the different fields must be normalized to the same physical units (e.g., $\mathrm{M}_\odot/\mathrm{kpc}^3$ for densities). Similarly to the models with a one-component density profile, each $\Phi_{*,i}$ and the corresponding derivatives can be found analytically, or through equations (C.5) and (C.6).

Considering that the stellar components $\rho_{*,i}$ are physically distinct, each of them is described

by its own DF; therefore, each solution of the JEs gives the moments of each DF in the total potential Φ, and for each i-th component we have

$$\rho_{*,i}\,\sigma_i^2 = \int_z^\infty \rho_{*,i}\,\frac{\partial\Phi}{\partial z'}\,dz', \tag{C.19}$$

where $\sigma_i^2 \equiv \sigma_{z,i}^2 = \sigma_{R,i}^2$ in the two-integral case, and

$$\rho_{*,i}\,\Delta_i = R\left(\frac{\partial\rho_{*,i}\,\sigma_i^2}{\partial R} + \rho_{*,i}\,\frac{\partial\Phi}{\partial R}\right), \tag{C.20}$$

where $\Delta_i \equiv \overline{v_{\varphi,i}^2} - \sigma_i^2$. To take into account the contributions of the different components, we can compute the resulting mass-weighted fields as

$$\sigma^2 = \frac{\sum_i \rho_{*,i}\,\sigma_i^2}{\sum_i \rho_{*,i}}, \quad \Delta = \frac{\sum_i \rho_{*,i}\,\Delta_i}{\sum_i \rho_{*,i}}, \quad \overline{v_\varphi^2} = \frac{\sum_i \rho_{*,i}\,\overline{v_{\varphi,i}^2}}{\sum_i \rho_{*,i}}. \tag{C.21}$$

Finally, analogously to the models in Appendix C.1, the mean velocity and velocity dispersion in the azimuthal direction can be obtained by applying the Satoh (1980) decomposition to each i-th component, so that the resulting mass-weighted fields are

$$\overline{v_\varphi} = \frac{\sum_i \rho_{*,i}\,k_i\,\sqrt{\Delta_i}}{\sum_i \rho_{*,i}}, \quad \sigma_\varphi^2 = \overline{v_\varphi^2} - \overline{v_\varphi}^2; \tag{C.22}$$

notice that, being the difference between two fields, σ_φ^2 is not simply the mass-weighted sum of the single $\sigma_{\varphi,i}^2$. Of course, if $\Delta_i < 0$ at least for one of the components, the more general λ-decomposition can be applied as well, by choosing an appropriate λ_i for each of the components, and summing the fields similarly as in equation (C.22).

Finally, by knowing the (constant) mass-to-light ratio Υ_i of each i-th component, analogous luminosity-weighted fields can be computed as well: they are simply obtained by using the luminosity densities $\nu_{*,i} = \rho_{*,i}/\Upsilon_i$ instead of $\rho_{*,i}$ in equations (C.21) and (C.22). An application of this code is found in Merola (2024), for the dynamical modeling of the counter-rotating stellar component in the S0 galaxy NGC 1366.

APPENDIX D

The one-component Binney logarithmic halo

Here we discuss the solution of the JEs with the b-ansatz for the self-gravitating Binney logarithmic halo of asymptotic circular velocity $v_{\rm h}$, scale length $b_{\rm h}$ and potential flattening $q_{\rm h}$; a thorough discussion about the dynamical properties of this model is given in Evans (1993) (see also Evans 1994 and Evans and de Zeeuw 1994). The potential-density pair is (see BT08)

$$\begin{cases} \Phi_{\rm h} = \dfrac{v_{\rm h}^2}{2} \ln\left(1 + R^2 + \dfrac{z^2}{q_{\rm h}^2}\right), \\ \\ \rho_{\rm h} = \dfrac{v_{\rm h}^2}{4\pi\, G\, b_{\rm h}^2} \dfrac{1 + 2\, q_{\rm h}^2 + R^2 + \left(2 - q_{\rm h}^{-2}\right)\, z^2}{q_{\rm h}^2\, \left(1 + R^2 + q_{\rm h}^{-2}\, z^2\right)^2}, \end{cases} \tag{D.1}$$

where, as for the remainder of this Appendix, all the lengths are assumed normalized to $b_{\rm h} \neq 0$. Notice that $\rho_{\rm h}$ becomes negative on the z-axis for $q_{\rm h} < 1/\sqrt{2}$, and so physically acceptable models are those with $q_{\rm h} \geq 1/\sqrt{2}$. From equations (2.24) and (2.25), we get

$$\begin{cases} \rho_{\rm h}\sigma_z^2 = \dfrac{v_{\rm h}^4}{G\,b_{\rm h}^2}\,\dfrac{q_{\rm h}^4\,R^2+(2\,q_{\rm h}^2-1)\,z^2+2\,q_{\rm h}^4}{8\pi\,(q_{\rm h}^2\,R^2+z^2+q_{\rm h}^2)^2}, \\ \\ [\rho_{\rm h},\Phi_{\rm h}] = \dfrac{v_{\rm h}^4}{G\,b_{\rm h}^3}\,\dfrac{q_{\rm h}^2\,(1-q_{\rm h}^2)\,R}{4\pi\,(q_{\rm h}^2\,R^2+z^2+q_{\rm h}^2)^2}, \end{cases} \tag{D.2}$$

where the condition $q_{\rm h} \geq 1/\sqrt{2}$ for the positivity of $\rho_{\rm h}$ ensures that $\sigma_z^2 \geq 0$. Moreover, the commutator $[\rho_{\rm h},\Phi_{\rm h}]$ is positive for $1/\sqrt{2} \leq q_{\rm h} < 1$, it vanishes for $q_{\rm h} = 1$ (the spherical limit), and it becomes negative for $q_{\rm h} > 1$. We finally notice that, in the two-integral case,

$$\rho_{\rm h}\overline{v_\varphi^2} = R\,[\rho_{\rm h},\Phi_{\rm h}] + \rho_{\rm h}\sigma_z^2 = \frac{v_{\rm h}^4}{G\,b_{\rm h}^2}\,\frac{q_{\rm h}^2\,(2-q_{\rm h}^2)\,R^2+(2q_{\rm h}^2-1)\,z^2-2\,q_{\rm h}^4}{8\pi\,(q_{\rm h}^2R^2+z^2+q_{\rm h}^2)^2}, \tag{D.3}$$

so that $\overline{v_\varphi^2}$ becomes negative (and the models physically inconsistent) for $q_{\rm h} > \sqrt{2}$. Actually, Evans (1993) proved that the two-integral DF of a self-gravitating Binney halo becomes negative for $q_{\rm h} \gtrsim 1.08$, so that models with $1.08 \lesssim q_{\rm h} \leq \sqrt{2}$, although they have non-negative σ_z^2 and $\overline{v_\varphi^2}$, do not exist[1]. From now on, we limit to models with $1/\sqrt{2} \leq q_{\rm h} \leq 1$, which are fully consistent in the two-integral case, and have $[\rho_{\rm h},\Phi_{\rm h}] \geq 0$ everywhere. For reference, in the top panels of Figure D.1 we show the 2D maps of σ_z^2, $R\,[\rho_{\rm h},\Phi_{\rm h}]\,/\rho_{\rm h}$ and $R\,\partial\Phi_{\rm h}/\partial R$ for $q_{\rm h} = 0.85$; we see that the maximum of σ_z^2 is reached at high z, while the other two fields peaks close to the equatorial plane. In the bottom panels of Figure D.1, we show the same fields for a smaller value of q, i.e. for an higher potential flattening; we see that the main effect is an increase of the commutator close to the equatorial plane, while the profile of σ_z^2 slightly shrinks around the z-axis.

The $\mathscr{B}$, $\mathscr{C}$ and $\mathscr{D}$ regions can all be determined analytically. From equation (D.2), we have

$$\begin{aligned} \mathscr{B}^- = \Big\{(R,z) : {} & q_{\rm h}^6\,R^4 + 3\,q_{\rm h}^2\,\left(q_{\rm h}^2\,z^2 - z^2 + q_{\rm h}^4\right)\,R^2 \\ & - \left(q_{\rm h}^2+z^2\right)\left(2\,q_{\rm h}^2\,z^2 - z^2 + 2\,q_{\rm h}^4\right) > 0\Big\}, \end{aligned} \tag{D.4}$$

a biquadratic in R with positive discriminant independently of $q_{\rm h}$, and a permanence and a variation of the sign of its coefficients for $q_{\rm h} \geq 1/\sqrt{2}$; therefore, $\mathscr{B}^-$ is the portion of the (R,z)-plane to the right of the (positive) square root of the (positive) solution. In Figure D.2, we show the $\mathscr{B}^-$ regions (to the right of the $\mathscr{B}^0$ curves) of the model for three representative values of $q_{\rm h}$.

[1] This case exemplifies that $\sigma_z^2 \geq 0$ and $\overline{v_\varphi^2} \geq 0$ are only necessary conditions for the model consistency, while $\sigma_z^2 < 0$ or $\overline{v_\varphi^2} < 0$ are sufficient to prove the model inconsistency.

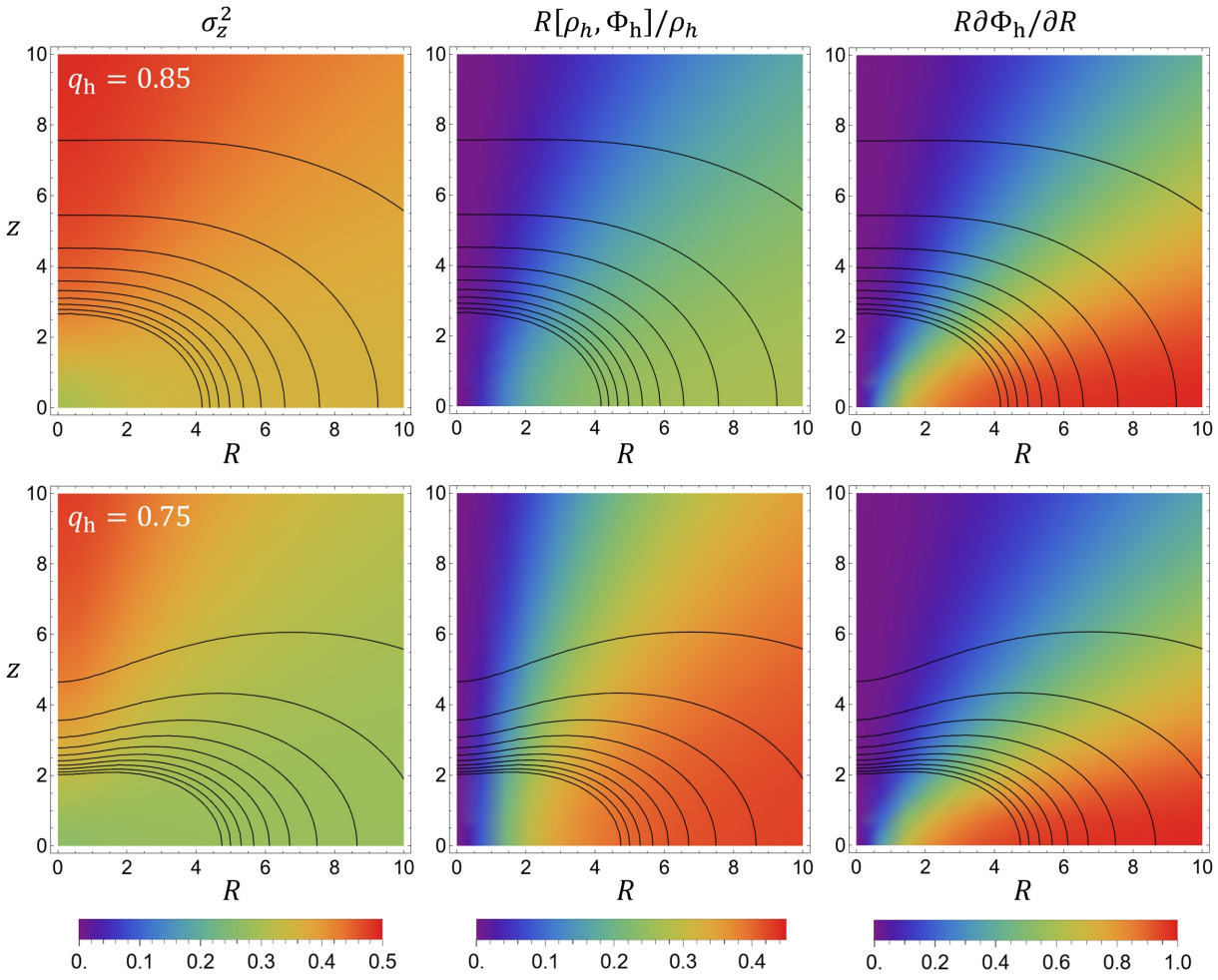


Figure D.1. Maps in the (R, z)-plane of σ_z^2 (left column), $R\left[\rho_\mathrm{h}, \Phi_\mathrm{h}\right]/\rho_\mathrm{h}$ (central column) and $R\,\partial\Phi_\mathrm{h}/\partial R$ (right column), in units of v_h^2, for the Binney logarithmic halo with $q_\mathrm{h} = 0.85$ (top row) and $q_\mathrm{h} = 0.75$ (bottom row). Black solid lines show equally spaced isodensity contours.

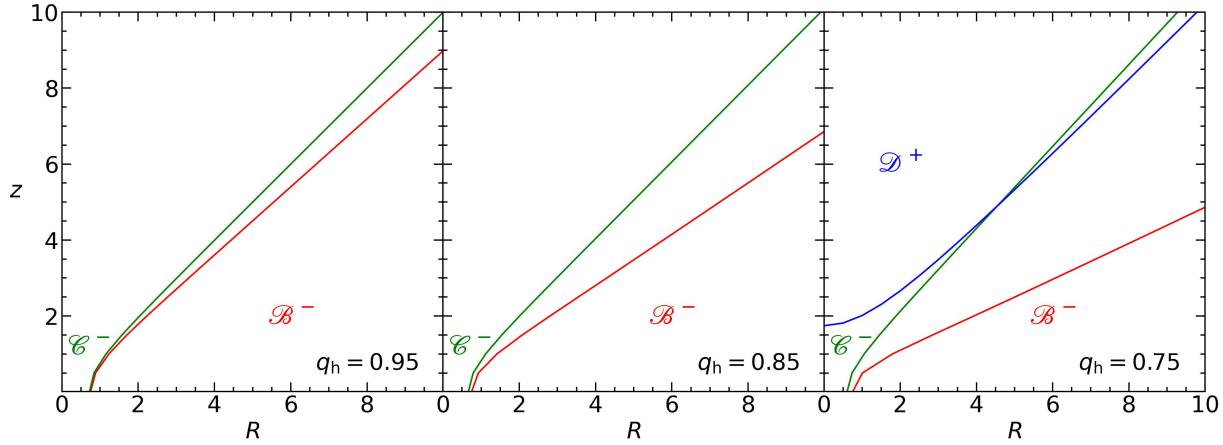


Figure D.2. The ansatz-independent regions $\mathscr{B}$, $\mathscr{C}$ and $\mathscr{D}$ of the Binney logarithmic halo for different values of q_h; from left to right, the potential (and the stellar density profile) becomes more flattened. The $\mathscr{B}^-$ and $\mathscr{C}^-$ regions are, respectively, to the right of the red curves ($\mathscr{B}^0$) and to the left of the green curves ($\mathscr{C}^0$), and $\mathrm{Pr}(\mathscr{B}^-)$ and $\mathrm{Pr}(\mathscr{C}^-)$ coincide with the z-axis. For the model with $q_h = 0.75$, the $\mathscr{D}^+$ region is to the left of the blue curve ($\mathscr{D}^0$), while for the other models $\mathscr{D}^-$ fully covers the (R, z)-plane, with $\mathscr{D}^0$ coinciding with the z-axis.

We see that it becomes smaller as q_h decreases, i.e. for a more flattened potential (and stellar density profile); moreover, $\mathrm{Pr}(\mathscr{B}^-)$ always coincides with the z-axis.

The properties of the $\mathscr{D}$ region are more complicated: in fact, while $D < 0$ everywhere for $q_h \geq \sqrt{2/3}$ (with $D = 0$ on the z-axis), for $q_h < \sqrt{2/3}$ we have

$$\mathscr{D}^- = \left\{(R, z) : z - \frac{q_h^2 \sqrt{3 + R^2}}{\sqrt{2 - 3\,q_h^2}} < 0\right\}, \tag{D.5}$$

so that a $\mathscr{D}^+$ region does exist. In the right panel of Figure D.2, the blue curve shows $\mathscr{D}^0$ for $q_h = 0.75$, and $\mathscr{D}^+$ is the part of the plane above it; notice how $\mathrm{Pr}(\mathscr{D}^-)$ coincides with the z-axis independently of q_h. Finally, from equation (3.5),

$$\begin{aligned}\mathscr{C}^- = \Big\{(R, z) : & q_h^4\,\left(2 - q_h^2\right)\,R^4 + q_h^2\,\left(q_h^2\,z^2 - z^2 + q_h^4 + 2\,q_h^2\right)\,R^2 \\ & - \left(q_h^2 + z^2\right)\left(2\,q_h^2\,z^2 - z^2 + 2\,q_h^4\right) < 0\Big\},\end{aligned} \tag{D.6}$$

a biquadratic in R that, in the considered range $1/\sqrt{2} \leq q_h \leq 1$, presents a positive discriminant and a permanence and a variation of the sign in the coefficients; therefore, $\mathscr{C}^-$ is the region between the z-axis and the (positive) square root of the (positive) solution. In Figure D.2, we show the $\mathscr{C}^-$ regions (to the left of the $\mathscr{C}^0$ curves) of the model for three representative values of

q_h. Notice that $\mathscr{C}^-$ becomes slightly smaller as q_h decreases, and so the $\mathscr{B}^+ \cap \mathscr{C}^+$ region becomes larger; also, $\mathrm{Pr}(\mathscr{C}^-)$ coincides with the z-axis. Given that $[\rho_*, \Phi_\mathrm{h}] \geq 0$ everywhere, we also have $\mathscr{B}^- \cap \mathscr{C}^+ = \mathscr{B}^-$ and $\mathscr{B}^+ \cap \mathscr{C}^- = \mathscr{C}^-$; in the spherical case ($q_\mathrm{h} = 1$), the $\mathscr{B}^0$ and $\mathscr{C}^0$ curves would coincide, and $\mathscr{B}^- = \mathscr{C}^+$ and $\mathscr{B}^+ = \mathscr{C}^-$.

We now determine the limits for $b(z)$ that ensure the positivity of $\overline{v_\varphi^2}$, Δ_R and Δ in the considered range $1/\sqrt{2} \leq q_\mathrm{h} \leq 1$. From equation (3.11),

$$b_\mathrm{M}(z) = \frac{2}{q_\mathrm{h}^2}, \quad z \geq z_\mathrm{M}(q_\mathrm{h}) \equiv \frac{q_\mathrm{h}^2\sqrt{1-q_\mathrm{h}^2}}{\sqrt{q_\mathrm{h}^4 - 2\,q_\mathrm{h}^2 + 3/2}}, \tag{D.7}$$

while, for $z \leq z_\mathrm{M}$, $b_\mathrm{M}(z)$ is a more complicated function monotonically decreasing from $2/q_\mathrm{h}^2$ to the minimum

$$b_\mathrm{M} = \frac{14 + 12\,q_\mathrm{h}^2 + 8\sqrt{2 + q_\mathrm{h}^2 - 2\,q_\mathrm{h}^4}}{17\,q_\mathrm{h}^2}, \tag{D.8}$$

which is reached for $z = 0$; in the spherical case ($q_\mathrm{h} = 1$), $b_\mathrm{M}(z) = 2$. From equation (3.13),

$$b_0(z) = \frac{1}{q_\mathrm{h}^2}, \quad z \geq z_0(q_\mathrm{h}) \equiv \frac{q_\mathrm{h}^2}{\sqrt{1-q_\mathrm{h}^2}}, \tag{D.9}$$

and, for $z \leq z_0$, $b_0(z)$ is a function monotonically decreasing from $1/q_\mathrm{h}^2$ to the minimum

$$b_0 = \frac{2}{3} + \frac{1}{3\,q_\mathrm{h}^2}, \tag{D.10}$$

reached again on the equatorial plane; in the spherical case, as expected from general considerations, $b_0 = 1$. Finally, from equations (3.15) and (3.16), $b_1(z) = 1$ and

$$b_2(z) = \frac{2}{q_\mathrm{h}^2} - 1, \quad z \geq z_2(q_\mathrm{h}) \equiv \frac{\sqrt{2}\,q_\mathrm{h}^2}{\sqrt{3 - 2\,q_\mathrm{h}^2}}, \tag{D.11}$$

while, for $z \leq z_2$, $b_2(z)$ is again monotonically decreasing function with minimum

$$b_2 = \frac{14 + 8\sqrt{2} + (3 - 8\sqrt{2})\,q_\mathrm{h}^2}{17\,q_\mathrm{h}^2}, \tag{D.12}$$

reached for $z = 0$; in the spherical case, $b_2(z) = 1$ for all z. In the bottom-right panel of Figure 4.4, we show the four $b(z)$ functions above for three representative case of q (for simplicity, b_2 is

shown only for the $q_{\rm h} = 0.75$ case): we see that $b_1 = 1 \leq b_0 \leq b_2 < b_{\rm M}$, as expected from the positivity of $[\rho_*, \Phi_{\rm h}]$, and all the limits increases for decreasing $q_{\rm h}$.

In Figure D.3, we show the 2D maps of $\overline{v_\varphi^2}$, Δ_R and Δ for $q_{\rm h} = 0.85$ and three values of constant b. The behavior of the fields for increasing b is the one expected from general considerations, i.e. $\overline{v_\varphi^2}$ and Δ increase in $\mathscr{B}^+$ and decrease in $\mathscr{B}^-$, and Δ_R decreases everywhere; for $b > b_{\rm M} \simeq 2.68$, the negativity region of $\overline{v_\varphi^2}$ is adjacent to the equatorial plane, similarly to that of Δ for $b > b_2 \simeq 1.57$. In Figure D.4, we show the same fields for $q_{\rm h} = 0.75$; we see that the fields are higher close to the equatorial plane, and the negativity regions of the fields become smaller or disappear, as the limits for b have increased. Moreover, for $b > b_0 \simeq 1.26$, Δ_R remains positive (and would increase, by increasing b) in the region $\mathscr{D}^+$.

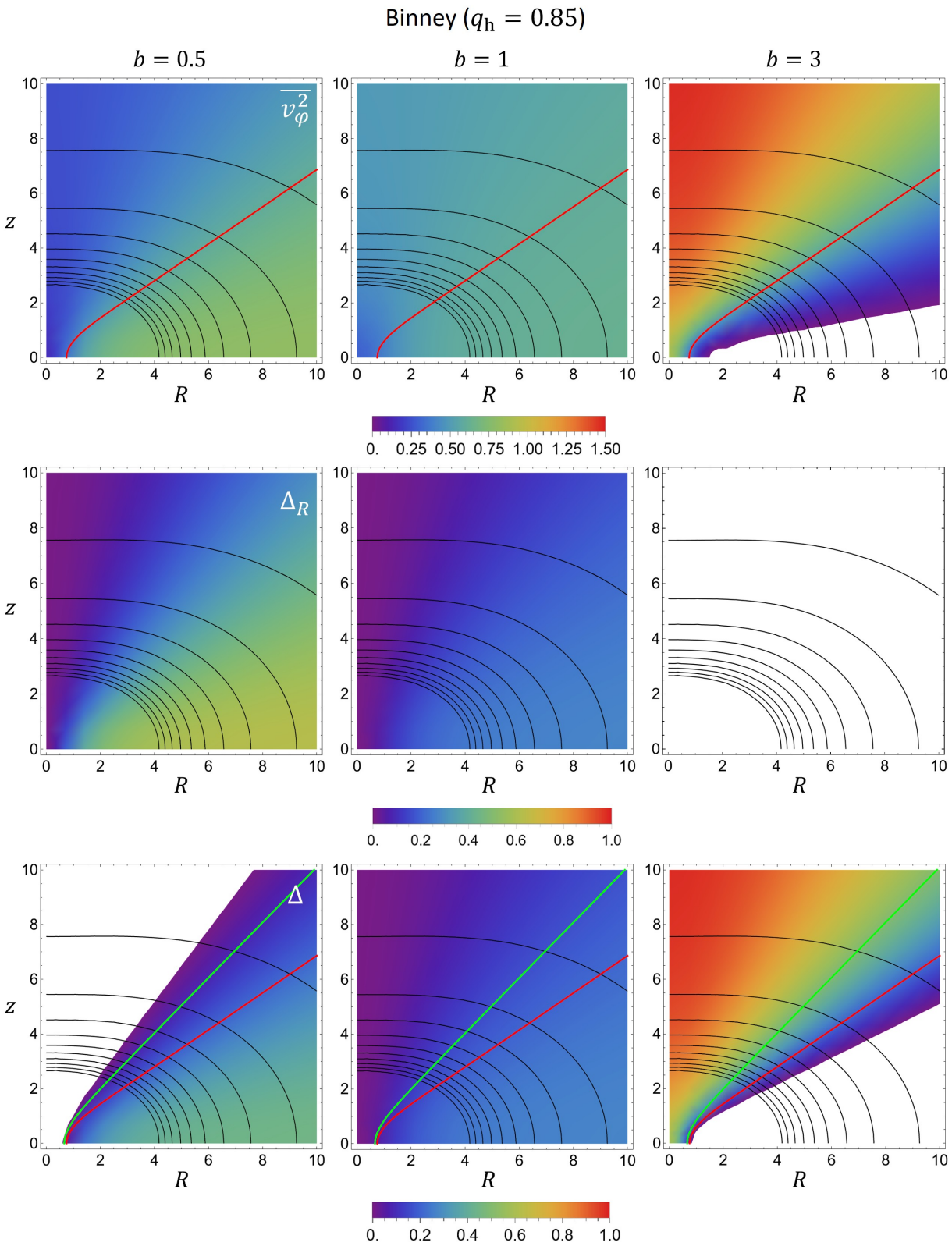


Figure D.3. Maps in the (R, z)-plane of $\overline{v_\varphi^2}$ (top row), Δ_R (central row) and Δ (bottom row), in units of v_h^2, for the Binney logarithmic halo with $q_h = 0.85$, and constant $b = 0.5$ (left column), $b = 1$ (central column) and $b = 2$ (right column). The red and green lines show, respectively, the $\mathscr{B}^0$ and $\mathscr{C}^0$ curves, while $\mathscr{D}^0$ coincides with the z-axis. Black solid lines show equally spaced isodensity contours. White regions correspond to negative values of the fields.

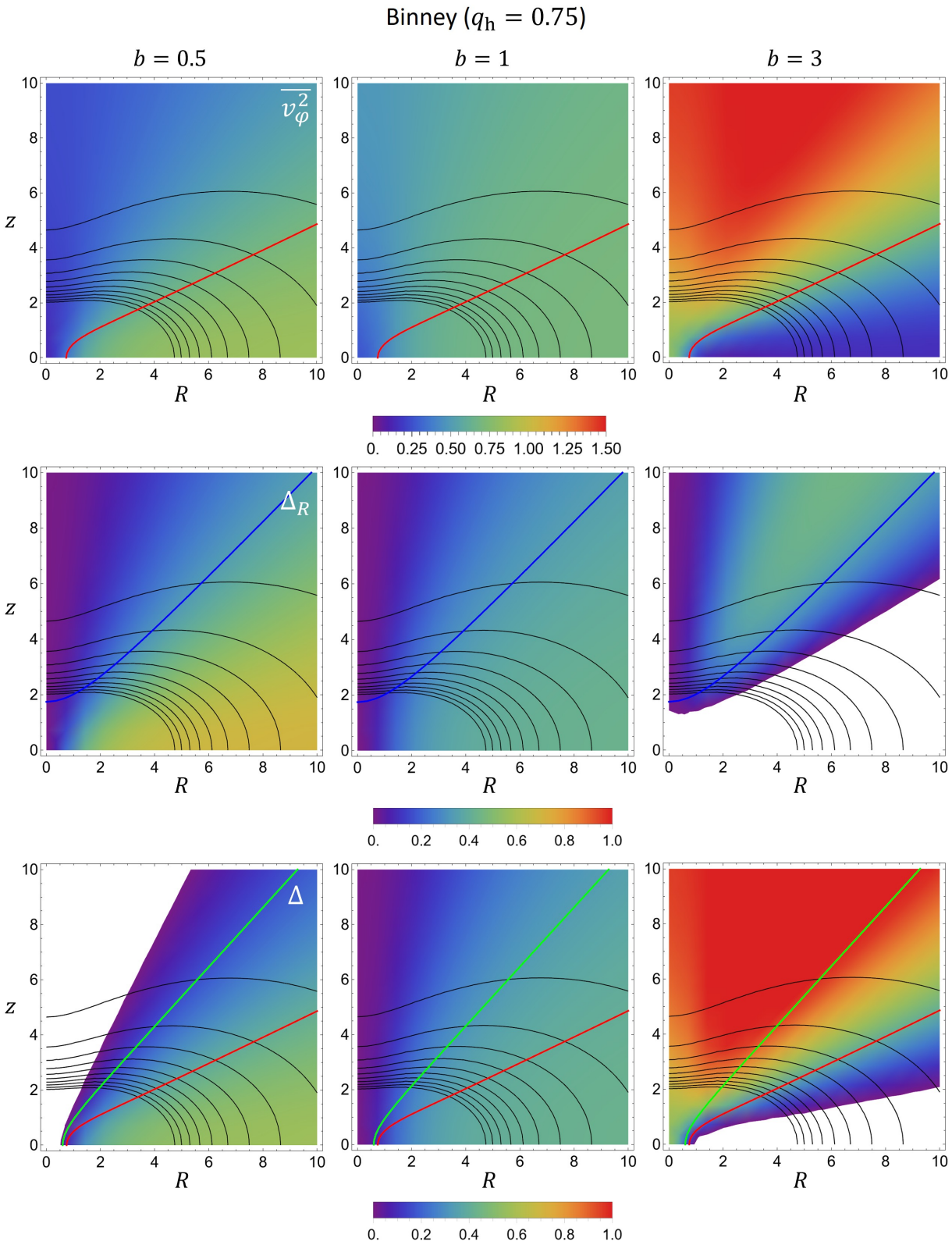


Figure D.4. Same as in Figure D.3, but for $q_h = 0.75$. The blue lines show the $\mathscr{D}^0$ curves.

APPENDIX E

A new deprojection formula for the Sérsic law

One of the most realistic models to reproduce the density distribution of ETGs is the Sérsic (1968) law (e.g., Caon, Capaccioli, and D'Onofrio 1993), a generalization of the de Vaucouleurs (1948) profile. It has also been used to model dwarf galaxies (see e.g. A. W. Graham and Guzmán 2003, Battaglia et al. 2006), the bulges of spiral galaxies (Andredakis, Peletier, and Balcells 1995), and globular clusters (see e.g. Barmby et al. 2007); for this reason, a deep investigation from a theoretical point of view has already been carried out (see e.g. A. W. Graham and Driver 2005 and references therein). Unfortunately, the deprojection of the Sérsic law cannot be expressed in terms of elementary functions for generic values of its shape parameter n, and different families of approximate deprojection formulae have been proposed over the years. In the framework of the Jeans modeling of galaxies, where the three-dimensional density profile is needed to solve the JEs, we thus searched for a very simple, accurate, and theoretically motivated deprojection formula of the Sérsic law without free parameters, and not based on fits of the numerical deprojection. We found the formula by requiring it to reproduce the analytical expressions for the inner and outer asymptotic expansions of the deprojected Sérsic law of a given n, and by matching the two expansions at intermediate radii with the request that the total luminosity coincides with that of the original Sérsic profile of the same n. Our resulting formula is algebraically very simple, exact

at inner and outer radii, and it depends on two coefficients that are analytical functions of the n of immediate evaluation. The accuracy of the formula over the whole radial range is very good and increases for increasing n, with a maximum of relative deviations from the true numerical deprojection of $\simeq 8\,10^{-3}$ for the dV profile.

This Appendix is structured as follows. In Appendix E.1, a general overview of the Sérsic law is made, and the main approaches which are nowadays used to deproject the profile are presented (Appendix E.1.1). Then, in Appendix E.2 our asymptotically matched formula will be presented, together with its extensions to the $n < 1$ case (Appendix E.2.1), and to ellipsoidal models (Appendix E.2.2). Finally, in Appendix E.3 a comparison between our formula and the numerical deprojection will be presented, proving its high accuracy despite its simplicity.

E.1 Overview on the Sérsic law

In the following, we restrict our discussion to the spherically symmetric systems, while the generalization to ellipsoidal models will be discussed in Appendix E.2.2. With this assumption, the Sérsic profile can be written as

$$I(R) = I_0 \mathrm{e}^{-b\,\eta^{1/n}}, \quad \eta \equiv \frac{R}{R_\mathrm{e}}, \tag{E.1}$$

where n is the Sérsic index, I_0 is the central surface brightness, R is the radius in the projection plane, R_e is the effective radius (i.e., the radius in the projection plane enclosing half of the total luminosity of the profile), and b_n is a dimensionless parameter depending on n. The total luminosity associated with the profile in equation (E.1) is

$$L = I_0 R_\mathrm{e}^2 \frac{2\pi n}{b_n^{2n}} \Gamma(2n), \tag{E.2}$$

where $\Gamma(x)$ is the Euler gamma function (see Appendix A.1). Usually, the equation above is used to express I_0 in equation (E.1) as a function of L. The value of the parameter b in equation (E.1) depends on n via the transcendental equation $\Gamma(2n)/2 = \gamma(2n, b)$, where $\gamma(a, x)$ is the lower incomplete gamma function (see Appendix A.1). This equation comes from the request that R_e is the effective radius, and since $b_n(n)$ cannot be expressed in terms of elementary functions, several high-quality fits of the numerical solution have been presented in literature (see e.g. Ciotti and Pellegrini 1996, C21); finally, Ciotti and Pellegrini (1996) showed that $b_n(n)$ for $n \to \infty$ can be

expressed as the following asymptotic series:

$$b_n = 2n - \frac{1}{3} + \frac{4}{405\,n} + \frac{46}{25515\,n^2} + O(n^{-3}). \tag{E.3}$$

For practical purposes, it should be noticed that when comparing equation (E.3) to the true solution for $1 \leq n \leq 10$, the relative error (in absolute value) is already as small as $\simeq 3.8 \times 10^{-6}$ for $n \simeq 1.2$, decreasing down to $\approx 10^{-8}$ for increasing n; even for n as low as $1/2$, the relative error is $\simeq 7 \times 10^{-4}$.

E.1.1 Approaches for the deprojection

The deprojected luminosity density profile $\nu(r)$ of the Sérsic law, where r is the spherical radius, is given by the well-known Abel deprojection integral (see e.g. BT08, C21)

$$\nu(r) = -\frac{1}{\pi} \int_r^\infty \frac{dI(R)}{dR} \frac{dR}{\sqrt{R^2 - r^2}}. \tag{E.4}$$

Unfortunately, $\nu(r)$ cannot be expressed in terms of elementary functions for generic values of n, and a purely numerical deprojection is often adopted (see e.g. the early works of Poveda, Iturriaga, and Orozco 1960, Young 1976). However, for practical purposes, a great effort has been devoted to build sufficiently accurate and manageable analytical approximations of the true (i.e., numerical) $\nu(r)$, usually valid over some more or less extended radial interval. We mention here a few of the main adopted approaches, although the list is almost certainly not complete:

1. Multi-Gaussian deprojections: The $\nu(r)$ profiles are determined from the property that the deprojection of a centered Gaussian is a Gaussian. The weights and dispersions of the Gaussian components adopted to expand $I(R)$ in equation (E.1) are determined numerically and given in tables. This approach was used for the $n = 4$ profile by Bendinelli, Ciotti, and Parmeggiani 1993, and successively extended to generic Sérsic profiles (e.g. Pechetti et al. 2020).

2. Single slope power-law fits: In this important family, $\nu(r)$ is approximated as

$$\nu(r) = \frac{L}{R_{\rm e}^3} \frac{b_n^{(3-\beta_n)\,n}}{4\pi\,n\,\Gamma[(3-\beta_n)\,n]} s^{-\beta_n}\, e^{-b\,s^{1/n}}, \quad s \equiv \frac{r}{R_{\rm e}}, \tag{E.5}$$

(see e.g. Mellier and Mathez 1987, Prugniel and Simien 1997; see also Gerbal et al. 1997, Lima Neto, Gerbal, and Márquez 1999, Márquez et al. 2000, Terzić and A. W. Graham 2005). The expression for $\nu(r)$ in equation (E.5) guarantees that, for a generic $\beta_z < 3$, its total luminosity L is the same as that of the Sérsic profile of index n, effective radius R_e, and central surface brightness I_0. The parameter β_z is a function of n, and it is obtained from a fit of the numerically deprojected profile over some prescribed radial range; in this way, its value naturally depends on the radial range used for the fit. We notice that R_e is the effective radius of the true profile, and not that of the deprojected approximated formula (although they can be almost identical).

3. Refined single slope power-law fits: In this approach, $\nu(r)$ is reproduced by considering more complicated functions than the exponential term in equation (E.5), as a sum of exponential functions (Simonneau and Prada 2004). We also mention the very high-accuracy deprojected profile of Vitral and Mamon (2020), which is obtained by fitting the residuals of equation (E.5) with respect to the true profile with bivariate polynomials of order ten in the variables $\log^i(s)\log^j(n)$. The coefficients of these polynomials are given in numerical tables, and the lower limit of the range of r/R_e was set to 10^{-3}; in a following work (Vitral and Mamon 2021), the lower limit was further reduced to 10^{-4}.

4. Special functions fits: A high-quality fit of $\nu(r)$ is given in terms of special functions as the modified Bessel functions of the second kind K_m (see Appendix A.3), supplemented by tables for the numerical values of the parameters as a function of n (Trujillo et al. 2002); a refinement of this formula is given in Emsellem and van de Ven (2008).

5. Analytical deprojections: The profile of $\nu(r)$ is a Gaussian for $n = 1/2$, and a modified Bessel function of the second kind K_0 (see Appendix A.3) for $n = 1$ (see e.g. Baes and Ciotti 2019). Moreover, $\nu(r)$ can be expressed in terms of Meijer G and Fox H functions (see Appendix A.2) for, respectively, all rational values of n (Mazure and Capelato 2002), and generic n (Baes and Gentile 2011, Baes and van Hese 2011); however, these advanced transcendental functions are rarely used in common applications, and they are not even implemented in the majority of numerical packages. In this family of analytically exact formulae, we also mention those based on the method of asymptotic expansion (Ciotti 1991, hereafter C91), that give the asymptotic formulae for $\nu(r)$ for $r \to 0$ and for $r \to \infty$; these

formulae are the starting point of the present study.

Nowadays, available computer algebra systems allow one to numerically integrate equation (E.4) with arbitrarily large numerical precision, so that the need for sophisticated analytical approximations of $\nu(r)$ is not as compelling as it was in the past years. However, an analytical approximation of $\nu(r)$ can still be useful if it satisfies the following properties:

P1) Correct analytical behavior at the center and at large radii: In fact, one of the common uses of an analytical $\nu(r)$ is to obtain the radial trends of dynamical quantities near the center (e.g., the solutions of the JEs in presence of a central SMBH). Quite often, the approximations of $\nu(r)$, obtained as fits over some finite radial range, are not correct at the center or at large radii, unless the correct trend is imposed to the functional form of the fitting function.

P2) Monotonically decreasing behavior for increasing r: This property of the Sérsic law for $n \geq 1/2$ follows from the identity

$$\frac{d\,\nu(r)}{dr} = -\frac{r}{\pi}\int_r^\infty \frac{d}{dR}\left[\frac{1}{R}\frac{dI(R)}{dR}\right]\frac{dR}{\sqrt{R^2-r^2}}, \tag{E.6}$$

which is established with integration by parts of equation (E.4), followed by a differentiation with respect to r. For $n \geq 1/2$, it is easy to show that the integrand is nowhere negative, while for $0 < n < 1/2$, an asymptotic analysis shows that the profile is non-monotonic, with $d\nu(r)/dr > 0$ near the center and $d\nu(r)/dr < 0$ at large radii.

P3) Conservation of the total luminosity: The proposed formula should have the same L as the true Sérsic profile of a given n, R_e and I_0. It should be noticed that, in general, the effective radius appearing in the approximate formulae is the one of the true profile, and not the effective radius of the approximated formula (even though the two values are very similar, especially for high accuracy formulae).

P4) Accuracy over a large or the whole radial range: The relevance of this request is apparent; however, for practical purposes, differences of less than a few percent from the true $\nu(r)$ can be safely ignored in almost all observational and theoretical works.

P5) Simplicity: As fast numerical deprojection with arbitrarily high accuracy is currently possible, only sufficiently simple formulae can really turn out to be useful in applications.

The different formulae proposed so far satisfy some of the properties above, while they are less satisfactory for some others; in our work, however, we followed a totally different approach which do not make use of any fit. In particular, we build a formula starting from the exact asymptotic deprojection of the Sérsic law for large and small radii (restricting in particular to $n > 1$), and then we matched the two regimes by the use of a "matching parameter" p_n, whose value is uniquely determined by the request that the total luminosity coincides with that of the original Sérsic profile. The resulting formula is extremely simple and it turns out to perform extremely well over the entire radial range, with relative errors of the order of 10^{-3} or less (with accuracy improving with increasing n).

E.2 The asymptotically matched deprojection formula

In our study, we mainly focus on the deprojection of the Sérsic profile for $n > 1$, i.e. the range encompassing the vast majority of cases of interest for ETGs. We do not consider the approximation of the deprojection of the $n = 1$ profile, because in this case $\nu(r)$ can be expressed in the form of a Bessel K_0 function (Appendix A.3):

$$\nu(r) = \frac{I_0}{R_\mathrm{e}} \frac{b_n(1)}{\pi} \mathrm{K}_0(bs), \tag{E.7}$$

where $s \equiv r/R_\mathrm{e}$, and $b_n(1) \simeq 1.67835$. For future reference, we recall that close to the origin

$$\nu(r) \sim \frac{I_0}{R_\mathrm{e}} \frac{b_n(1)}{\pi} \left[\ln \frac{2}{b_n(1)\, s} - \gamma \right], \quad r \to 0, \tag{E.8}$$

where $\gamma \simeq 0.57721$ is the so-called Euler constant, and the central logarithmic divergence of the deprojected exponential profile is apparent (see e.g. C91, Gradshteyn et al. 2007).

For $n > 1$, as shown in C91, $\nu(r)$ near the origin diverges as[1]

[1]Due to a typo, the coefficient $2\, m\, b^{m-1}$ at the denominator of equation (9) in C91 and of equation (13.25) in C21 (for $m > 1$) should be $2\pi\, m\, b^{-1}$. We notice that equation (A5) in C91, from which the correct equation (E.9) and the two mentioned equations in C91 and C21 are derived, is correct. Again, due to a typo in equation (13.25) in C21 (for $m = 1$), the $s^{1/2}$ at the denominator should be s, as in the correct equation (E.7) and (A6) in C91.

$$\nu(r) \sim \nu_{\rm i}(r) \equiv \frac{I_0}{R_{\rm e}} {\rm B}\left(\frac{1}{2}, \frac{n-1}{2n}\right) \frac{b_n}{2\pi\, n} \frac{{\rm e}^{-b\, s^{1/n}}}{s^{1-1/n}}, \quad r \to 0, \tag{E.9}$$

where ${\rm B}(x, y)$ is the Euler Beta function (Appendix A.1). In the external regions, instead, the leading term of the asymptotic expansion of $\nu(r)$ for a generic n is given by

$$\nu(r) \sim \nu_{\rm e}(r) \equiv \frac{I_0}{R_{\rm e}} \sqrt{\frac{b_n}{2\pi\, n}} \frac{{\rm e}^{-b_n\, s^{1/n}}}{s^{1-1/(2n)}}, \quad r \to \infty. \tag{E.10}$$

These asymptotic expansions show that equation (E.5) cannot be simultaneously correct at the center and in the external regions; therefore, single power-law fits cannot be used to evaluate rigorously the dynamical properties of $\nu(r)$. However, the asymptotic expansions also explain why, after all, the accuracy of equation (E.5) in reproducing the true profile increases for increasing n. In fact, the algebraic factors in equations (E.9) and (E.10) behave, respectively, as $r^{1/n-1}$ and $r^{1/(2n)-1}$, so that, for n large enough, the two exponents tend to the common limit of -1. For example, for $n = 4$, the inner and outer power-law exponents are already quite similar: -0.75 at the center, and -0.875 in the external regions (in the Mellier and Mathez 1987 formula, the best-fit exponent is $\simeq -0.855$).

Thanks to equations (E.9) and (E.10), we can thus proceed to the construction of an approximated deprojected Sérsic profile that is not a fit, has no free parameters, is monotonically decreasing, and has the same total luminosity and the same exact trend at small and large radii as the true deprojected profile. The idea is to exploit the fact that, for $n > 1$, the ratio $\nu_{\rm i}(r)/\nu_{\rm e}(r) \propto r^{1/(2n)}$ is a monotonically increasing function that vanishes at the origin and diverges for $r \to \infty$. This allows us to satisfy all the mentioned requirements (except the conservation of L, which we discuss later), with the elementary trial function

$$\nu_{\rm a}(r) \equiv \frac{\nu_{\rm i}(r)}{1 + \nu_{\rm i}(r)/\nu_{\rm e}(r)} = \frac{\nu_{\rm e}(r)}{1 + \nu_{\rm e}(r)/\nu_{\rm i}(r)}. \tag{E.11}$$

We note that the request of exact central and external behaviors (i.e., that $\lim_{r\to 0} \nu_{\rm a}/\nu_{\rm i} = 1$ and $\lim_{r\to\infty} \nu_{\rm a}/\nu_{\rm e} = 1$) implies that the coefficients in front of $\nu_{\rm i}(r)$ and $\nu_{\rm e}(r)$ in equation (E.11) must be 1, as the additive constant at the denominator. We also notice that the proposed $\nu_{\rm a}$ approaches both $\nu_{\rm i}$ and $\nu_{\rm e}$ from below.

Of course, $\nu_{\rm a}(r)$ cannot be expected to describe well the true profile in the intermediate radial region. In addition to this, the volume integration of $\nu_{\rm a}(r)$ gives a total luminosity that

underestimates L of the associated Sérsic profile by $\simeq 19\%$ for $n = 2$, $\simeq 24\%$ for $n = 4$, and $\simeq 27\%$ for $n = 10$. As a consequence, while preserving all its positive features, we must modify equation (E.11) so that its total luminosity coincides with L. The idea is to introduce a matching parameter p_n, dependent on n, to be uniquely determined by the conservation of L. The most natural choice is to modify equation (E.11) as

$$\nu_{\rm a}(r) = \frac{\nu_{\rm i}(r)}{\left\{1 + \left[\dfrac{\nu_{\rm i}(r)}{\nu_{\rm e}(r)}\right]^{p_n}\right\}^{1/p_n}} = \frac{L}{R_{\rm e}^3} \frac{c_1\, {\rm e}^{-b\, s^{1/n}}}{\left[1 + c_2^{p_n}\, s^{p_n/(2n)}\right]^{1/p_n}\; s^{1-1/n}}, \tag{E.12}$$

where b_n is again given in equation (E.3), the second formula is expressed in terms of L and $R_{\rm e}$ of the true Sérsic profile, and from equations (E.9) and (E.10) the two coefficients are the analytical functions

$$c_1 \equiv \frac{b_n^{2n+1}}{4\pi^2\, n^2\, \Gamma(2n)}\, {\rm B}\left(\frac{1}{2}, \frac{n-1}{2n}\right), \quad c_2 \equiv \sqrt{\frac{b_n}{2\pi\, n}}\, {\rm B}\left(\frac{1}{2}, \frac{n-1}{2n}\right). \tag{E.13}$$

For $p > 0$, the asymptotic properties of equation (E.11) are retained, in agreement with the requests P1), P2) and P5) in Section E.1.1. Moreover, for $p > 1$, it follows that $1 + x \geq (1 + x^p)^{1/p}\ \forall x \geq 0$ (while the inequality inverts for $0 < p < 1$) so that the denominator of equation (E.12) stays below that of equation (E.11), correcting the total luminosity deficiency of the latter. Summarizing, the value of p_n is uniquely determined by the request that equation (E.12) satisfies P3), i.e. that

$$4\pi \int_0^\infty \nu_{\rm a}(r)\, r^2\, dr = L. \tag{E.14}$$

We numerically determined the values p_n that lead to the luminosity conservation for a selection of representative values of n: they are plotted in Figure E.1, and given in Table E.1. Notice how p_n is greater than one for $n \gtrsim 1.08$, and how it increases as expected for increasing n, converging to the limit[2] of $p_n \simeq 2.136$ for very large n. For $n \to 1$, the value of p_n drops below unity, and in fact in Appendix E.2.1 we will prove that $p(1) = 0$. When decreasing n further, the asymptotically matched deprojection $\nu_{\rm a}$ changes as in equation (E.18), and the function $p(n)$ then increases.

It is also useful to define the transition radius $r_{\rm t}$, depending on n, as the radius at which

[2] Volume integration of equation (E.12) in the limit of $n \to \infty$ can be performed noticing that the denominator of $\nu_{\rm a}$ tends to the constant $\left(1 + \pi^{p_n/2}\right)^{1/p_n}$, and an asymptotic analysis shows that the limit of p_n is given by the solution of $1 + \pi^{p_n/2} = 2^{p_n}$, in agreement with the value determined numerically and reported in the text.

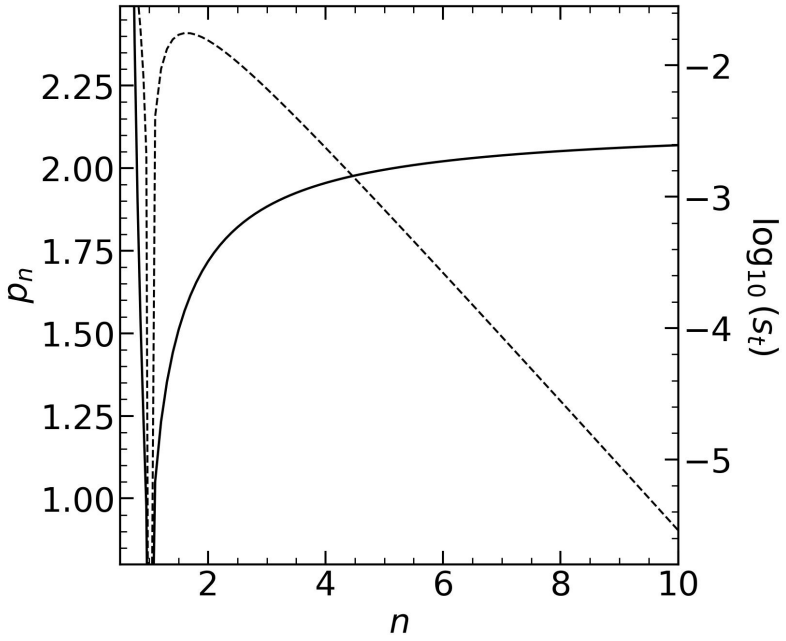


Figure E.1. Matching parameter p_n as a function of the Sérsic index n (solid line) determined by numerically solving equation (E.14), so that the total luminosity of the profile in equation (E.12) coincides with the one of the true profile. The dashed line shows the transition radius (here in units of R_e, and in logarithmic scale) as a function of n, as defined in equation (E.15).

Table E.1: Values of the matching parameter p_n for a grid of values of n. Two decimal digits of p_n are sufficient to guarantee that the total luminosity of $\nu_a(r)$ is practically the same as that of the Sérsic profile of given I_0, R_e and n, with relative differences smaller than 10^{-3} for all the values of n shown here; with three decimal digits, the differences become much smaller than 10^{-4}. For values of n which are not reported in the Table, $p(n)$ can be easily computed by numerical integration of equation (E.14), or by numerical interpolation of the values provided.

n	p_n	n	p_n	n	p_n	n	p_n	n	p_n	n	p_n	n	p_n
0.55	13.19	1.5	1.511	3.2	1.902	4.9	1.992	6.6	2.032	8.3	2.055	10.0	2.069
0.60	6.479	1.6	1.568	3.3	1.910	5.0	1.995	6.7	2.034	8.4	2.056	10.1	2.070
0.65	4.224	1.7	1.615	3.4	1.918	5.1	1.998	6.8	2.035	8.5	2.057	10.2	2.071
0.70	3.082	1.8	1.654	3.5	1.925	5.2	2.001	6.9	2.037	8.6	2.058	10.3	2.071
0.75	2.383	1.9	1.688	3.6	1.932	5.3	2.004	7.0	2.038	8.7	2.059	10.4	2.072
0.80	1.903	2.0	1.718	3.7	1.938	5.4	2.007	7.1	2.040	8.8	2.060	10.5	2.073
0.85	1.542	2.1	1.743	3.8	1.944	5.5	2.009	7.2	2.041	8.9	2.061	10.6	2.073
0.90	1.248	2.2	1.766	3.9	1.950	5.6	2.012	7.3	2.043	9.0	2.061	10.7	2.074
0.95	0.974	2.3	1.786	4.0	1.955	5.7	2.014	7.4	2.044	9.1	2.062	10.8	2.075
1.05	0.906	2.4	1.805	4.1	1.961	5.8	2.016	7.5	2.045	9.2	2.063	10.9	2.075
1.10	1.051	2.5	1.821	4.2	1.965	5.9	2.019	7.6	2.047	9.3	2.064	11.0	2.076
1.15	1.153	2.6	1.836	4.3	1.969	6.0	2.021	7.7	2.048	9.4	2.065	11.1	2.076
1.20	1.232	2.7	1.849	4.4	1.974	6.1	2.023	7.8	2.049	9.5	2.066	11.2	2.077
1.25	1.293	2.8	1.862	4.5	1.978	6.2	2.025	7.9	2.050	9.6	2.066	11.3	2.077
1.30	1.352	2.9	1.873	4.6	1.981	6.3	2.027	8.0	2.052	9.7	2.067	11.4	2.078
1.35	1.400	3.0	1.883	4.7	1.985	6.4	2.029	8.1	2.053	9.8	2.068	11.5	2.079
1.40	1.441	3.1	1.893	4.8	1.989	6.5	2.030	8.2	2.054	9.9	2.069	11.6	2.079

$\nu_i(r_t) = \nu_e(r_t)$; from equation (E.12), we have

$$s_t = \frac{r_t}{R_e} = \frac{1}{c_2^{2n}}. \tag{E.15}$$

Qualitatively, at distances from the center smaller than s_t, the profile is dominated by $\nu_i(r)$, while at larger radii the profile is increasingly better described by $\nu_e(r)$. In Figure E.1, the dashed line shows s_t as a function of n; notice the non-monotonicity at low values of $n \lesssim 2$, with a maximum of $s_t \simeq 0.02$ reached at $n \simeq 1.63$, and the following decrease to $s_t(4) \simeq 0.002$ and so on, with $s_t \to 0$ for $n \to 1$. In practice, s_t is always very small, an indication that $\nu(r)$ is almost completely dominated by the external asymptotic profile. For the sake of completeness, we notice that, for $n < 1$, s_t instead increases for decreasing n, as will be proved in Section E.2.1.

E.2.1 The $n \leq 1$ case

Having focused on the case of $n > 1$, representative of the majority of ETGs, it is now interesting to illustrate how the proposed approach works for the cases $n \leq 1$. We first show that the limit of equation (E.12) for $n \to 1^+$ and an arbitrary but fixed $p_n > 0$ converges to

$$\nu_a(r) = \frac{L}{R_e^3} \frac{b_n(1)^{5/2}}{(2\pi)^{3/2}} \frac{e^{-b_n(1)\, s}}{\sqrt{s}}. \tag{E.16}$$

In fact, both the coefficients c_1 and c_2 in equation (E.13) diverge for $n \to 1$, due to the divergence of the Beta function; in particular, the divergence of c_2 implies that, for arbitrary but fixed $p > 0$, the profile ν_a in equation (E.12) converges everywhere to the profile ν_e in equation (E.7). The volume integral of equation (E.16) gives a total luminosity of $3L/\left(2\sqrt{2}\right) \simeq 1.06\, L$. Therefore, for a generic but fixed $p > 0$, the total luminosity of the limit of our formula for $n \to 1$ does not converge to the total luminosity of the true $n = 1$ profile (even if quite close to it). In fact, this behavior is to be expected, as the limit of ν_a for $n \to 1$ should be taken not at a fixed p_n, but along a sequence of different $p_n(n)$ implicitly defined by equation (E.14). It immediately follows that $\lim_{n \to 1^+} p_n(n) = 0$, because for any strictly positive limit value $p_n(1) > 0$, equation (E.16) would be retrieved, so violating the total luminosity conservation. Indeed, we numerically find that $p(n)$ is already below unity for $n = 1.05$ (see Table E.1), with values monotonically decreasing for decreasing n towards unity.

We now consider the $n < 1$ profiles; for $0 < n < 1$, near the origin, $\nu(r)$ converges to a finite value as

$$\nu(r) \sim \frac{I_0}{R_e} \frac{b_n^n\, \Gamma(1-n)}{\pi}\, e^{-b_n\, s^{1/n}}, \quad r \to 0. \tag{E.17}$$

From equations (E.10) and (E.17) it follows that, for $1/2 < n < 1$, again $\nu_{\rm i}/\nu_{\rm e} \to \infty$ for $s \to \infty$, and $\nu_{\rm i}/\nu_{\rm e} \to 0$ for $s \to 0$; therefore, the arguments used to build equation (E.12) still apply, and

$$\nu_{\rm a}(r) = \frac{\nu_{\rm i}(r)}{\left\{1 + \left[\dfrac{\nu_{\rm i}(r)}{\nu_{\rm e}(r)}\right]^p\right\}^{1/p}} = \frac{L}{R_{\rm e}^3} \frac{c_1\, e^{-b_n\, s^{1/n}}}{\left[1 + c_2^{p_n}\, s^{p_n - p_n/(2n)}\right]^{1/p_n}}, \tag{E.18}$$

where the two coefficients are now defined as

$$c_1 \equiv \frac{b_n^{3n}\, \Gamma(1-n)}{2\pi^2\, n\, \Gamma(2n)}, \quad c_2 \equiv \sqrt{\frac{2n}{\pi}}\, b_n^{n-1/2}\, \Gamma(1-n). \tag{E.19}$$

For $n = 1/2$, the deprojected Sérsic profile is Gaussian:

$$\nu(r) = \frac{I_0}{R_{\rm e}} \sqrt{\frac{b}{\pi}}\, e^{-b_n(1/2)\, s^2} = \frac{L}{R_{\rm e}^3} \left[\frac{b_n(1/2)}{\pi}\right]^{3/2} e^{-b_n(1/2)\, s^2}, \tag{E.20}$$

where $b_n(1/2) = \ln 2$, and $\nu(r) = \nu_{\rm i}(r) = \nu_{\rm e}(r)$. This means that, for $n = 1/2$, the true deprojected profile coincides at all radii with the asymptotic profiles in equations (E.17) and (E.10). It follows that $\nu_{\rm i}(r)/\nu_{\rm e}(r) = 1$ everywhere, and so equations (E.18) and (E.14) require that $\lim_{n \to 1/2^+} p(n) = \infty$: this is nicely confirmed by the values of p_n in Table E.1.

As for the $n > 1$ case, it is natural to define a transition radius $r_{\rm t}$, and from equation (E.18) we obtain

$$s_{\rm t} = c_2^{\frac{2n}{1-2n}}. \tag{E.21}$$

Again, a careful asymptotic analysis shows that $s_{\rm t} \sim \pi\,(n-1)^2/\left[2\, b_n(1)\right]$ for $n \to 1^-$, while $\lim_{n \to 1/2^+} s_{\rm t} = e^{-(1+\gamma)/2}/(2\sqrt{\ln 2}) \simeq 0.273$, in agreement with Figure E.1; however, notice that for $n = 1/2$ the concept of transition radius loses its meaning, as $\nu_{\rm i}(r) = \nu_{\rm e}(r)$ everywhere.

For the sake of completeness, we also consider the range $0 < n < 1/2$, where the situation changes. In fact, now $\nu_{\rm i}/\nu_{\rm e} \to 0$ for $s \to \infty$, and it diverges for $s \to 0$: therefore, equation (E.18) with a positive p_n fail to reproduce the correct asymptotic trends of the true profile. However, it is not difficult to show that $\nu_{\rm a}(r)$ in equation (E.18) with negative values of p_n recovers the asymptotic trends of the true deprojected $\nu(r)$.

E.2.2 Generalization to ellipsoidal density distributions

Here we report the very useful generalization of the formula to axisymmetric and triaxial ellipsoidal systems, which is basically immediate. In fact, in order to get a Sérsic profile for triaxial system of total luminosity L stratified on

$$m^2 = \frac{x^2}{a^2} + \frac{y^2}{q_y^2\, a^2} + \frac{z^2}{q_z^2\, a^2}, \quad q_y \equiv \frac{b}{a}, \quad q_z \equiv \frac{c}{a}, \quad a > b > c, \tag{E.22}$$

one substitutes in the expression for $\nu_{\rm a}(r)$ in equation (E.12) the scaled radius s with m, and $R_{\rm e}$ with a; then, one divides the resulting formula by the product $q_y\, q_z$, so that the total luminosity is independent of the flattening. The projection of $\nu_{\rm a}$ for such a triaxial system at any inclination of the line of sight can be done as described in Chapter 11 in C21. In particular, it turns out that a is the semimajor axis of the effective isophotal ellipse when projecting $\nu_{\rm a}(m)$ along the intermediate (y) or short (z) axis, and its value coincides with $R_{\rm e}$ of the spherical limit of $\nu_{\rm a}(m)$. This ellipsoidal generalization of $\nu_{\rm a}(r)$ could be a useful improvement for the modeling technique based on triaxial Sérsic ellipsoids presented in van de Ven and van der Wel (2021).

E.3 Accuracy of the new formula

To test the accuracy of our formula, we compute the relative error profile

$$\mathcal{E}(r) \equiv \frac{\nu_{\rm a}(r) - \nu(r)}{\nu(r)}, \tag{E.23}$$

where $\nu(r)$ is the numerically deprojected profile. As $\nu(r)$ diverges at the center for $n \geq 1$, a poor treatment of the integral in equation (E.4) can easily lead to a significant accuracy loss for small radii, affecting in turn the robustness of $\mathcal{E}(r)$. In order to control the deprojection, we started from equation (7) of C91 (which holds for generic $n > 0$), written in terms of the reduced radius $\alpha \equiv b_n\, s^{1/n}$ and where the central divergence of $\nu(r)$ for $n > 1$ is factored out:

$$\nu(r) = \frac{I_0}{R_{\rm e}} \frac{b_n^n\, \alpha^{1-n}}{\pi} \int_1^\infty \frac{{\rm e}^{-\alpha\, t}\, dt}{\sqrt{t^{2n}-1}}$$
$$= \frac{I_0}{R_{\rm e}} \frac{b_n^n\, \alpha^{1-n}\, e^{-\alpha}}{n\, \pi} \int_0^\infty \frac{e^{-\alpha\left[\left(x^2+1\right)^{1/(2n)}-1\right]}}{\left(x^2+1\right)^{1-1/(2n)}}\, dx. \tag{E.24}$$

where in the second line we adopted the substitution $x = \sqrt{t^{2n}-1}$, so that the new integrand is free of the singularity, and the numerical stability is further improved; in this way, the resulting integral becomes convergent. Motivated by the functional form of equations (E.9) and (E.10), we also factored out the exponential term $e^{-\alpha}$. For reference, in analogy with equation (E.24), we also give the integral expression of $\nu(r)$ to be used for high-accuracy deprojection when $n < 1$:

$$\nu(r) = \frac{I_0}{R_{\rm e}} \frac{b_n^n\, {\rm e}^{-\alpha}}{n\, \pi} \int_0^\infty \frac{e^{-\left[\left(x^2+\alpha^{2n}\right)^{1/(2n)}-\alpha\right]}}{\left(x^2+\alpha^{2n}\right)^{1-1/(2n)}}\, dx, \tag{E.25}$$

obtained with the change of variable $x = t/\alpha^n$ in equation (E.24). Notice that equation (E.25) avoids the problem of equation (E.24) when used with $n < 1$, i.e. that the factor α^{1-n} therein vanish for $s \to 0$, and the integral diverges, as obvious from the fact that $\nu(0)$ is finite for $n < 1$.

In the left panel of Figure E.2, we show the profile of $\mathcal{E}(r)$ for three representative values of n. The results are surprisingly good and qualitatively similar for all values of n, with accuracy increasing for increasing n. In general, $\nu_{\rm a}(r)$ tends to overestimate the true $\nu(r)$ at small radii before converging to it (by construction) for $r \to 0$. Similarly, at large radii, $\nu_{\rm a}(r)$ tends to underestimate the true profile before converging to it (by construction) for $r \to \infty$. This behavior is due to the fact that while $\nu_{\rm a}(r)$ lies below $\nu_{\rm i}(r)$ and $\nu_{\rm e}(r)$, the leading terms $\nu_{\rm i}(r)$ and $\nu_{\rm e}(r)$ remain above the true $\nu(r)$. In the central regions, $\nu(r) < \nu_{\rm a}(r) < \nu_{\rm i}(r)$, and at outer radii $\nu_{\rm a}(r) < \nu(r) < \nu_{\rm e}(r)$; of course, for $r \to 0$ and $r \to \infty$, the two inequalities become equalities. Table E.2 reports (with its sign) the maximum relative deviation of $\mathcal{E}(r)$ over the whole radial range, and the radius $s^{\rm max}$ at which the maximum deviation is reached. As shown also in the left panel of Figure E.2, $s^{\rm max}$ moves toward the center and $\mathcal{E}^{\rm max}$ decreases for increasing n. When $s^{\rm max} < 10^{-4}$ (corresponding to models with $n \gtrsim 4.2$), the largest deviation is reached at radii which are too small to have an astrophysical meaning for continuous stellar density profiles, and in the $\mathcal{E}^{\rm max}$ column we just report the value of $\mathcal{E}$ at $s = 10^{-4}$. In general, due to the shape of

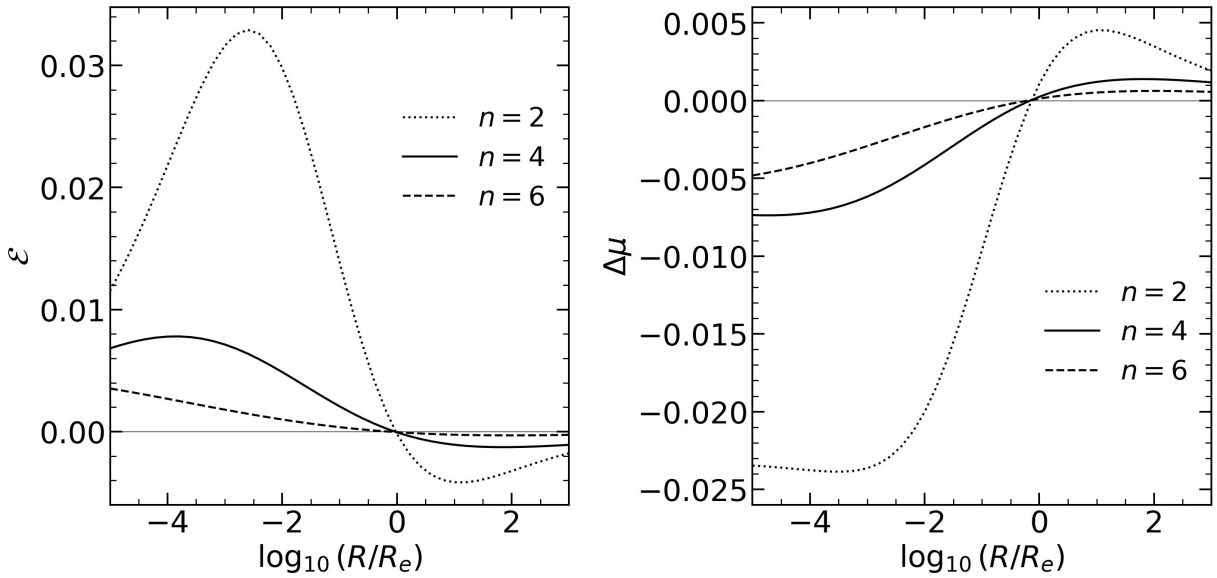


Figure E.2. Left panel: radial profile of $\mathcal{E}(r)$ as defined in equation (E.23) for three representative values of $n > 1$. Right panel: radial profile of $\Delta\mu(R)$ as defined in equation (E.26), for the same values of n.

$\mathcal{E}(r)$, this value is the maximum deviation for all $s > 10^{-4}$.

To quantify the deviation of $\nu_{\rm a}(r)$ from the true profile, we also considered the difference (in magnitudes) between the Sérsic profile in equation (E.1), and the profile $I_{\rm a}(R)$ obtained by projecting (edge-on) $\nu_{\rm a}(r)$:

$$\Delta\mu(R) \equiv -2.5 \log \frac{I_{\rm a}(R)}{I(R)}. \tag{E.26}$$

In the right panel of Figure E.2, we show $\Delta\mu(R)$ for the same values of $n = 2$, 4, 6. The behavior is qualitatively similar for all $n > 1$, and the errors are extremely small, decreasing for increasing n; this confirms that the accuracy of $\nu_{\rm a}(r)$ allows to use this formula for all practical applications. In the last two columns of Table E.2, we report the value of the largest magnitude difference, and the radius at which it is reached, for different values of $n > 1$; again, when this deviation is reached inside $s = 10^{-4}$, we give the magnitude difference at $s = 10^{-4}$.

As a last test, in Figure E.3 we show the analogous of Figure E.2, but comparing our formula to the widely used Mellier and Mathez (1987) profile, where β_n is given in Lima Neto, Gerbal, and Márquez (1999). Notice that, especially at low and large radii, the difference between the two profiles is apparent, allowing for a more accurate modeling of dynamical quantities in these two regimes. Of course, it is particularly important that the errors of our formula compare well with those obtained from other high-accuracy fitting methods as well (see e.g. Figure 4 of Vitral and

n	$\mathcal{E}^{\max}$	$\log s^{\max}$	$\Delta\mu^{\max}$	$\log \eta^{\max}$
1.5	0.089	−2.616	−0.047	−3.778
2.0	0.033	−2.591	−0.024	−3.499
2.5	0.018	−2.789	−0.015	−3.624
3.0	0.012	−3.071	−0.011	−3.911
3.5	0.009	−3.445	−0.009	−4.000
4.0	0.008	−3.854	−0.007	−4.000
4.5	0.007	−4.000	−0.006	−4.000
5.0	0.006	−4.000	−0.005	−4.000
5.5	0.005	−4.000	−0.005	−4.000
6.0	0.004	−4.000	−0.004	−4.000
6.5	0.004	−4.000	−0.003	−4.000
7.0	0.003	−4.000	−0.003	−4.000
7.5	0.003	−4.000	−0.003	−4.000
8.0	0.003	−4.000	−0.003	−4.000
8.5	0.002	−4.000	−0.002	−4.000
9.0	0.002	−4.000	−0.002	−4.000
9.5	0.002	−4.000	−0.002	−4.000
10	0.002	−4.000	−0.002	−4.000

Table E.2: Largest relative errors and magnitude difference between our formula and the true profile. First column: Sérsic index n. Second column: largest relative error of $\nu_{\rm a}(r)$ in equation (E.12) compared to the true, numerically deprojected $\nu(r)$ in equation (E.24), computed from $\mathcal{E}(r)$ in equation (E.23). Third column: radius (in units of $R_{\rm e}$) of $\mathcal{E}^{\max}$; when $s^{\max} < 10^{-4}$, the deviation at $s = 10^{-4}$ is shown. Fourth column: largest surface brightness difference (in magnitudes) between the true Sérsic profile and the projection of $\nu_{\rm a}(r)$, as computed from $\Delta\mu(R)$ in equation (E.26). Fifth column: projected radius (in units of $R_{\rm e}$) $\eta^{\max}$ of $\Delta\mu^{\max}$; when $\eta^{\max} < 10^{-4}$, the magnitude deviation at $\eta = 10^{-4}$ is shown.

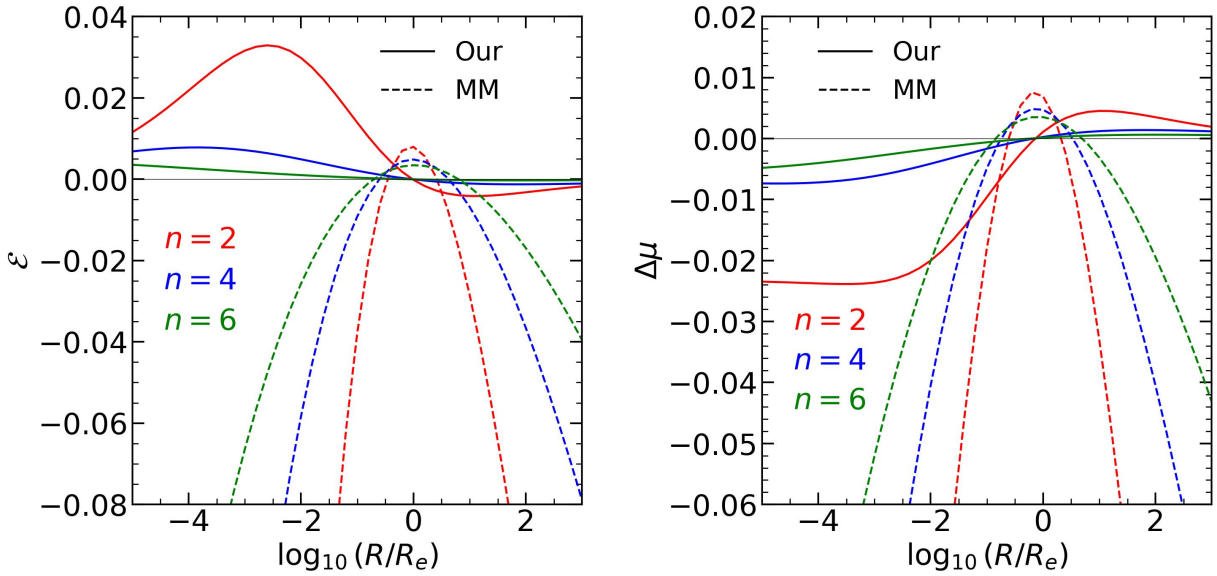


Figure E.3. Same as in Figure E.2, but comparing the errors between our formula and the true profile (solid line) with those relative to the Mellier and Mathez (1987) profile (dashed line), where the β_n parameter is given in Lima Neto, Gerbal, and Márquez (1999).

Mamon 2020): however, they are now associated with a mathematically motivated, algebraically simple, and (except for the p_n value) fully analytical formula, which is not the result of a fit.

APPENDIX F

Ellipsoidal power-law models

With the aid of simple power-law models that allow for a fully analytical treatment, we investigate the underlying reasons for the results obtained numerically for the more realistic ellipsoidal models in Sections 4.1 and 4.2. For all the models in this Appendix, the general considerations at the beginning of Section 4.1 show that $[\rho_*, \Phi] \geq 0$ and $D \leq 0$ everywhere.

This Appendix is structured as follows. In Appendix F.1, we discuss the very idealized case of a power-law density profile in a dominant logarithmic potential with same flattening, so that $[\rho_*, \Phi_\mathrm{h}] = 0$ everywhere, and the general considerations in Section 3.3.2 can be retrieved. Then, in Appendix F.2 we analyze the case of a power-law density profile in a dominant SIS potential, which is indicative of the behavior of halo-dominated models. Finally, in Appendix F.3 we repeat the analysis for a dominant monopole potential, representative of any finite-mass model at large distances from the center.

F.1 Power-law density profile in a dominant logarithmic potential

We consider an ellipsoidal, power-law stellar density profile with finite central density ρ_0, minor-to-major semiaxes ratio q and density slope $0 < \gamma < 3$:

$$\rho_* = \frac{\rho_0}{q m^\gamma}, \quad m = \sqrt{\frac{R^2}{a_*^2} + \frac{z^2}{q^2\, a_*^2}}; \tag{F.1}$$

for the remainder of the Appendix, all lengths are intended normalized to some scale length a_*, and densities to ρ_0. The stellar density is embedded in a dominant DM halo with potential

$$\Phi_{\rm h} = v_{\rm h}^2 \ln m, \tag{F.2}$$

where $v_{\rm h}$ is the circular velocity, and the flattening is the same of the stellar density profile; in the following, all the potentials and squared velocities are in units of $v_{\rm h}^2$. From equations (2.24) and (2.25), it follows that

$$\rho_* \sigma_z^2 = \frac{q^{\gamma-1}}{\gamma\,(q^2R^2+z^2)^{\gamma/2}}, \qquad [\rho_*, \Phi_{\rm h}] = 0, \tag{F.3}$$

so that $\sigma_z^2 = 1/\gamma$, independent of q. Moreover, from equations (2.26), (3.4) and (3.6) we have

$$D = -\frac{q^{\gamma+1}}{R^{1+\gamma}\,(q^2+s^2)^{\gamma/2+1}}, \qquad s \equiv \frac{z}{R}, \tag{F.4}$$

$$B = \frac{(1-\gamma)\,q^2+s^2}{\gamma\,(q^2+s^2)} = -\,C, \tag{F.5}$$

so that the B and C functions are constant on straight lines $z = s\,R$, and $\mathscr{B}^- = \mathscr{C}^+$ and $\mathscr{B}^+ = \mathscr{C}^-$. For $\gamma < 1$, $\mathscr{B}^+$ covers the whole (R,z)-plane; otherwise, for $\gamma \geq 1$, $\mathscr{B}^-$ is the portion of the (R,z)-plane below the $\mathscr{B}^0$ curve

$$z = q\,\sqrt{\gamma-1}\,R, \tag{F.6}$$

so that $\mathscr{B}^-$ becomes larger for increasing q and γ.

The limits for $b(z)$ can easily be obtained. Because $[\rho_*, \Phi] = 0$ everywhere, equations (3.13), (3.15) and (3.16) show that $b_0 = b_1 = b_2 = 1$, while from equation (3.11) (for $\gamma > 1$) we get

$$b_{\rm M} = \frac{\gamma}{\gamma-1}, \tag{F.7}$$

independently of z and q. Therefore, $b_{\rm M}$ decreases for increasing γ; however, for this simple class of models, no dependency on the stellar density flattening is present.

In Figure F.1, we show the $\overline{v_\varphi^2}$, Δ_R and Δ fields for the model with $\gamma = 2$ and $q = 0.5$, and for three different values of constant b. We see that the negativity regions are now delimited by

straight lines, as $\mathscr{B}^-$ and $\mathscr{C}^-$, and the behavior of the fields with b is analogous to that discussed in Section 3.3.2; as $\gamma > 1$, the upper limit $b_{\rm M}$ exists, and so both $\overline{v_\varphi^2}$ and Δ become negative for $b > b_{\rm M}$. In Figure F.2, instead, we show the effects of varying the density (and potential) flattening q. We see that increasing the flattening (for $\gamma > 1$) makes the $\mathscr{B}^- = \mathscr{C}^+$ region smaller, as the negativity regions of $\overline{v_\varphi^2}$ and Δ inside it; notice however that $b_{\rm M}$ is independent of the flattening, so that both Δ_R and Δ remain negative somewhere for $b = 2.5$. In Figure F.3, instead, we investigate the effects of changing γ: increasing the parameter makes $\mathscr{B}^-$ and the negativity regions larger, as now $b_{\rm M}$ decreases, but the effects are globally less relevant than those produced by changing q. Finally, in Figure F.4 we show the case with $\gamma = 1$ and $q = 0.5$. Notice that, as $\mathscr{B}^- = \mathscr{C}^+ = \emptyset$, the $\overline{v_\varphi^2}$ and Δ fields both remain positive and continue to increase everywhere for increasing b; instead, as for the other cases, $\Delta_R < 0$ for $b > 1$, and $\Delta < 0$ over $\mathscr{C}^-$ (i.e., everywhere) for $b < 1$.

F.2 Power-law density profile in a dominant singular isothermal sphere

In this model, the stellar density profile is the same as in equation (F.1), while the (dominant) DM halo potential is modeled as a SIS, i.e. by fixing $q = 1$ in equation (F.2). In the following, all the lengths are normalized to a_*, densities to ρ_0, and potential and squared velocities to $v_{\rm h}^2$. From Exercise 13.31 in C21, we have:

$$\begin{cases} \rho_* \sigma_z^2 = \dfrac{q^{\gamma-1} R^{-\gamma}}{2(1-q^2)^{\gamma/2}} \mathrm{B}_x\left(\dfrac{\gamma}{2}, 1-\dfrac{\gamma}{2}\right), \\ \\ [\rho_*, \Phi_{\rm h}] = \dfrac{\gamma q^{\gamma-1} R^{-\gamma-1}}{2(1-q^2)^{\gamma/2}} \mathrm{B}_x\left(1+\dfrac{\gamma}{2}, -\dfrac{\gamma}{2}\right), \end{cases} \tag{F.8}$$

where $\mathrm{B}_x(a,b)$ is the Euler incomplete beta function (see Appendix A.1), and

$$x \equiv \frac{(1-q^2)R^2}{R^2+z^2} = \frac{1-q^2}{1+s^2}; \quad s \equiv \frac{z}{R}. \tag{F.9}$$

Also for these models, σ_z^2, $R\,[\rho_*, \Phi_{\rm h}]\,/\rho_*$ and $R\,\partial\Phi_{\rm h}/\partial R$ are constant on the straight lines $z = s\,R$; in the spherical limit, $\sigma_z^2 = 1/\gamma$ and $[\rho_*, \Phi_{\rm h}] = 0$ as for the model in Section F.1, while in the oblate case $[\rho_*, \Phi_{\rm h}] \geq 0$ everywhere. For reference, in Figure F.5, we show the three kinematic

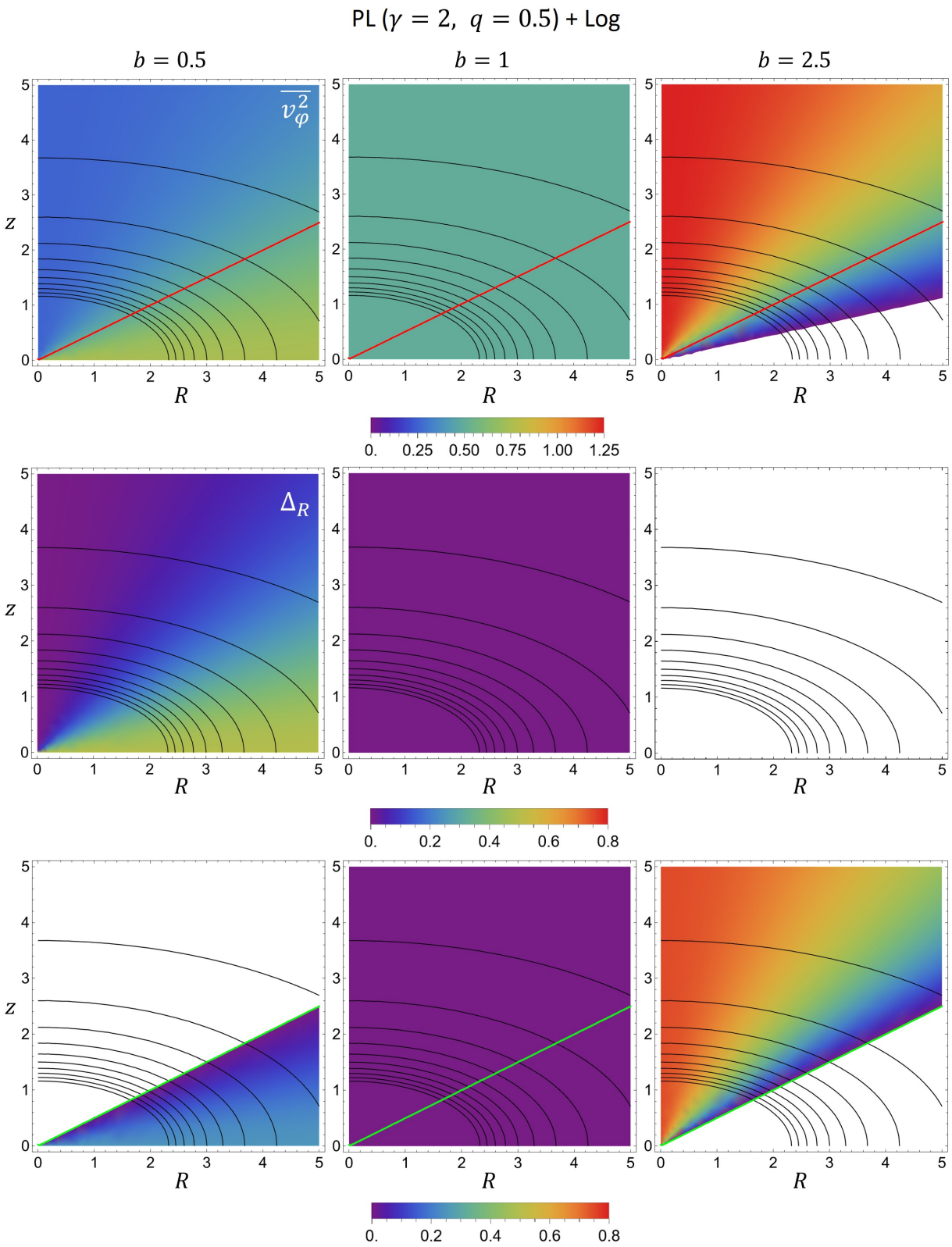


Figure F.1. Maps in the (R, z)-plane of $\overline{v_\varphi^2}$ (top row), Δ_R (central row) and Δ (bottom row), in units of v_h^2, for the power-law ellipsoid with $\gamma = 2$ and $q = 0.5$ in a dominant logarithmic potential of same flattening, for constant $b = 0.5$ (left column), $b = 1$ (central column) and $b = 2.5$ (right column). Black solid lines show equally spaced isodensity contours of the stellar distribution. The red and green lines show, respectively, the $\mathscr{B}^0$ and $\mathscr{C}^0$ curves, while $\mathscr{D}^0$ coincides with the z-axis. White regions correspond to negative values of the fields.

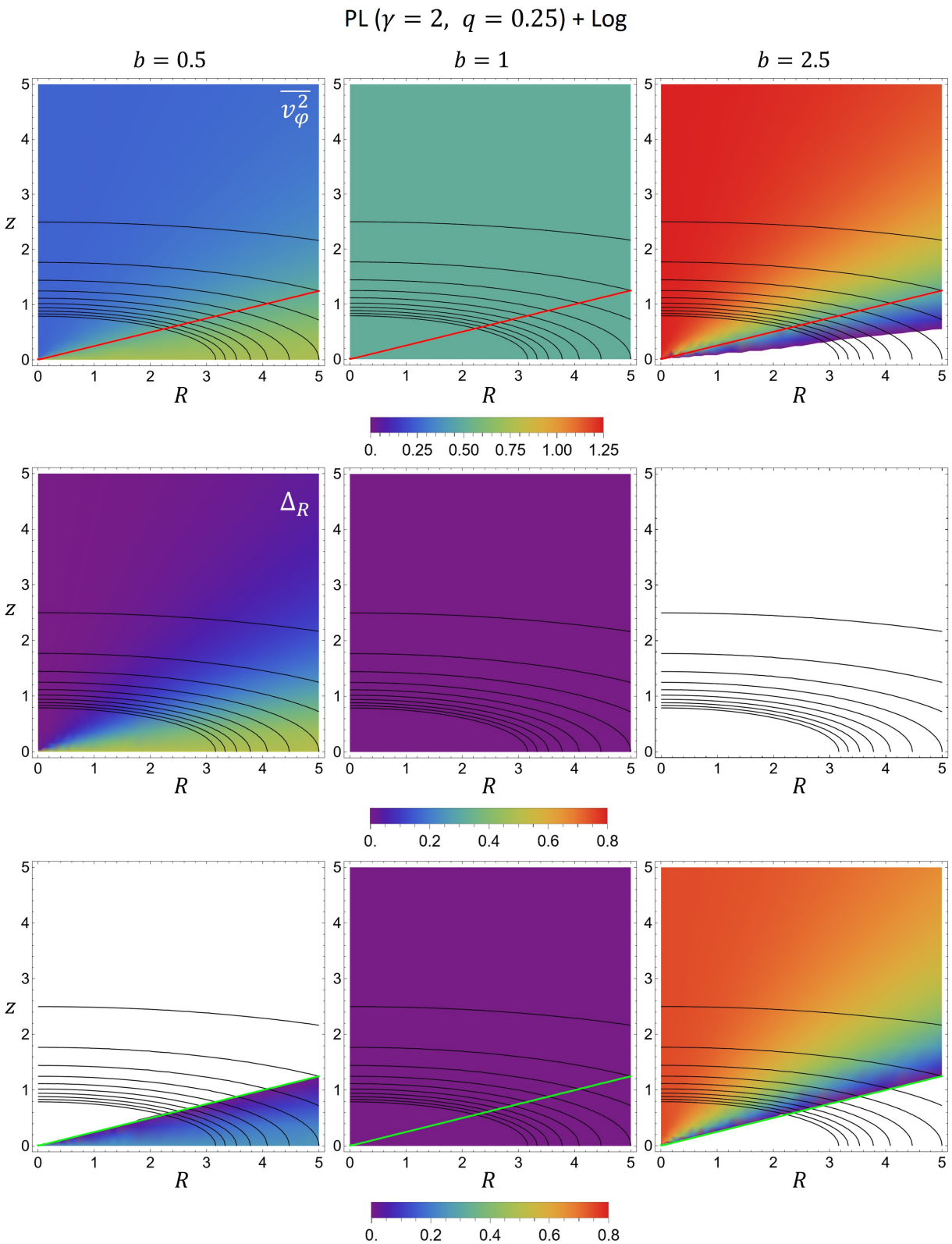


Figure F.2. Same as in Figure F.1, but for $q = 0.25$.

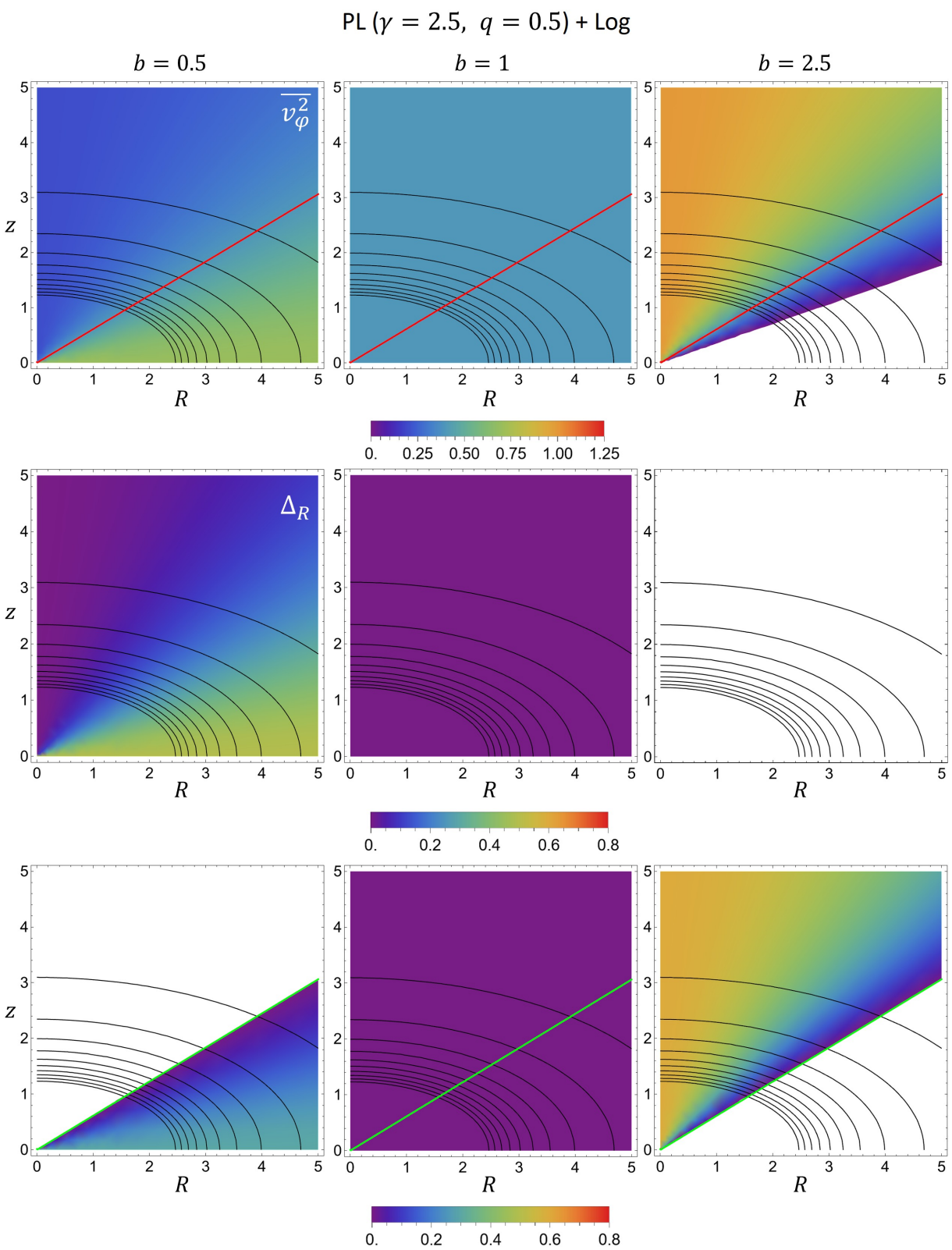


Figure F.3. Same as in Figure F.1, but for $\gamma = 2.5$.

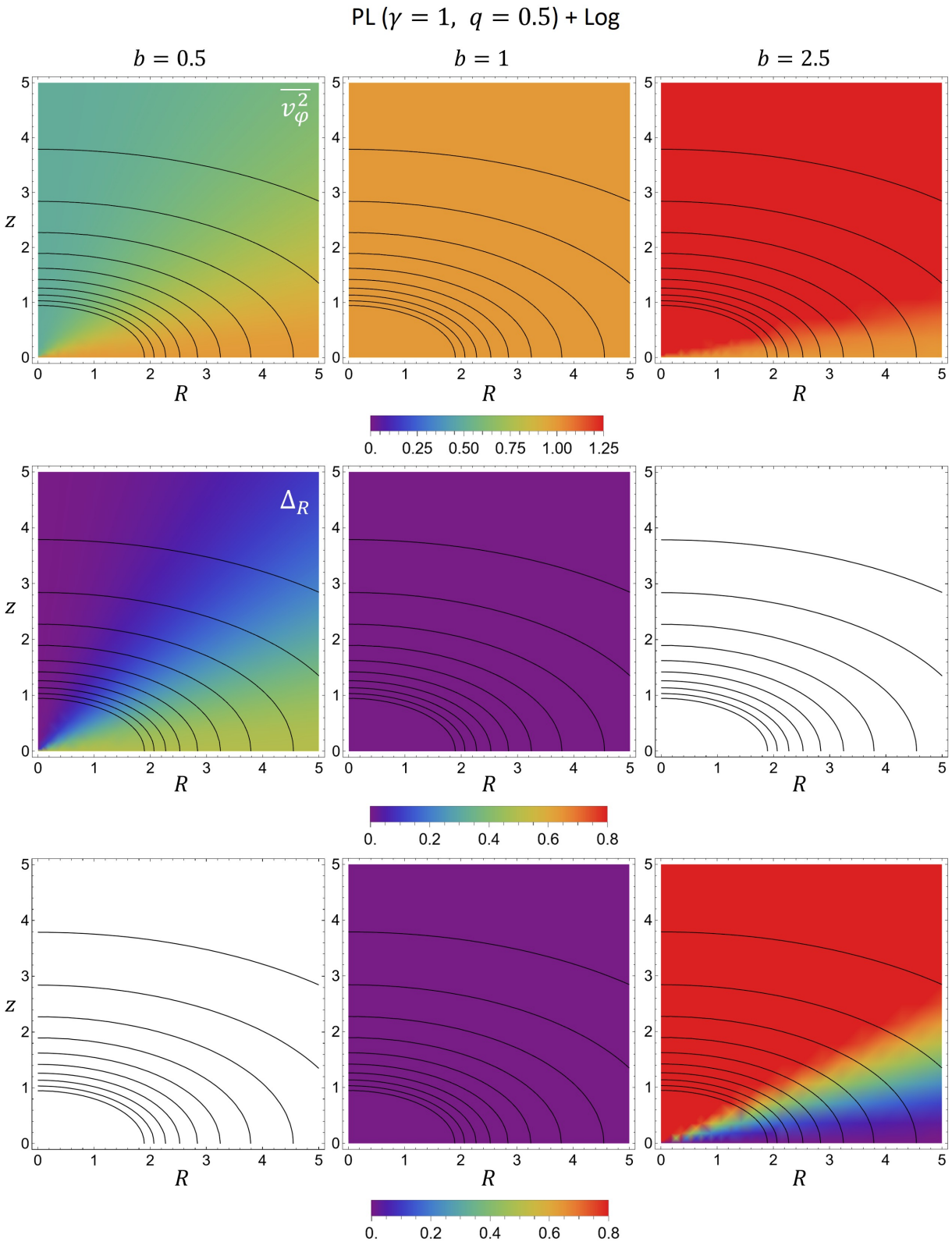


Figure F.4. Same as in Figure F.1, but for $\gamma = 1$. In this case, $\mathscr{B}^+ = \mathscr{C}^-$ covers the whole (R, z)-plane.

fields for different values of γ and q. We see that increasing γ slightly decrease σ_z^2 everywhere and increase $R\left[\rho_*, \Phi_{\rm h}\right]/\rho_*$ near the equatorial plane, while decreasing q has the more relevant effect of decreasing σ_z^2 close to the equatorial plane, and increasing $R\left[\rho_*, \Phi_{\rm h}\right]/\rho_*$ in the same region; by construction, the $R\,\partial\Phi_{\rm h}/\partial R$ field is always the same.

The D, B and C functions can be obtained from equations (2.26), (3.4), and (3.6) as:

$$D = \frac{q^{\gamma-1}}{R^{\gamma+1}}\left[\frac{s^2\left(q^2+s^2\right)^{-\gamma/2}}{1+s^2} - \frac{\gamma\,\mathrm{B}_x\left(\gamma/2, 1-\gamma/2\right)}{2\left(1-q^2\right)^{\gamma/2}}\right], \tag{F.10}$$

$$B = \frac{s^2}{1+s^2} + \frac{1-\gamma}{2}\left(\frac{q^2+s^2}{1-q^2}\right)^{\gamma/2}\mathrm{B}_x\left(\frac{\gamma}{2}, 1-\frac{\gamma}{2}\right), \tag{F.11}$$

$$C = \frac{1}{1+s^2} - \frac{1}{2}\left(\frac{q^2+s^2}{1-q^2}\right)^{\gamma/2}\mathrm{B}_x\left(\frac{\gamma}{2}, 1-\frac{\gamma}{2}\right); \tag{F.12}$$

in particular, as for the model in Section F.1, $\mathscr{B}^+$ covers the whole (R,z)-plane for $\gamma \leq 1$. In the spherical limit, the D, B, and C functions are elementary, and are given by equations (F.4) and (F.5) with $q = 1$. In the top panels of Figure F.6, the red and green curves show, respectively, the B and C functions for three different values of q at fixed γ, and for three different values of γ at fixed q. The $\mathscr{B}^-$ region, represented in the bottom panels of the same Figure, corresponds to the condition $s \leq s_{\mathscr{B}}$, where $s_{\mathscr{B}}$ is given by $B(s_{\mathscr{B}}) = 0$; therefore, $\mathscr{B}^-$ becomes larger (i.e., the intersection point $s_{\mathscr{B}}$ moves to the right) for increasing q and γ. Analogously, the $\mathscr{C}^-$ region corresponds to the condition $s \leq s_{\mathscr{C}}$, where $s_{\mathscr{C}}$ is given by $C(s_{\mathscr{C}}) = 0$; we see that $\mathscr{C}^-$ becomes larger for increasing q and decreasing γ. Notice how the separation between $\mathscr{B}^0$ and $\mathscr{C}^0$ (i.e.. the $\mathscr{B}^+ \cap \mathscr{C}^+$ region) becomes smaller as q increases, with $s_{\mathscr{B}} = s_{\mathscr{C}} = 1$ and $\mathscr{B}^0 = \mathscr{C}^0$ in the spherical case. Finally, from numerical inspection of the C function, it is found that for each γ there exists a critical value of the flattening $q_{\mathscr{C}}(\gamma)$ such that, for $q \geq q_{\mathscr{C}}$, $\mathscr{C}^-$ covers the whole (R,z)-plane. We find that $q_{\mathscr{C}}(\gamma)$ is a monotonic function, with $q_{\mathscr{C}} \leq 1$ for $\gamma \leq 1$ (being equal to 1 for $\gamma = 1$), and $q_{\mathscr{C}} > 1$ for $\gamma > 1$; therefore, the models in the Figure all present a $\mathscr{C}^-$ region.

The limits for $b(z)$ can be easily determined thanks to the fact that all the relevant functions are stratified on straight lines; therefore, the problem reduces to the study of a function of one variable, and the resulting minimum (or maximum) is a constant depending of γ and q, but independent of z. From equation (3.11) (for $\gamma > 1$), the $\mathscr{B}_z^-$ set is identified with the range $0 < s < s_{\mathscr{B}}(\gamma, q)$, and the minimum is reached for $s = 0$ (i.e., on the equatorial plane) as

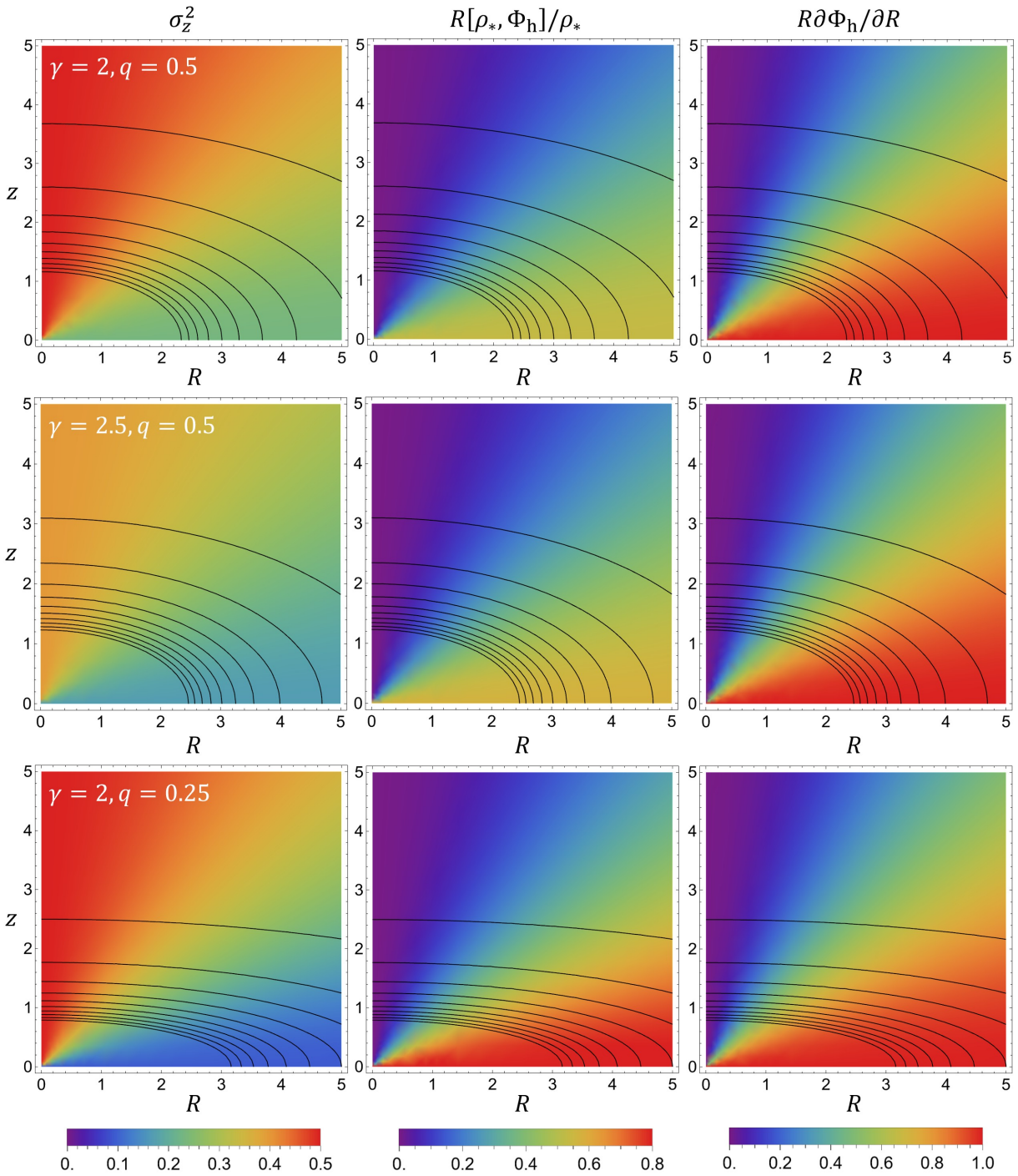


Figure F.5. Maps in the (R, z)-plane of σ_z^2 (left column), $R\,[\rho_*, \Phi_h]\,/\rho_*$ (central column) and $R\,\partial\Phi_h/\partial R$ (right column), in units of v_h^2, for the power-law ellipsoid in a dominant SIS, for different values of γ and q. Black solid lines show equally spaced isodensity contours.

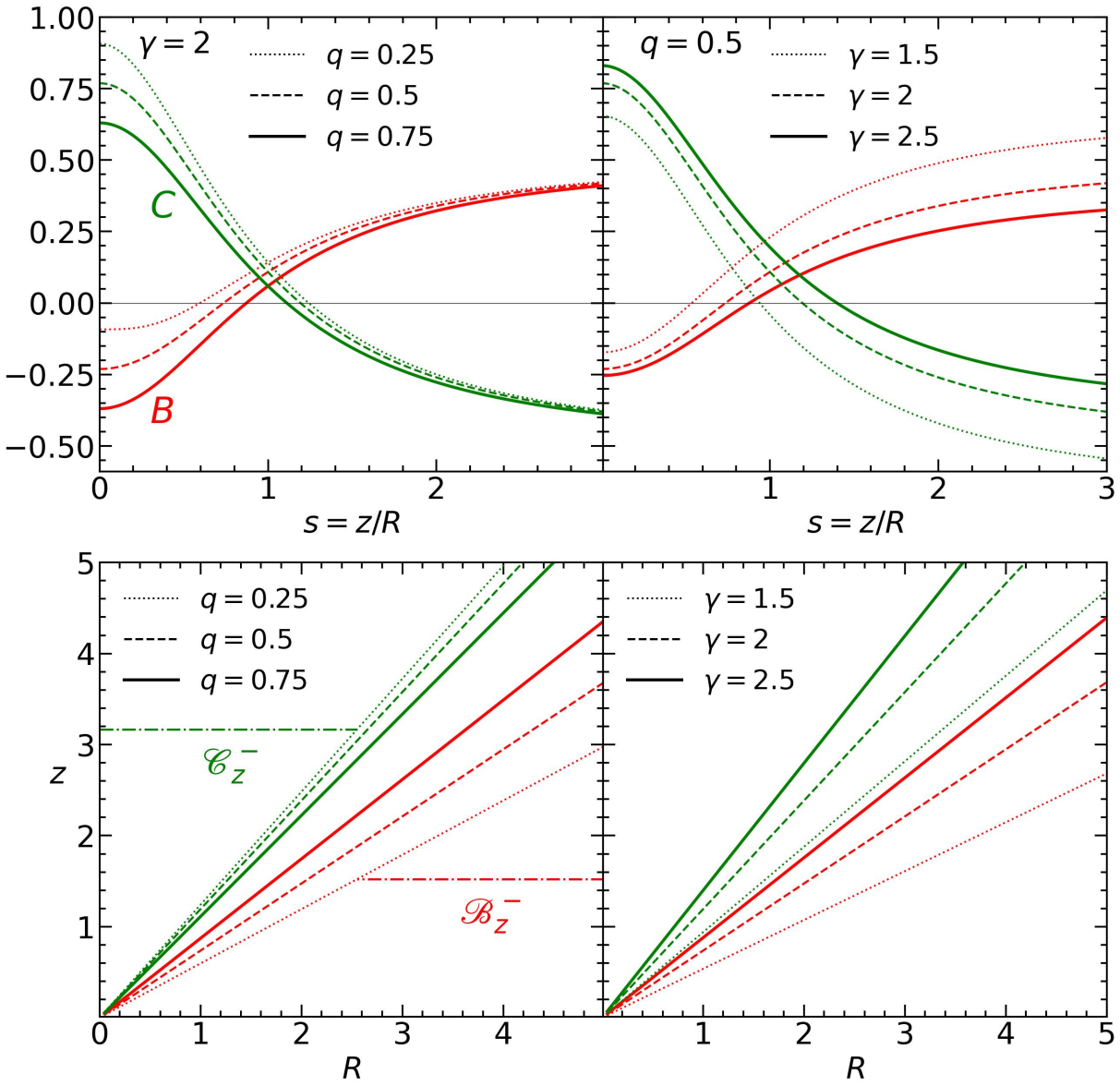


Figure F.6. Top panels: The B (red) and C (green) functions in equations (F.10) and (F.11) for the power-law ellipsoid in a dominant SIS, for $\gamma = 2$ and different values of q (left panel), and for $q = 0.5$ and different values of γ (right panel). For each model, the intersection point of B and C with the axis of abscissae gives the critical slopes, respectively, $s_{\mathscr{B}}(q,\gamma)$ and $s_{\mathscr{C}}(q,\gamma)$. Bottom panels: The $\mathscr{B}^0$ (red) and $\mathscr{C}^0$ (green) curves for the same models in the top panels, where $\mathscr{B}^-$ is the region below $\mathscr{B}^0$, and $\mathscr{C}^-$ is the region above $\mathscr{C}^0$; two radial sections of $\mathscr{B}^-$ and $\mathscr{C}^-$ at fixed z are also shown.

$$b_{\rm M} = \frac{2\,(1/q^2-1)^{\gamma/2}}{\mathrm{B}_{1-q^2}\,(\gamma/2, 1-\gamma/2)}, \tag{F.13}$$

with $b_{\rm M}(1) = \gamma/(\gamma-1)$ in the spherical limit; notice that $b_{\rm M}$ decreases for increasing q and decreasing γ. From equation (3.13), with $\mathscr{D}^-$ covering the whole (R,z)-plane, the minimum is reached for $s \to \infty$ (i.e., on the z-axis) as

$$b_0 = \frac{2+\gamma}{2+\gamma\,q^2}, \tag{F.14}$$

where $b_0 = 1$ in the spherical limit, as expected; analogously to $b_{\rm M}$, b_0 decreases for increasing q and decreasing γ. Finally, for the two functions in equations (3.15) and (3.16), the intervals of s where to look for the maximum or minimum are, respectively, $s_{\mathscr{C}} < s < \infty$ and $0 < s < s_{\mathscr{B}}$. We verify that $b_1 = 1$ independently of γ, while for $\gamma > 1$

$$b_2 = \frac{1}{\gamma-1}\left[\frac{2\,(1/q^2-1)^{\gamma/2}}{\mathrm{B}_{1-q^2}\,(\gamma/2, 1-\gamma/2)} - 1\right], \tag{F.15}$$

where the minimum is reached for $s = 0$; as expected, $b_2 = 1$ in the spherical limit, and again it decreases for increasing q and decreasing γ. These constraints are shown as a function of q in the bottom-right panel of Figure 4.13, for the representative case of $\gamma = 2$; the monotonic trend with increasing q is apparent, analogously to the other models in the Figure.

Finally, in Figure F.7 we show $\overline{v_\varphi^2}$, Δ_R and Δ for the model with $\gamma = 2$ and $q = 0.5$, for three different values of constant b. Given that both the $\mathscr{B}^-$ and $\mathscr{C}^-$ regions exist, the behavior of the fields with b is the one discussed in Section 3.3.1, with all the functions stratified on straight lines. For comparison, in Figure F.8 we show the same fields for a lower q: the effect is apparent, as the negativity regions reduce or even disappear (being the limits for b higher), and the fields globally increase. In Figure F.9, instead, we see that increasing γ slightly decreases the values of the fields, making the negativity regions larger; however, this effect is not so large as the one produced by the variation of q. Finally, in Figure F.10 we show the case with $\gamma = 1$ and $q = 0.5$. As $\mathscr{B}^- = \emptyset$, the $\overline{v_\varphi^2}$ and Δ fields both continue to increase everywhere for increasing b-anisotropy; however, as for the other cases, $\Delta_R < 0$ for high values of b, and $\Delta < 0$ in $\mathscr{C}^-$ for $b < 1$.

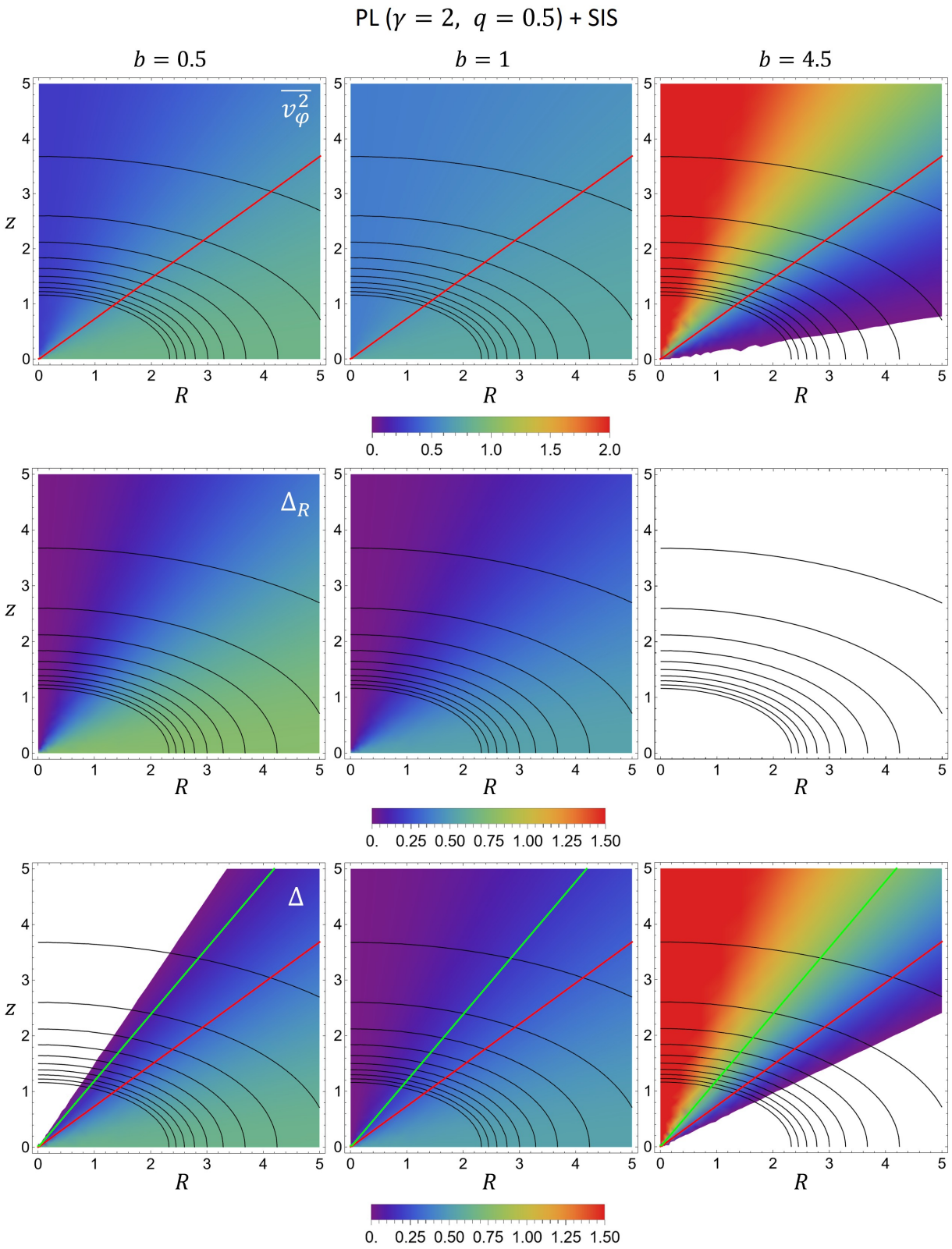


Figure F.7. Maps in the (R, z)-plane of $\overline{v_\varphi^2}$ (top row), Δ_R (central row) and Δ (bottom row), in units of v_h^2, for the power-law ellipsoid with $\gamma = 2$ and $q = 0.5$ in a dominant SIS, and constant $b = 0.5$ (left column), $b = 1$ (central column) and $b = 4.5$ (right column). Black solid lines show equally spaced isodensity contours of the stellar distribution. The red and green lines show, respectively, the $\mathscr{B}^0$ and $\mathscr{C}^0$ curves, while $\mathscr{D}^0$ coincides with the z-axis. White regions correspond to negative values of the fields.

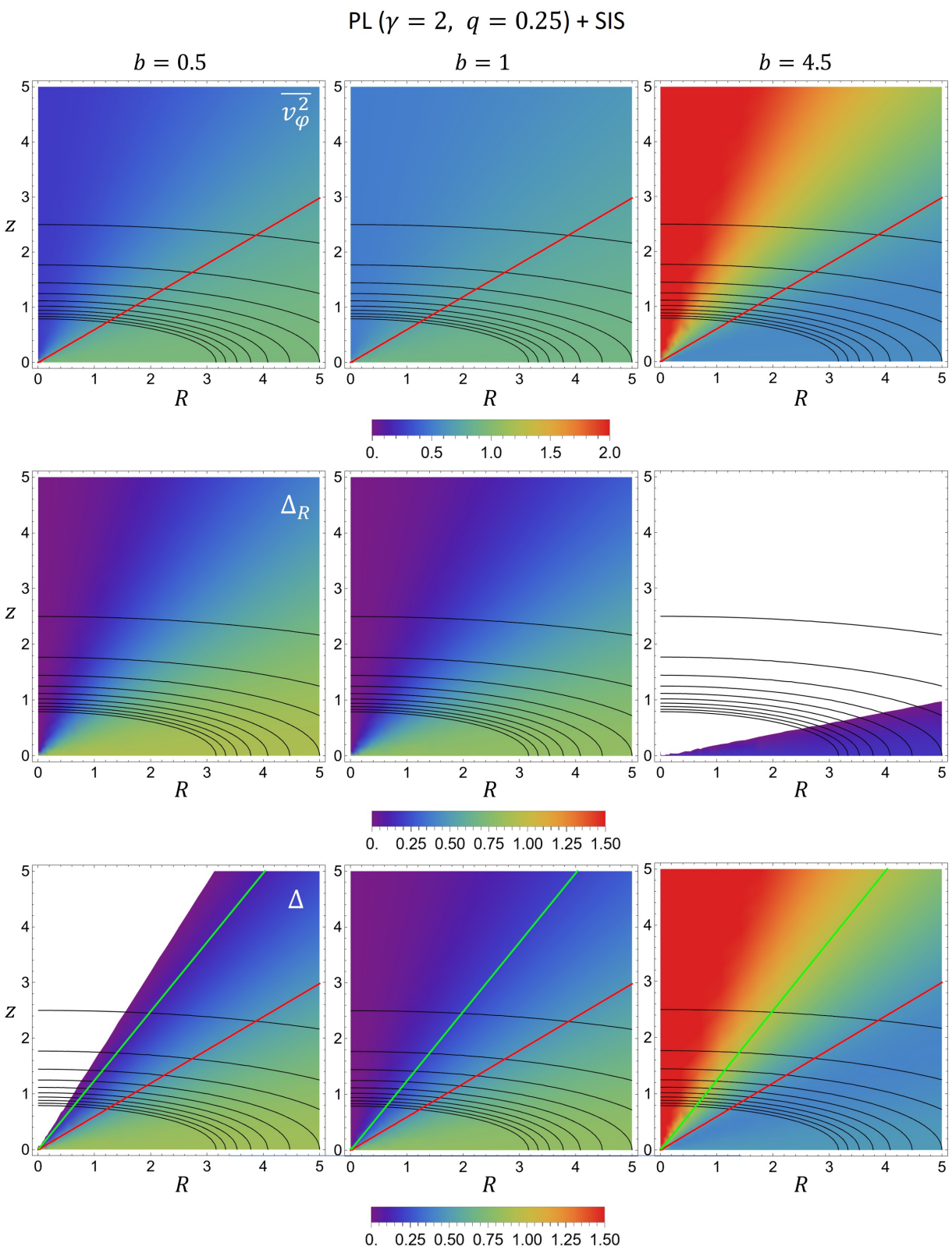


Figure F.8. Same as in Figure F.7, but for $q = 0.25$.

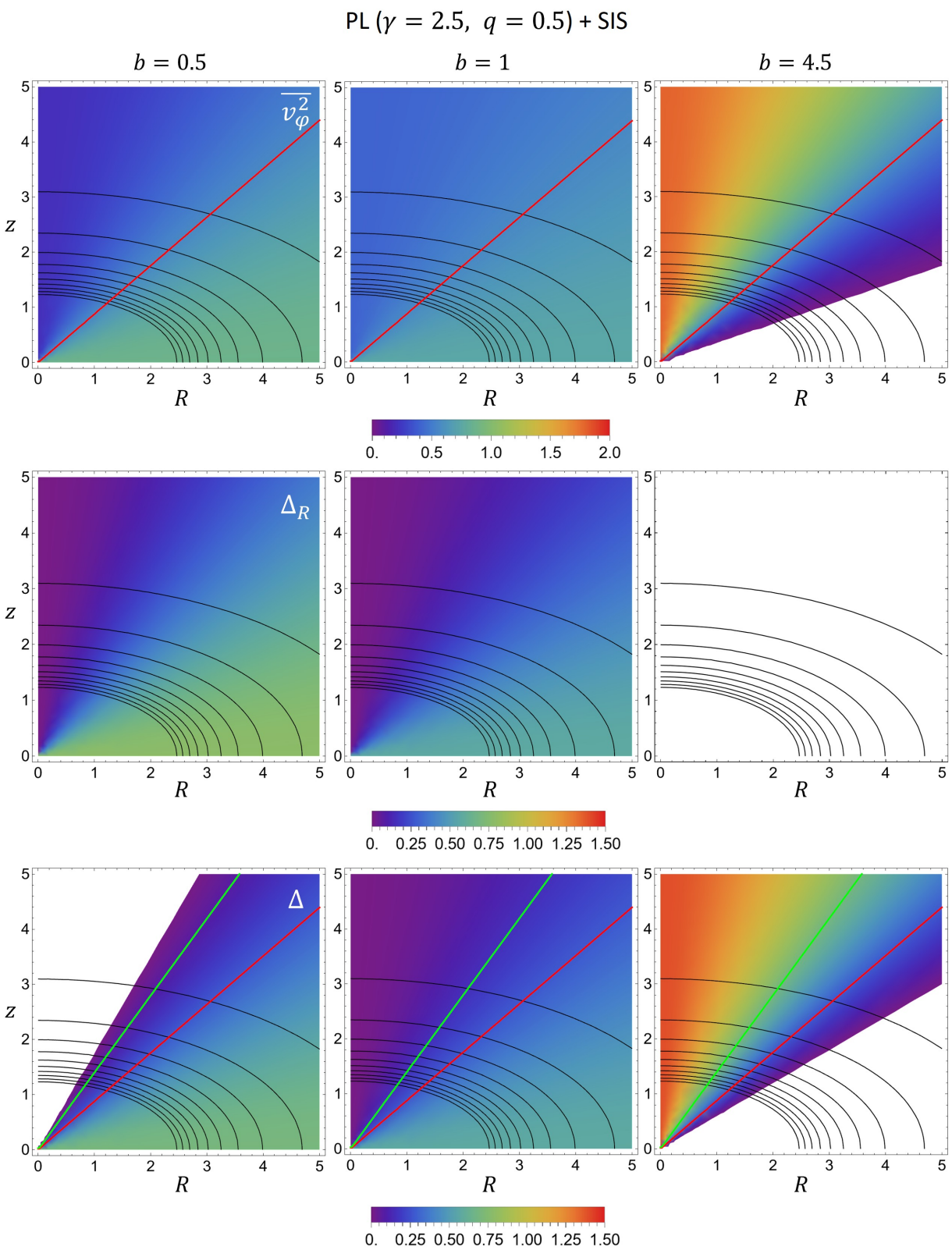


Figure F.9. Same as in Figure F.7, but for $\gamma = 2.5$.

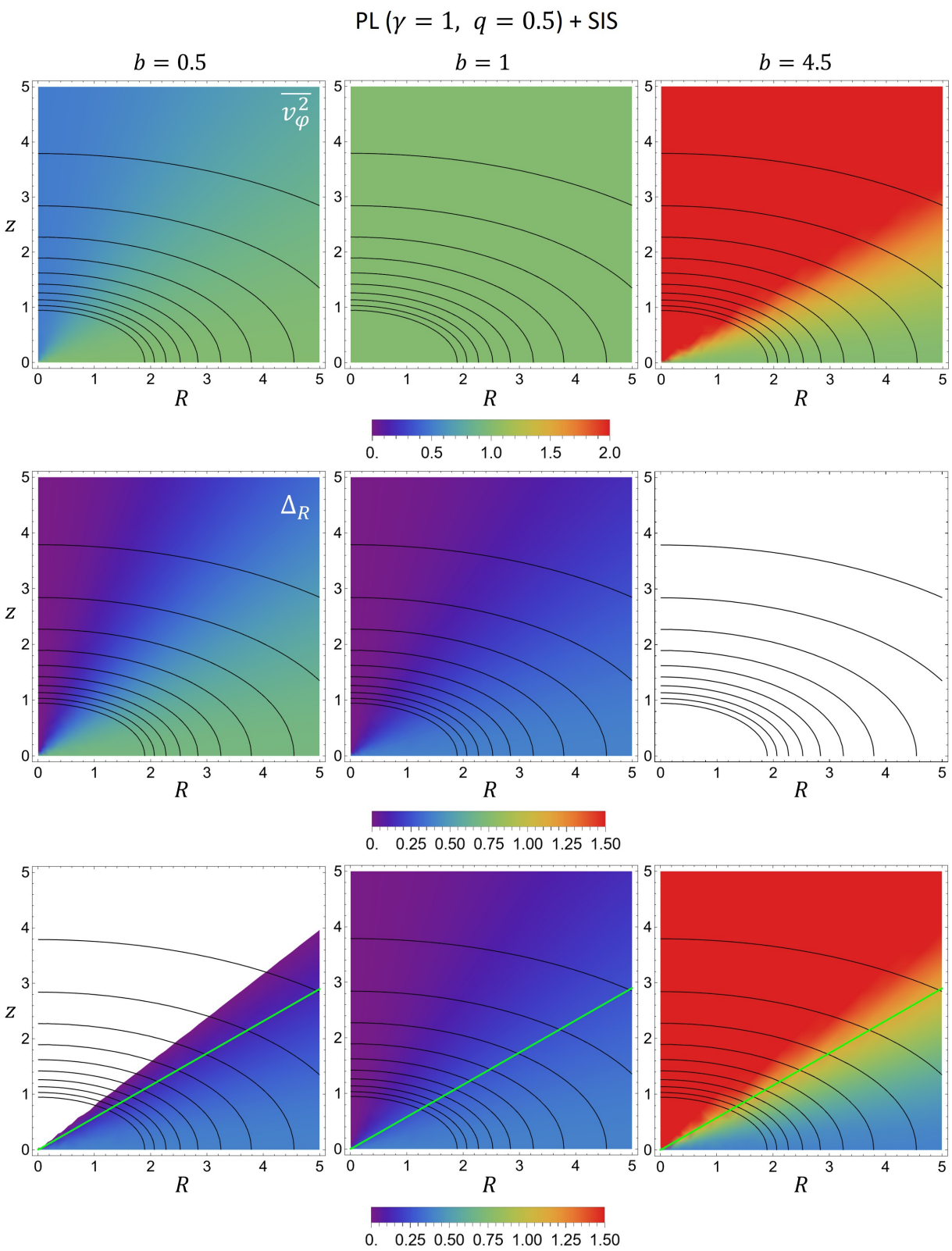


Figure F.10. Same as in Figure F.7, but for $\gamma = 1$. In this case, $\mathscr{B}^+$ covers the whole (R, z)-plane.

F.3 Power-law density profile in a dominant monopole potential

The stellar density profile of these models is the same as in equation (F.1), while the (dominant) DM halo potential is now modeled as a monopole potential $\Phi_{\rm h} = -GM/r$; therefore, it can be interpreted as the case of a central dominant black hole, or as the potential at large radii of a finite mass system, as the ones discussed before. In the following, all the lengths are normalized to a_*, densities to ρ_0, and potential and squared velocities to GM/a_*. From Exercise 13.31 in C21, we have:

$$\begin{cases} \rho_* \sigma_z^2 = \dfrac{q^{\gamma-1}\, R^{-\gamma-1}}{2\,(1-q^2)^{(\gamma+1)/2}}\, \mathrm{B}_x\left(\dfrac{\gamma+1}{2}, 1-\dfrac{\gamma}{2}\right), \\ \\ [\rho_*, \Phi_{\rm h}] = \dfrac{\gamma\, q^{\gamma-1}\, R^{-\gamma-2}}{2\,(1-q^2)^{\gamma/2}}\, \mathrm{B}_x\left(\dfrac{\gamma+3}{2}, -\dfrac{\gamma}{2}\right), \end{cases} \tag{F.16}$$

where x is defined in equation (F.9); in the spherical limit ($q = 1$), $\sigma_z^2 = 1/[(\gamma+1)r]$, and $[\rho_*, \Phi_{\rm h}] = 0$. For reference, in Figure F.11 we show the σ_z^2, $R\,[\rho_*, \Phi_{\rm h}]\,/\rho_*$ and $R\,\partial\Phi_{\rm h}/\partial R$ fields for different values of γ and q. Compared to Figure F.5, we see that the effects of changing the two parameters is much less apparent for this model, apart from a slight decrease of σ_z^2 and increase of $R\,[\rho_*, \Phi_{\rm h}]\,/\rho_*$ near the equatorial plane for decreasing q.

The D, B and C functions are given by

$$D = \frac{q^{\gamma-1}}{R^{\gamma+2}}\left[\frac{s^2\,(q^2+s^2)^{-\gamma/2}}{(1+s^2)^{3/2}} - \frac{\gamma+1}{2\,(1-q^2)^{\frac{\gamma+1}{2}}}\, \mathrm{B}_x\left(\frac{\gamma+1}{2}, 1-\frac{\gamma}{2}\right)\right], \tag{F.17}$$

$$B = \frac{1}{R}\left[\frac{s^2}{(1+s^2)^{3/2}} - \frac{\gamma\,(q^2+s^2)^{\gamma/2}}{2\,(1-q^2)^{\frac{\gamma+1}{2}}}\, \mathrm{B}_x\left(\frac{\gamma+1}{2}, 1-\frac{\gamma}{2}\right)\right], \tag{F.18}$$

$$C = \frac{1}{R}\left[\frac{1}{(1+s^2)^{3/2}} - \frac{(q^2+s^2)^{\gamma/2}}{2\,(1-q^2)^{\frac{\gamma+1}{2}}}\, \mathrm{B}_x\left(\frac{\gamma+1}{2}, 1-\frac{\gamma}{2}\right)\right]; \tag{F.19}$$

in the spherical limit, these functions are elementary, and in particular B is negative for $s < \sqrt{\gamma}$, i.e. a straight line with a slope steeper than that in equation (F.6). In analogy with Figure F.6, in the top panels of Figure F.12 we investigate the positivity of B and C for different values of q and γ; in particular, we notice that while B and C are not scale-free, their sign is given by the functions in the square brackets, which depend only on s. The $\mathscr{B}^-$ regions, represented in the

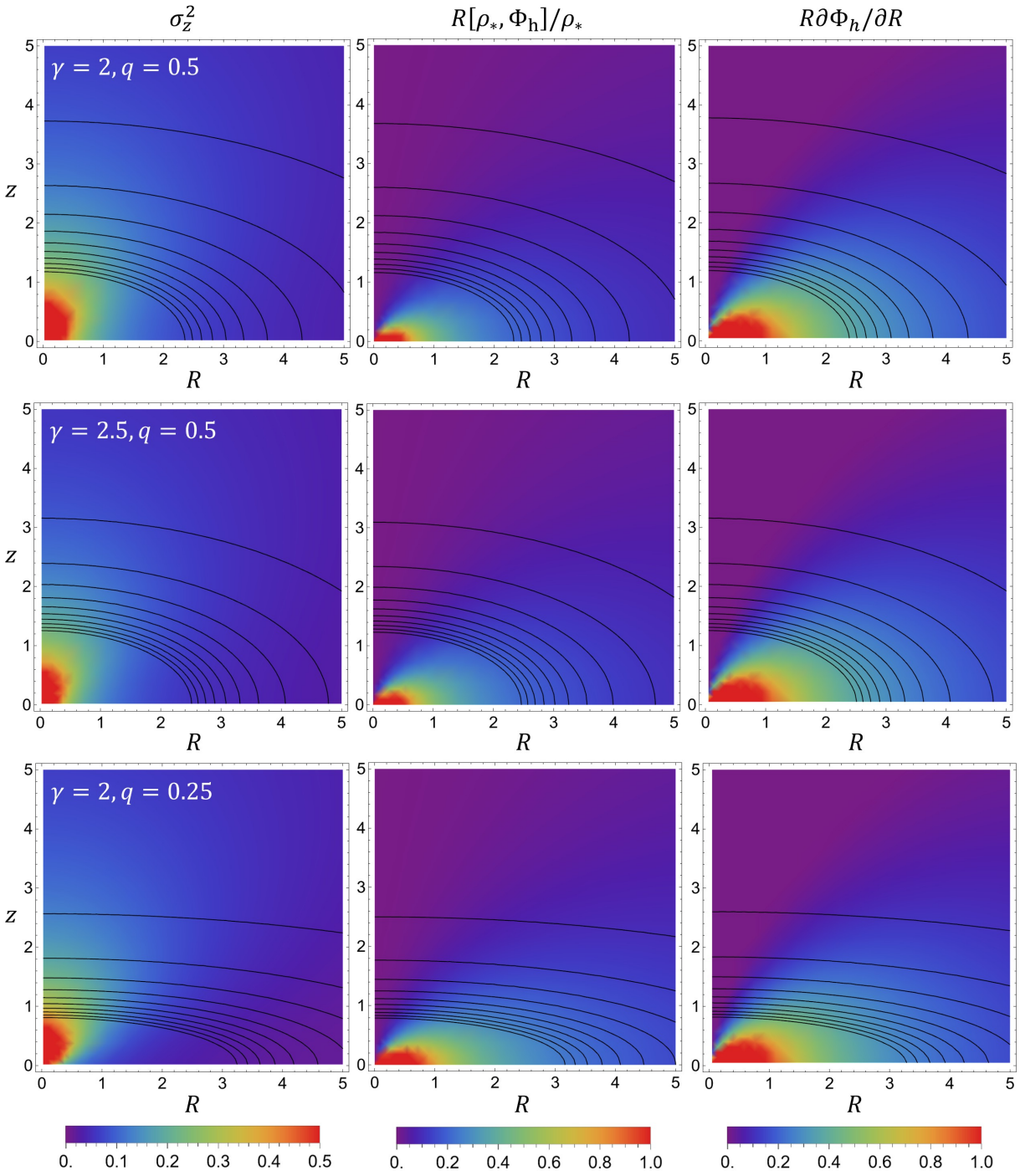


Figure F.11. Maps in the (R, z)-plane of σ_z^2 (left column), $R\left[\rho_*, \Phi_\mathrm{h}\right]/\rho_*$ (central column), and $R\partial\Phi_\mathrm{h}/\partial R$ (right column), in units of GM/a_*, for the power-law ellipsoid in a dominant monopole potential, for different values of γ and q. Black solid lines show equally spaced isodensity contours.

bottom panels of the same Figure, correspond to the condition $s \leq s_{\mathscr{B}}$, where $s_{\mathscr{B}}$ is the value of s such that $RB = 0$; we see that $\mathscr{B}^-$ becomes larger for increasing q and γ. Analogously, the $\mathscr{C}^-$ regions correspond to $s \leq s_{\mathscr{C}}$, where $s_{\mathscr{C}}$ is the value of s such that $RC = 0$; we see that $\mathscr{C}^-$ becomes larger for increasing q and decreasing γ. As expected, the separation between $\mathscr{B}^0$ and $\mathscr{C}^0$ (i.e., the region $\mathscr{B}^+ \cap \mathscr{C}^+$) becomes smaller as q increases, with $s_{\mathscr{B}} = s_{\mathscr{C}} = 1$ and $\mathscr{B}^0 = \mathscr{C}^0$ in the spherical case.

Concerning the limits for b, we repeat the analysis of Appendix F.2, and we retrieve all the trends with the flattening q. In particular,

$$b_{\rm M} = \frac{2\,q\,(1/q^2-1)^{(\gamma+1)/2}}{\gamma\,{\rm B}_{1-q^2}\,(1/2+\gamma/2, 1-\gamma/2)}, \tag{F.20}$$

with $b_{\rm M} = \gamma/(\gamma-1)$ in the spherical case, and

$$b_0 = \frac{3+\gamma}{3+\gamma q^2}; \tag{F.21}$$

moreover, $b_1 = 1$ and

$$b_2 = \frac{1}{\gamma}\left[\frac{2\,q\,(1/q^2-1)^{(1+\gamma)/2}}{{\rm B}_{1-q^2}\,(1/2+\gamma/2, 1-\gamma/2)} - 1\right], \tag{F.22}$$

with $b_0 = b_1 = b_2 = 1$ in the spherical limit. In the bottom-right panel of Figure 4.13, we show all the functions above for the illustrative case of $\gamma = 2$. As for the other models, all the limits decrease for increasing q, and $b_{\rm M}$ and b_0 both decrease for increasing γ; the behavior of b_2 with γ, instead, is less trivial.

Finally, in Figure F.13 we show the $\overline{v_\varphi^2}$, Δ_R and Δ fields for the model with $\gamma = 2$ and $q = 0.5$, for three different values of constant b. The global behavior of the fields is analogous to that shown in Figure F.7 in the case of a SIS halo, but in this case the critical $\mathscr{B}^0$ and $\mathscr{C}^0$ curves are steeper. For comparison, in Figures F.14 and F.15 we show the same fields for, respectively, a lower q and a higher γ. We see that the effects due to a change of flattening are again the most dominant ones, and they are analogous to those explored in the previous models; in particular, the negativity regions reduce or disappear for sufficiently high b (as all the limits have increased).

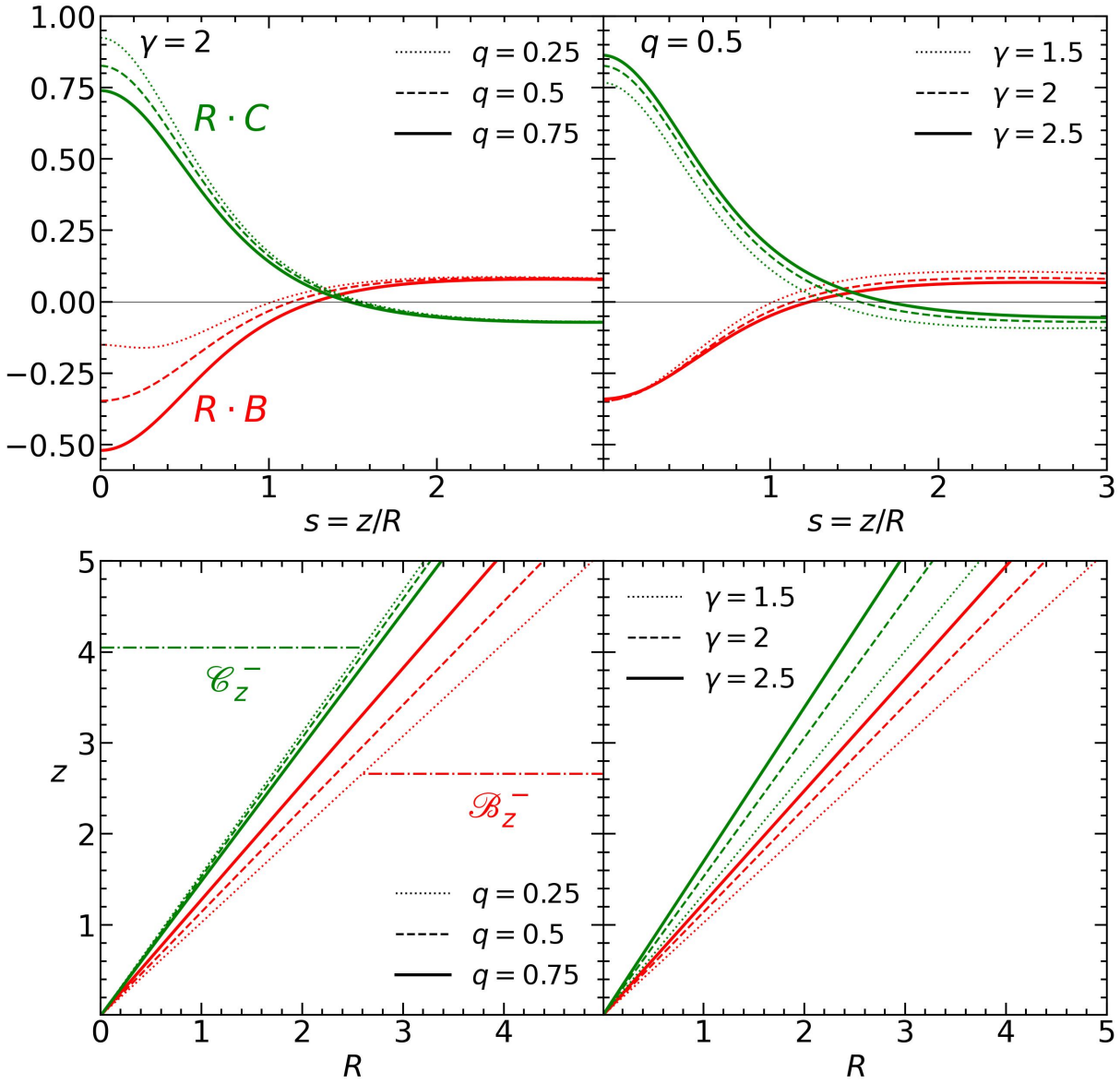


Figure F.12. Top panels: The B (red) and C (green) functions in equations (F.10) and (F.11) (multiplied by R, to study their positivity as a function of s) for the power-law ellipsoid in a dominant monopole potential, for $\gamma = 2$ and different values of q (left panel), and for $q = 0.5$ and different values of γ (right panel). For each model, the intersection point of B and C with the axis of abscissae gives the critical slopes, respectively, $s_{\mathscr{B}}(q,\gamma)$ and $s_{\mathscr{C}}(q,\gamma)$. Bottom panels: The $\mathscr{B}^0$ (red) and $\mathscr{C}^0$ (green) curves for the same models in the top panels, where $\mathscr{B}^-$ is the region below $\mathscr{B}^0$, and $\mathscr{C}^-$ is the region above $\mathscr{C}^0$; two radial sections of $\mathscr{B}^-$ and $\mathscr{C}^-$ at fixed z are also shown.

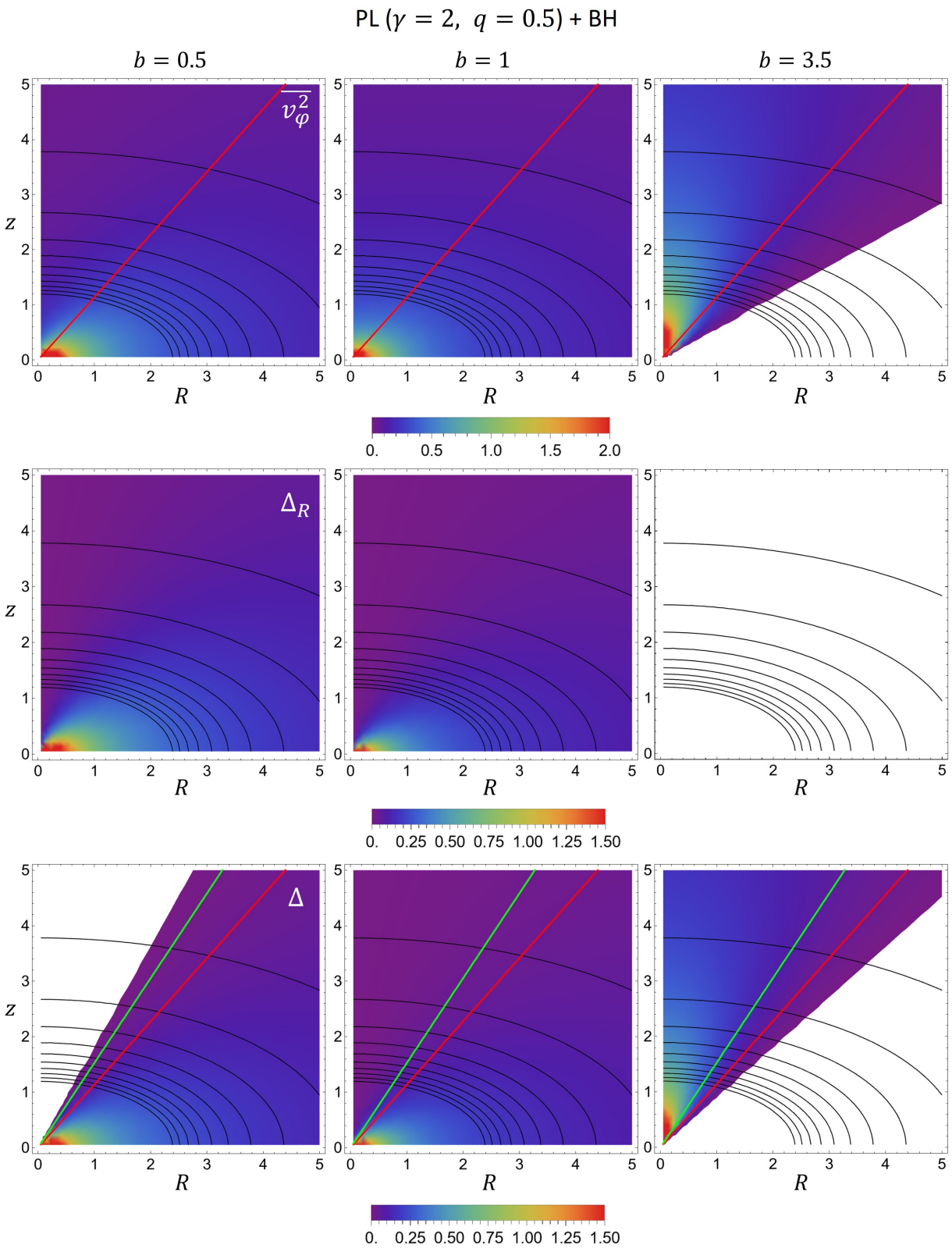


Figure F.13. Maps in the (R, z)-plane of $\overline{v_\varphi^2}$ (top row), Δ_R (central row) and Δ (bottom row), in units of GM/a_*, for the power-law ellipsoid with $\gamma = 2$ and $q = 0.5$ in a dominant monopole potential, for constant $b = 0.5$ (left column), $b = 1$ (central column) and $b = 4.5$ (right column). Black solid lines show equally spaced isodensity contours of the stellar distribution. The red and green lines show, respectively, the $\mathscr{B}^0$ and $\mathscr{C}^0$ curves, while $\mathscr{D}^0$ coincides with the z-axis. White regions correspond to negative values of the fields.

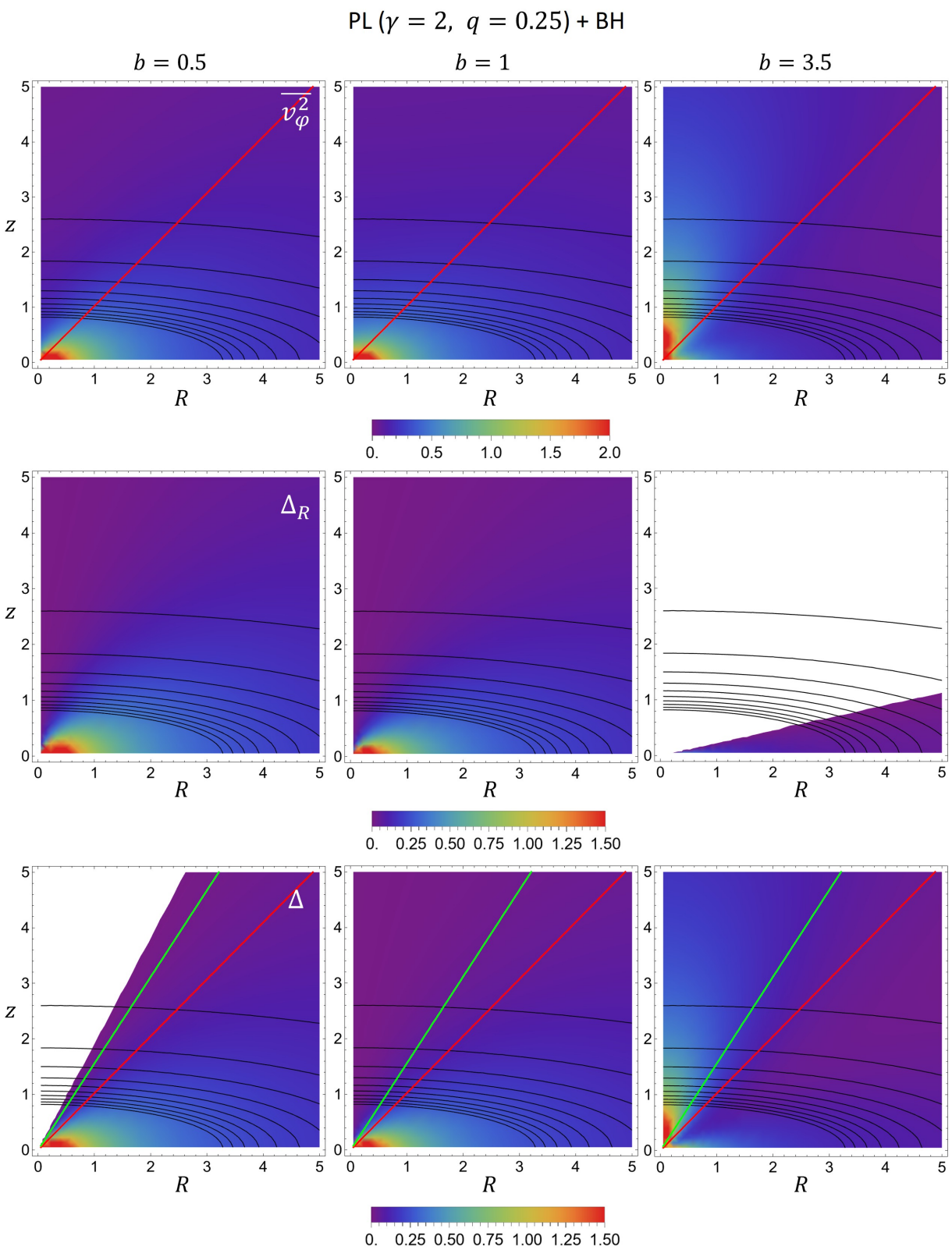


Figure F.14. Same as in Figure F.13, but for $q = 0.25$.

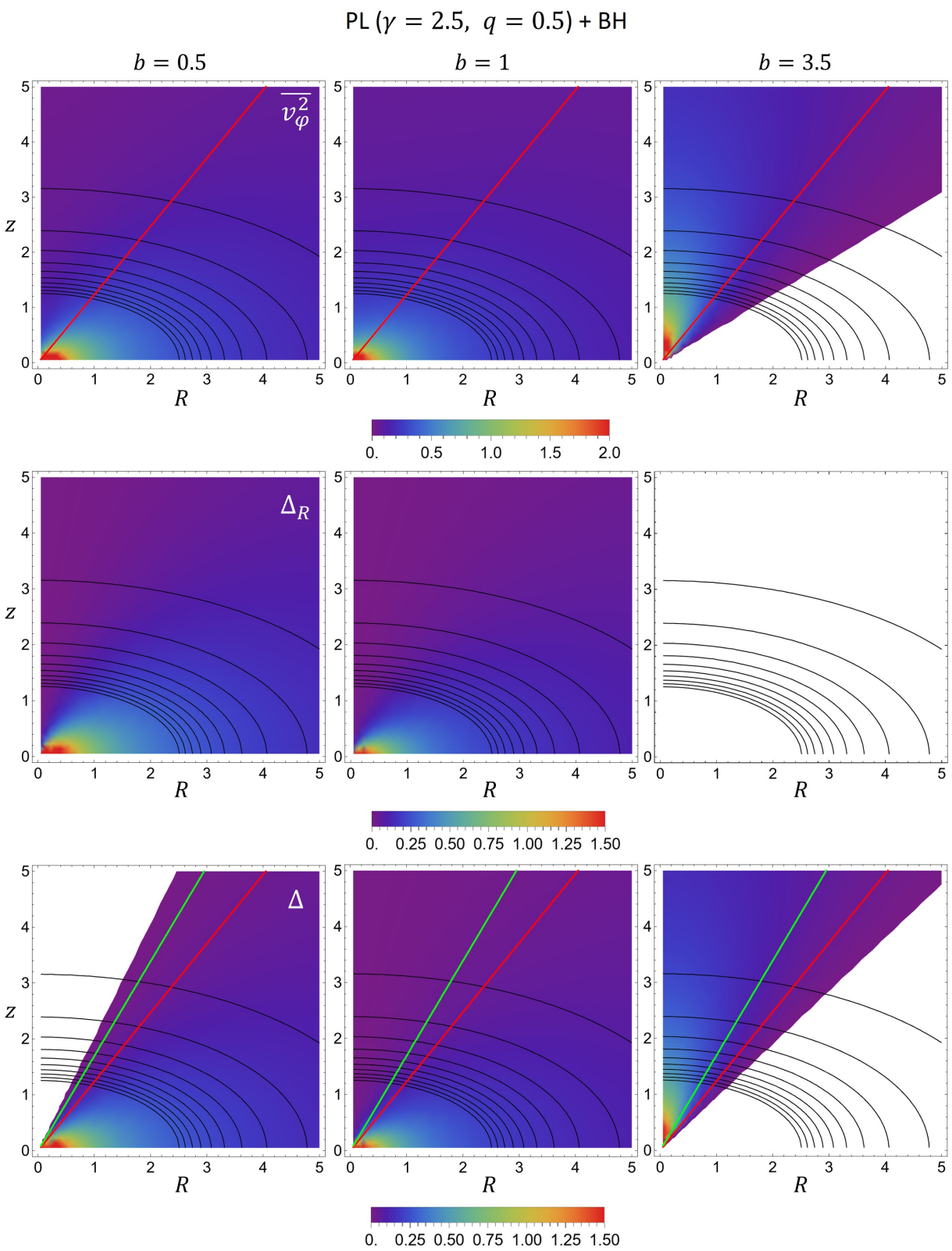


Figure F.15. Same as in Figure F.13, but for $\gamma = 2.5$.

APPENDIX G

TECHNICAL RESULTS ON THE ANSATZ-INDEPENDENT REGIONS AND THE LIMITS FOR b

In this Appendix, we prove some general results about the ansatz-independent $\mathscr{B}$, $\mathscr{C}$ and $\mathscr{D}$ regions (Appendix G.1), and the limits for b (Appendix G.2) of axisymmetric systems described by the three-integral JEs presented in Section 2.3.2. For all the Theorems, we assume that $\partial\Phi/\partial R \geq 0$ everywhere, and we restrict to $b = b(z)$ functions (including the constant b case).

G.1 Relations between the $\mathscr{B}$, $\mathscr{C}$ and $\mathscr{D}$ regions

We define the following ansatz-independent regions, based on the sign of the commutator, which are important for the following discussion:

$$\begin{aligned} \Omega^{\pm} &= \{(R,z) : [\rho_*, \Phi] \gtrless 0\}\,, \quad \Omega^{0} = \{(R,z) : [\rho_*, \Phi] = 0\}\,, \\ \Omega_2^{\pm} &= \{(R,z) : [R\,\rho_*, \Phi] \gtrless 0\}\,, \quad \Omega_2^{0} = \{(R,z) : [R\,\rho_*, \Phi] = 0\}\,, \end{aligned} \tag{G.1}$$

where we recall that $[R\,\rho_*, \Phi] = R\,[\rho_*, \Phi] + \rho_* \sigma_z^2$; also, $\Omega^{\pm 0} \equiv \Omega^{\pm} \cup \Omega^{0}$ (and similarly for Ω_2).

Theorem G.1.1. *For all the systems,* $\mathscr{B}^- \subseteq \mathscr{D}^-$, $\Omega^- \subseteq \mathscr{D}^-$, *and* $\Omega_2^- \subseteq \Omega^-$.

Proof. Let $\mathrm{P} = (R, z) \in \mathscr{B}^-$. From the first of equation (3.4), and given $\sigma_z^2 \geq 0$, then $\mathrm{P} \in \mathscr{D}^-$, and the first inclusion is proved. Let $\mathrm{P} = (R, z) \in \Omega^-$. From equation (2.26), and given $\partial\Phi/\partial R \geq 0$, then $\mathrm{P} \in \mathscr{D}^-$, and the second inclusion is proved. Let $\mathrm{P} = (R, z) \in \Omega_2^-$. From the definition of $[R\,\rho_*, \Phi]$, and given $\rho_* \sigma_z^2 \geq 0$, then $\mathrm{P} \in \Omega^-$, and the second inclusion is proved. From these results, it immediately follows that $\mathscr{D}^{+0} \subseteq \mathscr{B}^{+0}$, $\mathscr{D}^{+0} \subseteq \Omega^{+0}$, and $\Omega^{+0} \subseteq \Omega_2^{+0}$. □

G.1.1 Results for $[\rho_*, \Phi] \geq 0$

The following results hold specifically for systems with positive commutator, at least in the regions of interest:

Theorem G.1.2. *If* $\mathscr{B}^- \subseteq \Omega^{+0}$, *then* $\mathscr{B}^- \subseteq \mathscr{C}^+$. *If* $\mathscr{C}^- \subseteq \Omega^{+0}$, *then* $\mathscr{C}^- \subseteq \mathscr{B}^+$.

Proof. Let $\mathrm{P} = (R, z) \in \mathscr{B}^-$, and $[\rho_*, \Phi] \geq 0$ there. From the second of equation (3.5), with $B < 0$ and $[\rho_*, \Phi] \geq 0$, then $\mathrm{P} \in \mathscr{C}^+$, and the first part the Theorem follows immediately if $[\rho_*, \Phi] \geq 0$ for all the points in $\mathscr{B}^-$. The second part is proved in an analogous way, but considering $C < 0$ and $[\rho_*, \Phi] \geq 0$ in equation (3.5). □

G.1.2 Results for $[\rho_*, \Phi] < 0$

The following results hold specifically for systems with negative commutator, at least in the regions of interest:

Theorem G.1.3. *If* $\mathscr{B}^{+0} \subseteq \Omega^-$, *then* $\mathscr{B}^{+0} \subset \mathscr{C}^-$. *If* $\mathscr{C}^{+0} \subseteq \Omega^-$, *then* $\mathscr{C}^{+0} \subset \mathscr{B}^-$.

Proof. Let $\mathrm{P} = (R, z) \in \mathscr{B}^+$, and $[\rho_*, \Phi] < 0$ there. From the second of equation (3.5), with $B \geq 0$ and $[\rho_*, \Phi] < 0$, then $\mathrm{P} \in \mathscr{C}^-$, and the first part the Theorem follows immediately if $[\rho_*, \Phi] < 0$ for all the points in $\mathscr{B}^{+0}$. The second part is proved in an analogous way, but considering $C \geq 0$ and $[\rho_*, \Phi] < 0$ in equation (3.5). □

G.2 Relations between the limits for b

Theorem G.2.1. *For all the systems,* $b_0(z) \leq b_{\mathrm{M}}(z)$ *over the rectangular strip* $R \geq 0$ *and* $z \in \mathrm{Pr}(\mathscr{B}^-)$.

Proof. From equations (3.11) and (3.13), $b_{\mathrm{M}}(z)$ is defined over the strip with $z \in \Pr(\mathscr{B}^-)$, and $b_0(z)$ is defined over the strip with $z \in \Pr(\mathscr{D}^-)$. From Theorem G.1.1, $\mathscr{B}^- \subseteq \mathscr{D}^-$, so that $b_0(z)$ is certainly defined for $z \in \Pr(\mathscr{B}^-)$. Over $\mathscr{B}^-$, both B and D are negative: therefore, from the first of equation (3.4), $|B| = R|D|/\rho_* - \sigma_z^2 \leq R|D|/\rho_*$. It follows that, in the first of equation (3.11), the minimum of the function over $\mathscr{B}_z^-$ is larger than the minimum obtained when $|B|$ is replaced by $R|D|/\rho_*$, and in turn this minimum is larger than that evaluated over the wider set $\mathscr{D}_z^- \supseteq \mathscr{B}_z^-$. From the first of equation (3.13), this last minimum is the value of $b_0(z)$ for points with $z \in \Pr(\mathscr{B}^-)$, concluding the proof. □

G.2.1 Results for $[\rho_*, \Phi] \geq 0$

Theorem G.2.2. *Let $\mathscr{C}^- \subseteq \Omega^{+0}$: then $b_1(z) \leq 1$ over the rectangular strip $R \geq 0$ and $z \in \Pr(\mathscr{C}^-)$.*

Proof. As $\mathscr{C}^- \subseteq \Omega^{+0}$ by assumption, from Theorem G.1.2 it follows that $\mathscr{B}^+ \cap \mathscr{C}^- = \mathscr{C}^-$. Therefore, from equation (3.15) with $[\rho_*, \Phi] \geq 0$, $b_1(z) \leq 1$ for $z \in \Pr(\mathscr{C}^-)$. □

Theorem G.2.3. *Let $\mathscr{B}^- \subseteq \Omega^{+0}$: then $b_2(z) \geq 1$ and $b_0(z) \leq b_2(z) \leq b_{\mathrm{M}}(z)$ over the rectangular strip $R \geq 0$ and $z \in \Pr(\mathscr{B}^-)$.*

Proof. From equation (3.16) and Theorem G.1.2, $b_2(z)$ is defined over $\mathscr{B}^- \cap \mathscr{C}^+ = \mathscr{B}^-$, and as by assumption $[\rho_*, \Phi] \geq 0$ over $\mathscr{B}^-$, it follows that $b_2(z) \geq 1$ for $z \in \Pr(\mathscr{B}^-)$. Moreover, from Theorem G.2.1, the functions $b_2(z)$, $b_0(z)$ and $b_{\mathrm{M}}(z)$ are all defined for points with $z \in \Pr(\mathscr{B}^-)$. Again from equation (3.16), by using the inequality $|B| \leq R|D|/\rho_*$ (see the proof of Theorem G.2.1) and finally from the assumed positivity of the commutator over $\mathscr{B}^-$, it follows that $b_2(z)$ is larger than the minimum of the function appearing in the second of equation (3.13), now computed over $\mathscr{B}^-$. As $\mathscr{B}^- \subseteq \mathscr{D}^-$ (see Theorem G.1.1), extending this minimum over $\mathscr{D}^-$ further decreases its value, proving that $b_2(z) \geq b_0(z)$. The inequality $b_{\mathrm{M}}(z) \geq b_2(z)$ follows by comparing equations (3.11) and (3.16), where $\mathscr{B}^- \cap \mathscr{C}^+ = \mathscr{B}^-$, and of course $\sigma_z^2 \geq 0$. Notice that $b_0(z)$ can be larger or lower than 1 depending on the sign of $[\rho_*, \Phi]$ over the region $\mathscr{D}^- \cap \mathscr{B}^+$, for $z \in \Pr(\mathscr{B}^-)$. □

Theorem G.2.4. *Let $\mathscr{D}^- \subseteq \Omega^{+0}$: then $b_0(z) \geq 1$ over the rectangular strip $R \geq 0$ and $z \in \Pr(\mathscr{D}^-)$, and $1 \leq b_0(z) \leq b_2(z) \leq b_{\mathrm{M}}(z)$ over the strip with $z \in \Pr(\mathscr{B}^-)$.*

Proof. As $\mathscr{D}^- \subseteq \Omega^{+0}$ by assumption, from equation (3.13) it follows that $b_0(z) \geq 1$ for $z \in \Pr(\mathscr{D}^-)$. The second part of the Theorem descends immediately from the inequality just proved

and Theorem G.2.3, as, from Theorem G.1.1, we know that $\mathscr{B}^- \subseteq \mathscr{D}^-$ ($\subseteq \Omega^{+0}$ by assumption). Notice how strengthening the hypothesis of Theorem G.2.3 (i.e., $\mathscr{B}^- \subseteq \Omega^{+0}$) to that of the present case (i.e., $\mathscr{D}^- \subseteq \Omega^{+0}$) allows to establish whether $b_0(z)$ is larger or smaller than unity, thus resolving the indeterminacy mentioned at the end of the proof of Theorem G.2.3. □

G.2.2 Results for $[\rho_*, \Phi] < 0$

Theorem G.2.5. *Let $\mathscr{B}^+ \subseteq \Omega^-$: then $b_1(z) = +\infty$ over the rectangular strip $R \geq 0$ and $z \in \Pr(\mathscr{B}^+)$.*

Proof. As $\mathscr{B}^+ \subseteq \Omega^-$ by assumption, from Theorem G.1.3 we have $\mathscr{B}^+ \cap \mathscr{C}^- = \mathscr{B}^+$. Therefore, from equation (3.15), the maximum of the function is reached approaching the $\mathscr{B}^0$ region from the one where $B > 0$ (i.e., for $B \to 0^+$), so that $b_1 = +\infty$ for $z \in \Pr(\mathscr{B}^+)$. □

Theorem G.2.6. *Let $\mathscr{C}^+ \subseteq \Omega^-$: then $b_2(z) = 0$ over the rectangular strip $R \geq 0$ and $z \in \Pr(\mathscr{C}^+)$.*

Proof. As $\mathscr{C}^+ \subseteq \Omega^-$ by assumption, from Theorem G.1.3 we have $\mathscr{C}^+ \cap \mathscr{B}^- = \mathscr{C}^+$. Therefore, from equation (3.16), the minimum of the function is reached approaching the $\mathscr{C}^0$ region from the one where $C > 0$ (i.e., for $C \to 0^+$), so that $b_2 = 0$ for $z \in \Pr(\mathscr{C}^+)$. □

Theorem G.2.7. *Let $\mathscr{D}^- \subseteq \Omega^-$: then $b_0(z) < 1$ over the rectangular strip $R \geq 0$ and $z \in \Pr(\mathscr{D}^-)$.*

Proof. As $\mathscr{D}^- \subseteq \Omega^-$ by assumption, from equation (3.13) with $[\rho_*, \Phi] < 0$ it follows that $b_0(z) < 1$ for $z \in \Pr(\mathscr{D}^-)$. □

Theorem G.2.8. *Let $\mathscr{B}^- \subseteq \Omega_2^-$: then $b_{\mathrm{M}}(z) < 1$ over the rectangular strip $R \geq 0$ and $z \in \Pr(\mathscr{B}^-)$.*

Proof. As $\mathscr{B}^- \subseteq \Omega_2^-$ by assumption, from equation (3.11) with $[R\,\rho_*, \Phi] < 0$ it follows that $b_{\mathrm{M}}(z) < 1$ for $z \in \Pr(\mathscr{B}^-)$. □

APPENDIX H

Kinematic maps of the selected TNG50 galaxies

In this Appendix, we show the main kinematic maps for the whole sample of 29 galaxies analyzed in this thesis, extracted from the TNG50 simulation (at redshift $z = 0$) with stellar mass $10^{10.5} \leq M_*/\mathrm{M}_\odot \leq 10^{12}$, specific star formation rate $\leq 10^{-12}$, and differences between the intermediate and the major semiaxes of the stellar density distribution inside two stellar half-mass radii smaller than 5%. The content of the Figures, shown for a box of two stellar half-mass radii side, is the following:

- First row: stellar density in units of $\mathrm{M}_\odot/\mathrm{kpc}^3$;
- Second row: first velocity moments $\overline{v_R}$, $\overline{v_\varphi}$ and $\overline{v_z}$ in units of km/s;
- Third row: square root of the second velocity moments $\overline{v_\varphi^2}$, and $\overline{v_R v_z}$ (in absolute value), in units of km/s;
- Fourth row: velocity dispersions σ_R, σ_φ and σ_z, in units of km/s, and $b = \sigma_R^2/\sigma_z^2$ (adimensional);
- Fifth row: left and right-hand sides of the first (JE1) and the second (JE2) JEs (in absolute value), in units of $\mathrm{M}_\odot\,\mathrm{kpc}^{-4}\,\mathrm{km}^2\,\mathrm{s}^{-2}$.

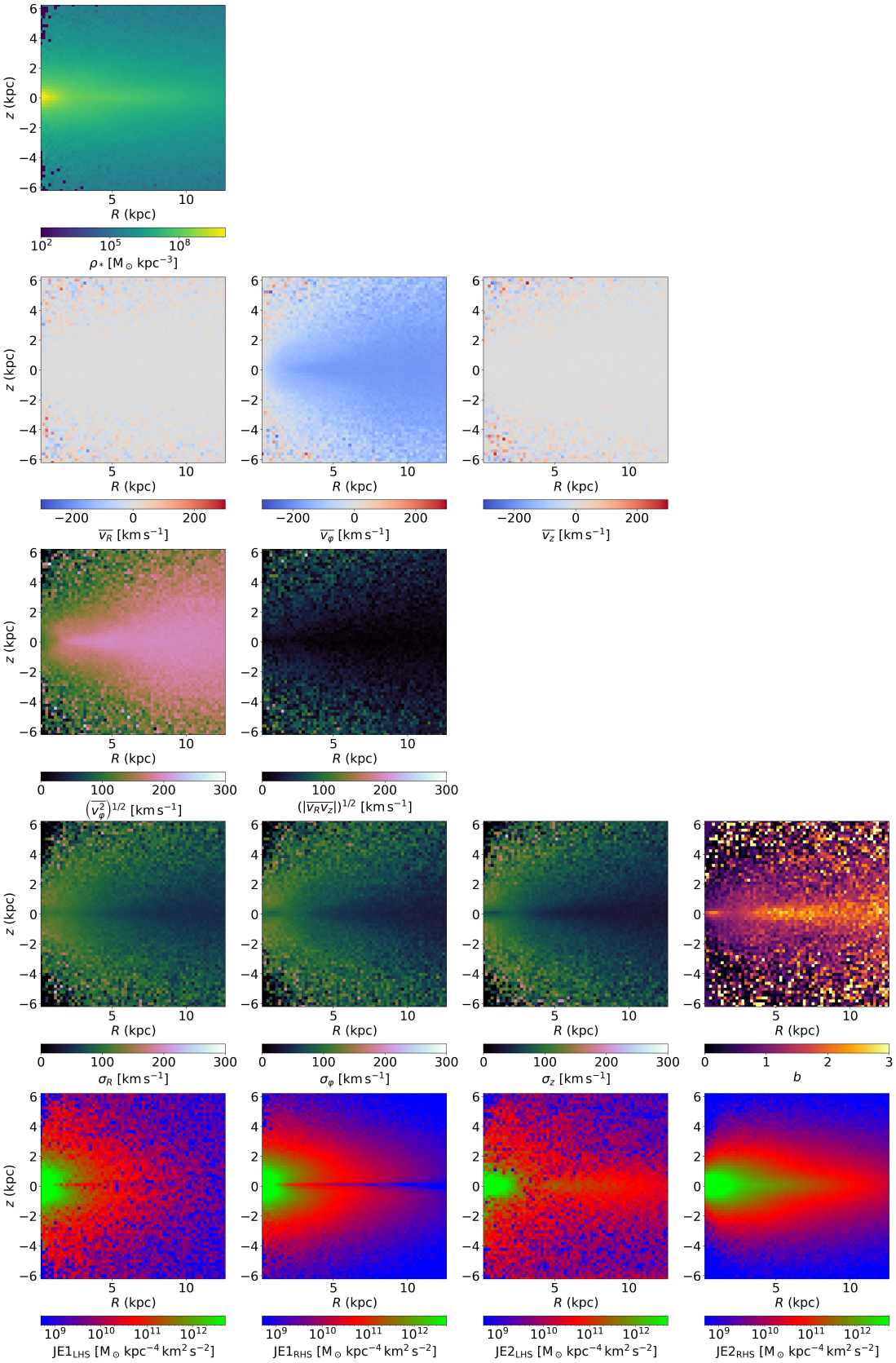


Figure H.1. Kinematic maps for the TNG000001 galaxy ($M_* = 3.95 \times 10^{11}\,\mathrm{M}_\odot$, $r_{1/2} = 8.43\,\mathrm{kpc}$, $q = 0.562$).

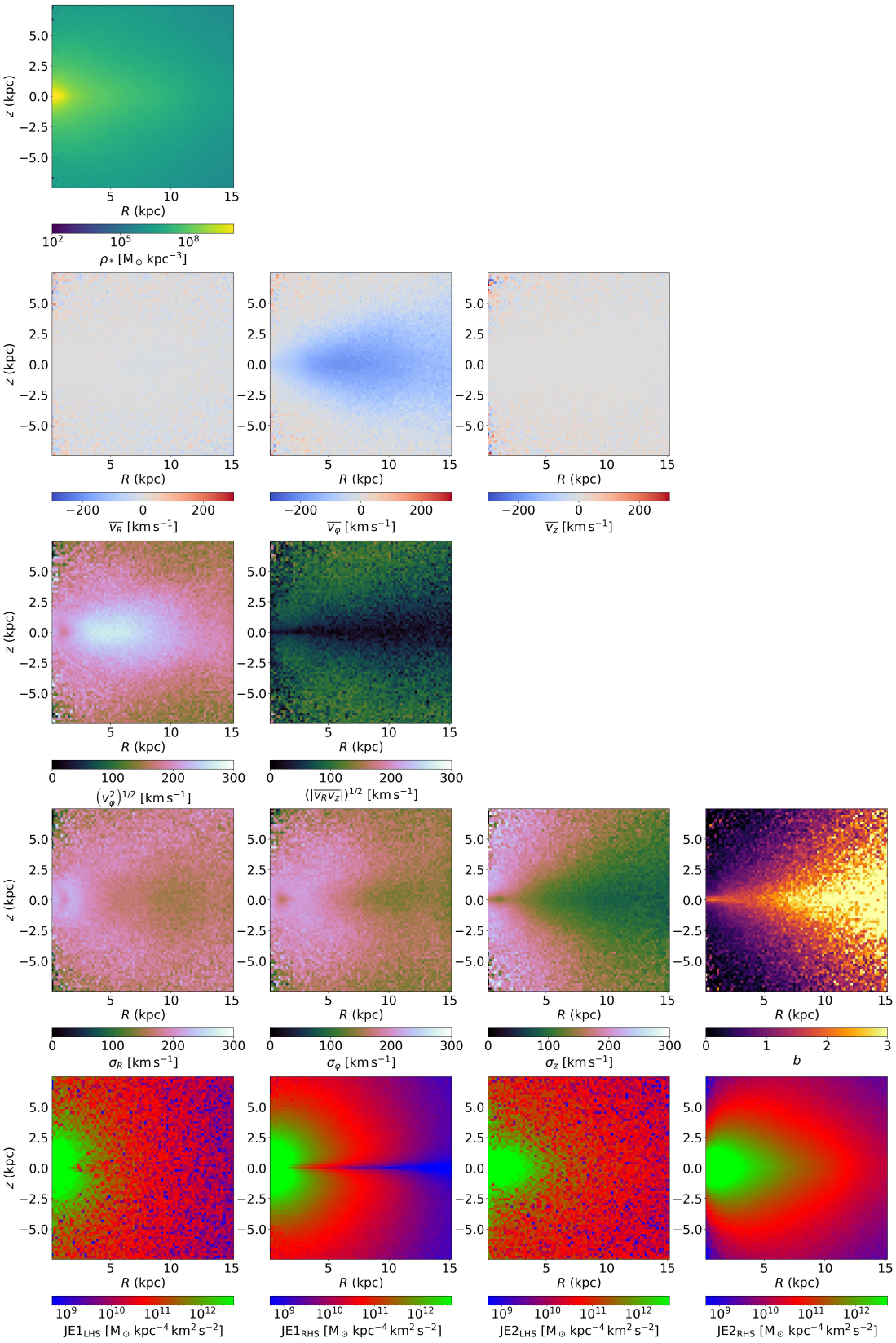


Figure H.2. Kinematic maps for the TNG000002 galaxy ($M_* = 1.92 \times 10^{11}\,\mathrm{M}_\odot$, $r_{1/2} = 7.69\,\mathrm{kpc}$, $q = 0.654$).

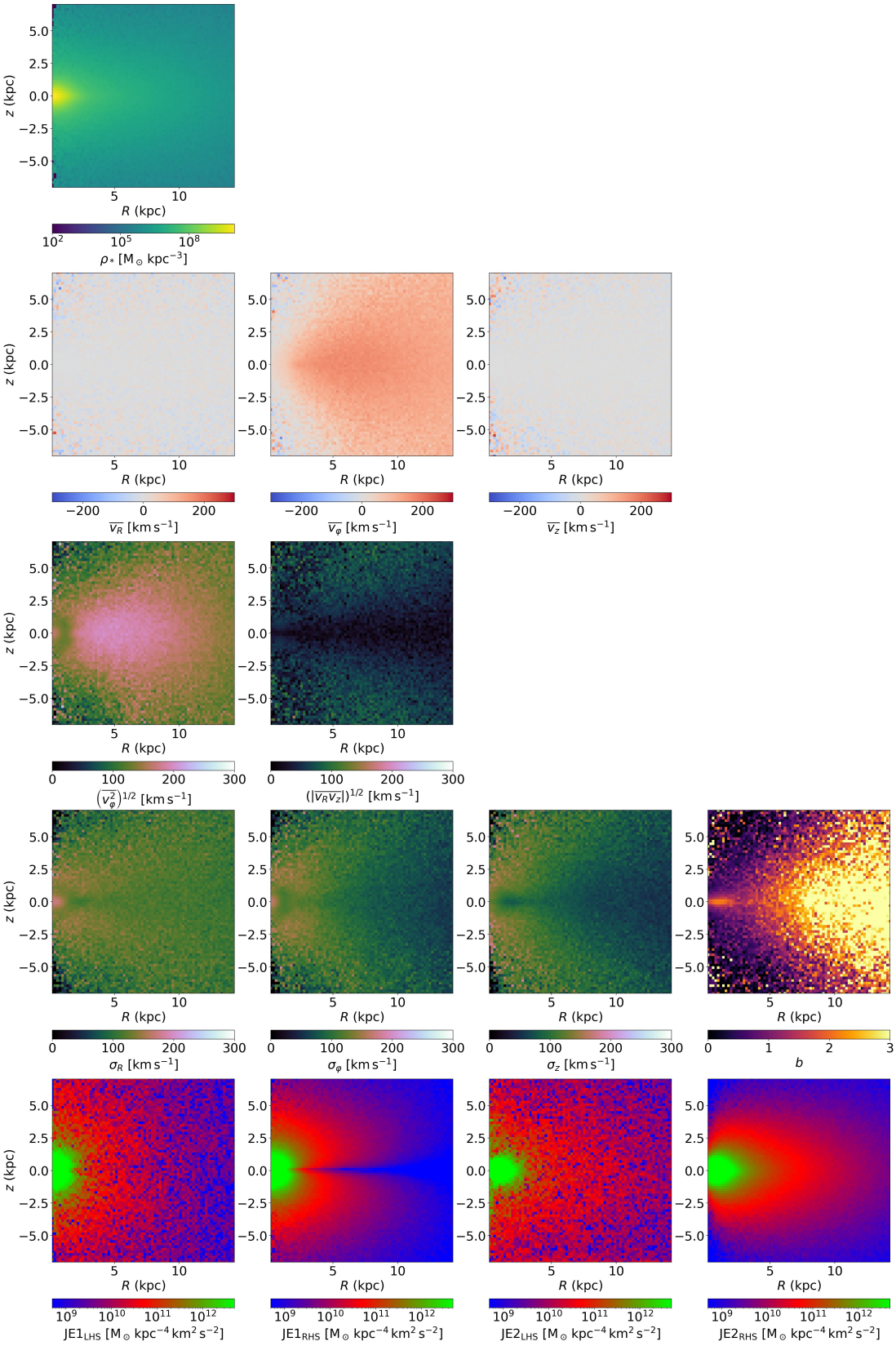


Figure H.3. Kinematic maps for the TNG000005 galaxy ($M_* = 7.21 \times 10^{10}\,\mathrm{M}_\odot$, $r_{1/2} = 7.23\,\mathrm{kpc}$, $q = 0.565$).

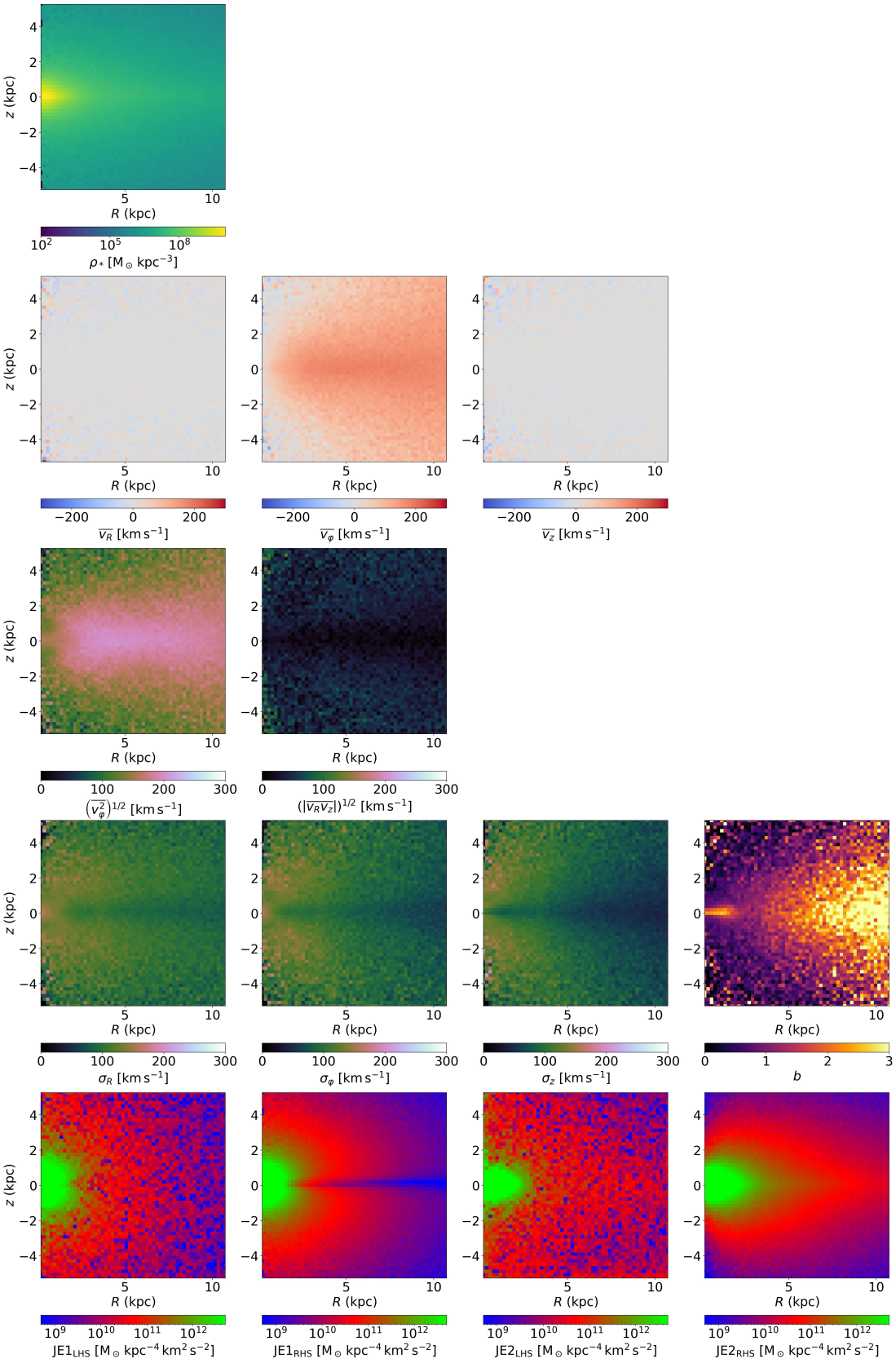


Figure H.4. Kinematic maps for the TNG000009 galaxy ($M_* = 6.48 \times 10^{10}\,\mathrm{M}_\odot$, $r_{1/2} = 5.47\,\mathrm{kpc}$, $q = 0.506$),

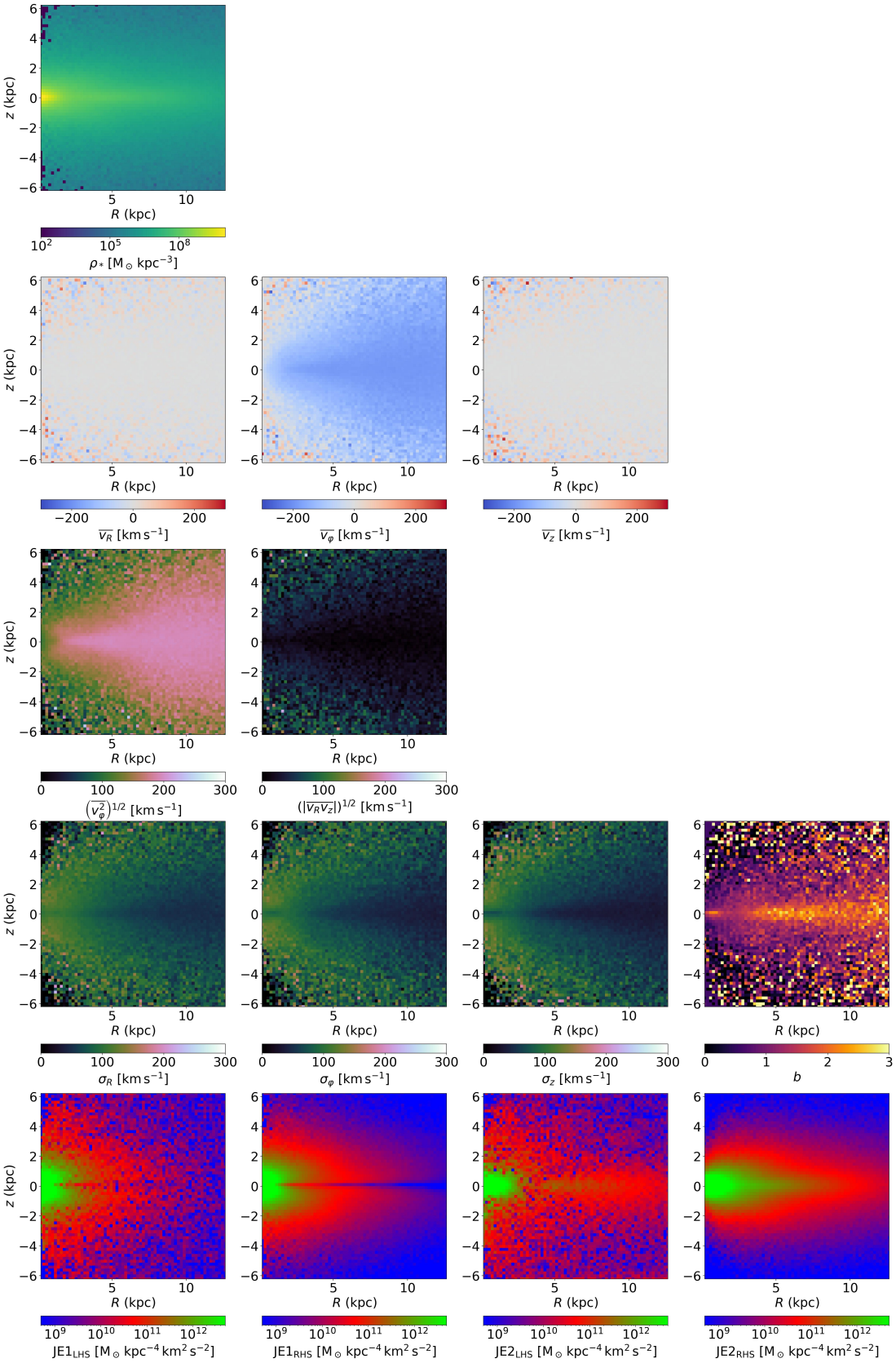


Figure H.5. Kinematic maps for the TNG000010 galaxy ($M_* = 6.12 \times 10^{10}\,\mathrm{M}_\odot$, $r_{1/2} = 6.41\,\mathrm{kpc}$, $q = 0.327$).

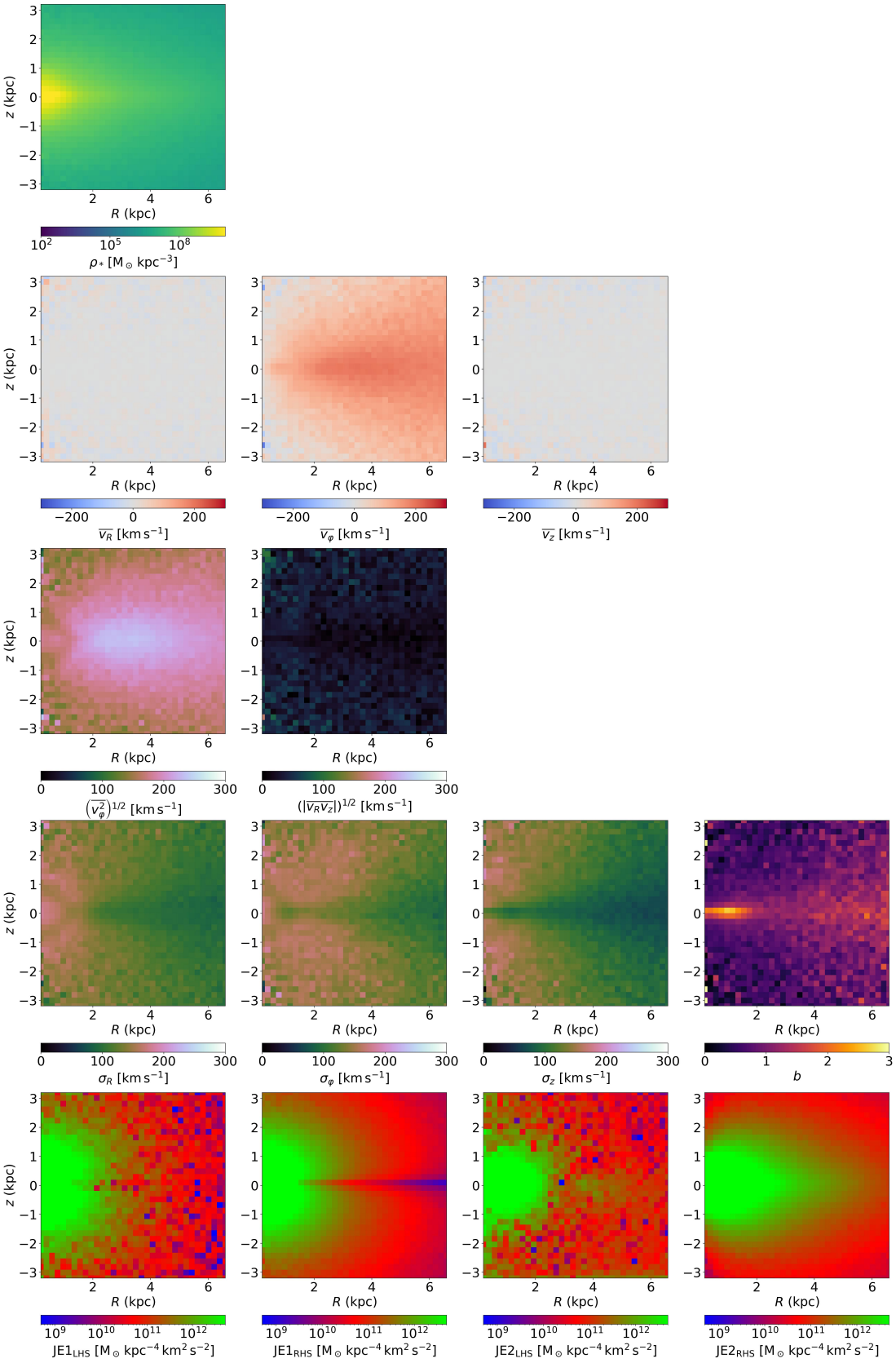


Figure H.6. Kinematic maps for the TNG063874 galaxy ($M_* = 7.26 \times 10^{10}\,\mathrm{M}_\odot$, $r_{1/2} = 3.40\,\mathrm{kpc}$, $q = 0.589$).

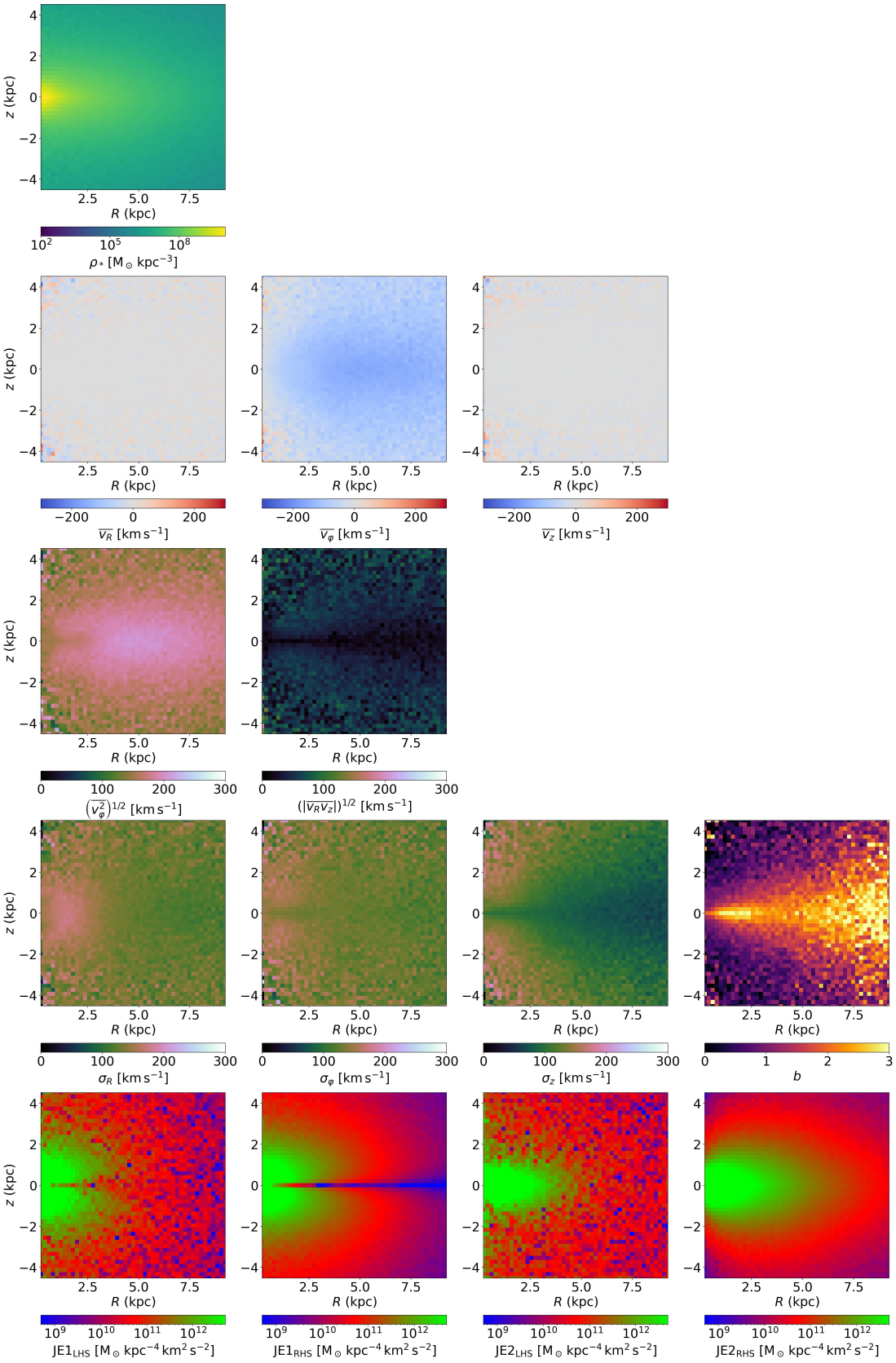


Figure H.7. Kinematic maps for the TNG096763 galaxy ($M_* = 7.76 \times 10^{10}\,\mathrm{M}_\odot$, $r_{1/2} = 4.72\,\mathrm{kpc}$, $q = 0.548$).

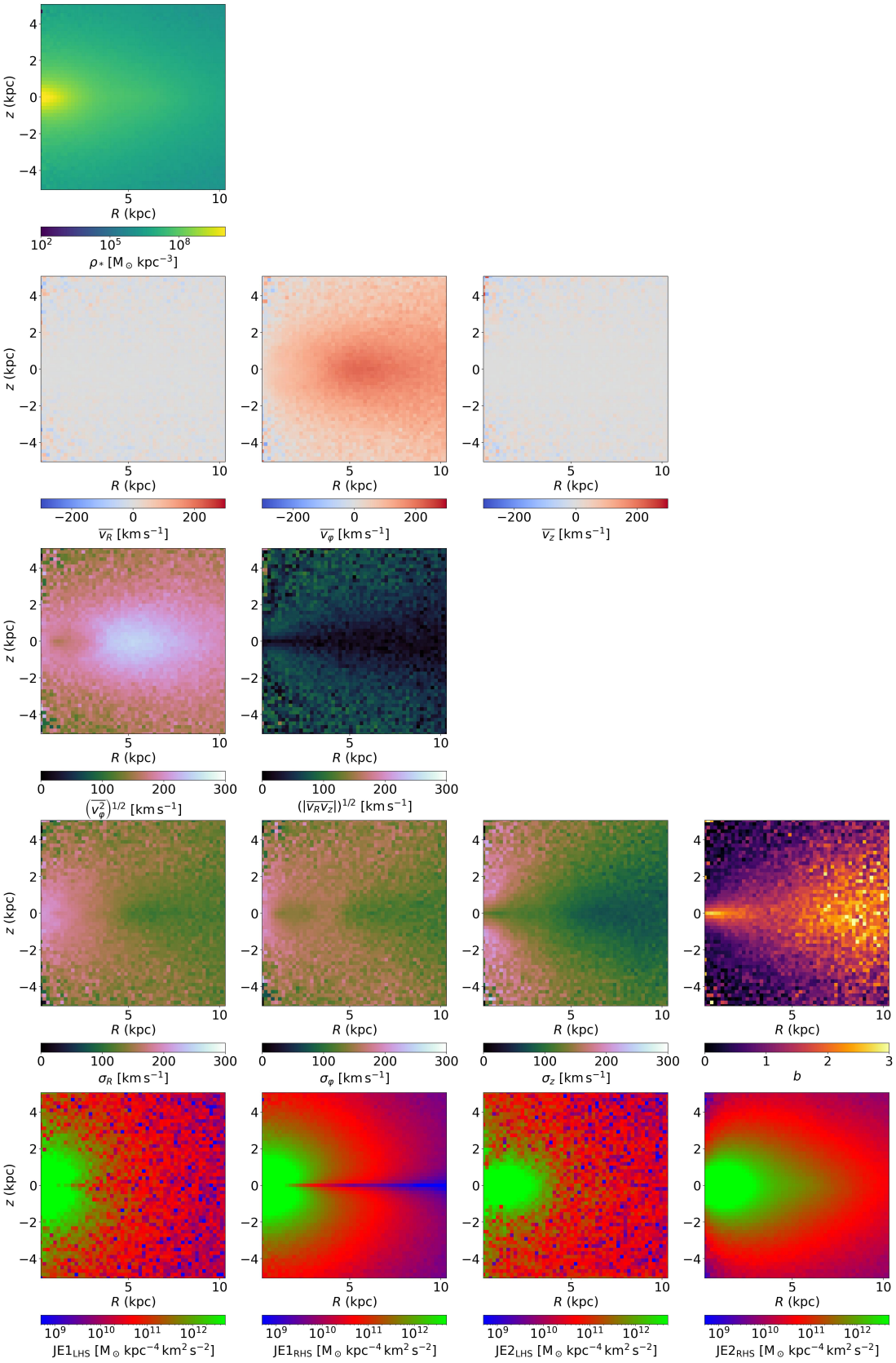


Figure H.8. Kinematic maps for the TNG096764 galaxy ($M_* = 1.05 \times 10^{11}\,\mathrm{M}_\odot$, $r_{1/2} = 5.26\,\mathrm{kpc}$, $q = 0.585$).

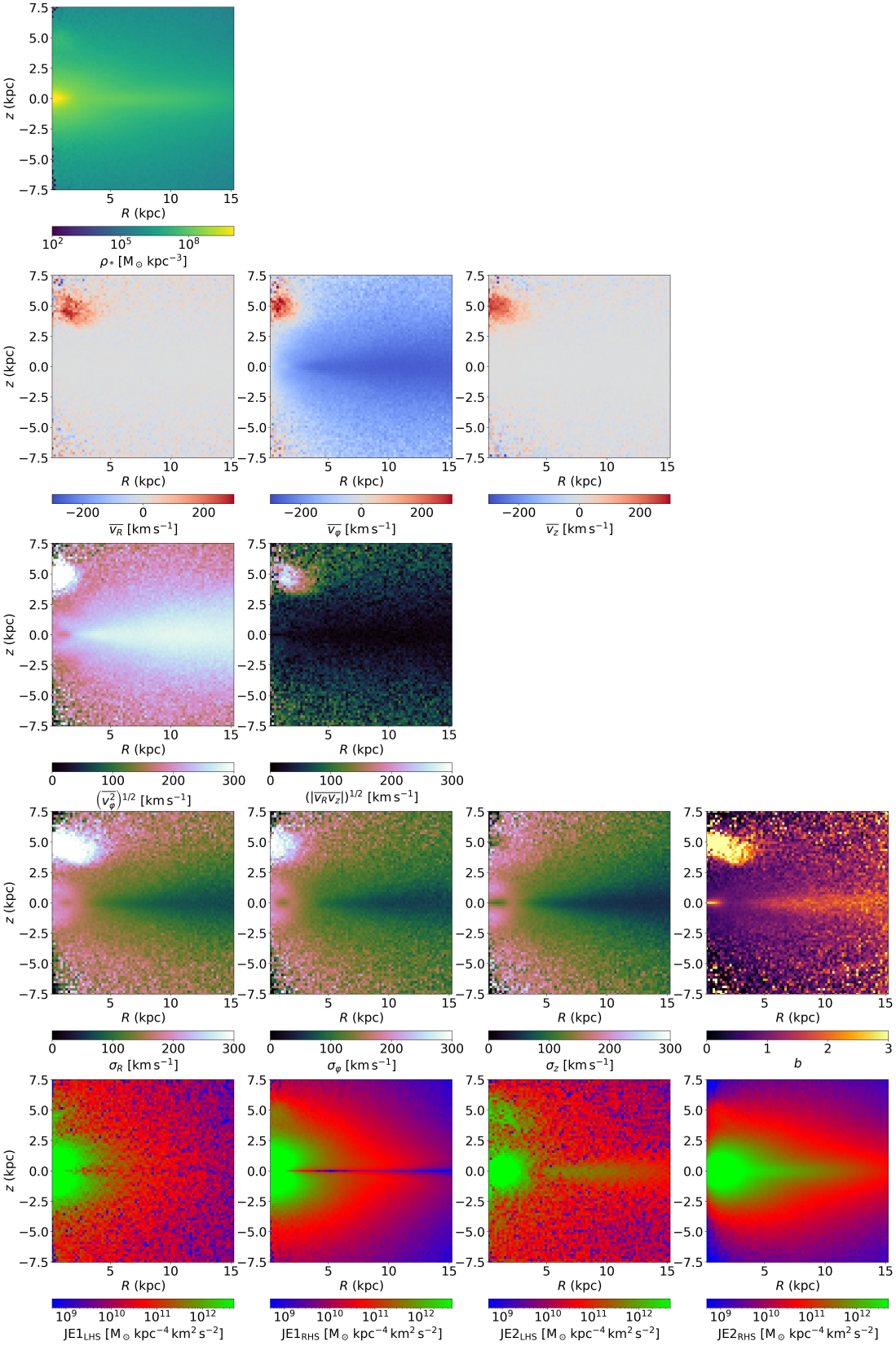


Figure H.9. Kinematic maps for the TNG117252 galaxy ($M_* = 1.93 \times 10^{11}\,\mathrm{M}_\odot$, $r_{1/2} = 7.72\,\mathrm{kpc}$, $q = 0.403$).

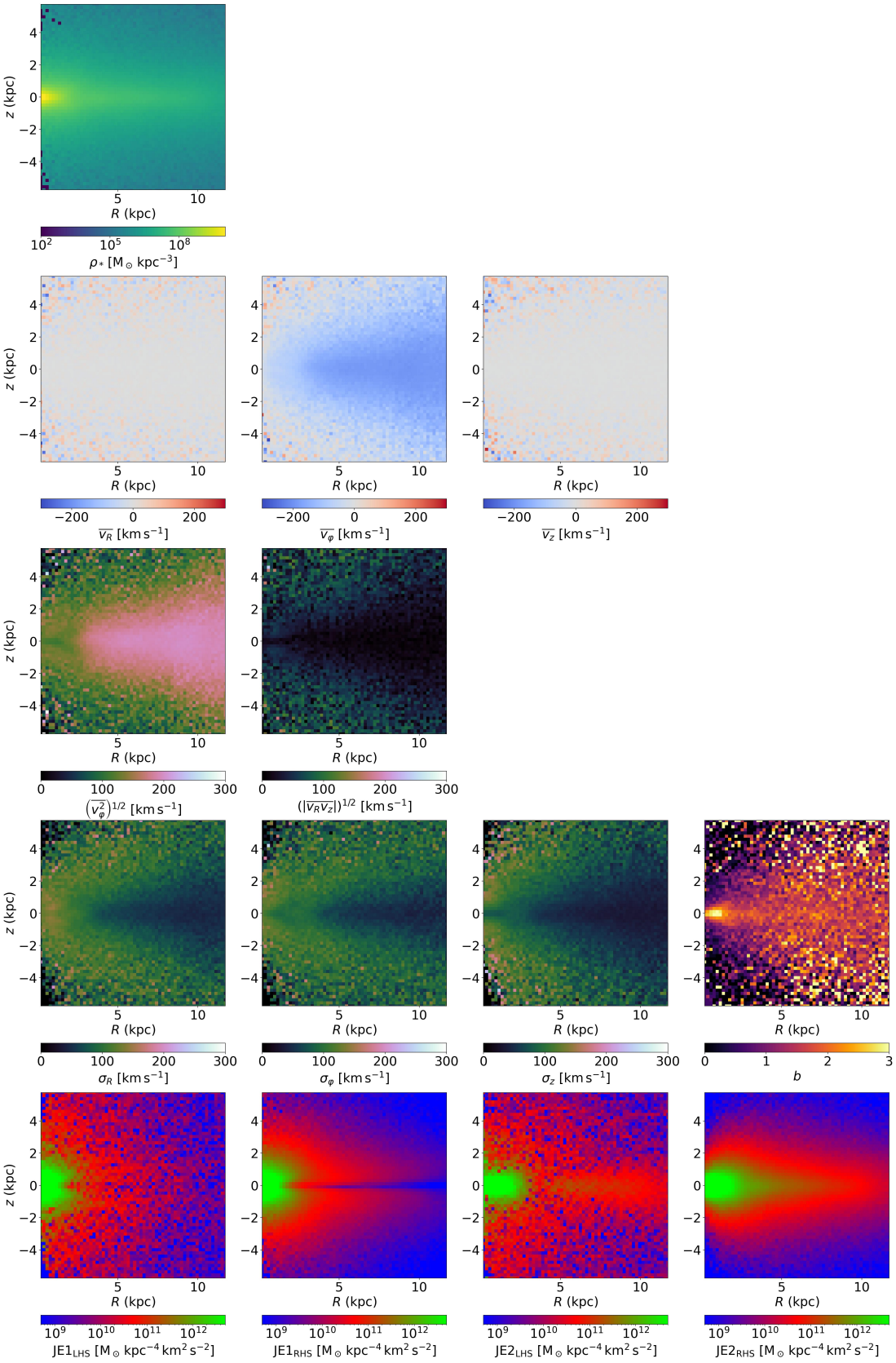


Figure H.10. Kinematic maps for the TNG117259 galaxy ($M_* = 4.91 \times 10^{10}\,\mathrm{M}_\odot$, $r_{1/2} = 5.96\,\mathrm{kpc}$, $q = 0.358$).

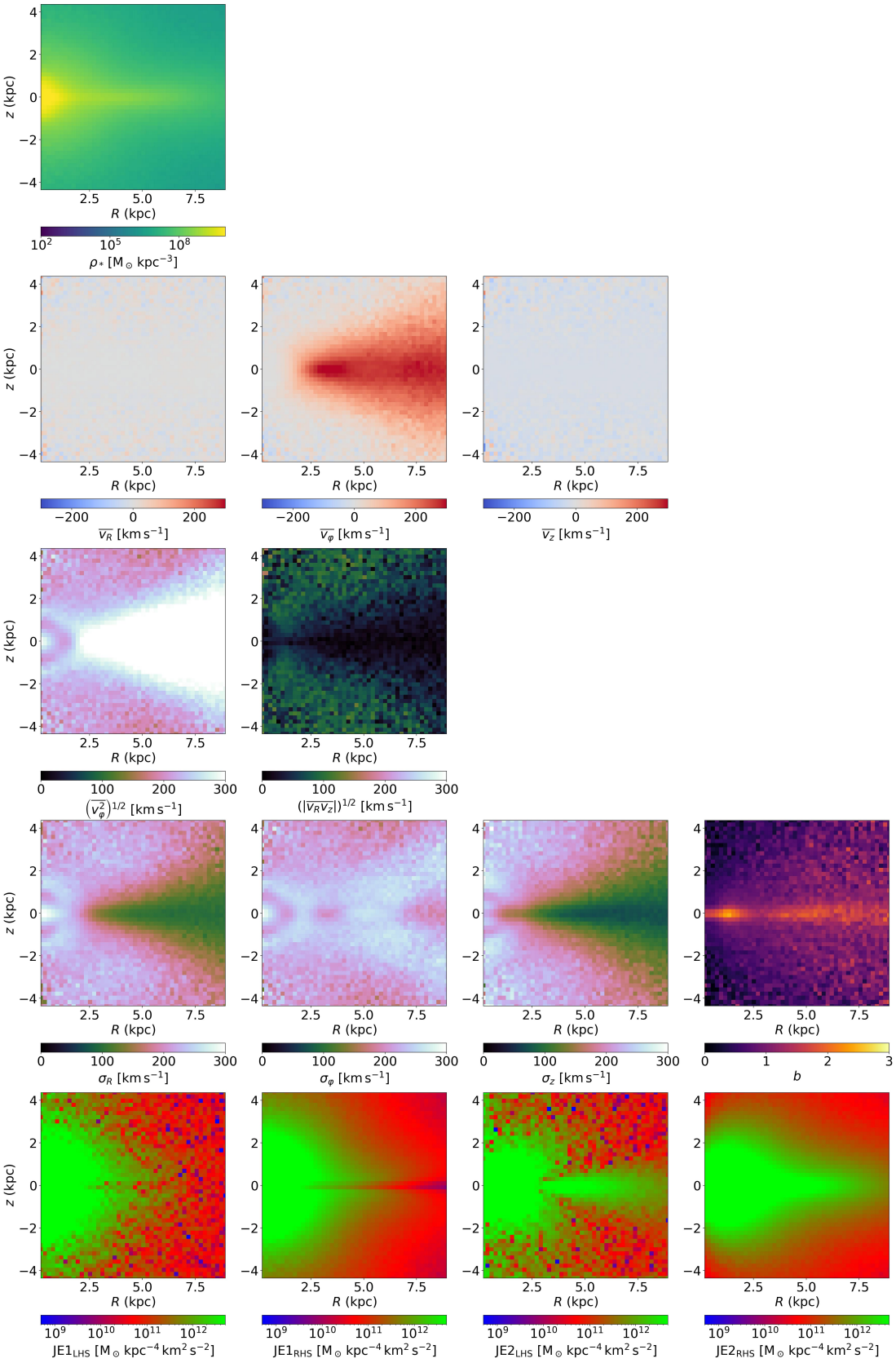


Figure H.11. Kinematic maps for the TNG143883 galaxy ($M_* = 2.16 \times 10^{11}\,\mathrm{M}_\odot$, $r_{1/2} = 4.56\,\mathrm{kpc}$, $q = 0.525$).

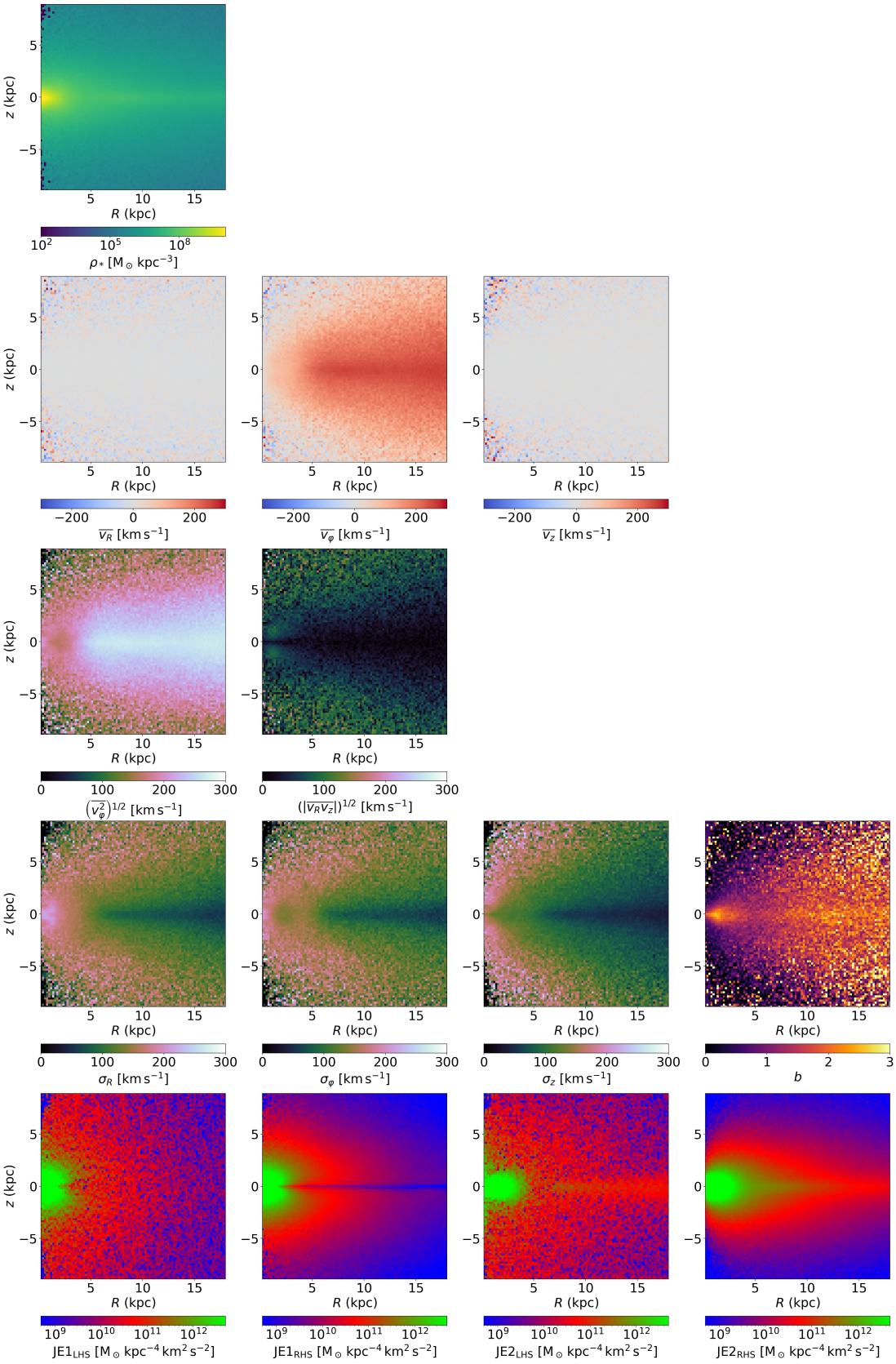


Figure H.12. Kinematic maps for the TNG184932 galaxy ($M_* = 1.60 \times 10^{11}\,\mathrm{M}_\odot$, $r_{1/2} = 9.09\,\mathrm{kpc}$, $q = 0.391$).

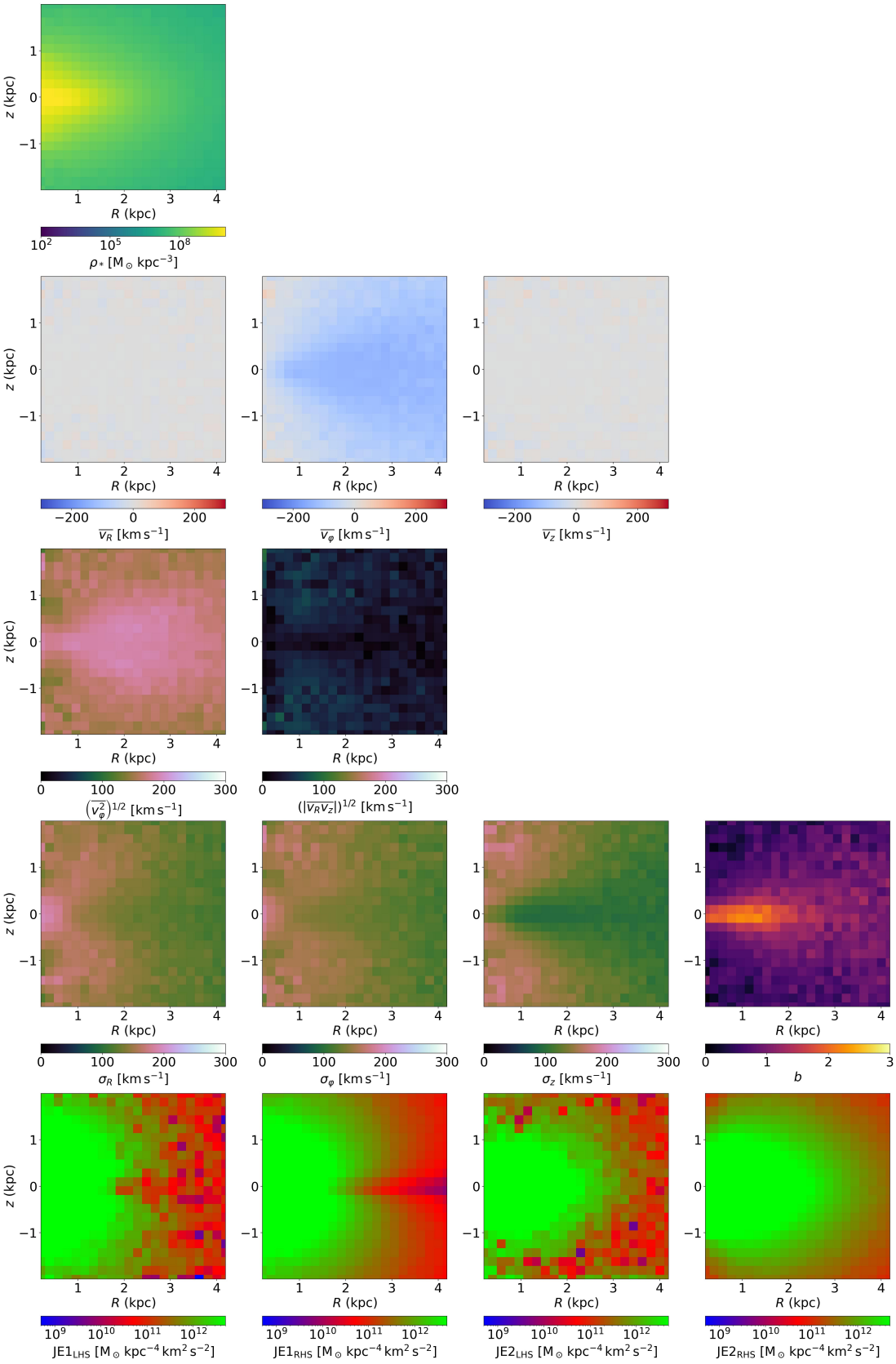


Figure H.13. Kinematic maps for the TNG184937 galaxy ($M_* = 6.07 \times 10^{10}\,\mathrm{M}_\odot$, $r_{1/2} = 2.20\,\mathrm{kpc}$, $q = 0.712$).

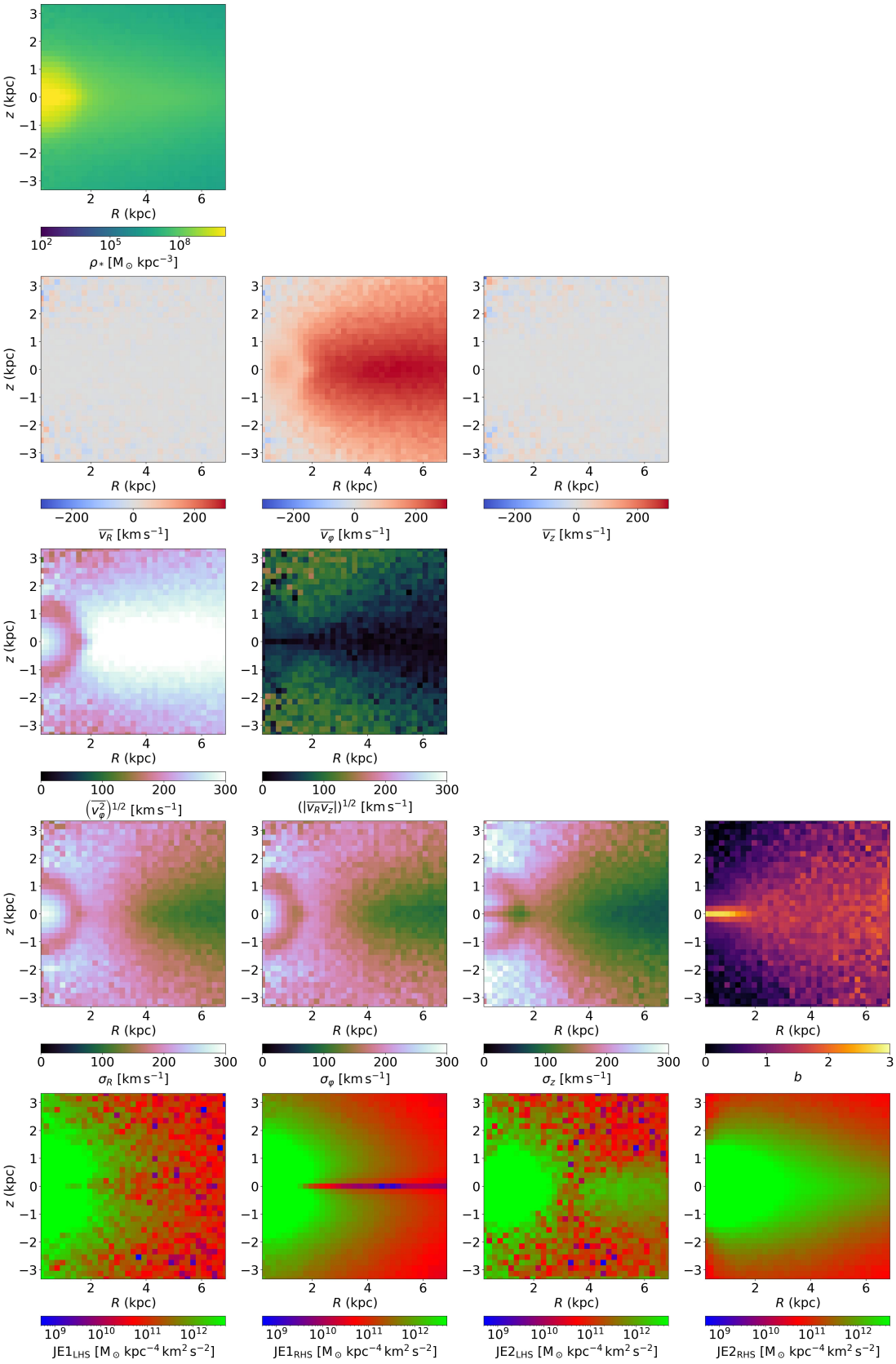


Figure H.14. Kinematic maps for the TNG264885 galaxy ($M_* = 1.31 \times 10^{11}\,\mathrm{M}_\odot$, $r_{1/2} = 3.53\,\mathrm{kpc}$, $q = 0.546$).

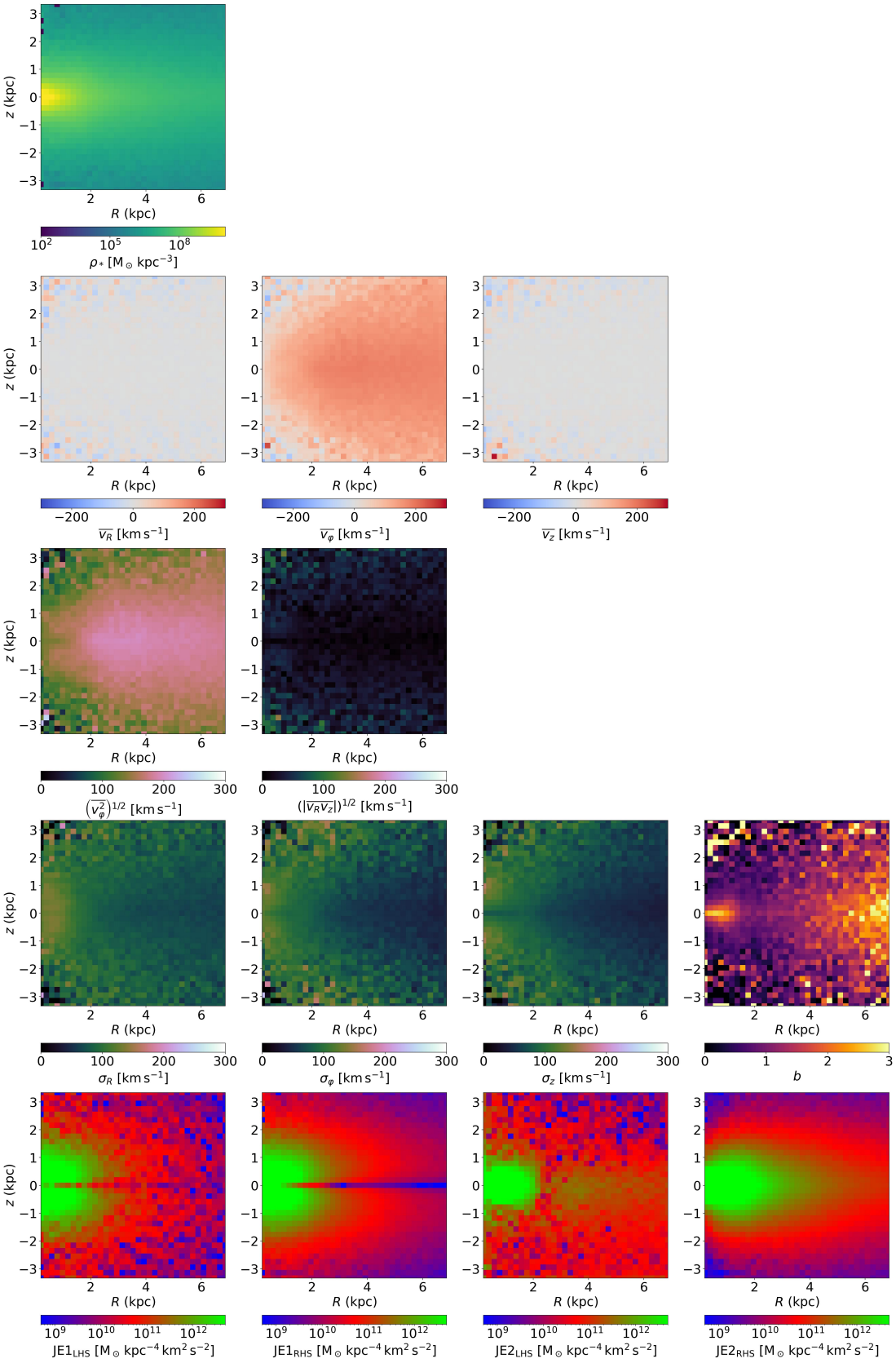


Figure H.15. Kinematic maps for the TNG313694 galaxy ($M_* = 4.23 \times 10^{10}\,\mathrm{M}_\odot$, $r_{1/2} = 3.54\,\mathrm{kpc}$, $q = 0.386$).

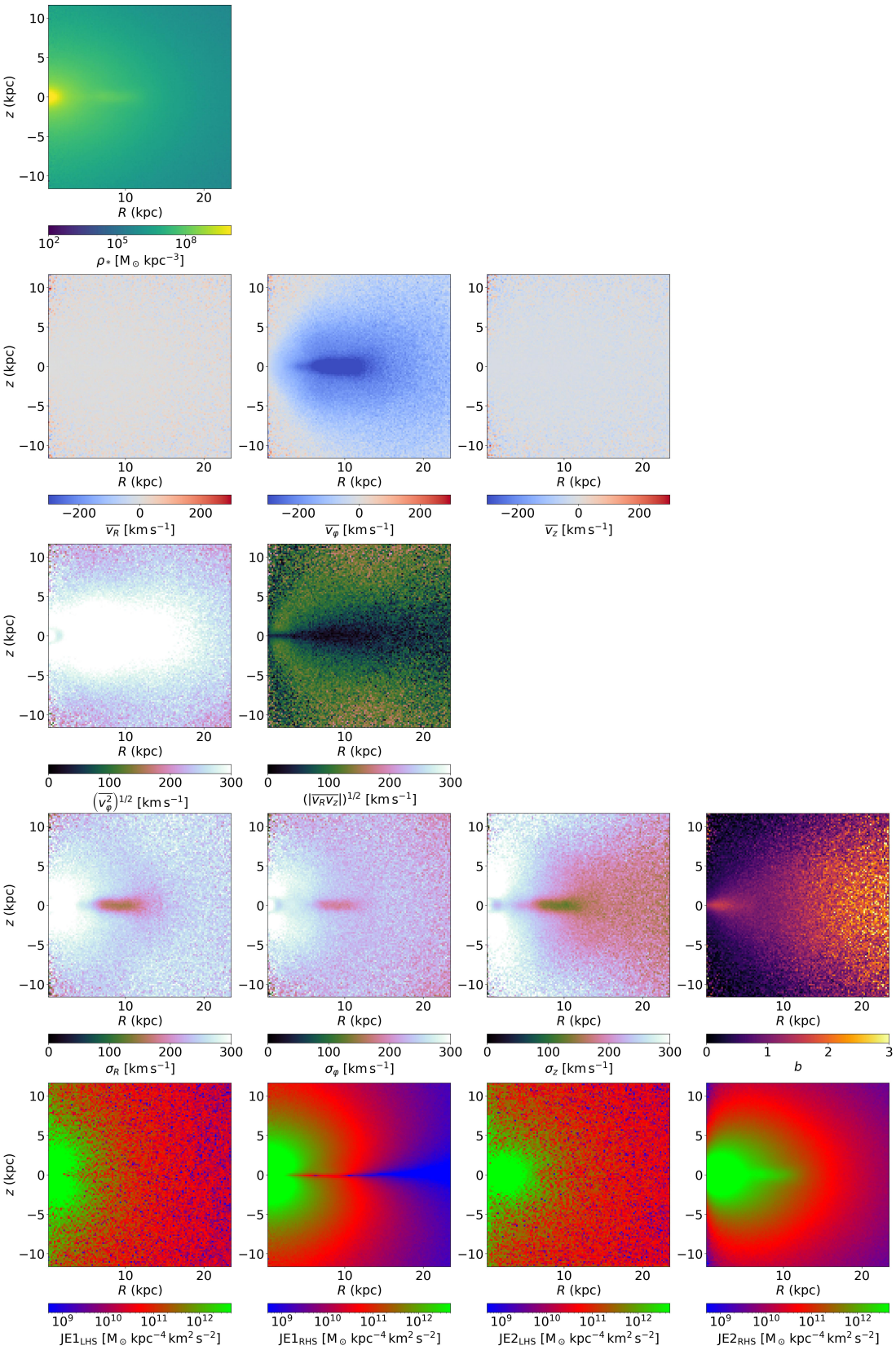


Figure H.16. Kinematic maps for the TNG319730 galaxy ($M_* = 6.60 \times 10^{11}\,\mathrm{M}_\odot$, $r_{1/2} = 11.8\,\mathrm{kpc}$, $q = 0.771$).

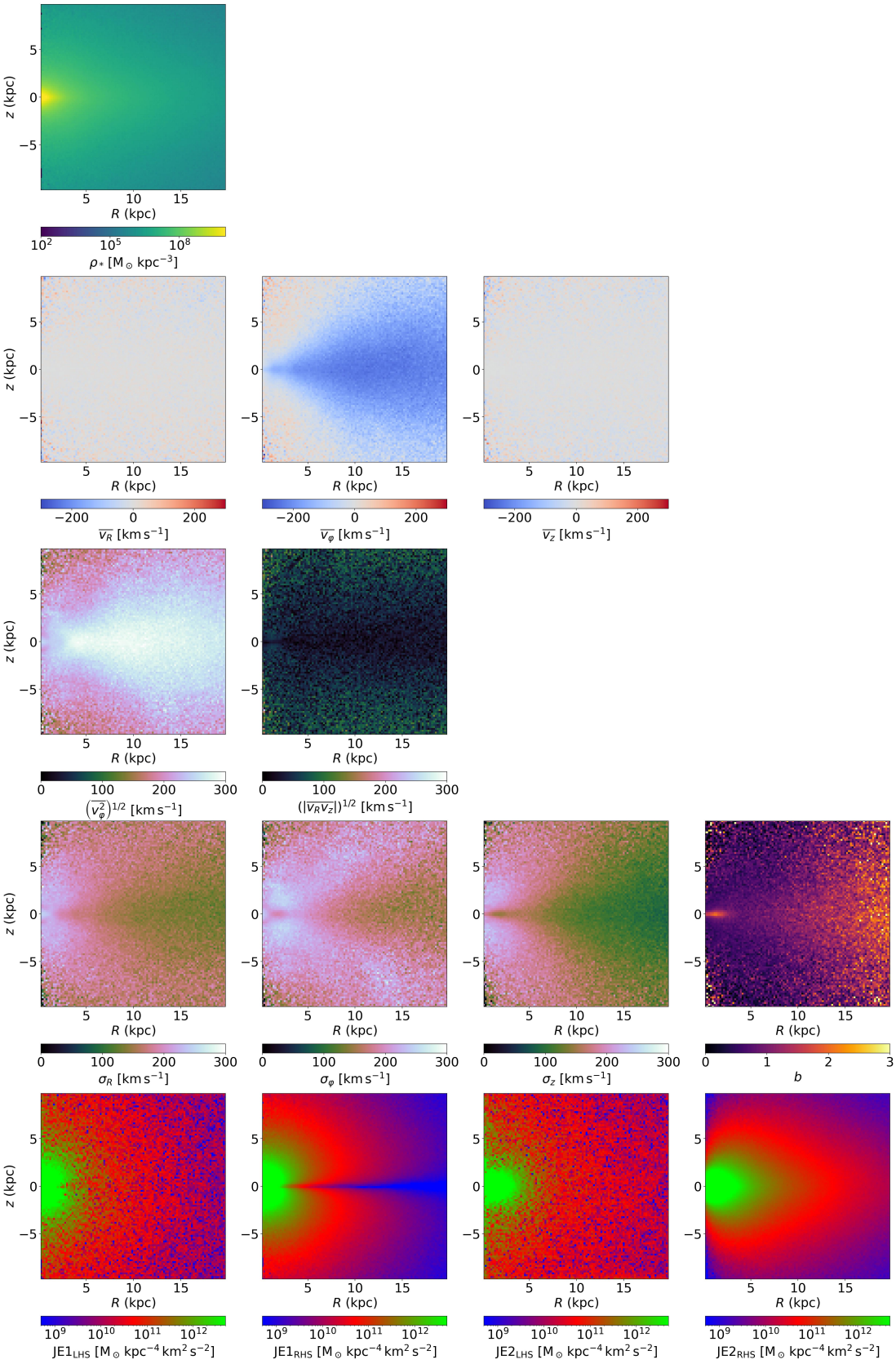


Figure H.17. Kinematic maps for the TNG390932 galaxy ($M_* = 2.62 \times 10^{11}\,\mathrm{M}_\odot$, $r_{1/2} = 9.97\,\mathrm{kpc}$, $q = 0.633$).

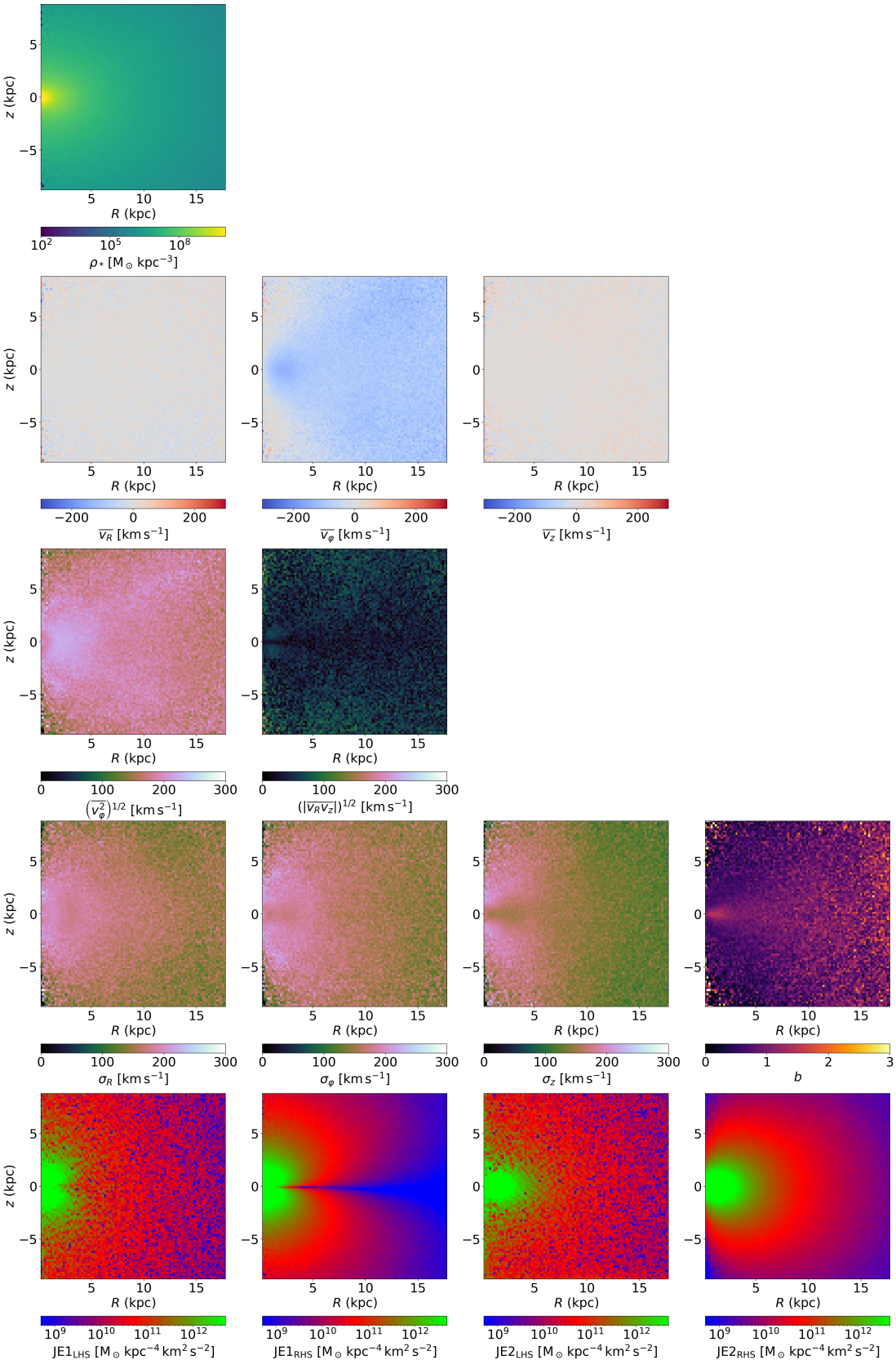


Figure H.18. Kinematic maps for the TNG418335 galaxy ($M_* = 1.85 \times 10^{11}\,\mathrm{M}_\odot$, $r_{1/2} = 8.98\,\mathrm{kpc}$, $q = 0.800$).

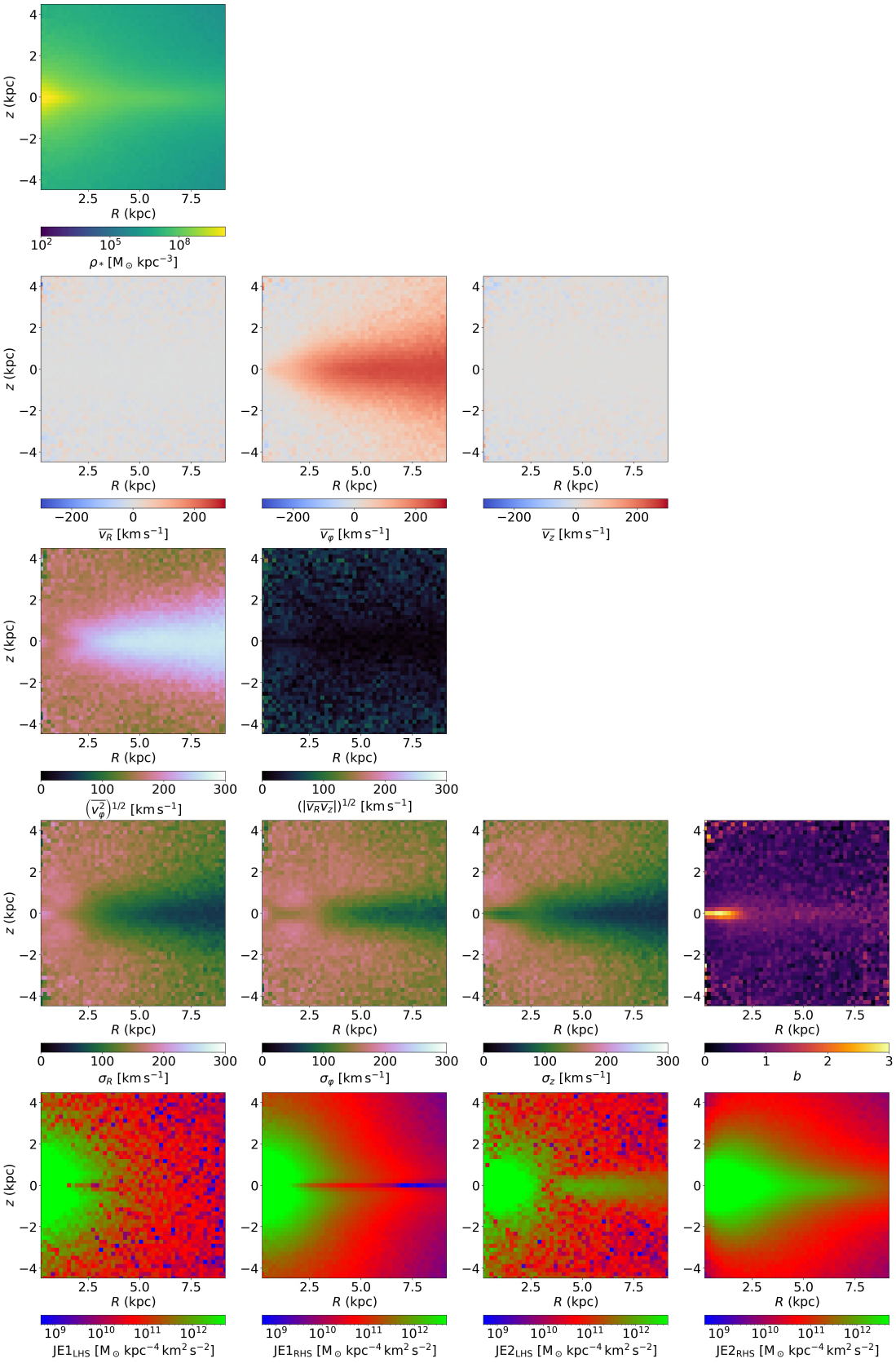


Figure H.19. Kinematic maps for the TNG428177 galaxy ($M_* = 1.04 \times 10^{11}\,\mathrm{M}_\odot$, $r_{1/2} = 4.68\,\mathrm{kpc}$, $q = 0.581$).

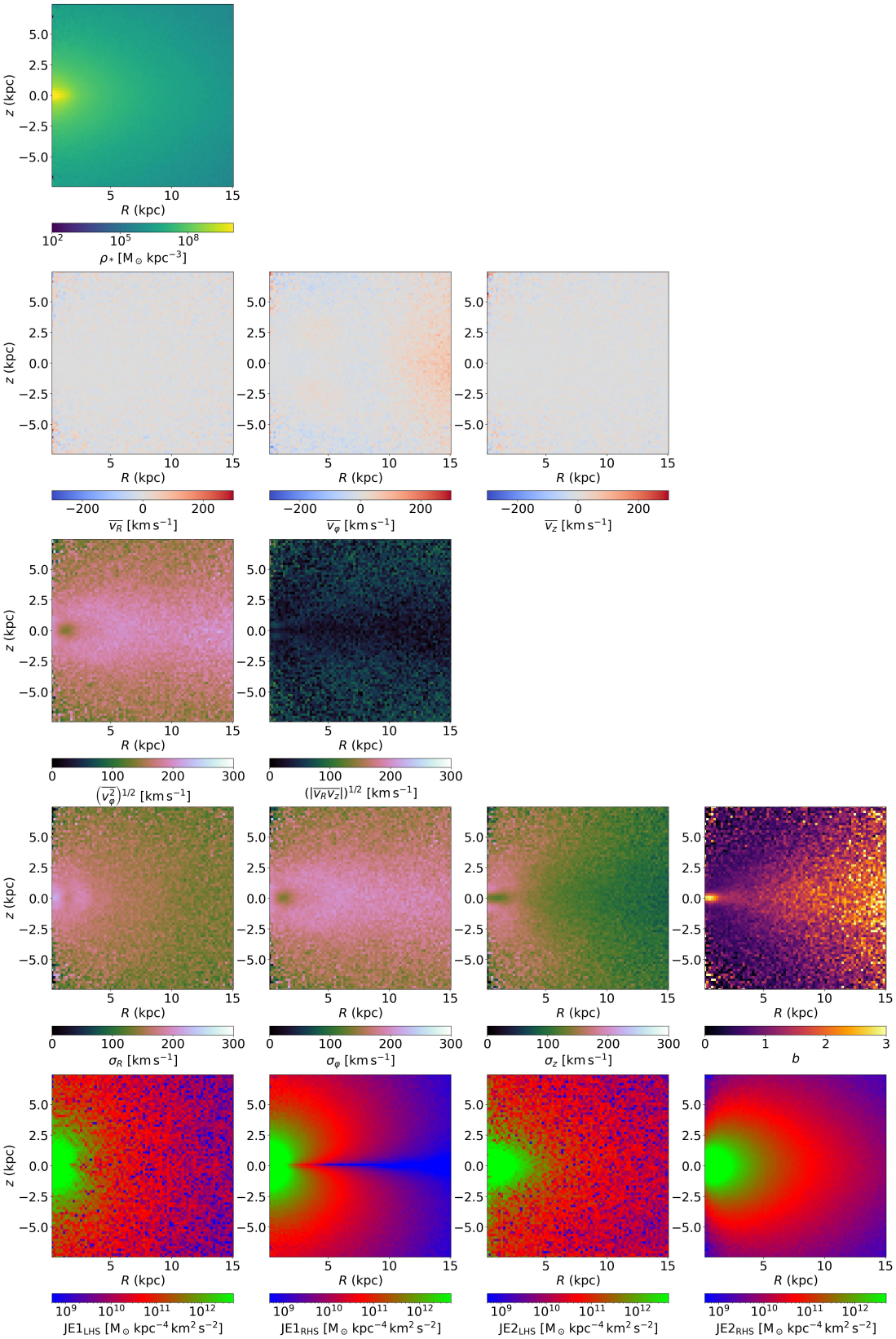


Figure H.20. Kinematic maps for the TNG450916 galaxy ($M_* = 1.31 \times 10^{11}\,\mathrm{M}_\odot$, $r_{1/2} = 7.64\,\mathrm{kpc}$, $q = 0.725$).

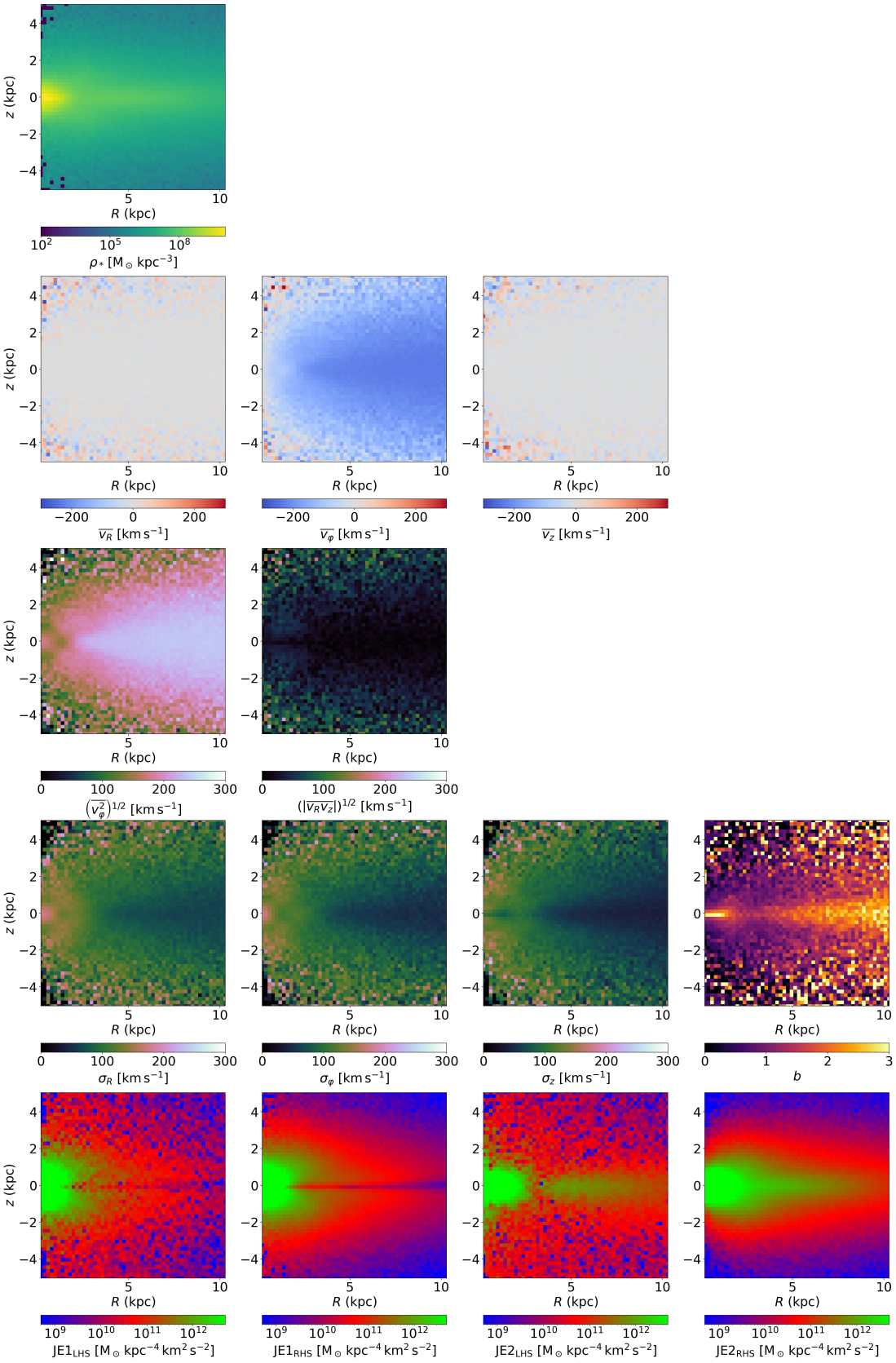


Figure H.21. Kinematic maps for the TNG454171 galaxy ($M_* = 7.57 \times 10^{10}\,\mathrm{M}_\odot$, $r_{1/2} = 5.24\,\mathrm{kpc}$, $q = 0.294$).

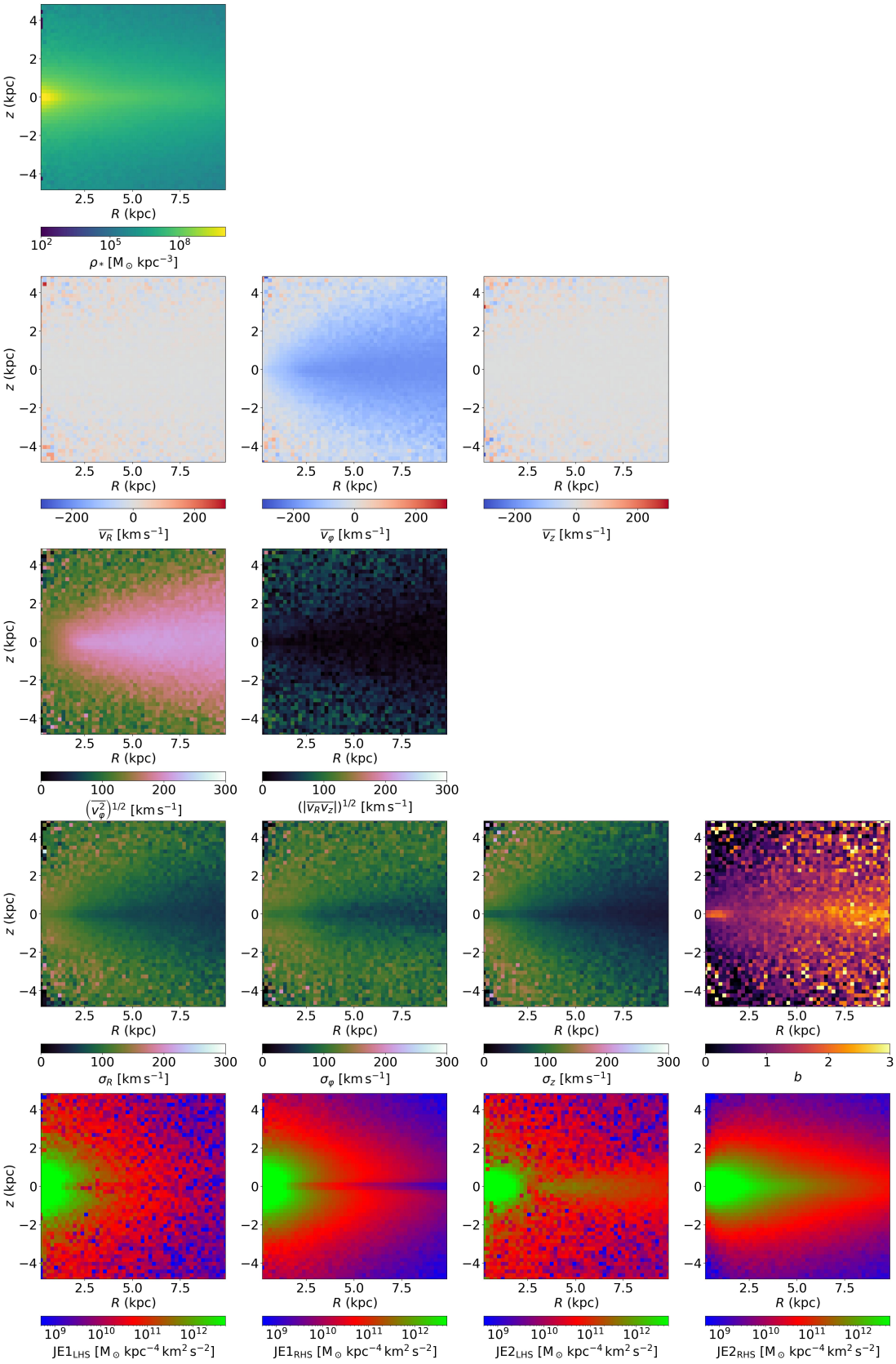


Figure H.22. Kinematic maps for the TNG478216 galaxy ($M_* = 5.93 \times 10^{10}\,\mathrm{M}_\odot$, $r_{1/2} = 5.04\,\mathrm{kpc}$, $q = 0.378$).

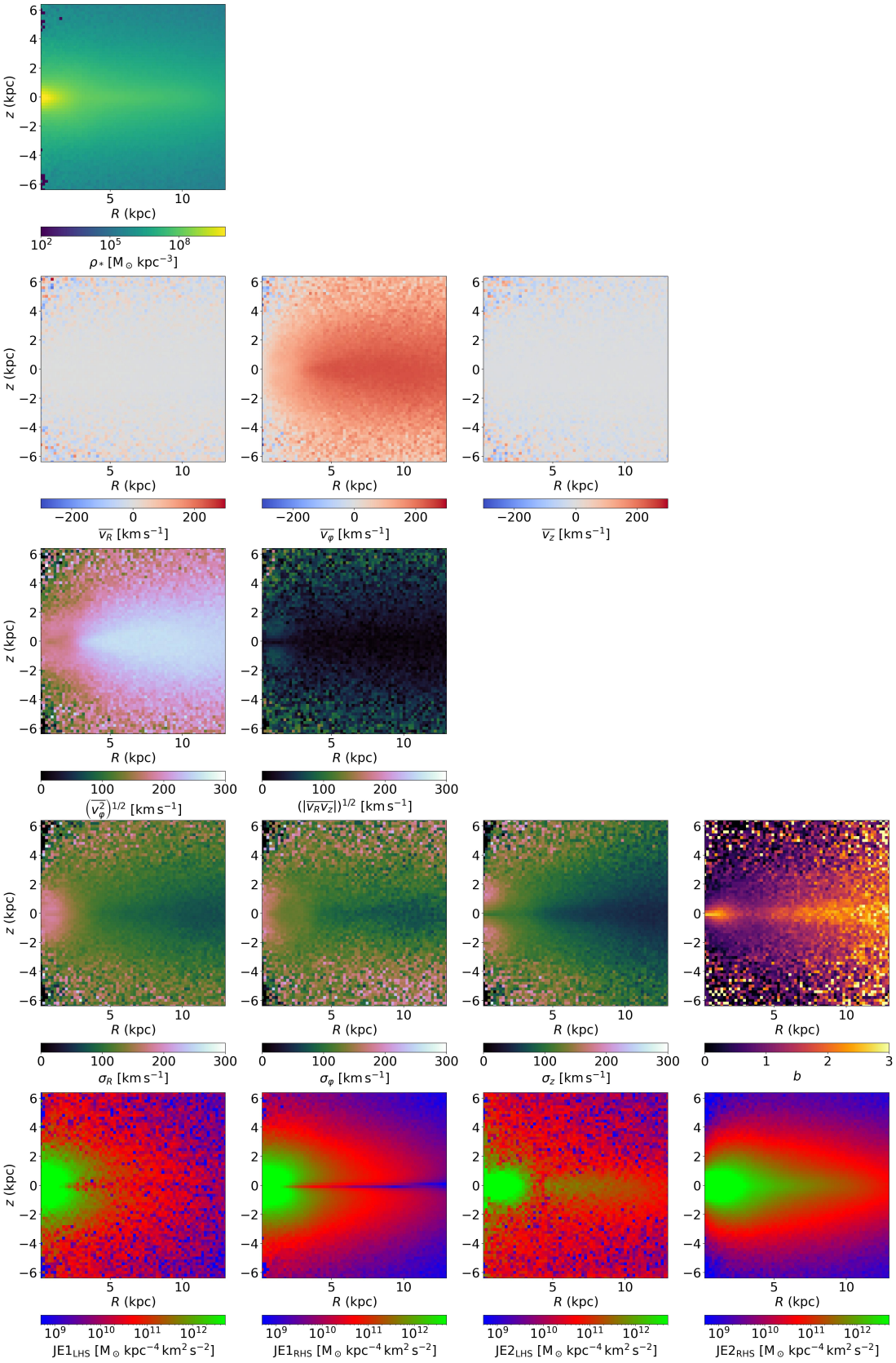


Figure H.23. Kinematic maps for the TNG482155 galaxy ($M_* = 1.20 \times 10^{11}\,\mathrm{M}_\odot$, $r_{1/2} = 6.58\,\mathrm{kpc}$, $q = 0.341$).

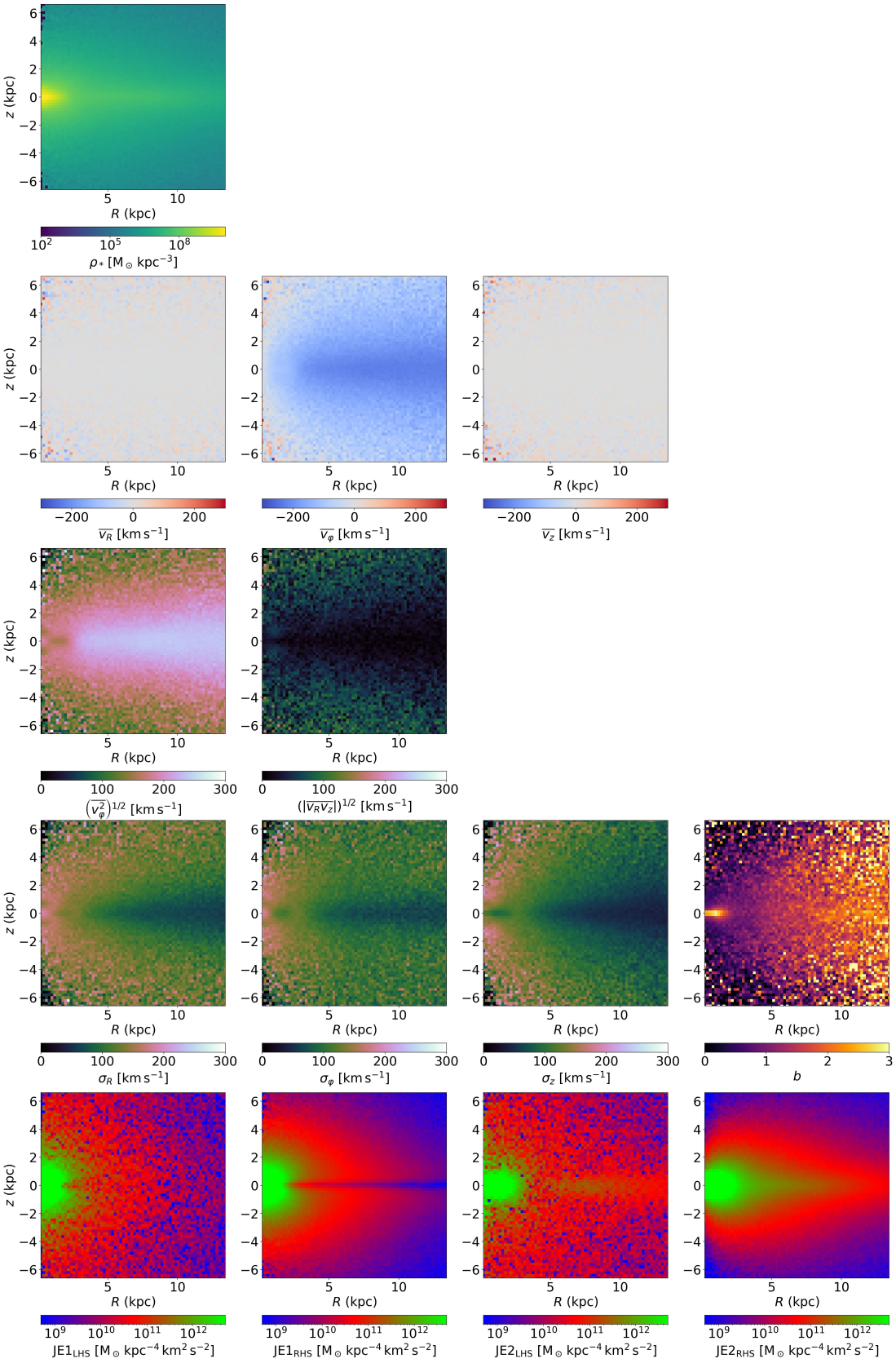


Figure H.24. Kinematic maps for the TNG498522 galaxy ($M_* = 1.01 \times 10^{11}\,\mathrm{M}_\odot$, $r_{1/2} = 6.81\,\mathrm{kpc}$, $q = 0.407$).

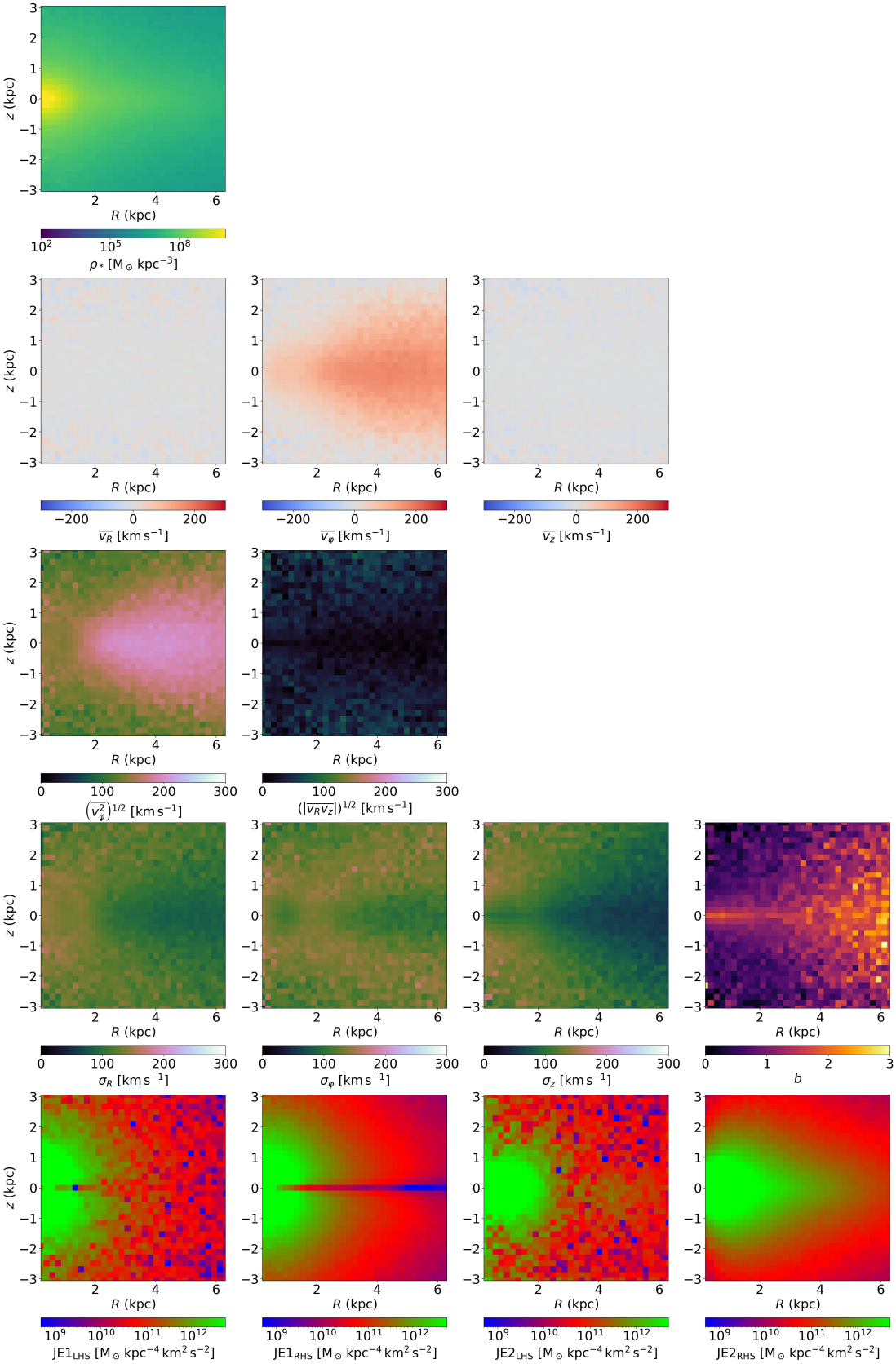


Figure H.25. Kinematic maps for the TNG516101 galaxy ($M_* = 4.88 \times 10^{10}\,\mathrm{M}_\odot$, $r_{1/2} = 3.25\,\mathrm{kpc}$, $q = 0.582$).

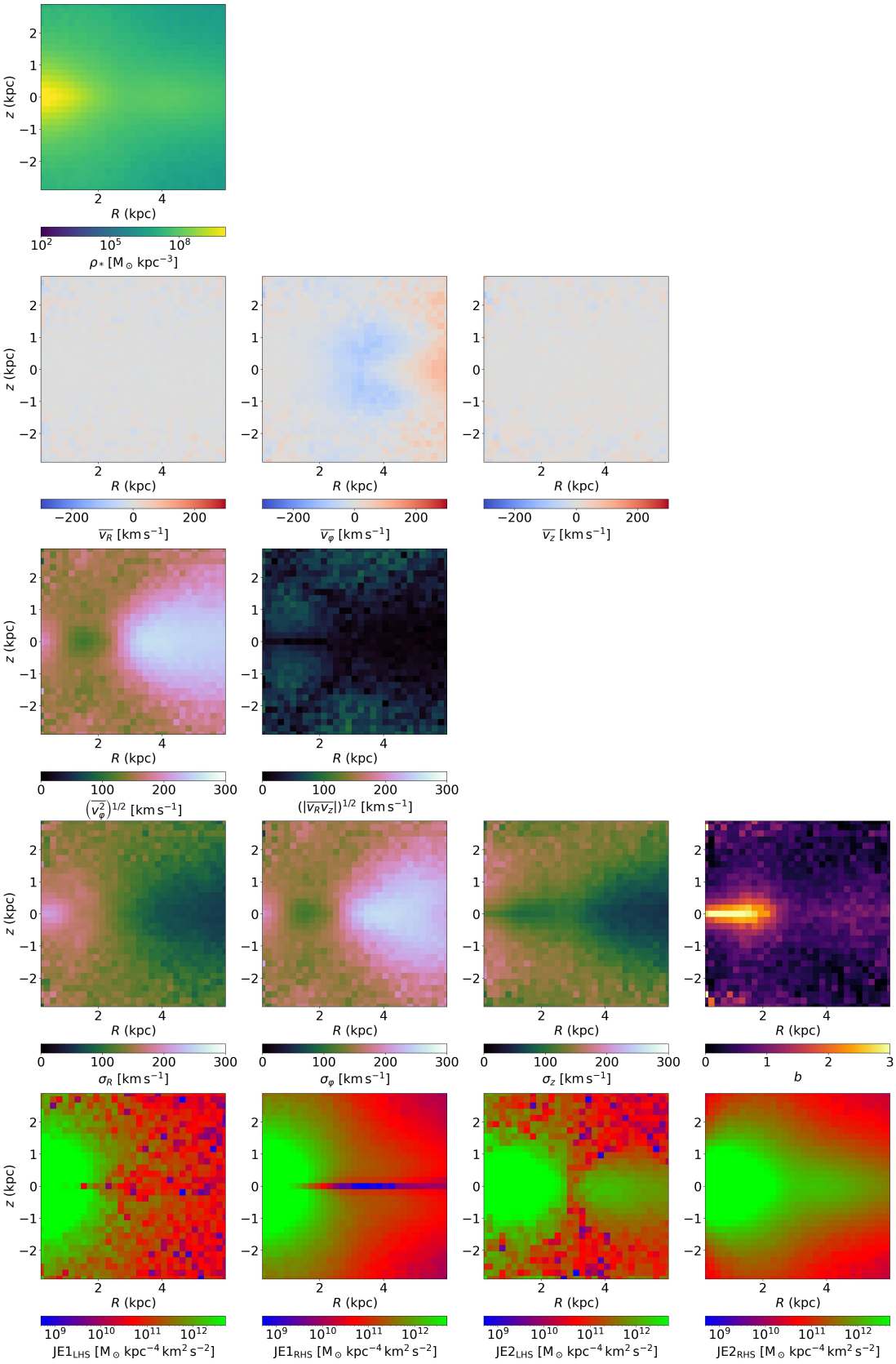


Figure H.26. Kinematic maps for the TNG543114 galaxy ($M_* = 6.55 \times 10^{10}\,\mathrm{M}_\odot$, $r_{1/2} = 3.09\,\mathrm{kpc}$, $q = 0.441$).

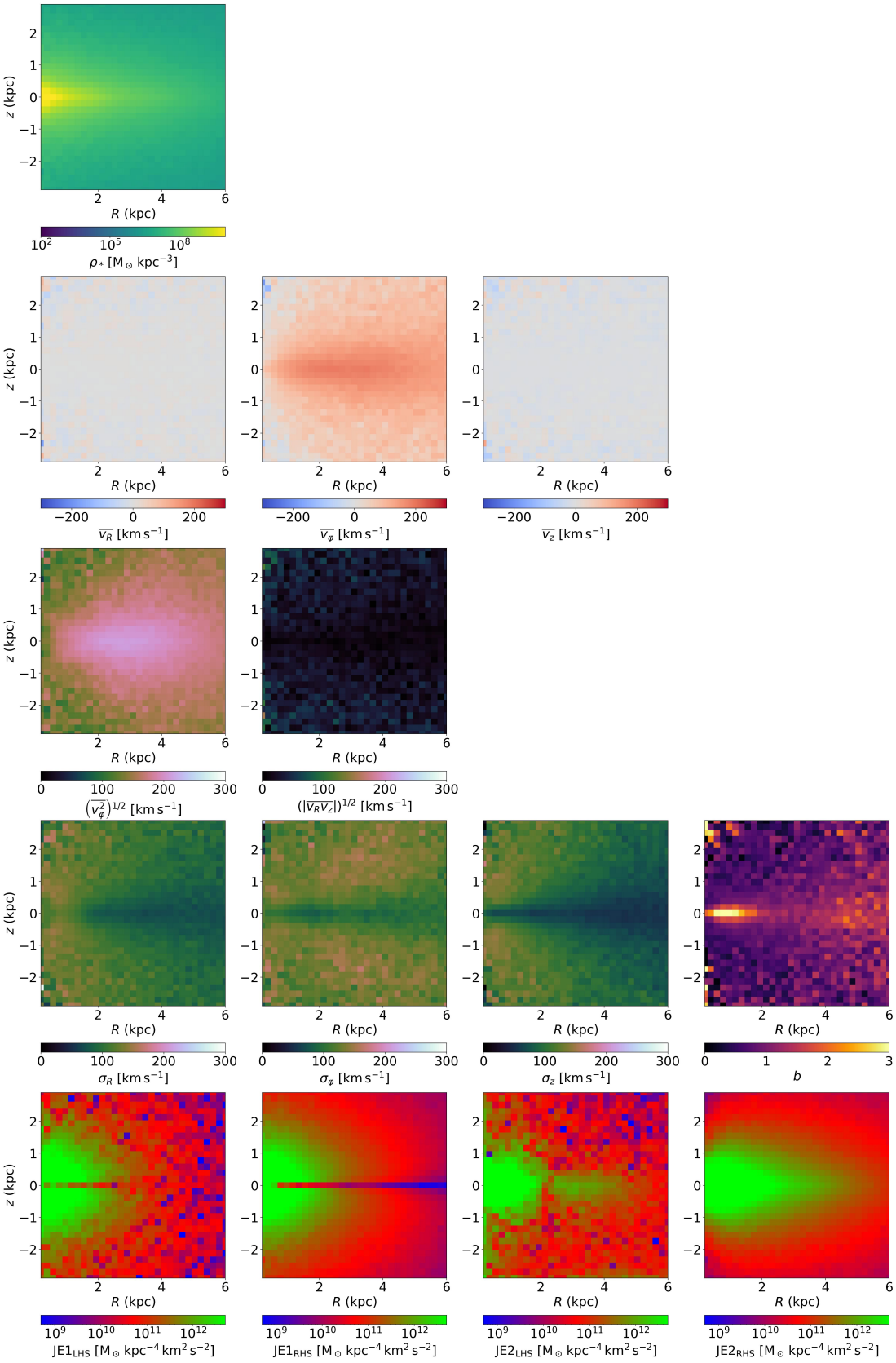


Figure H.27. Kinematic maps for the TNG546114 galaxy ($M_* = 4.54 \times 10^{10}\,\mathrm{M}_\odot$, $r_{1/2} = 3.10\,\mathrm{kpc}$, $q = 0.501$).

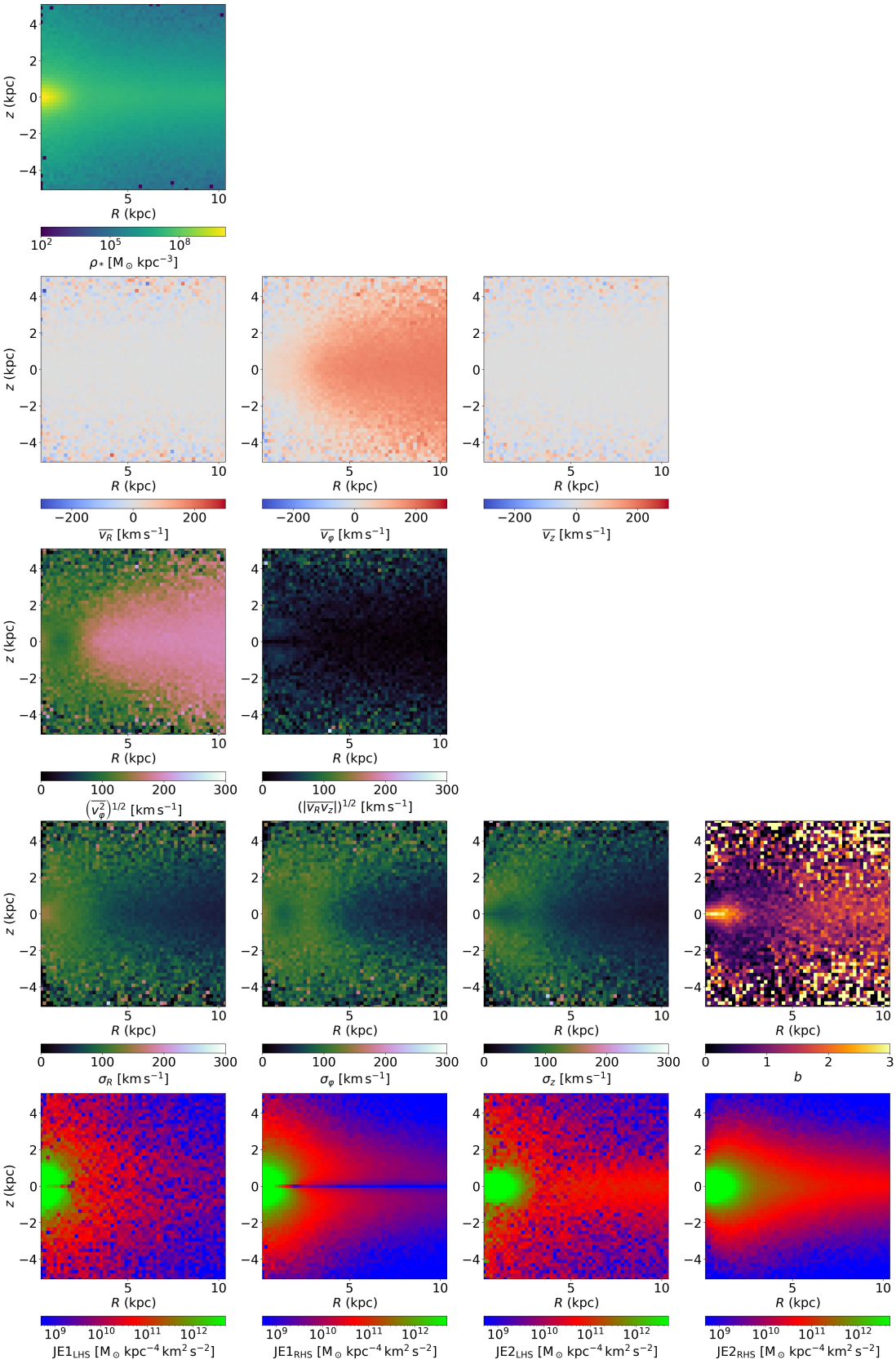


Figure H.28. Kinematic maps for the TNG563732 galaxy ($M_* = 3.67 \times 10^{10}\,\mathrm{M}_\odot$, $r_{1/2} = 5.29\,\mathrm{kpc}$, $q = 0.329$).

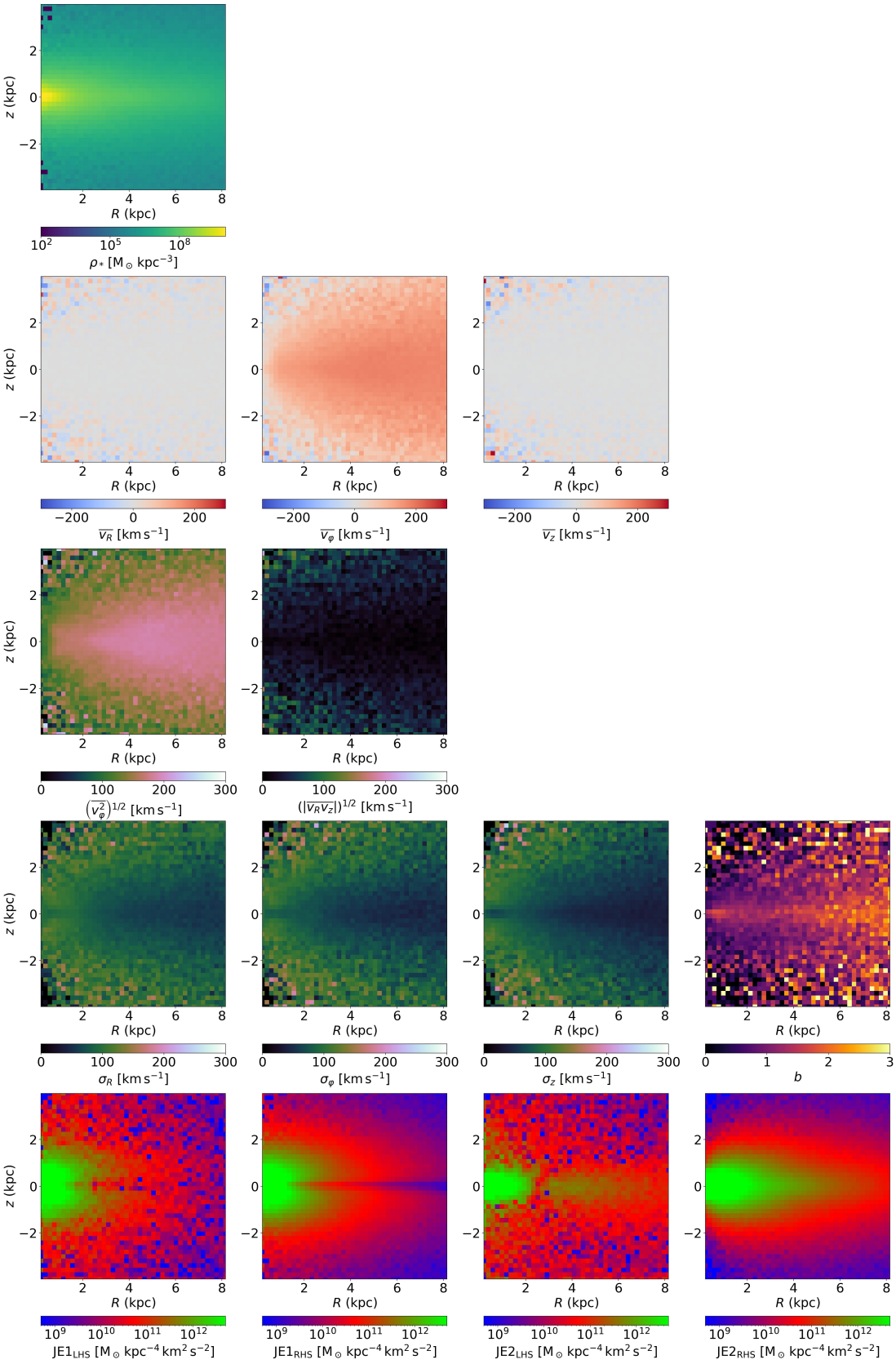


Figure H.29. Kinematic maps for the TNG572328 galaxy ($M_* = 4.34 \times 10^{10}\,\mathrm{M}_\odot$, $r_{1/2} = 4.18\,\mathrm{kpc}$, $q = 0.358$).

References

Andredakis, Y. C., R. F. Peletier, and M. Balcells (1995). "The shape of the luminosity profiles of bulges of spiral galaxies." In: *Monthly Notices of the Royal Astronomical Society* 275, pp. 874–888. DOI: 10.1093/mnras/275.3.874.

Arfken, G. B. and H. J. Weber (2005). *Mathematical methods for physicists (6th Ed.)* Elsevier Academic Press.

Baes, M. and L. Ciotti (2019). "Stellar systems following the $R^{1/m}$ luminosity law. IV. The total energy and the central concentration of galaxies". In: *Astronomy & Astrophysics* 630, A113, A113. DOI: 10.1051/0004-6361/201936354. arXiv: 1909.00959 [astro-ph.GA].

Baes, M. and G. Gentile (2011). "Analytical expressions for the deprojected Sérsic model". In: *Astronomy & Astrophysics* 525, A136, A136. DOI: 10.1051/0004-6361/201015716. arXiv: 1009.4713 [astro-ph.CO].

Baes, M. and E. van Hese (2011). "Analytical expressions for the deprojected Sérsic model. II. General expressions in terms of the Fox H function". In: *Astronomy & Astrophysics* 534, A69, A69. DOI: 10.1051/0004-6361/201117708. arXiv: 1108.1618 [astro-ph.CO].

Barmby, P. et al. (2007). "Structural Parameters for Globular Clusters in M31 and Generalizations for the Fundamental Plane". In: *The Astrophysical Journal* 133.6, pp. 2764–2786. DOI: 10.1086/516777. arXiv: 0704.2057 [astro-ph].

Barnabè, M. et al. (2006). "Hydrostatic models for the rotation of extra-planar gas in disk galaxies". In: *Astronomy & Astrophysics* 446.1, pp. 61–69. DOI: 10.1051/0004-6361:20053386. arXiv: astro-ph/0509021 [astro-ph].

Battaglia, G. et al. (2006). "The DART imaging and CaT survey of the Fornax dwarf spheroidal galaxy". In: *Astronomy & Astrophysics* 459.2, pp. 423–440. DOI: 10.1051/0004-6361:20065720. arXiv: astro-ph/0608370 [astro-ph].

Bender, R. (1988). "Velocity anisotropies and isophote shapes in elliptical galaxies." In: *Astronomy and Astrophysics* 193, pp. L7–L10.

Bendinelli, O., L. Ciotti, and G. Parmeggiani (1993). "Series inversion of Abel equation for very peaked profiles: The $R^{1/4}$-law". In: *Astronomy & Astrophysics* 279.2, pp. 668–673.

Bertin, G., L. Ciotti, and M. Del Principe (2002). "Weak homology of elliptical galaxies." In: *Astronomy and Astrophysics* 386, pp. 149–168. DOI: 10.1051/0004-6361:20020248. arXiv: astro-ph/0202208 [astro-ph].

Bertin, G. and A. L. Varri (2008). "The Construction of Nonspherical Models of Quasi-Relaxed Stellar Systems". In: *The Astrophysical Journal* 689.2, pp. 1005–1019. DOI: 10.1086/592684. arXiv: 0808.2432 [astro-ph].

Binney, J. (2010). "Distribution functions for the Milky Way". In: *Monthly Notices of the Royal Astronomical Society* 401.4, pp. 2318–2330. DOI: 10.1111/j.1365-2966.2009.15845.x. arXiv: 0910.1512 [astro-ph.GA].

Binney, J. and G. A. Mamon (1982). "M/L and velocity anisotropy from observations of spherical galaxies, or must M87 have a massive black hole?" In: *Monthly Notices of the Royal Astronomical Society* 200, pp. 361–375. DOI: 10.1093/mnras/200.2.361.

Binney, J. and S. Tremaine (2008). *Galactic Dynamics: Second Edition*. Princeton University Press.

Binney, J. and E. Vasiliev (2023). "Self-consistent models of our Galaxy". In: *Monthly Notices of the Royal Astronomical Society* 520.2, pp. 1832–1847. DOI: 10.1093/mnras/stad094. arXiv: 2206.03523 [astro-ph.GA].

Binney, J. (2005). "Rotation and anisotropy of galaxies revisited". In: *Monthly Notices of the Royal Astronomical Society* 363.3, pp. 937–942. DOI: 10.1111/j.1365-2966.2005.09495.x. arXiv: astro-ph/0504387 [astro-ph].

Blumenthal, G. R. et al. (1984). "Formation of galaxies and large-scale structure with cold dark matter." In: *Nature* 311, pp. 517–525. DOI: 10.1038/311517a0.

Caon, N., M. Capaccioli, and M. D'Onofrio (1993). "On the shape of the light profiles of early-type galaxies." In: *Monthly Notices of the Royal Astronomical Society* 265, pp. 1013–1021. DOI: 10.1093/mnras/265.4.1013. arXiv: astro-ph/9309013 [astro-ph].

Cappellari, M. (2008). "Measuring the inclination and mass-to-light ratio of axisymmetric galaxies via anisotropic Jeans models of stellar kinematics". In: *Monthly Notices of the Royal Astronomical Society* 390.1, pp. 71–86. DOI: 10.1111/j.1365-2966.2008.13754.x. arXiv: 0806.0042 [astro-ph].

— (2016). "Structure and Kinematics of Early-Type Galaxies from Integral Field Spectroscopy". In: *Annual Review of Astronomy and Astrophysics* 54, pp. 597–665. DOI: 10.1146/annurev-astro-082214-122432. arXiv: 1602.04267 [astro-ph.GA].

— (2020). "Efficient solution of the anisotropic spherically aligned axisymmetric Jeans equations of stellar hydrodynamics for galactic dynamics". In: *Monthly Notices of the Royal Astronomical Society* 494.4, pp. 4819–4837. DOI: 10.1093/mnras/staa959. arXiv: 1907.09894 [astro-ph.GA].

Cappellari, M., E. Emsellem, R. Bacon, et al. (2007). "The SAURON project - X. The orbital anisotropy of elliptical and lenticular galaxies: revisiting the (V/σ,) diagram with integral-field stellar kinematics". In: *Monthly Notices of the Royal Astronomical Society* 379.2, pp. 418–444. DOI: 10.1111/j.1365-2966.2007.11963.x. arXiv: astro-ph/0703533 [astro-ph].

Cappellari, M. et al. (2013). "The ATLAS^{3D} project - XX. Mass-size and mass-σ distributions of early-type galaxies: bulge fraction drives kinematics, mass-to-light ratio, molecular gas fraction and stellar initial mass function". In: *Monthly Notices of the Royal Astronomical Society* 432.3, pp. 1862–1893. DOI: 10.1093/mnras/stt644. arXiv: 1208.3523 [astro-ph.CO].

Cappellari, M. (2002). "Efficient multi-Gaussian expansion of galaxies". In: *Monthly Notices of the Royal Astronomical Society* 333.2, pp. 400–410. DOI: 10.1046/j.1365-8711.2002.05412.x. arXiv: astro-ph/0201430 [astro-ph].

— (2026). "Early-type galaxies: Elliptical and S0 galaxies, or fast and slow rotators". In: *Encyclopedia of Astrophysics, Volume 4*. Vol. 4, pp. 122–152. DOI: 10.1016/B978-0-443-21439-4.00109-7. arXiv: 2503.02746 [astro-ph.GA].

Cappellari, M., E. Emsellem, D. Krajnović, et al. (2011). "The ATLAS^{3D} project - I. A volume-limited sample of 260 nearby early-type galaxies: science goals and selection criteria". In:

Monthly Notices of the Royal Astronomical Society 413.2, pp. 813–836. DOI: 10.1111/j.1365-2966.2010.18174.x. arXiv: 1012.1551 [astro-ph.CO].

Cappellari, M., N. Scott, et al. (2013). "The ATLAS^{3D} project - XV. Benchmark for early-type galaxies scaling relations from 260 dynamical models: mass-to-light ratio, dark matter, Fundamental Plane and Mass Plane". In: *Monthly Notices of the Royal Astronomical Society* 432.3, pp. 1709–1741. DOI: 10.1093/mnras/stt562. arXiv: 1208.3522 [astro-ph.CO].

Caravita, C., L. Ciotti, and S. Pellegrini (2021). "Jeans modelling of axisymmetric galaxies with multiple stellar populations". In: *Monthly Notices of the Royal Astronomical Society* 506.1, pp. 1480–1497. DOI: 10.1093/mnras/stab1786. arXiv: 2102.09440 [astro-ph.GA].

Chandrasekhar, S. (1969). *Ellipsoidal figures of equilibrium*. Yale University Press, New Haven.

Ciotti, L. (1991). "Stellar systems following the R1/m luminosity law." In: *Astronomy & Astrophysics* 249, pp. 99–106.

Ciotti, L. and S. Pellegrini (1992). "Self-consistent two-component models of elliptical galaxies". In: *Monthly Notices of the Royal Astronomical Society* 255, pp. 561–571. DOI: 10.1093/mnras/255.4.561.

— (1996). "The energetics of flat and rotating early-type galaxies and their X-ray luminosity". In: *Monthly Notices of the Royal Astronomical Society* 279, p. 240. DOI: 10.1093/mnras/279.1.240.

Ciotti, L. (2021). *Introduction to Stellar Dynamics*. Cambridge University Press. DOI: 10.1017/9780511736117.

Congera, G. (2025). *Dynamics of prolate galaxies*. Master Thesis (University of Bologna, Master Degree in "Astrophysics and Cosmology").

Crain, R. A. and F. van de Voort (2023). "Hydrodynamical Simulations of the Galaxy Population: Enduring Successes and Outstanding Challenges". In: *Annual Review of Astronomy and Astrophysics* 61, pp. 473–515. DOI: 10.1146/annurev-astro-041923-043618. arXiv: 2309.17075 [astro-ph.GA].

D'Onofrio, M., M. Capaccioli, and N. Caon (1994). "On the shape of the light profiles of early-type galaxies - II. The (Dn/Ae)-<mu>e diagram." In: *Monthly Notices of the Royal Astronomical Society* 271, pp. 523–529. DOI: 10.1093/mnras/271.3.523.

de Vaucouleurs, G. (1948). "Recherches sur les Nebuleuses Extragalactiques". In: *Annales d'Astrophysique* 11, p. 247.

de Zeeuw, P. T. et al. (2002). "The SAURON project - II. Sample and early results". In: *Monthly Notices of the Royal Astronomical Society* 329.3, pp. 513–530. DOI: 10.1046/j.1365-8711.2002.05059.x. arXiv: astro-ph/0109511 [astro-ph].

Dehnen, W. (1993). "A Family of Potential-Density Pairs for Spherical Galaxies and Bulges". In: *Monthly Notices of the Royal Astronomical Society* 265, p. 250. DOI: 10.1093/mnras/265.1.250.

Diemer, B. et al. (2018). "Modeling the Atomic-to-molecular Transition in Cosmological Simulations of Galaxy Formation". In: *The Astrophysical Journal Supplement* 238.2, 33, p. 33. DOI: 10.3847/1538-4365/aae387. arXiv: 1806.02341 [astro-ph.GA].

Donnari, M. et al. (2019). "The star formation activity of IllustrisTNG galaxies: main sequence, UVJ diagram, quenched fractions, and systematics". In: *Monthly Notices of the Royal Astronomical Society* 485.4, pp. 4817–4840. DOI: 10.1093/mnras/stz712. arXiv: 1812.07584 [astro-ph.GA].

Emsellem, E., G. Monnet, and R. Bacon (1994). "The multi-gaussian expansion method: a tool for building realistic photometric and kinematical models of stellar systems I. The formalism". In: *Astronomy and Astrophysics* 285, pp. 723–738.

Emsellem, E., M. Cappellari, D. Krajnović, K. Alatalo, et al. (2011). "The ATLAS^{3D} project - III. A census of the stellar angular momentum within the effective radius of early-type galaxies: unveiling the distribution of fast and slow rotators". In: *Monthly Notices of the Royal Astronomical Society* 414.2, pp. 888–912. DOI: 10.1111/j.1365-2966.2011.18496.x. arXiv: 1102.4444 [astro-ph.CO].

Emsellem, E., M. Cappellari, D. Krajnović, G. van de Ven, et al. (2007). "The SAURON project - IX. A kinematic classification for early-type galaxies". In: *Monthly Notices of the Royal Astronomical Society* 379.2, pp. 401–417. DOI: 10.1111/j.1365-2966.2007.11752.x. arXiv: astro-ph/0703531 [astro-ph].

Emsellem, E., M. Cappellari, R. F. Peletier, et al. (2004). "The SAURON project - III. Integral-field absorption-line kinematics of 48 elliptical and lenticular galaxies". In: *Monthly Notices of the Royal Astronomical Society* 352.3, pp. 721–743. DOI: 10.1111/j.1365-2966.2004.07948.x. arXiv: astro-ph/0404034 [astro-ph].

Emsellem, E. and G. van de Ven (2008). "Formation of Central Massive Objects via Tidal Compression". In: *The Astrophysical Journal* 674.2, pp. 653–659. DOI: 10.1086/524720. arXiv: 0710.3161 [astro-ph].

Evans, N. W. (1993). "Simple galaxy models with massive haloes". In: *Monthly Notices of the Royal Astronomical Society* 260.1, pp. 191–201. DOI: 10.1093/mnras/260.1.191.

— (1994). "The power-law galaxies." In: *Monthly Notices of the Royal Astronomical Society* 267, pp. 333–360. DOI: 10.1093/mnras/267.2.333.

Evans, N. W. and P. T. de Zeeuw (1994). "Observable properties of the power-law galaxies." In: *Monthly Notices of the Royal Astronomical Society* 271, pp. 202–222. DOI: 10.1093/mnras/271.1.202.

Falcón-Barroso, J. et al. (2019). "The CALIFA view on stellar angular momentum across the Hubble sequence". In: *Astronomy & Astrophysics* 632, A59, A59. DOI: 10.1051/0004-6361/201936413. arXiv: 1910.06236 [astro-ph.GA].

Genel, S. et al. (2018). "The size evolution of star-forming and quenched galaxies in the IllustrisTNG simulation". In: *Monthly Notices of the Royal Astronomical Society* 474.3, pp. 3976–3996. DOI: 10.1093/mnras/stx3078. arXiv: 1707.05327 [astro-ph.GA].

Gerbal, D. et al. (1997). "The entropy of elliptical galaxies in Coma: a clue for a distance indicator". In: *Monthly Notices of the Royal Astronomical Society* 285.4, pp. L41–L45. DOI: 10.1093/mnras/285.4.L41. arXiv: astro-ph/9701078 [astro-ph].

Gerhard, O. E. and J. J. Binney (1996). "On the deprojection of axisymmetric bodies". In: *Monthly Notices of the Royal Astronomical Society* 279, p. 993. DOI: 10.1093/mnras/279.3.993. arXiv: astro-ph/9508116 [astro-ph].

Gradshteyn, I. S. et al. (2007). *Table of Integrals, Series, and Products*. Elsevier Academic Press.

Graham, A. W. and S. P. Driver (2005). "A Concise Reference to (Projected) Sérsic $R^{1/n}$ Quantities, Including Concentration, Profile Slopes, Petrosian Indices, and Kron Magnitudes". In: *Publications of the Astronomical Society of Australia* 22.2, pp. 118–127. DOI: 10.1071/AS05001. arXiv: astro-ph/0503176 [astro-ph].

Graham, A. W. and R. Guzmán (2003). "HST Photometry of Dwarf Elliptical Galaxies in Coma, and an Explanation for the Alleged Structural Dichotomy between Dwarf and Bright Elliptical Galaxies". In: *The Astrophysical Journal* 125.6, pp. 2936–2950. DOI: 10.1086/374992. arXiv: astro-ph/0303391 [astro-ph].

Graham, M. T. et al. (2018). "SDSS-IV MaNGA: stellar angular momentum of about 2300 galaxies: unveiling the bimodality of massive galaxy properties". In: *Monthly Notices of the Royal Astronomical Society* 477.4, pp. 4711–4737. DOI: 10.1093/mnras/sty504. arXiv: 1802.08213 [astro-ph.GA].

Harborne, K. E. et al. (2024). "From particles to pixels: how many particles do I really need to construct stellar kinematic mock observational measurements?" In: *Monthly Notices of the Royal Astronomical Society* 535.3, pp. 2844–2862. DOI: 10.1093/mnras/stae2526. arXiv: 2411.03791 [astro-ph.GA].

Hayashi, K., M. Chiba, and T. Ishiyama (2020). "Diversity of Dark Matter Density Profiles in the Galactic Dwarf Spheroidal Satellites". In: *The Astrophysical Journal* 904.1, 45, p. 45. DOI: 10.3847/1538-4357/abbe0a. arXiv: 2007.13780 [astro-ph.GA].

Hubble, E. P. (1926). "Extragalactic nebulae." In: *The Astrophysical Journal* 64, pp. 321–369. DOI: 10.1086/143018.

— (1936). *Realm of the Nebulae*. Yale University Press, New Haven.

Jeans, J. H. (1915). "On the theory of star-streaming and the structure of the universe". In: *Monthly Notices of the Royal Astronomical Society* 76, pp. 70–84. DOI: 10.1093/mnras/76.2.70.

— (1922). "The Motions of Stars in a Kapteyn Universe". In: *Monthly Notices of the Royal Astronomical Society* 82, pp. 122–132. DOI: 10.1093/mnras/82.3.122.

Jeans, J. H. (1928). *Astronomy and cosmogony*. Cambridge University Press. DOI: 10.1017/CBO9780511694363.

King, I. (1963). "Dynamical Models for Spherical Stellar Systems." In: *The Astrophysical Journal* 68, p. 282. DOI: 10.1086/109040.

Kormendy, J. and R. Bender (1996). "A Proposed Revision of the Hubble Sequence for Elliptical Galaxies". In: *Astrophysical Journal Letters* 464, p. L119. DOI: 10.1086/310095.

Kormendy, J., D. B. Fisher, et al. (2009). "Structure and Formation of Elliptical and Spheroidal Galaxies". In: *The Astrophysical Journal Supplement* 182.1, pp. 216–309. DOI: 10.1088/0067-0049/182/1/216. arXiv: 0810.1681 [astro-ph].

Krajnović, D. et al. (2011). "The ATLAS^{3D} project - II. Morphologies, kinemetric features and alignment between photometric and kinematic axes of early-type galaxies". In: *Monthly Notices of the Royal Astronomical Society* 414.4, pp. 2923–2949. DOI: 10.1111/j.1365-2966.2011.18560.x. arXiv: 1102.3801 [astro-ph.CO].

Kuzmin, G. (1956). "Model of the steady galaxy allowing of the triaxial distribution of velocities". In: *Astronomicheskii Zhurnal* 33, p. 27.

Li, H. et al. (2018). "SDSS-IV MaNGA: global stellar population and gradients for about 2000 early-type and spiral galaxies on the mass–size plane". In: *Monthly Notices of the Royal Astronomical Society* 476.2, pp. 1765–1775.

Lima Neto, G. B., D. Gerbal, and I. Márquez (1999). "The specific entropy of elliptical galaxies: an explanation for profile-shape distance indicators?" In: *Monthly Notices of the Royal Astronomical Society* 309.2, pp. 481–495. DOI: 10.1046/j.1365-8711.1999.02849.x. arXiv: astro-ph/9905048 [astro-ph].

Loubser, S. I. et al. (2020). "Dynamical masses of brightest cluster galaxies I: stellar velocity anisotropy and mass-to-light ratios". In: *Monthly Notices of the Royal Astronomical Society* 496.2, pp. 1857–1880. DOI: 10.1093/mnras/staa1682.

Marinacci, F. et al. (2018). "First results from the IllustrisTNG simulations: radio haloes and magnetic fields". In: *Monthly Notices of the Royal Astronomical Society* 480.4, pp. 5113–5139. DOI: 10.1093/mnras/sty2206. arXiv: 1707.03396 [astro-ph.CO].

Márquez, I. et al. (2000). "Gravo-thermal properties and formation of elliptical galaxies". In: *Astronomy & Astrophysics* 353, pp. 873–886. DOI: 10.48550/arXiv.astro-ph/9911464. arXiv: astro-ph/9911464 [astro-ph].

Mathai, A. M., R. K. Saxena, and H. J. Haubold (2009). *The H-function: theory and applications*. Springer Science & Business Media.

Mazure, A. and H. V. Capelato (2002). "Exact solutions for the spatial de Vaucouleurs and Sérsic laws and related quantities". In: *Astronomy & Astrophysics* 383, pp. 384–389. DOI: 10.1051/0004-6361:20011751. arXiv: astro-ph/0112147 [astro-ph].

Mellier, Y. and G. Mathez (1987). "Deprojection of the de Vaucouleurs R exp 1/4 brightness profile". In: *Astronomy & Astrophysics* 175.1-2, pp. 1–3.

Merola, M. (2024). *Dynamical modelling of the counterrotating stellar components in the S0 galaxy NGC 1366*. Master Thesis (University of Padua, Master Degree in "Astrophysics and Cosmology").

Miyamoto, M. and R. Nagai (1975). "Three-dimensional models for the distribution of mass in galaxies." In: *Publications of the Astronomical Society of Japan* 27, pp. 533–543.

Naiman, J. P. et al. (2018). "First results from the IllustrisTNG simulations: a tale of two elements - chemical evolution of magnesium and europium". In: *Monthly Notices of the Royal Astronomical Society* 477.1, pp. 1206–1224. DOI: 10.1093/mnras/sty618. arXiv: 1707.03401 [astro-ph.GA].

Negri, A., S. Pellegrini, and L. Ciotti (2013). "Disk dynamics and the X-ray emission of S0 and flat early-type galaxies". In: *Memorie della Società Astronomica Italiana* 84, p. 762. DOI: 10.48550/arXiv.1302.6725. arXiv: 1302.6725 [astro-ph.CO].

Nelson, D., A. Pillepich, V. Springel, R. Pakmor, et al. (2019). "First results from the TNG50 simulation: galactic outflows driven by supernovae and black hole feedback". In: *Monthly Notices of the Royal Astronomical Society* 490.3, pp. 3234–3261. DOI: 10.1093/mnras/stz2306. arXiv: 1902.05554 [astro-ph.GA].

Nelson, D., A. Pillepich, V. Springel, R. Weinberger, et al. (2018). "First results from the IllustrisTNG simulations: the galaxy colour bimodality". In: *Monthly Notices of the Royal Astronomical Society* 475.1, pp. 624–647. DOI: 10.1093/mnras/stx3040. arXiv: 1707.03395 [astro-ph.GA].

Nelson, D., V. Springel, et al. (2019). "The IllustrisTNG simulations: public data release". In: *Computational Astrophysics and Cosmology* 6.1, 2, p. 2. DOI: 10.1186/s40668-019-0028-x. arXiv: 1812.05609 [astro-ph.GA].

Pandya, V. et al. (2024). "Galaxies Going Bananas: Inferring the 3D Geometry of High-redshift Galaxies with JWST-CEERS". In: *The Astrophysical Journal* 963.1, 54, p. 54. DOI: 10.3847/1538-4357/ad1a13. arXiv: 2310.15232 [astro-ph.GA].

Pechetti, R. et al. (2020). "Luminosity Models and Density Profiles for Nuclear Star Clusters for a Nearby Volume-limited Sample of 29 Galaxies". In: *The Astrophysical Journal* 900.1, 32, p. 32. DOI: 10.3847/1538-4357/abaaa7. arXiv: 1911.09686 [astro-ph.GA].

Pillepich, A., D. Nelson, L. Hernquist, et al. (2018). "First results from the IllustrisTNG simulations: the stellar mass content of groups and clusters of galaxies". In: *Monthly Notices of the Royal Astronomical Society* 475.1, pp. 648–675. DOI: 10.1093/mnras/stx3112. arXiv: 1707.03406 [astro-ph.GA].

Pillepich, A., D. Nelson, V. Springel, et al. (2019). "First results from the TNG50 simulation: the evolution of stellar and gaseous discs across cosmic time". In: *Monthly Notices of the Royal*

Astronomical Society 490.3, pp. 3196–3233. DOI: 10.1093/mnras/stz2338. arXiv: 1902.05553 [astro-ph.GA].

Pillepich, A., V. Springel, et al. (2018). "Simulating galaxy formation with the IllustrisTNG model". In: *Monthly Notices of the Royal Astronomical Society* 473.3, pp. 4077–4106. DOI: 10.1093/mnras/stx2656. arXiv: 1703.02970 [astro-ph.GA].

Planck Collaboration et al. (2016). "Planck 2015 results. XIII. Cosmological parameters". In: *Astronomy Astrophysics* 594, A13, A13. DOI: 10.1051/0004-6361/201525830. arXiv: 1502.01589 [astro-ph.CO].

Plummer, H. C. (1911). "On the problem of distribution in globular star clusters". In: *Monthly Notices of the Royal Astronomical Society* 71, pp. 460–470. DOI: 10.1093/mnras/71.5.460.

Posti, L. et al. (2015). "Action-based distribution functions for spheroidal galaxy components". In: *Monthly Notices of the Royal Astronomical Society* 447.4, pp. 3060–3068. DOI: 10.1093/mnras/stu2608. arXiv: 1411.7897 [astro-ph.GA].

Poveda, A., R. Iturriaga, and I. Orozco (1960). "Densidades, potenciales y funciones asociadas en una galaxia esférica reducida". In: *Boletin de los Observatorios Tonantzintla y Tacubaya* 2, pp. 3–18.

Prudnikov, A., Y. A. Brychkov, O. Marichev, et al. (1990). "Integrals and series, volume 3: more special functions". In: *Gordon and Breech Science*.

Prugniel, P. and F. Simien (1997). "The fundamental plane of early-type galaxies: non-homology of the spatial structure." In: *Astronomy & Astrophysics* 321, pp. 111–122.

Rodriguez-Gomez, V. et al. (2019). "The optical morphologies of galaxies in the IllustrisTNG simulation: a comparison to Pan-STARRS observations". In: *Monthly Notices of the Royal Astronomical Society* 483.3, pp. 4140–4159. DOI: 10.1093/mnras/sty3345. arXiv: 1809.08239 [astro-ph.GA].

Romanowsky, A. J. and C. S. Kochanek (1997). "Structural and Dynamical Uncertainties in Modelling Axisymmetric Elliptical Galaxies". In: *Monthly Notices of the Royal Astronomical Society* 287.1, pp. 35–50. DOI: 10.1093/mnras/287.1.35. arXiv: astro-ph/9609202 [astro-ph].

Rubin, V. C., J. A. Graham, and J. D. P. Kenney (1992). "Cospatial Counterrotating Stellar Disks in the Virgo E7/S0 Galaxy NGC 4550". In: *Astrophysical Journal Letters* 394, p. L9. DOI: 10.1086/186460.

Sandage, A. (1961). *The Hubble atlas of galaxies*. Vol. 618. 2. Carnegie Institution of Washington Washington, DC.

— (2005). "The Classification of Galaxies: Early History and Ongoing Developments". In: *Annual Review of Astronomy Astrophysics* 43.1, pp. 581–624. DOI: 10.1146/annurev.astro.43.112904.104839.

Satoh, C. (1980). "Dynamical Models of Axisymmetric Galaxies and Their Applications to the Elliptical Galaxy NGC4697". In: *Publications of the Astronomical Society of Japan* 32, p. 41.

Schwarzschild, M. (1979). "A numerical model for a triaxial stellar system in dynamical equilibrium." In: *The Astrophysical Journal* 232, pp. 236–247. DOI: 10.1086/157282.

Scott, N. et al. (2015). "The SAMI Pilot Survey: the fundamental and mass planes in three low-redshift clusters". In: *Monthly Notices of the Royal Astronomical Society* 451.3, pp. 2723–2734. DOI: 10.1093/mnras/stv1127. arXiv: 1505.04354 [astro-ph.GA].

Sérsic, J. L. (1968). *Atlas de Galaxias Australes*. Cordoba, Argentina: Observatorio Astronomico.

Shi, R. et al. (2024). "Inferring the Mass Content of Galaxy Clusters with Satellite Kinematics and Jeans Anisotropic Modeling". In: *The Astrophysical Journal* 973.2, 82, p. 82. DOI: 10.3847/1538-4357/ad64cf. arXiv: 2407.11721 [astro-ph.CO].

Simonneau, E. and F. Prada (2004). "Structural Properties of Spherical Galaxies: a Semi-Analytical Approach". In: *Revista Mexicana de Astronomía y Astrofísica* 40, pp. 69–79.

Smet, C. O., S. Posacki, and L. Ciotti (2015). "Miyamoto-Nagai discs embedded in the Binney logarithmic potential: analytical solution of the two-integrals Jeans equations". In: *Monthly Notices of the Royal Astronomical Society* 448.3, pp. 2921–2933. DOI: 10.1093/mnras/stv202. arXiv: 1412.4794 [astro-ph.GA].

Springel, V. et al. (2018). "First results from the IllustrisTNG simulations: matter and galaxy clustering". In: *Monthly Notices of the Royal Astronomical Society* 475.1, pp. 676–698. DOI: 10.1093/mnras/stx3304. arXiv: 1707.03397 [astro-ph.GA].

Stiavelli, M. and G. Bertin (1985). "A family of self-consistent models of elliptical galaxies." In: *Monthly Notices of the Royal Astronomical Society* 217, pp. 735–752. DOI: 10.1093/mnras/217.4.735.

Strateva, I. et al. (2001). "Color Separation of Galaxy Types in the Sloan Digital Sky Survey Imaging Data". In: *The Astronomical Journal* 122.4, pp. 1861–1874. DOI: 10.1086/323301. arXiv: astro-ph/0107201 [astro-ph].

Surti, T. et al. (2024). "The Central Kinematics and Black Hole Mass of 4C+37.11". In: *The Astrophysical Journal* 960.2, 110, p. 110. DOI: 10.3847/1538-4357/ad14fa.

Syer, D. and S. Tremaine (1996). "Made-to-measure N-body systems". In: *Monthly Notices of the Royal Astronomical Society* 282.1, pp. 223–233. DOI: 10.1093/mnras/282.1.223. arXiv: astro-ph/9605061 [astro-ph].

Terzić, B. and A. W. Graham (2005). "Density-potential pairs for spherical stellar systems with Sérsic light profiles and (optional) power-law cores". In: *Monthly Notices of the Royal Astronomical Society* 362.1, pp. 197–212. DOI: 10.1111/j.1365-2966.2005.09269.x. arXiv: astro-ph/0506192 [astro-ph].

Toomre, A. (1963). "On the Distribution of Matter Within Highly Flattened Galaxies." In: *The Astrophysical Journal* 138, p. 385. DOI: 10.1086/147653.

Trujillo, I. et al. (2002). "Triaxial stellar systems following the $r^{1/n}$ luminosity law: an analytical mass-density expression, gravitational torques and the bulge/disc interplay". In: *Monthly Notices of the Royal Astronomical Society* 333.3, pp. 510–516. DOI: 10.1046/j.1365-8711.2002.05367.x. arXiv: astro-ph/0201485 [astro-ph].

van de Sande, J. et al. (2021). "The SAMI Galaxy Survey: a statistical approach to an optimal classification of stellar kinematics in galaxy surveys". In: *Monthly Notices of the Royal Astronomical Society* 505.2, pp. 3078–3106. DOI: 10.1093/mnras/stab1490. arXiv: 2011.08199 [astro-ph.GA].

van de Ven, G. and A. van der Wel (2021). "Deprojecting Sérsic Profiles for Arbitrary Triaxial Shapes: Robust Measures of Intrinsic and Projected Galaxy Sizes". In: *The Astrophysical Journal* 914.1, 45, p. 45. DOI: 10.3847/1538-4357/abf047. arXiv: 2104.01810 [astro-ph.GA].

van den Bosch, F. C. (1997). "On the uncertainties of the central density in axisymmetric galaxies resulting from deprojection". In: *Monthly Notices of the Royal Astronomical Society* 287.3, pp. 543–555. DOI: 10.1093/mnras/287.3.543. arXiv: astro-ph/9611145 [astro-ph].

van den Bosch, R. C. E. and G. van de Ven (2009). "Recovering the intrinsic shape of early-type galaxies". In: *Monthly Notices of the Royal Astronomical Society* 398.3, pp. 1117–1128. DOI: 10.1111/j.1365-2966.2009.15177.x. arXiv: 0811.3474 [astro-ph].

Vega-Ferrero, J. et al. (2024). "On the Nature of Disks at High Redshift Seen by JWST/CEERS with Contrastive Learning and Cosmological Simulations". In: *The Astrophysical Journal* 961.1, 51, p. 51. DOI: 10.3847/1538-4357/ad05bb. arXiv: 2302.07277 [astro-ph.CO].

Vitral, E. and G. A. Mamon (2020). "A precise analytical approximation for the deprojection of the Sérsic profile". In: *Astronomy & Astrophysics* 635, A20, A20. DOI: 10.1051/0004-6361/201937202. arXiv: 2001.03121 [astro-ph.GA].

— (2021). "Does NGC 6397 contain an intermediate-mass black hole or a more diffuse inner subcluster?" In: *Astronomy & Astrophysics* 646, A63, A63. DOI: 10.1051/0004-6361/202039650. arXiv: 2010.05532 [astro-ph.GA].

Vitral, E., R. P. van der Marel, et al. (2024). "HSTPROMO Internal Proper-motion Kinematics of Dwarf Spheroidal Galaxies. I. Velocity Anisotropy and Dark Matter Cusp Slope of Draco". In: *The Astrophysical Journal* 970.1, 1, p. 1. DOI: 10.3847/1538-4357/ad571c. arXiv: 2407.07769 [astro-ph.GA].

Vogelsberger, M. et al. (2014). "Introducing the Illustris Project: simulating the coevolution of dark and visible matter in the Universe". In: *Monthly Notices of the Royal Astronomical Society* 444.2, pp. 1518–1547. DOI: 10.1093/mnras/stu1536. arXiv: 1405.2921 [astro-ph.CO].

Walo-Martín, D. et al. (2020). "Kinematic analysis of EAGLE simulations: evolution of λ_{Re} and its connection with mergers and gas accretion". In: *Monthly Notices of the Royal Astronomical Society* 494.4, pp. 5652–5665. DOI: 10.1093/mnras/staa1066. arXiv: 2004.08598 [astro-ph.GA].

Wang, B., M. Cappellari, and Y. Peng (2021). "Physical explanation for the galaxy distribution on the (λ_R, ε) and (V/σ, ε) diagrams or for the limit on orbital anisotropy". In: *Monthly Notices of the Royal Astronomical Society* 500.1, pp. L27–L31. DOI: 10.1093/mnrasl/slaa176.

Wang, B., Y. Peng, et al. (2024). "On the Kinematic Nature of Apparent Disks at High Redshifts: Local Counterparts are Not Dominated by Ordered Rotation but by Tangentially Anisotropic Random Motion". In: *The Astrophysical Journall* 973.1, L29, p. L29. DOI: 10.3847/2041-8213/ad772d. arXiv: 2408.10735 [astro-ph.GA].

Weinberger, R. et al. (2017). "Simulating galaxy formation with black hole driven thermal and kinetic feedback". In: *Monthly Notices of the Royal Astronomical Society* 465.3, pp. 3291–3308. DOI: 10.1093/mnras/stw2944. arXiv: 1607.03486 [astro-ph.GA].

White, S. D. M. and M. J. Rees (1978). "Core condensation in heavy halos: a two-stage theory for galaxy formation and clustering." In: *Monthly Notices of the Royal Astronomical Society* 183, pp. 341–358. DOI: 10.1093/mnras/183.3.341.

Young, P. J. (1976). "Tables of functions for a spherical galaxy obeying the 7-1/1 law in projection". In: *The Astrophysical Journal* 81, p. 807. DOI: 10.1086/111959.

Zemp, M. et al. (2011). "On Determining the Shape of Matter Distributions". In: *The Astrophysical Journal Supplement* 197.2, 30, p. 30. DOI: 10.1088/0067-0049/197/2/30. arXiv: 1107.5582 [astro-ph.IM].

Zhu, K. et al. (2023). "MaNGA DynPop - I. Quality-assessed stellar dynamical modelling from integral-field spectroscopy of 10K nearby galaxies: a catalogue of masses, mass-to-light ratios, density profiles, and dark matter". In: *Monthly Notices of the Royal Astronomical Society* 522.4, pp. 6326–6353. DOI: 10.1093/mnras/stad1299.